

**THE DEVELOPMENT AND APPLICATIONS OF NONLINEAR  
VIBRATIONAL SPECTROSCOPY FOR MATERIAL AND  
BIOLOGICAL STUDIES**

by

Chi Zhang

A dissertation submitted in partial fulfillment  
of the requirements for the degree of  
Doctor of Philosophy  
(Chemistry)  
in the University of Michigan  
2014

Doctoral Committee:

Professor Zhan Chen, Chair  
Assistant Professor Hui Deng  
Professor Raoul Kopelman  
Associate Professor Kevin J. Kubarych

© Chi Zhang

---

All rights reserved  
2014

# **DEDICATION**

To my family

## ACKNOWLEDGEMENTS

I would like to sincerely thank my advisor, Professor Zhan Chen for his support on my PhD work. He granted me very enjoyable and fruitful five years studying in his lab at the University of Michigan. He kindly instructed and guided me towards my scientific accomplishment and academic targets. He has also supported me financially with his best efforts and granted me enough research freedoms. The most important achievement I developed working with him was the extensive interest in doing science, which has already become my future career goal after graduation. Without his support in letting me attending summer workshops in nonlinear spectroscopy and imaging, I couldn't have established my academic interest in and scientific connections to my future postdoc work. Dr. Chen is not only an excellent researcher, but also a great teacher and an understanding mentor.

I have made a lot of friends in the five years at Michigan, especially with my colleagues working in Chen lab. It is always difficult to believe that I will leave everybody in a few weeks. I still clearly remember the first day I came to the lab, when everybody was kindly helping me to get familiar with everything. I appreciate the help from everybody that overlapped with me. For my colleagues joining the lab in my same year, Josh, Yuwei, Lauren and Bei, for younger members Jeanne, John,

Chuan, Peipei, Yaoxin, Mingyu and Nathan, for postdocs Alex, Xiaofeng, Pei, Fugen, Xiaoxian, Lei and Qiuming, as well as for visiting scholars and visiting students Dawei, Ting, Junqing, Fujuan, and Jintao, who will be sharing the great memories with me, thank you all for giving me help and support in these years. It's my great pleasure to be one of the Chen lab nerds. I would like to give my special thanks to Jie Wang, our former lab member, who gave me extensive help in the writing of Chapter 6.

I would also like to thank professors Raoul Kopelman, Kevin Kubarych, and Hui Deng, for being my thesis committee members. I appreciate their time and effort for helping me to achieve my doctoral degree.

I want to give my special thanks to my collaborators, without whom a large part of this thesis would not be possible. I appreciate Dr. Nick Shephard, Dr. Susan Rhodes, Professors Gary Smith and Jonathan Wilker for their time and valuable discussion with me on my work. I would also like to thank Professors Xueding Wang and Garth Simpson, Dr. Zhixing Xie and Dr. Jing Wu, from whom I have learnt a great deal during my PhD years.

I am grateful for the financial support from the Semiconductor Research Corporation. The funding supported me for much of my graduate career as well as helped to supply me with the resources necessary to complete my work.

In the end I want to thank my family, my father, mother, father-in-law, mother-

in-law, and especially my wife Yuying. No matter when I feel disappointed, I always have her most encouraging support. No matter when I feel exhausted, I always recover with great energy with her help. No matter when I feel lost, I am always able to find my way back with her suggestion. I appreciate her for giving me a warm family and my daughter Chloe. I also want to thank Chloe for giving me so much pleasure watching her growing up.

Chi Zhang

2014-03-14

# TABLE OF CONTENTS

<b>DEDICATION.....</b>	<b>ii</b>
<b>ACKNOWLEDGEMENTS .....</b>	<b>iii</b>
<b>LIST OF FIGURES .....</b>	<b>xi</b>
<b>LIST OF TABLES .....</b>	<b>xx</b>
<b>LIST OF ABBREVIATIONS .....</b>	<b>xxi</b>
<b>CHAPTER 1 INTRODUCTION.....</b>	<b>1</b>
<b>1.1 Motivation.....</b>	<b>1</b>
<b>1.2 Sum Frequency Generation (SFG) Vibrational Spectroscopy .....</b>	<b>4</b>
<b>1.2.1 SFG Background.....</b>	<b>4</b>
<b>1.2.2 SFG Selection Rule .....</b>	<b>8</b>
<b>1.2.3 SFG Experimental Setup.....</b>	<b>8</b>
<b>1.2.4 Basic SFG Theory .....</b>	<b>10</b>
<b>1.2.5 Molecular Orientation Calculation of Methyl Group Using Polarized SFG Spectroscopy .....</b>	<b>13</b>
<b>1.3 Presented Research.....</b>	<b>17</b>
<b>1.4 References.....</b>	<b>19</b>
<b>CHAPTER 2 SFG STUDIES ON THE BURIED POLY(DIMETHYL SILOXANE) (PDMS) ADHESIVE INTERFACES .....</b>	<b>23</b>
<b>2.1 Background and Motivation .....</b>	<b>23</b>
<b>2.2 Molecular Orientation Determination of PDMS Material at Buried Interfaces .....</b>	<b>26</b>
<b>2.2.1 Materials Used in the Research and Sample Preparation .....</b>	<b>26</b>
<b>2.2.2 PDMS Methyl Group Orientation Calculation Method.....</b>	<b>28</b>
<b>2.2.4 SFG Experimental Results .....</b>	<b>32</b>
<b>2.2.5 Deriving Molecular Orientation of PDMS Methyl Groups at Interfaces.....</b>	<b>37</b>

2.2.6 A Method to Derive the Absolute Orientation of PDMS Methyl Groups at Interfaces .....	47
2.2.7 Surface Hydrophobicity Studies and Their Relation to PDMS Interfacial Molecular Orientation.....	51
2.2.8 Conclusion .....	52
2.2.9 Appendix.....	53
2.3 Mechanical Adhesion Test .....	58
2.4 The Study of Methoxy-silane Adhesion Promoters at the PDMS/PET Interface.....	59
2.4.1 Materials Used in the Research and Sample Preparation .....	59
2.4.2 Interfaces between $d_4$ -PET and MVS or Silicone (Without Silanes).....	60
2.4.3 Interfaces between $d_4$ -PET and Silane or Silane-MVS Mixture.....	62
2.4.4 Interfaces between $d_4$ -PET and Uncured Silicone Mixed with Silane or Silane-MVS Mixture.....	65
2.4.5 Interfaces between $d_4$ -PET and Cured Silicone Mixed with Silane or Silane-MVS Mixture.....	67
2.4.6 Mechanical Adhesion Test Results.....	68
2.4.7 The Relation between Interfacial Molecular Ordering and Adhesion .....	69
2.4.8 Conclusion .....	71
2.4.9 Appendix.....	72
2.5 The Study of Ethoxy-silane Adhesion Promoters at PDMS/PET Interface .....	76
2.5.1 Materials Used in the Research and Sample Preparation .....	76
2.5.2 Mechanical Adhesion Test .....	77
2.5.3 SFG Experimental Results on $d_4$ -PET and Silane or Silane-MVS Mixture Interfaces .....	79
2.5.4 Silane Incorporated into PDMS .....	81
2.5.5 The Relation between Interfacial Molecular Ordering and Adhesion .....	87
2.5.6 Conclusion .....	93
2.6 Conclusions.....	93
2.7 References .....	95
<b>CHAPTER 3 MOLECULAR LEVEL UNDERSTANDING ON BURIED EPOXY ADHESIVE INTERFACES.....</b>	<b>98</b>



<b>3.1 Motivation.....</b>	<b>98</b>
<b>3.2 Epoxy Curing Chemistry .....</b>	<b>100</b>
<b>3.3 Interfacial Molecular Ordering and Its Relation to Adhesion .....</b>	<b>102</b>
<b>3.3.1 The Epoxy Systems and Sample Preparation .....</b>	<b>102</b>
<b>3.3.2 SFG Experimental Results of a Model Epoxy in Contact with PET.....</b>	<b>104</b>
<b>3.3.3 Interfacial Molecular Ordering and Its Relation to Adhesion .....</b>	<b>109</b>
<b>3.3.5 SFG Experimental Results of Commercial Epoxy Materials in Contact with Polymers.....</b>	<b>110</b>
<b>3.3.7 Conclusion .....</b>	<b>114</b>
<b>3.4 Adhesion Mechanism between Epoxy and PET.....</b>	<b>115</b>
<b>3.4.1 Materials and Experimental Methods .....</b>	<b>116</b>
<b>3.4.2 Epoxy/PET Interface .....</b>	<b>118</b>
<b>3.4.2 Amine/PET Interface.....</b>	<b>123</b>
<b>3.4.3 Amine Diffusion into PET .....</b>	<b>125</b>
<b>3.4.4 Epoxy-amine/PET Interface .....</b>	<b>128</b>
<b>3.4.5 Silane Incorporation into Epoxy-amine System .....</b>	<b>131</b>
<b>3.4.6 Adhesion Mechanism between PET and Epoxy-amine.....</b>	<b>136</b>
<b>3.4.7 Conclusion .....</b>	<b>139</b>
<b>3.5 Conclusions.....</b>	<b>140</b>
<b>3.6 References .....</b>	<b>141</b>

**CHAPTER 4 SFG SPECTROSCOPY STUDIES ON BIOLOGICAL INTERFACES  
SUPPLEMENTED BY ATR-FTIR SPECTROSCOPY: LIPID TRANSBILAYER  
MOVEMENT IN A MODEL CELL MEMBRANE.....**

<b>4.1 Background and Motivation .....</b>	<b>143</b>
<b>4.2 Molecules Used in the Study .....</b>	<b>146</b>
<b>4.3 SFG Spectroscopy Study of Lipid Transbilayer Movement .....</b>	<b>148</b>
<b>4.3.1 SFG Spectroscopy Experimental Geometry.....</b>	<b>148</b>
<b>4.3.2 Using SFG to Measure Lipid Translocation in a Lipid Bilayer .....</b>	<b>150</b>
<b>4.3.3 Lipid Translocation in dDPPG-DPPG Bilayer Induced by PEI at Different Temperatures .....</b>	<b>153</b>

4.3.4 Lipid Translocation in dDSPC-DSPC Bilayer Induced by PEI at Different Temperatures .....	157
4.3.5 Lipid Translocation in dPPC-DPPC Bilayer Induced by PEI at Room Temperature.....	161
4.4 ATR-FTIR Spectroscopy Study of PEI lipid bilayer Interaction.....	162
4.4.1 The Formation of a Lipid Bilayer on an ATR Crystal.....	163
4.4.2 ATR-FTIR Experimental Results .....	165
4.5 Significance of the Research .....	167
4.6 Conclusion .....	168
4.7 References.....	170
<b>CHAPTER 5 THE DEVELOPMENT OF MULTIMODAL SYSTEMS INVOLVING SFG SPECTROSCOPY .....</b>	<b>173</b>
5.1 Motivation.....	173
5.2 Combine SFG with CARS Spectroscopy for Material Studies.....	174
5.2.1 Motivation.....	174
5.2.2 System Design for the Combined Spectroscopic Technique .....	175
5.2.3 Polymer Thin Film Study Using the Combined Spectroscopic Technique .....	176
5.2.4 The Sensitivity Measurement of the CARS Spectroscopy System .....	178
5.2.5 Applying SFG and CARS Spectroscopies to Study Plasticizers.....	180
5.2.6 Conclusion .....	180
5.3 Combine SFG Spectroscopy with Optical Microscopy for Buried Biointerface Studies .....	181
5.3.1 Motivation.....	181
5.3.2 System Design of TIR-SFG Spectroscopy Combined with Optical Microscopy....	183
5.3.3 Proof of Concept Experiments.....	185
5.3.4 TIR-SFG Study of Cells and Solid Substrate Interface .....	186
5.3.5 TIR-SFG Study of Mussel Adhesive and Substrate Interface.....	188
5.3.5 Conclusion .....	190
5.4 Combine SFG Spectroscopy with TIRF Microscopy to Study Buried Biointerfaces....	191
5.4.1 Motivation.....	191

5.4.2 System Design of TIR-SFG Spectroscopy Combined with TIRF Microscopy.....	192
5.4.3 SFG and TIRF Study of Polystyrene Fluorescent Beads .....	193
5.4.4 SFG and TIRF Study of Fluorescent Labeled Lipid Monolayer.....	195
5.4.5 Conclusion .....	200
5.5 References .....	201
<b>CHAPTER 6 BOND ADDITIVITY THEORY IN COHERENT ANTI-STOKES RAMAN SCATTERING SPECTROSCOPY.....</b>	<b>203</b>
6.1 Motivation.....	203
6.2 Theoretical Development of Bond Additivity Method in CARS .....	205
6.2.1 Third Order Nonlinear Susceptibility and Molecular Hyperpolarizability .....	205
6.2.2 Bond Additivity for Methyl Group C-H Vibrational Stretching .....	211
6.2.3 Connecting CARS Measurement with Raman Depolarization Measurement.....	216
6.3 Experimental Results.....	217
6.4 Discussion.....	220
6.5 Conclusion .....	225
6.6 Appendix.....	226
6.6.1 The General Form of Third Order Nonlinear Hyperpolarizability Tensor.....	226
6.6.2 The Calculated Susceptibility Matrices .....	227
6.5 References .....	230
<b>CHAPTER 7 SUMMARY AND CONCLUSIONS.....</b>	<b>232</b>

## LIST OF FIGURES

<p><b>Figure 1-1. Layout of the EKSPLA SFG system used in this research. Adapted from <a href="http://www.ekspla.com/">http://www.ekspla.com/</a>. .....</b></p>	<b>9</b>
<p><b>Figure 1-2. Left: The co-propagating non-collinear SFG experimental geometry. The reflected infrared and visible beams and transmitted beams have been omitted for clarity. Right: Schematic of the SFG energy diagram which involves both IR and Raman transitions. ....</b></p>	<b>9</b>
<p><b>Figure 2-1. The near critical angle (NCA) geometry used in the experiment for interface studies. To clearly show the SFG reflection signal, the reflected mid-IR and visible beams were not plotted. The molecular formula of <math>d_4</math>-PET is displayed on the top right. ....</b></p>	<b>28</b>
<p><b>Figure 2-2. The molecular structure of PDMS, and the coordinate system chosen for orientation analysis. Each methyl group presents a <math>C_{3v}</math> symmetry. The entire <math>Si(CH_3)_2</math> group presents a <math>C_{2v}</math> symmetry. xyz coordinate demonstrates the lab frame. <math>\theta</math>, <math>\psi</math>, <math>\phi</math> are tilt angle, twist angle and azimuthal angle of vector <math>v</math> bisects <math>Si(CH_3)_2</math> group. The molecular formula of PDMS is displayed on the left. ....</b></p>	<b>29</b>
<p><b>Figure 2-3. Calculated values of (a) <math>\chi_{yyz,s} \cdot \epsilon_0 / N</math> and (b) <math>\chi_{yyz,as} \cdot \epsilon_0 / N</math>, ratios of (c) <math>\chi_{yyz,s} / \chi_{yyz,as}</math> and (d) <math>\chi_{yyz,as} / \chi_{zy,as}</math> are plotted as functions of tilt angle <math>\theta</math> and twist angle <math>\psi</math>, with the angle ranges between <math>0^\circ</math> and <math>90^\circ</math>. It was assumed that <math>\beta_{aac} : \beta_{ccc} : \beta_{caa} = 2.3:1:2.3</math> and <math>\beta_{ccc} = 1</math> based on the previous publications. ....</b></p>	<b>32</b>
<p><b>Figure 2-4. (a), (c) ssp and sps SFG spectra collected from the <math>d_4</math>-PET/PDMS interface before curing and (b), (d) after curing. Dots are measured data; lines are fitting results. ..</b></p>	<b>35</b>
<p><b>Figure 2-5. (a), (c) ssp and sps SFG spectra collected from the silica/PDMS interface before curing and (b), (d) after curing. Dots are measured data; lines are fitting results. ....</b></p>	<b>37</b>
<p><b>Figure 2-6. Plot <math>\chi_{yyz,s} / \chi_{yyz,as}</math> and <math>\chi_{yyz,as} / \chi_{zy,as}</math> values obtained from SFG experiment in Figure 2-4 to obtain: (a) Orientation angle range of <math>Si(CH_3)_2</math> at the <math>d_4</math>-PET/uncured PDMS interface using <math>\chi_{yyz,s} / \chi_{yyz,as} = 1.24</math>; (b) Orientation angle range of <math>Si(CH_3)_2</math> at the <math>d_4</math>-PET/uncured PDMS interface using <math>\chi_{yyz,as} / \chi_{zy,as} = 0.51</math>; (d) Orientation angle range of <math>Si(CH_3)_2</math> at the <math>d_4</math>-PET/cured PDMS interface using <math>\chi_{yyz,s} / \chi_{yyz,as} = 1.35</math>; (e) Orientation angle range of <math>Si(CH_3)_2</math> at the <math>d_4</math>-PET/cured PDMS interface using <math>\chi_{yyz,as} / \chi_{zy,as} = 0.51</math>; (c) Overlapping area of (a) and (b); (f) Overlapping area of (d) and (e). The error bar is 20%. ....</b></p>	<b>39</b>

**Figure 2-7. Plot  $\chi_{yyz,s} / \chi_{yyz,as}$  and  $\chi_{yyz,as} / \chi_{zy,as}$  values obtained from SFG experiment in Figures 2-5 to obtain: (a) Orientation angle range of Si(CH<sub>3</sub>)<sub>2</sub> at the silica/uncured PDMS interface using  $\chi_{yyz,s} / \chi_{yyz,as} = -0.98$ ; (b) Orientation angle range of Si(CH<sub>3</sub>)<sub>2</sub> at the silica/uncured PDMS interface using  $\chi_{yyz,as} / \chi_{zy,as} = -2.71$ ; (d) Orientation angle range of Si(CH<sub>3</sub>)<sub>2</sub> at the silica/cured PDMS interface using  $\chi_{yyz,s} / \chi_{yyz,as} = -1.53$ ; (e) Orientation angle range of Si(CH<sub>3</sub>)<sub>2</sub> at the silica/cured PDMS interface using  $\chi_{yyz,as} / \chi_{zy,as} = -1.83$ ; (c) Overlapping area of (a) and (b); (f) Overlapping area of (d) and (e). The error bar is 20%. .....** 41

**Figure 2-8. Possible orientation angle range of Si(CH<sub>3</sub>)<sub>2</sub> group at the silica/uncured PDMS interface further determined using (a)  $\frac{\chi_{yyz,s,(uncured)PDMS/Silica}}{\chi_{yyz,s,(uncured)PDMS/dPET}}$  and (b)  $\frac{\chi_{yyz,as,(uncured)PDMS/Silica}}{\chi_{yyz,as,(uncured)PDMS/dPET}}$ ; Possible orientation angle range of Si(CH<sub>3</sub>)<sub>2</sub> group at the silica/cured PDMS interface further determined using (c)  $\frac{\chi_{yyz,s,(cured)PDMS/Silica}}{\chi_{yyz,s,(uncured)PDMS/dPET}}$  and (d)  $\frac{\chi_{yyz,as,(cured)PDMS/Silica}}{\chi_{yyz,as,(uncured)PDMS/dPET}}$ . For (a) and (c), possible angle ranges are from white curve to the right; for (b) and (d), possible ranges are between two white lines. Arrows are used to demonstrate the possible angle range in all figures.....** 46

**Figure 2-9.  $\chi_{yyz,s} / \chi_{yyz,as}$  (solid red line) and  $\chi_{yyz,as} / \chi_{zy,as}$  (broken blue line) as functions of tilt angle (the ratio values are obtained by averaging twist angle  $\psi$  from 0 to 360°). The experimentally measured values are shown as dotted lines, and demonstrated by the red arrows.....** 47

**Figure 2-10. SFG ssp spectra collected from the *d*<sub>4</sub>-PET/PDMS interface (*d*<sub>4</sub>-PET on a TiO<sub>2</sub> layer): (a) before curing (b) after curing; SFG ssp spectra collected from the silica/PDMS interface (a thin layer of silica on a TiO<sub>2</sub> layer): (c) before curing (d) after curing. ....** 50

**Figure 2-11. SFG ssp spectra collected from the *d*<sub>8</sub>-PS/PDMS interface (*d*<sub>8</sub>-PS on a TiO<sub>2</sub> layer): (a) before curing (b) after curing; SFG ssp spectra collected from the *d*<sub>8</sub>-PMMA/PDMS interface (*d*<sub>8</sub>-PMMA on a TiO<sub>2</sub> layer): (c) before curing (d) after curing... 51**

**Figure 2-12. The near total reflection geometry used in the SFG experiment and the angle definitions.....** 54

**Figure 2-13. Plot  $\chi_{yyz,s} / \chi_{yyz,as}$  and  $\chi_{yyz,as} / \chi_{zy,as}$  values obtained from SFG experiment in Figures 2-3c and d respectively to obtain: (a) Orientation angle range of Si(CH<sub>3</sub>)<sub>2</sub> group at the *d*<sub>4</sub>-PET/uncured PDMS interface using  $\chi_{yyz,s} / \chi_{yyz,as} = 1.24$ ; (b) Orientation angle range of Si(CH<sub>3</sub>)<sub>2</sub> group at the *d*<sub>4</sub>-PET/uncured PDMS interface using  $\chi_{yyz,as} / \chi_{zy,as} = -0.51$ ; (c) Overlapping area of (a) and (b). No possible orientation angle range can be identified in (c). The error bar presented here is 20%......** 57

**Figure 2-14. Plot  $\chi_{yyz,s} / \chi_{yyz,as}$  and  $\chi_{yyz,as} / \chi_{yyz,as}$  values obtained from SFG experiment in Figure 2-3c and d respectively to obtain: (a) Orientation angle range of Si(CH<sub>3</sub>)<sub>2</sub> group at the *d*<sub>4</sub>-PET/cured PDMS interface using  $\chi_{yyz,s} / \chi_{yyz,as} = 1.35$ ; (b) Orientation angle range of Si(CH<sub>3</sub>)<sub>2</sub> group at the *d*<sub>4</sub>-PET/cured PDMS interface using  $\chi_{yyz,as} / \chi_{yyz,as} = -0.51$ ; (c) Overlapping area of (a) and (b). No possible orientation angle range can be identified in (c). The error bar presented here is 20% ..... 57**

**Figure 2-15. Adhesion test geometry for shear strength test. The top panel shows two test pieces adhered together by PDMS adhesive; the bottom panel shows that after the 180 degree shear test, two test pieces were pulled apart. .... 59**

**Figure 2-16. Chemical structures of polymers and silanes employed in the study: (a) Poly(ethylene terephthalate) (PET); (b) PET with aliphatic chain deuterated (*d*<sub>4</sub>-PET); (c) Methylvinylsiloxanol (MVS); (d) (3-glycidoxypropyl) trimethoxysilane ( $\gamma$ -GPS); (e). (3-glycidoxypropyl) methyl-dimethoxysilane ( $\gamma$ -GPMS); (f) (3-glycidoxypropyl) dimethyl-methoxysilane ( $\gamma$ - GPDMS)..... 60**

**Figure 2-17. SFG spectra collected from (a) the *d*<sub>4</sub>-PET/uncured silicone interface, (b) the *d*<sub>4</sub>-PET/cured silicone interface, (c) the *d*<sub>4</sub>-PET/MVS interface. The dots are experimental data and the lines are fitting results. .... 62**

**Figure 2-18. SFG spectra collected from (a) the *d*<sub>4</sub>-PET/ $\gamma$ -GPS ( $\Delta$ ) and *d*<sub>4</sub>-PET/ $\gamma$ -GPS:MVS interfaces ( $\circ$ ) using the window geometry, (b) the *d*<sub>4</sub>-PET/ $\gamma$ -GPS ( $\Delta$ ) and *d*<sub>4</sub>-PET/ $\gamma$ -GPS:MVS interfaces ( $\circ$ ) using the NCA geometry, (c) the *d*<sub>4</sub>-PET/ $\gamma$ -GPMS ( $\Delta$ ) and *d*<sub>4</sub>-PET/ $\gamma$ -GPMS:MVS interfaces ( $\circ$ ) using the NCA geometry, (d) the *d*<sub>4</sub>-PET/ $\gamma$ -GPDMS ( $\Delta$ ) and *d*<sub>4</sub>-PET/ $\gamma$ -GPDMS:MVS interfaces ( $\circ$ ) using the NCA geometry. For (b), (c), (d), the dots are experimental data and the lines are fitting results..... 63**

**Figure 2-19. SFG spectra collected from the interfaces between *d*<sub>4</sub>-PET and uncured silicones mixed with (a)  $\gamma$ -GPS ( $\Delta$ ) and  $\gamma$ -GPS:MVS ( $\circ$ ), (b)  $\gamma$ -GPMS ( $\Delta$ ) and  $\gamma$ -GPMS:MVS ( $\circ$ ), (c)  $\gamma$ -GPDMS ( $\Delta$ ) and  $\gamma$ -GPDMS:MVS ( $\circ$ ). The dots are experimental data and the lines are fitting results. .... 66**

**Figure 2-20. SFG spectra collected from the interfaces between *d*<sub>4</sub>-PET and cured silicone with (a)  $\gamma$ -GPS ( $\Delta$ ) and  $\gamma$ -GPS:MVS ( $\circ$ ), (b)  $\gamma$ -GPMS ( $\Delta$ ) and  $\gamma$ -GPMS:MVS ( $\circ$ ), and (c)  $\gamma$ -GPDMS ( $\Delta$ ) and  $\gamma$ -GPDMS:MVS ( $\circ$ ).The dots are experimental data and the lines are fitting results..... 68**

**Figure 2-21. The adhesion test results (using 180 degree shear test). Strength=Force/Contact area. .... 69**

**Figure 2-22. Chemical structures of silanes employed in the study: a. (3-glycidoxypropyl) triethoxysilane ( $\gamma$ -GPES); b. (3-glycidoxypropyl) methyl-diethoxysilane ( $\gamma$ -GPDES); c. (3-glycidoxypropyl) dimethyl-ethoxysilane ( $\gamma$ - GPDMES) . .... 77**

**Figure 2-23. Adhesion test results of ethoxy-silane incorporated in PDMS adhesives. Samples from left to right: PDMS,  $\gamma$ -GPES,  $\gamma$ -GPES:MVS,  $\gamma$ -GPDES,  $\gamma$ -GPDES:MVS,  $\gamma$ -GPDMEs,  $\gamma$ -GPDMEs:MVS. Only a very small amount of silane or silane:MVS mixture was added to PDMS here. .... 79**

**Figure 2-24. SFG ssp spectra of (a)  $d_4$ -PET/ $\gamma$ -GPES (bottom) and  $d_4$ -PET/ $\gamma$ -GPES:MVS mixture interfaces (top) (b)  $d_4$ -PET/ $\gamma$ -GPDES (bottom) and  $d_4$ -PET/ $\gamma$ -GPDES:MVS mixture interfaces (top) (c)  $d_4$ -PET/ $\gamma$ -GPDMEs (bottom) and  $d_4$ -PET/ $\gamma$ -GPDMEs:MVS mixture interfaces (top). .... 81**

**Figure 2-25. SFG spectra of (a)  $\gamma$ -GPES (bottom) and  $\gamma$ -GPES:MVS (top) (b)  $\gamma$ -GPDES (bottom) and  $\gamma$ -GPDES:MVS (top) (c)  $\gamma$ -GPDMEs (bottom) and  $\gamma$ -GPDMEs:MVS (top) at  $d_4$ -PET/uncured PDMS interfaces under ssp polarization combination. The dots are experimental data and the lines are fitting results. .... 84**

**Figure 2-26. SFG spectra of (a)  $\gamma$ -GPES (bottom) and  $\gamma$ -GPES:MVS (top) (b)  $\gamma$ -GPDES (bottom) and  $\gamma$ -GPDES:MVS (top) (c)  $\gamma$ -GPDMEs (bottom) and  $\gamma$ -GPDMEs:MVS (top) at  $d_4$ -PET/cured PDMS interfaces under ssp polarization combination. The dots are experimental data and the lines are fitting results. .... 86**

**Figure 3-1 Epoxy curing chemistry based on diethylenetriamine. .... 101**

**Figure 3-2. Chemicals used in the experiment: (a) Poly(ethylene terephthalate) with aliphatic chain deuterated ( $d_4$ -PET) (b) Deuterated polystyrene ( $d_8$ -PS) (c) bisphenol A diglycidyl ether (BADGE); (d) diethylenetriamine (DETA); (e) (3-glycidoxypropyl) trimethoxysilane ( $\gamma$ -GPS); (f) (3-Aminopropyl)trimethoxysilane (ATMS); (g) Octadecyltrimethoxysilane (OTMS(18C)); (h) Octyltrimethoxysilane (OTMS(8C)). .... 103**

**Figure 3-3. SFG spectrum collected from the BADGE (without the curing agent DETA)/ $d_4$ -PET interface. .... 104**

**Figure 3-4. SFG spectra collected from (a) BADGE/ $d_4$ -PET interface; (b) BADGE+DETA+ $\gamma$ -GPS/ $d_4$ -PET interface; (c) BADGE+DETA+ATMS/ $d_4$ -PET interface; (d) BADGE+DETA+OTMS(18C)/ $d_4$ -PET interface; (e) BADGE+DETA+OTMS(8C)/ $d_4$ -PET interface. Closed dots: spectra collected before curing. Open dots: spectra collected after curing. The spectral range is from 2750 to 3150  $\text{cm}^{-1}$ . .... 108**

**Figure 3-5. SFG spectra collected from the BADGE+DETA+ATMS/ $d_4$ -PET interface. Bottom spectrum: before curing; top spectrum: after curing. The spectral range is from 3000 to 3600  $\text{cm}^{-1}$ . .... 109**

**Figure 3-6. Adhesion testing results of model epoxy BADGE and BADGE silane mixtures to PET after curing. Adhesion strength = Maximum adhesion force/contact area. .... 110**

**Figure 3-7. SFG spectra collected from (a) the CE3302/*d*<sub>4</sub>-PET interface; (b) the CE3302/*d*<sub>8</sub>-PS interface. From the top to the bottom: SFG spectra from interfaces of the cured sample, the uncured sample, and the epoxy base without hardener. .... 112**

**Figure 3-8. Adhesion testing results of commercial epoxy 3302 to PET and PS..... 112**

**Figure 3-9. SFG spectra collected from (a) the CE3006/*d*<sub>4</sub>-PET interface; (b) the CE3006/*d*<sub>8</sub>-PS. From the top to the bottom: SFG spectra from interfaces of the cured sample, the uncured sample, and the epoxy base without hardener. For spectrum in the middle of (b), it is multiplied by a factor of five..... 113**

**Figure 3-10. Adhesion testing results of CE3006 to PET and PS. .... 114**

**Figure 3-11. Chemical structures of (a) (1,4-butanediol)diglycidyl ether (BDDGE) and (b) (1,4-cyclohexanedimethanol)diglycidyl ether (CDDGE). .... 117**

**Figure 3-12. Experimental geometries of (a) SFG spectroscopy and (b) ATR-FTIR spectroscopy..... 118**

**Figure 3-13. ATR-FTIR spectra of (a) PET (black), PET contacting BDDGE epoxy (red), PET washed using acetone and water after contacting BDDGE epoxy for 2 hr (blue). (b) PET (black), PET contacting CDDGE epoxy (red), PET washed using acetone and water after contacting CDDGE epoxy for 2 hr (blue). .... 119**

**Figure 3-14 ATR-FTIR spectra of (a) BDDGE and (b) CDDGE epoxy in contact with silicon substrate; No signal at 1722 cm<sup>-1</sup> can be detected. .... 120**

**Figure 3-15. SFG spectra collected from (a) BDDGE/blank CaF<sub>2</sub> interface (black square) and BDDGE/*d*<sub>4</sub>-PET (deposited on CaF<sub>2</sub>) interface (open circle); (b) BDDGE/blank silica interface (black square) and BDDGE/*d*<sub>4</sub>-PET (deposited on silica) interface (open circle); (c) CDDGE/blank CaF<sub>2</sub> interface (black square) and CDDGE/*d*<sub>4</sub>-PET (deposited on CaF<sub>2</sub>) interface (open circle); (d) CDDGE/blank silica interface (black square) and CDDGE/*d*<sub>4</sub>-PET (deposited on silica) interface (open circle)..... 122**

**Figure 3-16. (a) ATR-FTIR spectra of PET (black), PET contacting DETA (red), PET film after contacting DETA for 40 min and washed by water (blue); (b) Time dependent ATR-FTIR spectra of PET in contact with DETA. .... 124**

**Figure 3-17. SFG spectra collected from (a) DETA/CaF<sub>2</sub> interface (black square) and DETA/*d*<sub>4</sub>-PET (deposited on CaF<sub>2</sub>) interface (open circle); (b) DETA/silica interface (black square) and DETA/*d*<sub>4</sub>-PET (deposited on silica) interface (open circle) ..... 125**

**Figure 3-18. (a) SFG spectra of OTCS SAM (black square), OTCS SAM contacting with DETA after stabilization (red circle), OTCS SAM washed using water after contacting with DETA (blue triangle). (b) Time dependent SFG signal change of OTCS methyl group at 2875 and 2940 cm<sup>-1</sup> after contacting with DETA. (c) SFG spectra of PET coated on *d*<sub>8</sub>-PS**



deposited on an OTCS SAM (black square), the film was contacted with DETA after stabilization (red circle), the film was washed using water after contacting with DETA (blue triangle). (d) Time dependent SFG signal change of OTCS-*d*<sub>8</sub>-PS-PET film at 2875 and 2940 cm<sup>-1</sup> after contacting with DETA. .... 128

Figure 3-19. ATR-FTIR spectrum of a PET film spin coated on a *d*<sub>8</sub>-PS film on an OTCS SAM; PET C=O vibrational stretching signal at 1722 cm<sup>-1</sup> can be resolved. .... 128

Figure 3-20. ATR-FTIR spectra collected from (a) PET (black), PET contacting uncured BDDGE-DETA mixture (red), PET contacting cured BDDGE-DETA mixture (blue), the resulting PET surface after breaking the PET/BDDGE-DETA mixture interface (green); (b) PET (black), PET contacting uncured CDDGE-DETA (red), PET contacting cured CDDGE-DETA (blue), the resulting PET surface after breaking the PET/CDDGE-DETA mixture interface (green). .... 130

Figure 3-21. SFG spectra collected when *d*<sub>4</sub>-PET was contacted by (a) uncured or (b) cured BDDGE-DETA mixtures with  $\gamma$ -GPS (○) or ATMS (▲) or without silane (■) incorporated; (c) Time dependent SFG spectra of *d*<sub>4</sub>-PET contacted with BDDGE-DETA mixture incorporated with OTMS silane before curing the sample. The time interval between spectra is 15 min; (d) SFG spectra of *d*<sub>4</sub>-PET contacted with BDDGE-DETA mixture incorporated with OTMS silane after curing; SFG spectra collected when *d*<sub>4</sub>-PET contacted by (e) uncured or (f) cured BDDGE-DETA mixtures with  $\gamma$ -GPS (○) or ATMS (▲) or without silane (■) incorporated; SFG spectra of *d*<sub>4</sub>-PET contacted with CDDGE-DETA mixture incorporated with OTMS silane (g) before and (h) after curing the sample. .... 133

Figure 3-22. SFG spectra in the N-H stretching frequency range at the interface between *d*<sub>4</sub>-PET and uncured (○) or cured (■) BDDGE-DETA mixture coupled with ATMS silane. Other silane cases and the case without silane have similar results as shown. .... 134

Figure 3-23. Mechanical adhesion test results of PET blocks adhered by (a) BDDGE-DETA mixture and (b) CDDGE-DETA mixture with and without  $\gamma$ -GPS, ATMS and OTMS incorporated into the system. .... 136

Figure 3-24. The reaction of epoxy-amine mixture with PET. .... 138

Figure 4-1. Molecular formulas of lipid molecules used in the research. .... 148

Figure 4-2. (a) Schematic of the SFG experimental geometry for lipid translocation study (different components are not drawn to scale), (b) lipid compositions of the initial supported bilayers (top leaflet is attached to the prism, bottom leaflet is facing subphase), and (c) molecular structures of polyethylenimines (PEIs). PEI-B: branched PEI, PEI-L: linear PEI. .... 149

**Figure 4-3. SFG spectra in the (a) C-D and (b) C-H stretching frequency ranges of the dDPPG-DPPG bilayer before (black square) and after (red circle) the addition of PEI-L stock solution to the subphase to reach a 100 ppm PEI-L concentration at 21 °C. .... 154**

**Figure 4-4. Time-dependent SFG signals detected from the dDPPG-DPPG bilayer at 21 °C before and after the introduction of 100 ppm PEI-L to the subphase. SFG signals were monitored at 2070 (black) and 2875 (red)  $\text{cm}^{-1}$ . PEI stock solution was added to the subphase at ~1760 s..... 155**

**Figure 4-5. Time-dependent SFG signals of C-D stretching vibrational peak (2070  $\text{cm}^{-1}$ ) from the dDPPG-DPPG bilayer at 39 °C in contact with the subphase without and with 10 ppm, 20 ppm, 50 ppm, and 100 ppm concentrations of (a) PEI-B and (b) PEI-L. Dots are data points measured in the experiment; lines are fitting results using equation (4.5)..... 156**

**Figure 4-6. dDPPG-DPPG bilayer lipid translocation rates as functions of PEI concentrations in the subphase at 39 °C. Squares: PEI-B, triangles: PEI-L, Open: C-H signal, Filled: C-D signal. Lines are linear fitting results of the data points. .... 157**

**Figure 4-7. SFG spectra in the (a) C-D and (b) C-H stretching frequency ranges of the dDSPC-DSPC bilayer before (black square) and after (red circle) the addition of PEI-B to the subphase to reach 100 ppm at 21 °C. .... 159**

**Figure 4-8. Time-dependent SFG signals detected from the dDSPC-DSPC bilayer at 21 °C before and after the introduction of 100 ppm PEI-B to the subphase. SFG signals were monitored at 2070 (black) and 2875 (red)  $\text{cm}^{-1}$ . PEI-B stock solution was added to the subphase at ~1050 s..... 159**

**Figure 4-9. dDSPC-DSPC bilayer lipid translocation rates as functions of PEI concentrations in the subphase at 39 °C. Squares: PEI-B, triangles: PEI-L, Open: C-H signal, Filled: C-D signal. Lines are linear fitting results of the data points. .... 160**

**Figure 4-10. Time-dependent SFG signals at 2070  $\text{cm}^{-1}$  detected from the dDPPC-DPPC bilayer (square); dDPPC-DPPC bilayer in contact with the subphase of 100 ppm PEI-B (triangle); dDPPC-DPPC bilayer in contact with the subphase of 100 ppm PEI-L (sphere) at 21 °C. SFG signal curves are offset in the figure. Dots are data points measured in the experiment; lines are fitting results using equation (4.5). .... 162**

**Figure 4-11. The construction of a lipid bilayer on an ATR crystal for the ATR-FTIR spectroscopic study. .... 164**

**Figure 4-12. ATR-FTIR spectra of the (a) DPPG and (b) DSPC bilayers at different temperatures (21 and 39 °C) with and without PEI-B injected into the subphase. .... 166**

**Figure 4-13. ATR-FTIR spectrum collected from the ATR crystal/100 ppm PEI-B solution interface. The water background was corrected to avoid confusion..... 167**

<b>Figure 5-1. Experimental setup. SHG, Second harmonic generation; SFG, sum frequency generation; OPG/OPA, optical parametric generation/amplification; HWP1-4, half wave plates; P1-P4, polarizers; PMT, photomultiplier tube. Dotted line indicates CARS beam path.....</b>	<b>176</b>
<b>Figure 5-2. (a)/(b) SFG/CARS spectra of PMMA film before (top) and after (bottom) plasma treatment; (c)/(d) SFG/CARS spectra of PS film before (top) and after (bottom) plasma treatment. Dots are spectra collected in the experiments, lines are fitting results.</b>	<b>177</b>
<b>Figure 5-3. Absolute value of the peak amplitude/width ratio of the PMMA or PS mode centered at 2935 or 3069 <math>\text{cm}^{-1}</math> as a function of the polymer film thickness. ....</b>	<b>179</b>
<b>Figure 5-4. (a) DPPG monolayer SFG spectra collected with ssp and sps polarization combinations; (b) DPPG monolayer CARS spectra collected with ssss and spsp polarization combinations.....</b>	<b>180</b>
<b>Figure 5-5. Schematic of the beam tracking TIR-SFG system; The SFG spectrometer is not shown in the figure.....</b>	<b>184</b>
<b>Figure 5-6. Procedures of using the system to find desired location for sample studies. 1. Using the three dimensional translation stage on the microscope to find the focused laser beam spot on the sample surface; 2. Using the translation stage on the sample holder to find the desired sample location for SFG study; 3. Overlapping the desired sample location with the laser beam spot for SFG data collection. ....</b>	<b>185</b>
<b>Figure 5-7. (A) SFG spectra of a PMMA surface in air using 10, 20 and 30 <math>\mu\text{J}</math> (bottom to top) incident visible pulse energies. The spectra were fit (lines) using the method showed in Chapter 1. (B) BF image of the PMMA surface when the SFG spectrum was being collected with 30 <math>\mu\text{J}</math> incident visible pulse energy. Strong scattering indicates the surface photo-damage. (C) BF image of the same sample location collected using a white light source without the input lasers after the SFG experiment.....</b>	<b>186</b>
<b>Figure 5-8. (A) BF image of the visible beam focused on the buffer/substrate interface. (B) BF image of the visible beam focused on a mouse oocyte/substrate interface. (C) SFG spectra taken in (A) (top) and (B) (bottom). Dots are experimental collected data and lines are the fitting results.....</b>	<b>188</b>
<b>Figure 5-9. (A) Schematic of the SFG experiment at a mussel plaque/<math>\text{CaF}_2</math> interface and a water/<math>\text{CaF}_2</math> interface. (B) BF image of a position within the mussel plaque demonstrated in A. (C) BF image of a position in a ‘blank’ water/<math>\text{CaF}_2</math> area, demonstrated in A. (D) SFG spectrum in the C=O range collected in position 1. (E) SFG spectrum of the C-H/O-H range collected in position 1. (F) SFG spectrum of the C-H/O-H range collected in position 2.....</b>	<b>190</b>
<b>Figure 5-10. Schematic of our SFG-TIRF multimodal system used for interfacial studies. ....</b>	<b>193</b>

**Figure 5-11. TIRF images of 3  $\mu\text{m}$  fluorescent PS beads with high (a) and low (c) surface coverage on a silica prism. The corresponding SFG spectra in the circled locations are shown in (b) and (d), respectively. .... 194**

**Figure 5-12. (a) TIRF image of the boundary between a DPPG monolayer labeled using Dil and the ‘blank’ area with no lipids. (b) The corresponding SFG spectra of the lipid area (area 1) and the ‘blank’ area (area 2) in (a). .... 196**

**Figure 5-13. (a) TIRF image of a DPPG monolayer labeled using Dil in air and (b) the corresponding SFG spectrum in circled area. (c) TIRF image of the DPPG monolayer labeled using Dil in water and (d) the corresponding SFG spectrum in circled area. (e) TIRF image of the DPPG monolayer in air after contacting water and (f) the corresponding SFG spectrum from the restructured surface in circled area. .... 198**

**Figure 5-14. ATR-FTIR spectra of a DPPG monolayer in air (black), the same sample in air after contacting water (red), and their signal difference ((blue curve) = (black curve) – (red curve)). .... 200**

**Figure 6-1. (a) CARS experimental geometry used in this study. The pump/probe and Stokes beams lie in the x-z plane. The s and p polarizations are defined as perpendicular and parallel with respect to the x-z plane, respectively. (b) Energy diagram of CARS spectroscopy. .... 207**

**Figure 6-2. Left: the molecular formula of PDMS. Right: Schematic of a PDMS molecule residue in a lab frame coordinate system (x, y, z) defined in Figure 6-1. Each methyl group presents a  $C_{3v}$  symmetry. The molecular coordinate is shown by (a, b, c). Azimuthal angle  $\phi$ , tilt angle  $\theta$  and twist angle  $\psi$  are also defined. .... 210**

**Figure 6-3. (a) A single C-H bond and the molecular coordinate system (a', b', c') chosen for the bond. (b) A methyl group and its molecular coordinate system (a, b, c). Three C-H bonds and their independent molecular systems are also defined (a', b', c'; a'', b'', c''; a''', b''', c'''). C-H bond 1 is in the a-c plane. The c axis is set along the methyl group principal axis. (c) The ‘top view’ (a-b plane projection) of the picture depicted in (b), the c axis is perpendicular to the paper. (d) The ‘side view’ (a-c plane projection) of the picture depicted in (b), the b axis is perpendicular to the paper. .... 213**

**Figure 6-4. C-H vibrational stretching modes of a methyl group: (a) symmetric  $A_1$  mode; (b) asymmetric  $E_a$  mode; (c) asymmetric  $E_b$  mode. .... 214**

**Figure 6-5. (a) CARS spectrum of PDMS film collected using ssss polarization combination; (b) CARS spectrum of PDMS film collected using spps polarization combination. Dots are experimental data, lines are spectral fitting results using equation (6.2). .... 219**

## LIST OF TABLES

<b>Table 2-1. Spectral fitting results for the SFG spectra shown in Figure 2-4.....</b>	<b>35</b>
<b>Table 2-2. Spectral Fitting results for the SFG spectra shown in Figure 2-5.....</b>	<b>37</b>
<b>Table 2-3. Water contact angle measurement results of polymer and silica surfaces used in the experiment.....</b>	<b>52</b>
<b>Table 2-4. Fitting results for Figure 2-17.....</b>	<b>72</b>
<b>Table 2-5. Fitting results for Figure 2-18.....</b>	<b>73</b>
<b>Table 2-7. Fitting results for Figure 2-20.....</b>	<b>75</b>
<b>Table 2-8. Fitting results of Figure 2-25.....</b>	<b>84</b>
<b>Table 2-9. Fitting results of Figure 2-26.....</b>	<b>86</b>
<b>Table 2-10. Fitting result summary from Tables 2-8 and 2-9.....</b>	<b>87</b>
<b>Table 2-11. Fermi resonance signal strength differences for silane headgroup methyl before and after curing PDMS, as well as with and without the addition of MVS. The related adhesion strengths are shown in the right column. ....</b>	<b>88</b>
<b>Table 3-1. Summary of vibrational peak assignments for the SFG and ATR-FTIR spectra of molecules discussed in the paper. (s: symmetric; as: asymmetric; Fermi: Fermi resonance) .....</b>	<b>135</b>
<b>Table 3-2. Contact angle measurement results of the PET surface and the fractured PET/epoxy-amine interphase (after the removal of CDDGE-DETA or BDDGE-DETA epoxy chunk from the substrate after curing).....</b>	<b>139</b>
<b>Table 6-1. Spectral fitting parameters used for the fitting in Figure 6-5.....</b>	<b>219</b>

## LIST OF ABBREVIATIONS

AFM	atomic force microscopy
ATMS	(3-aminopropyl)trimethoxysilane
ATR-FTIR	attenuated total-internal reflectance-Fourier transform infrared
BADGE	bisphenol-A diglycidyl ether
BDDGE	(1,4-butanediol)diglycidyl ether
CARS	coherent anti-Stokes Raman scattering
CCD	charge-coupled device
CDDGE	(1,4-cyclohexanedimethanol)diglycidyl ether
CMOS	complementary metal-oxide-semiconductor
<i>d</i> <sub>4</sub> -PET	poly(ethylene terephthalate) with aliphatic chain deuterated
<i>d</i> <sub>8</sub> -PMMA	deuterated poly(methyl methacrylate)
<i>d</i> <sub>8</sub> -PS	deuterated polystyrene
DETA	diethylenetriamine
dDPPG	deuterated d <sub>62</sub> -dipalmitoylphosphatidylglycerol
dDSPC	deuterated d <sub>70</sub> -distearoylphosphatidylcholine
dDPPC	deuterated d <sub>62</sub> -dipalmitoylphosphatidylcholine
DBP	dibutyl phthalate
DEP	diethyl phthalate
DEHP	bis-2-ethylhexyl phthalate
DFG	difference frequency generation
DOPA	dihydroxyphenylalanine
DRSFG	double resonance SFG
DPPC	dipalmitoylphosphatidylcholine
DPPG	dipalmitoylphosphatidylglycerol
DSPC	distearoylphosphatidylcholine
EMCCD	electron-multiplying CCD

GVI	germinal vesicle intact
HWP	half-wave plate
IC	integrated circuits
MVS	methylvinylsiloxanol
NMR	nuclear magnetic resonance
OPA	optical parametric amplification
OPG	optical parametric generation
OTCS	octadecyltrichlorosilane
OTMS	octadecyltrimethoxysilane
OTMS(8C)	octyltrimethoxysilane
OTMS(18C)	octadecyltrimethoxysilane
PA	phosphatidic acid
PBMA	poly(n-butyl methacrylate)
PC	phosphatidylcholine
PCB	printed circuit board
PDMS	poly(dimethyl siloxane)
PE	phosphatidylethanolamine
PEI	polyethylenimine
PEI-B	branched polyethylenimine
PEI-L	linear polyethylenimine
PET	poly(ethylene terephthalate)
PG	phosphatidylglycerol
PI	polyimide
PMMA	poly(methyl methacrylate)
PMT	photomultiplier tube
PS	phosphatidylserine (in Chapter 4)
PS	polystyrene
PVC	polyvinyl chloride
$\gamma$ -GPDES	(3-glycidoxypropyl) methyl-diethoxysilane
$\gamma$ -GPDMS	(3-glycidoxypropyl) dimethyl-ethoxysilane

$\gamma$ -GPDMS	(3-glycidoxypropyl) dimethyl-methoxysilane
$\gamma$ -GPES	(3-glycidoxypropyl) triethoxysilane
$\gamma$ -GPMS	(3-glycidoxypropyl) methyl-dimethoxysilane
$\gamma$ -GPS	(3-glycidoxypropyl) trimethoxysilane
QCM	quartz crystal microbalance
SAM	self-assembled monolayer
SERS	surface-enhanced Raman spectroscopy
SFG	sum frequency generation
SIMS	secondary ion mass spectrometry
SPR	surface plasmon resonance
TEC	thermal expansion coefficients
TIR	total-internal reflection
TIR-SFG	total-internal reflection SFG
TIRF	total-internal reflection fluorescence
UV-vis	ultraviolet-visible
XPS	X-ray photoelectron spectroscopy
ZP	zona pellucida



# CHAPTER 1

## INTRODUCTION

### 1.1 Motivation

Vibrational spectroscopies are label free and non-invasive analytical techniques which can provide important molecular level insight of various samples and have found important applications in material and biological sciences, as well as the related research fields. Thanks to the fast development of laser technologies, nonlinear vibrational spectroscopies have emerged and were developed into powerful analytical tools for modern science and technology. Nonlinear vibrational spectroscopies have important advantages over traditional linear vibrational spectroscopies such as intrinsic surface sensitivity (second order nonlinear effects), strong signal collection efficiency due to the coherent signal generation, as well as the capability for fast label free or high contrast imaging, etc. The prosperity of nonlinear vibrational spectroscopy was benefited from the advancements in three directions: the theoretical development in basic spectral analysis and physical interpretation; the technical upgrade of modern nonlinear vibrational spectroscopic systems; and the extensive applications of the techniques in materials science, biology, or other industry-driven interdisciplinary fields. The goal of this thesis is to demonstrate my personal contributions in all three directions of advancement in nonlinear vibrational spectroscopy.

In this work, we focused on two nonlinear vibrational spectroscopic techniques, sum frequency generation (SFG) and coherent anti-Stokes Raman scattering (CARS) vibrational spectroscopies.

SFG is a second order nonlinear optical process, which is surface sensitive and has been widely applied to characterize surfaces or interfaces of various materials. First of all, we are interested in developing SFG into a unique analytical tool to study buried interfacial molecular structures of adhesives, including poly(dimethyl siloxane) (PDMS) and epoxy adhesives, to understand the adhesion mechanisms in physical means. Interfacial properties largely depend on interfacial molecular structures. Understanding interfacial structures of adhesives and substrates is particularly important for developing physical insight of adhesion mechanism and designing advanced adhesive materials with improved properties. Therefore, we will systematically use SFG to investigate interfaces involving PDMS and epoxy adhesives. Such adhesion studies can help to unveil the molecular level mechanisms and help to develop better adhesives or adhesion promoters for industrial purposes. Secondly, understanding the molecular structures of biomolecules such as phospholipids, peptides, proteins, and DNAs at interfaces is also important because their interfacial structures can impact many biological interactions and facilitate many chemical, biological, and medical applications. Applying SFG to biointerface studies, we are particularly interested in understanding lipid dynamics in a membrane bilayer, because SFG can provide unique lipid transbilayer movement information that no other technique can probe. In this thesis, we performed studies on lipid transbilayer movement induced by a polyelectrolyte, aiming to add our knowledge to the understanding of the mechanisms behind the cytotoxicity of such polyelectrolyte in biological systems. Such understanding is particularly important for biological research, which can help to synthesize functional polyelectrolyte with lower toxicity for biological use. The application

approaches (adhesives and lipid membrane dynamics) mentioned above extended SFG research territories, which can help develop SFG into a powerful analytical tool in broader interdisciplinary fields.

Technical development in SFG spectroscopy is also important for extending its possible applications. SFG spectroscopy has been combined with other spectroscopic techniques such as IR,<sup>1-3</sup> Raman,<sup>1,4-5</sup> XPS,<sup>6-8</sup> ultraviolet-visible (UV-vis)<sup>9</sup> absorption and nuclear magnetic resonance (NMR),<sup>10</sup> as well as microscopic techniques such as atomic force microscopy (AFM)<sup>11-14</sup> and nonlinear optical imaging<sup>15-16</sup> for surface and interfacial studies. Other analytical techniques such as surface plasmon resonance (SPR) and quartz crystal microbalance (QCM) have also been combined with SFG to depict clearer pictures of surface or interface molecular behavior.<sup>17-21</sup> The combined techniques can provide more detailed structural information for surfaces or interfaces. SFG imaging techniques, which can obtain important surface structural information with good spatial resolution, has been developed using picosecond or femtosecond lasers.<sup>22-29</sup> In this work we also carried out technique development by developing several unique platforms combining SFG with other spectroscopic or microscopic techniques such as CARS, optical microscopy, and total-internal reflection fluorescence (TIRF) microscopy for multimodal sample analysis. Our research aims to further extend SFG spectroscopy to its untouched fields to provide unique molecular level insight in such fields.

Comparing to SFG, the work in CARS spectroscopy in this thesis is mostly focused on the theoretical development. CARS is a third order nonlinear optical process involving a Stokes Raman and an anti-Stokes Raman process. CARS signal is coherent and can be orders of magnitude stronger as compared to that of the spontaneous Raman, which enables it to find applications in fast laser scanning microscopy to study materials and biological samples. Although

many excellent technical development and application research has been published in recent years, theoretical development, especially quantitative CARS spectral analysis based on molecular geometries, has achieved to a much lesser extent. Our theoretical focus is the quantitative spectral interpretation of CARS signal measurement under different polarization combinations. This work gives further understanding of the basic vibrational responses in CARS and can help to improve spectral analysis in advanced CARS spectroscopy and microscopy.

The general motivation of this thesis is to extend applications of nonlinear vibrational spectroscopy in material and biological related fields, to make technical development for nonlinear vibrational spectroscopy techniques, as well as to perform theoretical calculations for quantitative CARS spectral analysis.

## **1.2 Sum Frequency Generation (SFG) Vibrational Spectroscopy**

Since the major technique used in this thesis is SFG spectroscopy, here we will give brief introductions of the SFG background, the experimental system setup used in this thesis, and the basic SFG theory. The background introduction of CARS is presented in Chapter 6.

### **1.2.1 SFG Background**

In the last few decades, sum frequency generation (SFG) vibrational spectroscopy has been developed into a powerful analytical technique to study surfaces and interfaces.<sup>30-38</sup> A growing number of research groups currently use this technique to study different systems.

SFG is a second order nonlinear optical process. It occurs when two pulsed laser beams, one with a tunable IR frequency  $\omega_{\text{IR}}$ , and the other with a fixed visible frequency  $\omega_{\text{VIS}}$ , spatially and temporally overlap at an interface. A new signal beam could be generated at a specific direction given by phase matching conditions with a frequency  $\omega_{\text{SFG}} = \omega_{\text{IR}} + \omega_{\text{VIS}}$ . The intensity of this sum frequency beam is resonantly enhanced when the tunable IR frequency equals a

vibrational transition of a molecule. Therefore, SFG signal intensity plotted against the input IR frequency provides a vibrational spectrum. SFG can provide molecular level structural information because molecular vibrational modes are fingerprints of molecules. Narrowband SFG system is used throughout this thesis, the details of which will be introduced in section 1.2.3. In narrowband SFG spectroscopy (usually using picosecond laser systems), an SFG vibrational spectrum is obtained by detecting SFG signal intensity at each IR input frequency and continuously tuning the IR frequency.<sup>36, 39</sup> Recently, broadband SFG spectroscopy has been developed based on state-of-the-art femtosecond laser systems. In a broadband SFG system, the IR generated by the laser has a broad spectrum which covers the molecular vibrational signatures in a wide frequency range (up to several hundreds of wavenumbers). Overlapping this broad frequency IR beam and a narrow band visible beam, multiple vibrational features of the molecule at interfaces could be enhanced simultaneously, generating spectrally separated SFG signal for different vibrational modes.<sup>4, 33, 40</sup> With a spectrometer and a charge-coupled device (CCD) camera, these multiple molecular features at the interface could be obtained at the same time.

In addition to standard SFG which uses a frequency tunable IR beam and a fixed frequency visible beam, double resonance SFG (DRSFG) has been also developed. DRSFG uses a frequency tuneable IR beam and a frequency tuneable UV/visible beam to overlap at the interface to probe electronic and vibrational transitions of interfacial molecules.<sup>41-43</sup>

SFG has advantages over other surface sensitive techniques, making it unique in examining molecular structures of many surfaces or interfaces involving polymer materials and biomolecules.

Among surface sensitive techniques, X-ray photoelectron spectroscopy (XPS) is a technique that irradiates sample surfaces with a beam of high energy, monochromatic X-ray and then measures the kinetic energy of emitted photoelectrons.<sup>44-46</sup> The binding energy of the emitted

electrons can then be deduced to determine the elemental composition of the top surface layers (usually 1-10 nm thick). Secondary ion mass spectrometry (SIMS) is a technique that bombards a surface with a focused primary ion beam. Sputtered secondary ions are then collected and analyzed to examine the composition of the surface.<sup>47-50</sup> XPS and SIMS both require high vacuum to operate and cannot be used to study many biological interfaces which involve aqueous media. AFM is a high-resolution scanning probe microscopy which uses a sharp tip to interact with a sample surface.<sup>51-54</sup> AFM can provide a three-dimensional surface profile without the need for sample pretreatment or high vacuum environment. However, it is difficult for AFM to measure molecular structures or to probe buried solid/solid interfaces. SPR is a laser based interfacial sensitive technique which can study buried interfaces *in situ*. It is sensitive to local refractive index changes at a thin metal film surface due to the adsorption of various materials such as biomolecules or nanoparticles to the surface.<sup>55-59</sup> A linear relationship is often observed between the adsorbed mass and the resulting refractive index change in the SPR experiment which can then be used in a variety of biosensor applications. Ellipsometry is an optical technique used to study thin film dielectric properties.<sup>60-62</sup> The change of polarization of polarized input light is measured after interaction with the sample. Ellipsometry is especially sensitive for measuring the chirality of materials.<sup>63-64</sup> Although both SPR and ellipsometry can provide *in situ* measurements, they cannot provide molecular structural information.

Vibrational spectroscopies can provide molecular structural information about surfaces and interfaces. For example, molecular composition, orientation and time dependent dynamics at surfaces can be studied by using infrared light to characterize intrinsic vibrational modes of surface molecules. One important surface vibrational spectroscopy is attenuated total-internal reflectance-Fourier transform infrared (ATR-FTIR) spectroscopy.<sup>65-69</sup> The surface selectivity of ATR-FTIR is

provided by the penetration depth of the evanescent wave which has the same order of magnitude as the IR wavelength. By applying different polarized incident light beams, interfacial molecular orientations can be derived in ATR-FTIR measurements. However, the surface sensitivity of ATR-FTIR is poor; sometimes in order to probe surface/interfacial structures, it is necessary to subtract large signal contribution from the bulk media. Another surface specific vibrational technique is surface-enhanced Raman spectroscopy (SERS), which enhances the Raman scattering signal of molecules adsorbed on rough metal substrates (usually gold or silver).<sup>70-73</sup> The enhancement factor can be as high as  $10^{14}\sim 10^{15}$  which allows SERS to detect single molecules.<sup>74-76</sup> However, it is difficult to apply SERS to study other surfaces and interfaces. Buried solid/solid interfaces in particular are difficult to study using above surface sensitive techniques.

SFG can probe interfaces that are accessible to laser light. More importantly, second order nonlinear process selection rule (which will be discussed in the next part) indicates SFG has intrinsic sub-monolayer interfacial selectivity.<sup>40, 77-81</sup> It has been extensively shown that SFG can provide *in situ* measurements on buried interfaces in real time. By applying different polarization combinations of the input/output laser beams, SFG can also be used to determine molecular orientations at interfaces.<sup>34, 82-86</sup> SFG experiments do not require high vacuum to perform (as in XPS and SIMS experiments). Compared to AFM, SPR, and ellipsometry techniques, vibrational spectroscopic signatures can provide more detailed molecular structural information on surfaces. SFG spectroscopy also provides *in situ* measurement of molecular presence and orientation with great sensitivity at buried interfaces which cannot be obtained using ATR-FTIR or SERS techniques.

### 1.2.2 SFG Selection Rule

The interfacial sensitivity of SFG is provided by the selection rule which is different from linear vibrational spectroscopy (e.g. IR or Raman spectroscopy). SFG is a second order nonlinear optical process in which the signal intensity is proportional to the square of the second order nonlinear optical susceptibility of the material  $\chi^{(2)}$  under the electric dipole approximation.  $\chi^{(2)}$  is a third rank tensor which changes sign under inversion operation:  $\chi^{(2)}(-r) = -\chi^{(2)}(r)$ .<sup>87-88</sup> For materials with inversion symmetry, the relation  $\chi^{(2)}(-r) = \chi^{(2)}(r)$  holds. Comparing these two relations, we know  $\chi^{(2)}(r) = 0$ . This demonstrates that no SFG signal will be generated if the material has inversion symmetry under the electric dipole approximation. SFG signal can only be generated from a medium with no inversion symmetry. Most bulk materials have inversion symmetry and therefore do not generate SFG signal. However, at surfaces or interfaces where the centro-symmetry is broken,  $\chi^{(2)}(-r) \neq \chi^{(2)}(r)$ , so the SFG process can occur. In the systems studied in this thesis, signals contributed from surfaces or interfaces dominate the SFG spectra and bulk signal usually can be neglected.

### 1.2.3 SFG Experimental Setup

The SFG system layout is shown in Figure 1-1. The SFG spectrometer used here (EKSPLA, Vilnius, Lithuania) is composed of a pico-second Nd:YAG laser, a harmonic unit, an optical parametric generation (OPG)/amplification (OPA)/difference frequency generation (DFG) system, and a detection system. The visible beam (532 nm) is generated by frequency-doubling the fundamental output pulses of 20 ps pulsewidth from the Nd:YAG laser. OPG and OPA can generate a signal beam (420 to 680 nm) and an idler beam (740 to 2300 nm). The idler beam and the 1064 nm pump beam are used in DFG to generate a frequency tunable mid-IR beam ( $1000 \text{ cm}^{-1}$  to  $4300 \text{ cm}^{-1}$ ). For SFG experiments, the input visible and IR pulse energies are  $\sim 30 \mu\text{J}$  and  $\sim 100$



$\mu\text{J}$ , respectively. The pulses were overlapped at the sample surface or interface spatially and temporarily to generate the sum frequency signal beam. The incident angles of the visible and the IR input beams are  $60^\circ$  and  $57^\circ$  versus the surface normal, respectively. The SFG signal from the surface is collected by a photomultiplier tube (PMT) attached to a monochromator. In this thesis, the reference monochromator and detector were not used.

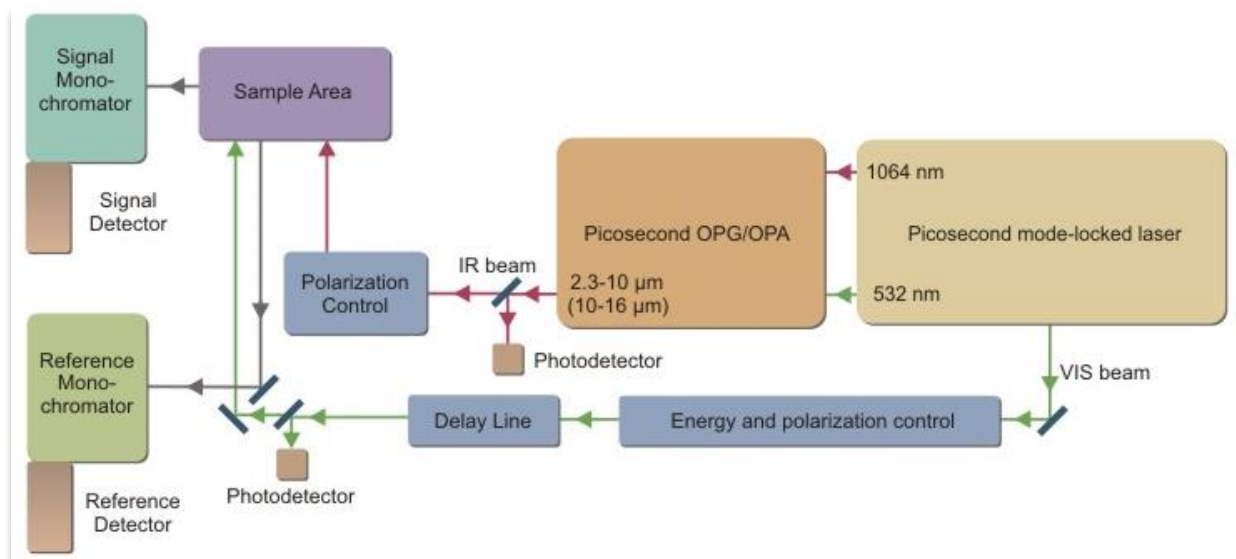


**Figure 1-1.** Layout of the EKSPLA SFG system used in this research. Adapted from <http://www.ekspla.com/>.

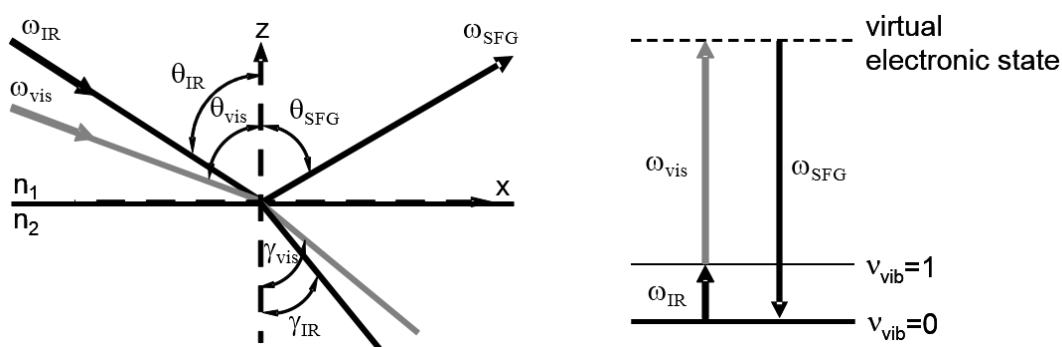


**Figure 1-2.** Left: The co-propagating non-collinear SFG experimental geometry. The reflected infrared and visible beams and transmitted beams have been omitted for clarity. Right: Schematic of the SFG energy diagram which involves both IR and Raman transitions.

A schematic of the general SFG experimental geometry and the SFG energy diagram are shown in Figure 1-2.

### 1.2.4 Basic SFG Theory

The theoretical background of SFG has been developed in early publications.<sup>31, 34, 81, 83, 89</sup> New SFG data analysis methods have also been developed.<sup>39, 90-95</sup>

Basically, SFG signal intensity can be expressed as:<sup>34</sup>

$$I_{SFG} \propto |\chi_{eff}^{(2)}|^2 I_{IR} I_{vis} \quad (1.1)$$

Here  $I_{IR}$  and  $I_{vis}$  are intensities of the input IR and visible beams, respectively.  $\chi_{eff}^{(2)}$  is the effective second order nonlinear optical susceptibility, which can be expressed as the sum of a nonresonant term and a resonant term:<sup>34</sup>

$$\chi_{eff}^{(2)} = \chi_{NR}^{(2)} + \sum_q \frac{A_q}{\omega_{IR} - \omega_q + i\Gamma_q} \quad (1.2)$$

Here  $\chi_{NR}^{(2)}$  is the nonresonant contribution from the sample. The resonant contribution can be modeled as the sum of Lorentzians with signal strength or amplitude  $A_q$ , frequency  $\omega_q$ , and linewidth  $\Gamma_q$ . Equation (1.2) can be used to fit SFG spectrum in the experiment to obtain quantitative vibrational strength comparisons of different functional groups.

For an isotropic interface in the x-y plane, the effective second order nonlinear optical susceptibility components can be related to the second order nonlinear optical susceptibility components of the sample in the lab-fixed coordinating system:<sup>34</sup>

$$\chi_{eff,ssp}^{(2)} = L_{yy}(\omega_{SF}) L_{yy}(\omega_{vis}) L_{zz}(\omega_{IR}) \sin \theta_{IR} \cdot \chi_{yyz}^{(2)} \quad (1.3)$$

$$\chi_{\text{eff},sps}^{(2)} = L_{yy}(\omega_{SF})L_{zz}(\omega_{vis})L_{yy}(\omega_{IR})\sin\theta_{vis} \cdot \chi_{yzy}^{(2)} \quad (1.4)$$

$$\chi_{\text{eff},pss}^{(2)} = L_{zz}(\omega_{SF})L_{yy}(\omega_{vis})L_{yy}(\omega_{IR})\sin\theta_{SFG} \cdot \chi_{zyy}^{(2)} \quad (1.5)$$

$$\begin{aligned} \chi_{\text{eff},ppp}^{(2)} = & -L_{xx}(\omega_{SF})L_{xx}(\omega_{vis})L_{zz}(\omega_{IR})\cos\theta_{SFG}\cos\theta_{vis}\sin\theta_{IR} \cdot \chi_{xxx}^{(2)} \\ & -L_{xx}(\omega_{SF})L_{zz}(\omega_{vis})L_{xx}(\omega_{IR})\cos\theta_{SFG}\sin\theta_{vis}\cos\theta_{IR} \cdot \chi_{xzx}^{(2)} \\ & +L_{zz}(\omega_{SF})L_{xx}(\omega_{vis})L_{xx}(\omega_{IR})\sin\theta_{SFG}\cos\theta_{vis}\cos\theta_{IR} \cdot \chi_{zxx}^{(2)} \\ & +L_{zz}(\omega_{SF})L_{zz}(\omega_{vis})L_{zz}(\omega_{IR})\sin\theta_{SFG}\sin\theta_{vis}\sin\theta_{IR} \cdot \chi_{zzz}^{(2)} \end{aligned} \quad (1.6)$$

In these expressions,  $\chi_{IJK}^{(2)}$  ( $IJK = x, y, z$ ) is a local nonlinear second order optical susceptibility component of the material at the interface defined in the lab-fixed coordination.<sup>34</sup>  $\theta_{IR}$  and  $\theta_{vis}$  are the incident angles of the input IR and visible beams vs. the surface normal, respectively. The angle  $\theta_{SFG}$  is the output angle of SFG signal vs. the surface normal.  $L_i$  ( $i = x, y, z$ ) is the Fresnel coefficient which is a function of beam input angles and the refractive indices of materials forming the interface.<sup>34</sup>  $\omega_{SF}$ ,  $\omega_{vis}$  and  $\omega_{IR}$  are frequencies of the sum frequency beam, the visible beam and the IR beam, respectively. Moreover, ssp, sps, pss and ppp are different polarization combinations of SFG measurement ('ssp' indicates s-polarized signal, s-polarized visible beam, and p-polarized IR beam).

$L_{xx}(\omega)$ ,  $L_{yy}(\omega)$ , and  $L_{zz}(\omega)$  are the Fresnel coefficients for beam  $\omega$  given by:

$$\begin{aligned} L_{xx}(\omega) &= \frac{2n_1(\omega)\cos\gamma}{n_1(\omega)\cos\gamma + n_2(\omega)\cos\theta}, \\ L_{yy}(\omega) &= \frac{2n_1(\omega)\cos\theta}{n_1(\omega)\cos\theta + n_2(\omega)\cos\gamma}, \\ L_{zz}(\omega) &= \frac{2n_2(\omega)\cos\theta}{n_1(\omega)\cos\gamma + n_2(\omega)\cos\theta} \left( \frac{n_1(\omega)}{n'(\omega)} \right)^2 \end{aligned} \quad (1.7)$$

where  $n'(\omega)$  is the refractive index of the interfacial layer,  $\theta$  is the incident angle of the beam in consideration, and  $\gamma$  is the corresponding refracted angle satisfies:

$$n_1(\omega) \sin \theta = n_2(\omega) \sin \gamma .$$

The measured SFG second order nonlinear optical susceptibility components defined in the lab-fixed coordination system can be related to the molecular hyperpolarizability components through molecular orientations considering the coordinate transformation.<sup>81</sup>

$$\chi_{IJK}^{(2)} = N \sum_{IJK=x,y,z} \langle R_{Ii} R_{Jj} R_{Kk} \rangle \beta_{ijk}^{(2)} \quad ijk = a, b, c \quad (1.8)$$

In this expression, N is the surface number density. R is the transformation matrix from the molecular frame (a,b,c) to the lab frame (x,y,z).  $\beta_{ijk}^{(2)}$  is the hyperpolarizability component. The angle brackets here mean ensemble average, indicating that the macroscopic susceptibility is the ensemble average of the hyperpolarizability of each molecule projected to the lab frame multiplied by the total molecule density and divided by vacuum permittivity. R is usually a function of three angles, azimuthal angle  $\phi$ , twist angle  $\psi$ , and tilt angle  $\theta$ .<sup>81</sup> Therefore, we have:

$$\chi_{IJK}^{(2)} = N \sum_{IJK=x,y,z} f(\phi, \psi, \theta) \beta_{ijk}^{(2)} \quad ijk = a, b, c \quad (1.9)$$

For an isotropic surface, the azimuthal angle can be averaged between 0 to  $2\pi$ . Then the expression is reduced to

$$\chi_{IJK}^{(2)} = N \sum_{IJK=x,y,z} f(\psi, \theta) \beta_{ijk}^{(2)} \quad ijk = a, b, c \quad (1.10)$$

If the distribution of twist angle is considered to be random, then

$$\chi_{IJK}^{(2)} = N \sum_{IJK=x,y,z} f(\theta) \beta_{ijk}^{(2)} \quad ijk = a, b, c \quad (1.11)$$

The resonant part of  $\beta_{ijk}^{(2)}$  is directly proportional to the product of the IR dipole derivative and the Raman polarizability derivative of the vibrational mode Q as described below:

$$\beta_{ijk}^{(2)} \propto \frac{\partial \mu_i}{\partial Q} \frac{\partial \alpha_{jk}}{\partial Q} \quad (1.12)$$

Therefore, only those vibrational modes that are both IR-active and Raman-active will be SFG-active.

Orientation analysis of different functional groups such as methyl (CH<sub>3</sub>),<sup>34, 83-84</sup> methylene (CH<sub>2</sub>),<sup>96-97</sup> aromatic C-H stretch,<sup>98-102</sup>  $\alpha$ -helical,<sup>2, 39</sup> and  $\beta$ -sheet<sup>93, 103</sup> has also been reported. As an example, the methyl group orientation calculation will be introduced below.

### 1.2.5 Molecular Orientation Calculation of Methyl Group Using Polarized SFG

#### Spectroscopy

The orientation analysis of functional groups at interfaces in SFG lies in the relation of interfacial second order nonlinear optical susceptibility and molecular hyperpolarizability demonstrated in equation (1.9). Three angles, azimuthal angle  $\phi$ , twist angle  $\psi$ , and tilt angle  $\theta$  are used in Euclidean space to describe the orientation of a rigid body. Therefore, the orientation of a functional group, such as a methyl group, pointing in any direction, can be described using these three angles in the lab-fixed frame. The relationship between  $\chi_{IJK}^{(2)}$  and  $\beta_{ijk}^{(2)}$  as described in equation (1.9) has been deduced systematically.<sup>89</sup> It has also been shown that the relationship can be greatly simplified based on certain assumptions or prior knowledge. An example is a functional group of a molecule on an isotropic surface with a free rotation symmetry vs. the principle axis, where azimuthal angle  $\phi$  and twist angle  $\psi$  can be averaged from 0 to  $2\pi$ .<sup>89</sup> To deduce the orientation angles, sometimes certain components of the molecular hyperpolarizability (or  $\beta_{ijk}^{(2)}$ ) need to be known. In such cases the bond additivity method is usually needed to obtain  $\beta_{ijk}^{(2)}$  from measured or calculated Raman polarizability  $\alpha_{ij}$  and dipole transition moment  $\mu_k$  of the vibration mode under study.<sup>96</sup>

What we can quantitatively obtain from an SFG spectrum after fitting the SFG signals detected using the Lorentzian equation (1.2) is the effective second order nonlinear optical susceptibility  $\chi_{eff}^{(2)}$ . Using the relations described in equations (1.3)~(1.6),  $\chi_{eff}^{(2)}$  can be correlated to  $\chi_{IJK}^{(2)}$  through Fresnel coefficients, which can be calculated at certain input angles for certain species with known refractive indices. Moreover,  $\chi_{IJK}^{(2)}$  can be further correlated to molecular hyperpolarizability  $\beta_{ijk}^{(2)}$  through surface number density N of the functional group and the three orientation angles as described in equation (1.9)~(1.11). The value of N may be estimated, but for many cases it is not required for orientation determination. “N” can be eliminated using the ratio of certain components of the nonlinear susceptibility, which can be measured using different polarizations of the input and output laser beams in the SFG experiment, or using the SFG signals detected in the same polarization combination but belonging to different vibrational modes. To further explain these approaches, we will use poly(methyl methacrylate) PMMA as an example to show the way to derive the surface molecular orientation of an ester methyl group in air.

Wang *et al.* have shown that ester methyl groups dominate the PMMA surface in air.<sup>84</sup> Methyl groups can be treated as holding  $C_{3v}$  symmetry in most cases. Molecular hyperpolarizability  $\beta_{ijk}^{(2)}$  can be simplified based on the molecular symmetry.<sup>96</sup> In SFG, such hyperpolarizability can be further simplified due to the isotropic surface and rotational symmetry for the  $C_{3v}$  symmetry. For example, in  $C_{3v}$ , the non-vanishing hyperpolarizability components  $\beta_{ijk}^{(2)}$  for the C-H symmetric stretches are  $\beta_{ccc}^{(2)}$  and  $\beta_{aac}^{(2)} = \beta_{bbc}^{(2)}$ , while for asymmetric stretches, the only non-zero component is  $\beta_{caa}^{(2)}$ .<sup>84, 89</sup> For the second-order nonlinear optical susceptibility of C-H stretching vibrational modes of molecules with  $C_{3v}$  symmetry, there are only four non-vanishing components:  $\chi_{xxz}^{(2)} = \chi_{yyz}^{(2)}$ ,  $\chi_{xzx}^{(2)} = \chi_{zyy}^{(2)}$ ,  $\chi_{zxx}^{(2)} = \chi_{zyy}^{(2)}$ ,  $\chi_{zzz}^{(2)}$ .<sup>82</sup> The relation between different second

order nonlinear optical susceptibility components in the lab frame and molecular hyperpolarizability components in the molecular coordinate system can be simplified and expressed as:<sup>34, 84, 89</sup>

For the symmetric C-H stretch:

$$\chi_{xz,s}^{(2)} = \chi_{yz,s}^{(2)} = \frac{1}{2} N \beta_{ccc}^{(2)} [(1+r) \langle \cos \theta \rangle - (1-r) \langle \cos^3 \theta \rangle] \quad (1.13)$$

$$\chi_{zx,s}^{(2)} = \chi_{zy,s}^{(2)} = \chi_{xx,s}^{(2)} = \chi_{yy,s}^{(2)} = \frac{1}{2} N \beta_{ccc}^{(2)} (1-r) [\langle \cos \theta \rangle - \langle \cos^3 \theta \rangle] \quad (1.14)$$

$$\chi_{zz,s}^{(2)} = N \beta_{ccc}^{(2)} [r \langle \cos \theta \rangle + (1-r) \langle \cos^3 \theta \rangle] \quad (1.15)$$

For the asymmetric stretches:

$$\chi_{yz,as}^{(2)} = \chi_{xz,as}^{(2)} = -\frac{1}{2} N \beta_{caa}^{(2)} [\langle \cos \theta \rangle - \langle \cos^3 \theta \rangle] \quad (1.16)$$

$$\chi_{zx,as}^{(2)} = \chi_{zy,as}^{(2)} = \chi_{yy,as}^{(2)} = \chi_{xx,as}^{(2)} = \frac{1}{2} N \beta_{caa}^{(2)} \langle \cos^3 \theta \rangle \quad (1.17)$$

$$\chi_{zz,as}^{(2)} = N \beta_{caa}^{(2)} [\langle \cos \theta \rangle - \langle \cos^3 \theta \rangle] \quad (1.18)$$

Here ‘s’ and ‘as’ indicate symmetric and asymmetric C-H stretching modes, respectively.

For the symmetric C-H stretching mode,  $r = \beta_{aac}^{(2)} / \beta_{ccc}^{(2)}$ . In these equations, it is assumed that the polymer film is isotropic, and the ester methyl group can rotate freely around the principle axis. Accordingly, the azimuthal angle  $\phi$  and twist angle  $\psi$  are averaged from 0 to  $2\pi$ . If we assume the distribution of  $\theta$  is a  $\delta$ -function, then  $\langle \cos \theta \rangle$  and  $\langle \cos^3 \theta \rangle$  can be substituted by  $\cos \theta$  and  $\cos^3 \theta$ . Sometimes, the orientation angle distribution can be modeled by a Gaussian function:  $f(\theta) = C \cdot \exp[-(\theta - \theta_0)^2 / (2\sigma^2)]$ , where  $\theta_0$  is the center of distribution,  $\sigma$  is the root-mean-square distribution width.<sup>104-105</sup>

An important relation for the above equations is that  $\chi_{xxz,s}^{(2)}$  and  $\chi_{yyz,s}^{(2)}$  always have the opposite sign as  $\chi_{xxz,as}^{(2)}$  and  $\chi_{yyz,as}^{(2)}$ . This indicates symmetric and asymmetric modes of the methyl group always negatively interfere with each other in an ssp spectrum. It is difficult to accurately measure the number density of surface molecules probed in the SFG experiment. Therefore, it is usually necessary to eliminate the number density N when using the above equations for orientation calculations. By taking the ratio of, for example,  $\chi_{yyz,s}^{(2)} / \chi_{zyz,s}^{(2)}$ , the number density N and molecular hyperpolarizability  $\beta_{ccc}$  can be eliminated. Thus the ratio of symmetric C-H stretch  $\chi_{yyz,s}^{(2)} / \chi_{zyz,s}^{(2)}$  can be expressed as a function of molecular tilt angle  $\theta$  and r. The value of r can be obtained by calculation.<sup>96</sup> However, sometimes it is difficult to obtain an accurate value of r. Instead, a range of r values were reported in the literature.<sup>34</sup> To avoid the use of r, one can choose to use the hyperpolarizability component ratio of the asymmetric C-H stretch such as  $\chi_{yyz,as}^{(2)} / \chi_{zyz,as}^{(2)}$ , which is only a function of  $\theta$  (r is canceled out). To deduce the tilt angle  $\theta$ ,  $|\chi_{yyz,as}^{(2)} / \chi_{zyz,as}^{(2)}|$  can be plotted as a function of  $\theta$  (equation (1.16) and (1.17)). In SFG experiments,  $\chi_{eff}^{(2)}$  (e.g.,  $\chi_{ssp}^{(2)}$  and  $\chi_{sps}^{(2)}$ ) can be measured in different polarizations (e.g. ssp and sps polarizations), and the value of  $|\chi_{ssp,as}^{(2)} / \chi_{sps,as}^{(2)}| = |(A_{ssp,as} / \Gamma_{ssp,as}) / (A_{sps,as} / \Gamma_{sps,as})|$  can be obtained through spectral fitting using equation (1.2). Further,  $|\chi_{ssp,as}^{(2)} / \chi_{sps,as}^{(2)}|$  value can be associated to  $|\chi_{yyz,as}^{(2)} / \chi_{zyz,as}^{(2)}|$  value through equations (1.3)-(1.6). Finally, according to the  $|\chi_{yyz,as}^{(2)} / \chi_{zyz,as}^{(2)}|$  value deduced from measurement and  $|\chi_{yyz,as}^{(2)} / \chi_{zyz,as}^{(2)}|$  plotted as the function of  $\theta$  (obtained from equation (1.16) and (1.17)), the tilt angle  $\theta$  can be deduced.

Using the asymmetric stretching mode of PMMA and the method mentioned above, the PMMA ester methyl group surface orientation can be derived to be between 33° vs. surface normal



with a  $\delta$ -angle distribution and  $0^\circ$  vs. surface normal with a Gaussian angle distribution of  $31^\circ$ .<sup>84</sup> Interfacial structures of poly(n-butyl methacrylate) (PBMA)/air and PBMA/water have also been investigated by Wang, *et al.*<sup>106</sup>

Similar orientation analysis method has also been developed for methylene group, which has  $C_{2v}$  symmetry.<sup>107</sup> Orientation analysis of phenyl ring has been developed and many compounds with aromatic groups have been studied using SFG.<sup>98-101</sup> Additionally, orientation information of protein secondary structures such as helices<sup>2</sup> and  $\beta$ -sheets<sup>93, 103</sup>, as well as the entire protein molecules<sup>95</sup> has also been obtained using SFG.

### 1.3 Presented Research

In this thesis, the development of SFG applications in studying adhesive interfaces will be presented in Chapters 2 and 3. More specifically, the extensive studies on PDMS adhesives, including interfacial methyl group orientation calculation and silane behaviors at interfaces, will be discussed in Chapter 2. In Chapter 3, the study will be extended to epoxy adhesives. Adhesion mechanism between epoxy-amine mixture and PET substrate will be discussed in detail. A mechanical adhesion test method based on 180 degree shearing was developed and will be presented in Chapter 2, which will also be extensively used in Chapter 3. One of the most important approaches in these Chapters is the correlation of the interfacial molecular structures measured using SFG to the mechanical adhesion strength of the interfaces, which will be discussed in detail. Overall, important molecular level understanding of interfacial structures and adhesion mechanisms has been achieved from SFG results.

In Chapter 4, SFG spectroscopy will be applied to investigate lipid transbilayer movement in supported bilayers. We investigated the lipid transbilayer dynamics induced by a polyelectrolyte polyethylenimine (PEI) which is widely used in gene delivery and shows cytotoxicity in biological

systems. We will show that SFG can provide important lipid dynamic information in PEI membrane interactions, which can help to better understand PEI's cytotoxicity in a molecular level. Additionally, ATR-FTIR spectroscopy was used to supplement SFG measurement to further confirm there is no significant lipid bilayer damage or removal from the substrate.

The technical development of multimodal analytical systems involving SFG spectroscopy will be discussed in Chapter 5, including SFG and CARS multi-spectroscopy system, which finds applications in thin film characterization; SFG and optical microscopy multimodal system, which can be used to examine buried heterogeneous biointerfaces; SFG and TIRF microscopy multimodal system, which can be used to simultaneously examine interfacial fluorescent label dynamics and molecular structure information. Such development can help to further extend SFG spectroscopy to more interdisciplinary fields, and to provide information that conventional SFG spectroscopy cannot provide.

The theoretical development in CARS vibrational spectroscopy based on bond additivity method and Raman measurement will be presented in Chapter 6. The methodology developed in this chapter can be used to quantitatively interpret methyl group C-H stretching CARS spectra measured in different polarizations. Symmetric and asymmetric stretching peak ratios can be calculated using the theory and the results show good agreements with the experimental data. This methodology can be used to analyze CARS vibrational spectra of other vibrational modes from other functional groups, providing quantitative understanding and assistance for CARS signal analysis in advanced CARS spectroscopy and microscopy.

In summary, the chapters which will be presented in this thesis show my research effort in applications, technical development, and theoretical data analysis of nonlinear vibrational spectroscopy, especially SFG and CARS.

## 1.4 References

1. Zhang, D.; Shen, Y.; Somorjai, G. A., *Chem. Phys. Lett.* **1997**, *281*, 394-400.
2. Chen, X.; Wang, J.; Boughton, A. P.; Kristalyn, C. B.; Chen, Z., *J. Am. Chem. Soc.* **2007**, *129*, 1420-1427.
3. Ye, S.; Nguyen, K. T.; Chen, Z., *J. Phys. Chem. B* **2010**, *114*, 3334-3340.
4. Ma, G.; Allen, H. C., *J. Phys. Chem. B* **2003**, *107*, 6343-6349.
5. Gopalakrishnan, S.; Jungwirth, P.; Tobias, D. J.; Allen, H. C., *J. Phys. Chem. B* **2005**, *109*, 8861-8872.
6. Morkel, M.; Kaichev, V. V.; Rupprechter, G.; Freund, H. J.; Prosvirin, I. P.; Bukhtiyarov, V. I., *J. Phys. Chem. B* **2004**, *108*, 12955-12961.
7. Keszthelyi, T.; Pászti, Z.; Rigó, T.; Hakkel, O.; Telegdi, J.; Guzzi, L., *J. Phys. Chem. B* **2006**, *110*, 8701-8714.
8. Hankett, J. M.; Zhang, C.; Chen, Z., *Langmuir* **2012**, *28*, 4654-4662.
9. Humbert, C.; Busson, B.; Abid, J. P.; Six, C.; Girault, H.; Tadjeddine, A., *Electrochim. Acta* **2005**, *50*, 3101-3110.
10. Weidner, T.; Breen, N. F.; Li, K.; Drobny, G. P.; Castner, D. G., *Proceedings of the National Academy of Sciences* **2010**, *107*, 13288-13293.
11. Zhang, D.; Gracias, D.; Ward, R.; Gauckler, M.; Tian, Y.; Shen, Y.; Somorjai, G., *J. Phys. Chem. B* **1998**, *102*, 6225-6230.
12. Gracias, D.; Zhang, D.; Lianos, L.; Ibach, W.; Shen, Y.; Somorjai, G., *Chem. Phys.* **1999**, *245*, 277-284.
13. Chen, C.; Wang, J.; Mark, A.; Chen, Z., *Macromolecules* **2002**, *35*, 8093-8097.
14. Kim, S. H.; Opdahl, A.; Marmo, C.; Somorjai, G. A., *Biomaterials* **2002**, *23*, 1657-1666.
15. Cimatu, K.; Baldelli, S., *J. Am. Chem. Soc.* **2006**, *128*, 16016-16017.
16. Cimatu, K.; Moore, H. J.; Lee, T. R.; Baldelli, S., *J. Phys. Chem. C* **2007**, *111*, 11751-11755.
17. Uosaki, K.; Yano, T.; Nihonyanagi, S., *J. Phys. Chem. B* **2004**, *108*, 19086-19088.
18. Mermut, O.; Phillips, D. C.; York, R. L.; McCrea, K. R.; Ward, R. S.; Somorjai, G. A., *J. Am. Chem. Soc.* **2006**, *128*, 3598-3607.
19. Evans-Nguyen, K. M.; Fuierer, R. R.; Fitchett, B. D.; Tolles, L. R.; Conboy, J. C.; Schoenfish, M. H., *Langmuir* **2006**, *22*, 5115-5121.
20. Somorjai, G. A.; York, R. L.; Butcher, D.; Park, J. Y., *Phys. Chem. Chem. Phys.* **2007**, *9*, 3500-3513.
21. Onorato, R. M.; Yoon, A. P.; Lin, J. T.; Somorjai, G. A., *J. Phys. Chem. C* **2012**, *116*, 9947-9954.
22. Inoue, K.; Fujii, M.; Sakai, M., *Appl. Spectrosc.* **2010**, *64*, 275-281.
23. Kogure, S.; Inoue, K.; Ohmori, T.; Ishihara, M.; Kikuchi, M.; Fujii, M.; Sakai, M., *Opt. Express* **2010**, *18*, 13402-13406.
24. Raghunathan, V.; Han, Y.; Korth, O.; Ge, N. H.; Potma, E. O., *Opt. Lett.* **2011**, *36*, 3891-3893.
25. Flörsheimer, M.; Brillert, C.; Fuchs, H., *Langmuir* **1999**, *15*, 5437-5439.
26. Hoffmann, D.; Kuhnke, K.; Kern, K., *Rev. Sci. Instrum.* **2002**, *73*, 3221-3226.
27. Cimatu, K.; Baldelli, S., *J. Phys. Chem. B* **2006**, *110*, 1807-1813.
28. Hieu, H. C.; Tuan, N. A.; Li, H.; Miyauchi, Y.; Mizutani, G., *Appl. Spectrosc.* **2011**, *65*, 1254-1259.

29. Smith, K. A.; Conboy, J. C., *Anal. Chem.* **2012**, *84*, 8122-8126.
30. Zhu, X.; Suhr, H.; Shen, Y., *Phys. Rev. B: Condens. Matter;(United States)* **1987**, *35*, 3047-3050.
31. Shen, Y., *Nature* **1989**, *337*, 519-525.
32. Cremer, P. S.; Su, X.; Shen, Y. R.; Somorjai, G. A., *J. Am. Chem. Soc.* **1996**, *118*, 2942-2949.
33. Richter, L. J.; Petralli-Mallow, T. P.; Stephenson, J. C., *Opt. Lett.* **1998**, *23*, 1594-1596.
34. Zhuang, X.; Miranda, P.; Kim, D.; Shen, Y., *Phy. Rev. B* **1999**, *59*, 12632-12640.
35. Kim, J.; Cremer, P. S., *ChemPhysChem* **2001**, *2*, 543-546.
36. Chen, Z.; Shen, Y.; Somorjai, G. A., *Annu. Rev. Phys. Chem.* **2002**, *53*, 437-465.
37. Kim, J.; Somorjai, G. A., *J. Am. Chem. Soc.* **2003**, *125*, 3150-3158.
38. Ye, S.; Morita, S.; Li, G. F.; Noda, H.; Tanaka, M.; Uosaki, K.; Osawa, M., *Macromolecules* **2003**, *36*, 5694-5703.
39. Nguyen, K. T.; Le Clair, S. V.; Ye, S.; Chen, Z., *J. Phys. Chem. B* **2009**, *113*, 12169-12180.
40. Ma, G.; Allen, H. C., *Langmuir* **2006**, *22*, 5341-5349.
41. Raschke, M.; Hayashi, M.; Lin, S.; Shen, Y., *Chem. Phys. Lett.* **2002**, *359*, 367-372.
42. Chou, K.; Westerberg, S.; Shen, Y.; Ross, P.; Somorjai, G., *Phy. Rev. B* **2004**, *69*, 153413.
43. Li, Q.; Hua, R.; Chou, K. C., *J. Phys. Chem. B* **2008**, *112*, 2315-2318.
44. Ratner, B. D.; Castner, D. G., *Electron spectroscopy for chemical analysis*. 1997; p 43-98.
45. McArthur, S. L., *Surf. Interface Anal.* **2006**, *38*, 1380-1385.
46. Roach, P.; Parker, T.; Gadegaard, N.; Alexander, M., *Surf. Sci. Rep.* **2010**, *65*, 145-173.
47. Benninghoven, A., *Surf. Sci.* **1975**, *53*, 596-625.
48. Henry, M.; Dupont-Gillain, C.; Bertrand, P., *Langmuir* **2003**, *19*, 6271-6276.
49. Bernsmann, F.; Lawrence, N.; Hannig, M.; Ziegler, C.; Gnaser, H., *Anal. Bioanal. Chem.* **2008**, *391*, 545-554.
50. Baugh, L.; Weidner, T.; Baio, J.; Nguyen, P. C. T.; Gamble, L. J.; Stayton, P. S.; Castner, D. G., *Langmuir* **2010**, *26*, 16434-16441.
51. Binnig, G.; Quate, C. F.; Gerber, C., *Phys. Rev. Lett.* **1986**, *56*, 930-933.
52. Giessibl, F. J., *Rev. Mod. Phys.* **2003**, *75*, 949-983.
53. Hörber, J.; Miles, M., *Science* **2003**, *302*, 1002-1005.
54. Carnally, S.; Barrow, K.; Alexander, M. R.; Hayes, C. J.; Stolnik, S.; Tendler, S. J. B.; Williams, P. M.; Roberts, C. J., *Langmuir* **2007**, *23*, 3906-3911.
55. Liedberg, B.; Nylander, C.; Lunstrom, I., *Sensors and Actuators* **1983**, *4*, 299-304.
56. Liedberg, B.; Nylander, C.; Lundström, I., *Biosensors and Bioelectronics* **1995**, *10*, i-ix.
57. Homola, J.; Yee, S. S.; Gauglitz, G., *Sensors and Actuators B: Chemical* **1999**, *54*, 3-15.
58. Green, R. J.; Frazier, R. A.; Shakesheff, K. M.; Davies, M. C.; Roberts, C. J.; Tendler, S. J. B., *Biomaterials* **2000**, *21*, 1823-1835.
59. Eustis, S.; El-Sayed, M. A., *Chem. Soc. Rev.* **2006**, *35*, 209-217.
60. De Feijter, J. A.; Benjamins, J.; Veer, F. A., *Biopolymers* **1978**, *17*, 1759-1772.
61. Azzam, R. M. A.; Bashara, N. M., *Ellipsometry and polarized light*. North Holland: 1987; Vol. 31.
62. Fujiwara, H., *Spectroscopic ellipsometry:Principles and Applications*. John Wiley&Sons: 2007.
63. Lekner, J., *Pure and Applied Optics: Journal of the European Optical Society Part A* **1999**, *5*, 417-443.
64. Simpson, G. J.; Dailey, C. A.; Plocinik, R. M.; Moad, A. J.; Polizzi, M. A.; Everly, R. M.,

- Anal. Chem.* **2005**, *77*, 215-224.
65. Harrik, N., *Internal reflection spectroscopy*. Interscience: New York, 1967.
  66. Mirabella Jr, F., *Appl. Spectrosc. Rev.* **1985**, *21*, 45-178.
  67. Axelsen, P. H.; Citra, M. J., *Prog. Biophys. Mol. Biol.* **1996**, *66*, 227-253.
  68. Le Coutre, J.; Kaback, H. R.; Patel, C. K. N.; Heginbotham, L.; Miller, C., *Proceedings of the National Academy of Sciences* **1998**, *95*, 6114-6117.
  69. Vinchurkar, M. S.; Chen, K. H. C.; Yu, S. S. F.; Kuo, S. J.; Chiu, H. C.; Chien, S. H.; Chan, S. I., *Biochemistry* **2004**, *43*, 13283-13292.
  70. Moskovits, M.; Suh, J., *J. Phy. Chem.* **1984**, *88*, 5526-5530.
  71. Moskovits, M., *Rev. Mod. Phys.* **1985**, *57*, 783-826.
  72. Moskovits, M., *J. Raman Spectrosc.* **2005**, *36*, 485-496.
  73. Orendorff, C. J.; Gole, A.; Sau, T. K.; Murphy, C. J., *Anal. Chem.* **2005**, *77*, 3261-3266.
  74. Nie, S.; Emory, S. R., *Science* **1997**, *275*, 1102-1106.
  75. Michaels, A. M.; Nirmal, M.; Brus, L., *J. Am. Chem. Soc.* **1999**, *121*, 9932-9939.
  76. Xu, H.; Bjerneld, E. J.; Käll, M.; Börjesson, L., *Phys. Rev. Lett.* **1999**, *83*, 4357-4360.
  77. Hunt, J.; Guyot-Sionnest, P.; Shen, Y., *Chem. Phys. Lett.* **1987**, *133*, 189-192.
  78. Bain, C. D.; Davies, P. B.; Ong, T. H.; Ward, R. N.; Brown, M. A., *Langmuir* **1991**, *7*, 1563-1566.
  79. Eisenthal, K. B., *Annu. Rev. Phys. Chem.* **1992**, *43*, 627-661.
  80. Ye, S.; Nihonyanagi, S.; Uosaki, K., *Phys. Chem. Chem. Phys.* **2001**, *3*, 3463-3469.
  81. Moad, A. J.; Simpson, G. J., *J. Phys. Chem. B* **2004**, *108*, 3548-3562.
  82. Guyot-Sionnest, P.; Hunt, J.; Shen, Y., *Phys. Rev. Lett.* **1987**, *59*, 1597-1600.
  83. Hirose, C.; Yamamoto, H.; Akamatsu, N.; Domen, K., *J. Phy. Chem.* **1993**, *97*, 10064-10069.
  84. Wang, J.; Chen, C.; Buck, S. M.; Chen, Z., *J. Phys. Chem. B* **2001**, *105*, 12118-12125.
  85. Baldelli, S., *J. Phys. Chem. B* **2003**, *107*, 6148-6152.
  86. Chen, X.; Clarke, M. L.; Wang, J.; Chen, Z., *International Journal of Modern Physics B* **2005**, *19*, 691-713.
  87. Shen, Y. R., *The principles of nonlinear optics*. Wiley: New York, 1984.
  88. Boyd, R. W., *Nonlinear optics*. Academic Pr: 2003.
  89. Hirose, C.; Akamatsu, N.; Domen, K., *Appl. Spectrosc.* **1992**, *46*, 1051-1072.
  90. Yeh, Y. L.; Zhang, C.; Held, H.; Mebel, A.; Wei, X.; Lin, S.; Shen, Y., *J. Chem. Phys.* **2001**, *114*, 1837-1843.
  91. Wang, J.; Clarke, M. L.; Chen, Z., *Anal. Chem.* **2004**, *76*, 2159-2167.
  92. Kataoka, S.; Cremer, P. S., *J. Am. Chem. Soc.* **2006**, *128*, 5516-5522.
  93. Nguyen, K. T.; King, J. T.; Chen, Z., *J. Phys. Chem. B* **2010**, *114*, 8291-8300.
  94. Curtis, A. D.; Asplund, M. C.; Patterson, J. E., *J. Phys. Chem. C* **2011**, *115*, 19303-19310.
  95. Boughton, A. P.; Yang, P.; Tesmer, V. M.; Ding, B.; Tesmer, J. J. G.; Chen, Z., *Proc. Natl. Acad. Sci. U. S. A.* **2011**, *108*, E667-E673.
  96. Hirose, C.; Akamatsu, N.; Domen, K., *J. Chem. Phys.* **1992**, *96*, 997-1004.
  97. Gan, W.; Zhang, Z.; Feng, R.; Wang, H., *J. Phys. Chem. C* **2007**, *111*, 8726-8738.
  98. Duffy, D. C.; Davies, P. B.; Bain, C. D., *J. Phy. Chem.* **1995**, *99*, 15241-15246.
  99. Gautam, K.; Schwab, A.; Dhinojwala, A.; Zhang, D.; Dougal, S.; Yeganeh, M., *Physical review letters* **2000**, *85*, 3854-3857.
  100. Harp, G. P.; Rangwalla, H.; Yeganeh, M. S.; Dhinojwala, A., *J. Am. Chem. Soc.* **2003**, *125*, 11283-11290.

101. Lu, X.; Han, J.; Shephard, N.; Rhodes, S.; Martin, A. D.; Li, D.; Xue, G.; Chen, Z., *J. Phys. Chem. B* **2009**, *113*, 12944-12951.
102. Lu, X.; Spanninga, S. A.; Kristalyn, C. B.; Chen, Z., *Langmuir* **2010**, *26*, 14231-14235.
103. Wang, J.; Chen, X. Y.; Clarke, M. L.; Chen, Z., *Proc. Natl. Acad. Sci. U. S. A.* **2005**, *102*, 4978-4983.
104. Wei, X.; Zhuang, X.; Hong, S. C.; Goto, T.; Shen, Y., *Phys. Rev. Lett.* **1999**, *82*, 4256-4259.
105. Simpson, G. J.; Rowlen, K. L., *J. Am. Chem. Soc.* **1999**, *121*, 2635-2636.
106. Wang, J.; Paszti, Z.; Even, M. A.; Chen, Z., *J. Am. Chem. Soc.* **2002**, *124*, 7016-7023.
107. Lu, R.; Gan, W.; Wu, B.; Chen, H.; Wang, H., *J. Phys. Chem. B* **2004**, *108*, 7297-7306.

## CHAPTER 2

# SFG STUDIES ON THE BURIED POLY(DIMETHYL SILOXANE) (PDMS) ADHESIVE INTERFACES

### 2.1 Background and Motivation

Silicone elastomers such as PDMS are extensively used in many important applications such as polymer adhesives, packaging materials for microelectronics, polymer MEMS, microfluidics, biomedical implants, and marine anti-fouling coatings. For example, polymer adhesives based on silicone materials including PDMS have played an important role in the development of electronic devices used in solar, LED, computer and automotive applications, as well as durable structures used in green housing, office buildings, bridges and roads. PDMS materials have such a wide variety of applications due to their high thermal stability, excellent rheological properties, low temperature flexibility, UV resistance, and simple, controllable cure chemistry.<sup>1-2</sup>

However, the adhesion between the addition-cured PDMS elastomers and polymers can be very weak due to the loss of intrinsic functional groups that are responsible for good adhesion. Many different methods to pretreat the substrate surfaces such as plasma treatment, corona discharge treatment, mechanical abrasion, or solvent cleaning followed by wet chemical etching were used to improve the adhesion strength.<sup>3-4</sup> Such pretreatments greatly increase the cost and are time-consuming. A different means to improve the PDMS adhesion which is more commercially attractive is to introduce adhesion promoters to the elastomer to make PDMS self-adhere to polymers.<sup>4</sup> Adhesion promoters are usually small molecules that typically employ as additives and

can enhance adhesion at the substrate/adhesive interface. Many organosilanes have been developed as adhesion promoters for silicone elastomer.<sup>4-12</sup> It is believed that these silane adhesion promoters modified the interfaces between the substrates and silicone elastomers. However, the detailed mechanism of how adhesion is improved has not been precisely understood at the molecular level due to the lack of appropriate techniques.

Many surface sensitive techniques have been used to study molecular structures on polymer surfaces or at polymer interfaces.<sup>13-16</sup> Currently it is still quite challenging to study molecular structures at buried interfaces *in situ*. Recently, SFG vibrational spectroscopy has been developed into a powerful tool to study molecular structures at buried interfaces.<sup>17-34</sup> SFG can probe vibrational modes of various functional groups at interfaces, providing molecular insight into interfacial structures of complicated molecules. Furthermore, by collecting SFG spectra with different input and output beam polarization combinations, the orientation of certain functional groups can be derived.<sup>35-39</sup>

Surface and interfacial structures of PDMS have been studied using SFG by several groups. The first SFG study on PDMS was published in 1997 by Zhang *et al.*<sup>40</sup> It was reported that the surface of a polyurethane material terminated with PDMS end groups restructured in water. In 2004, Chen *et al.* investigated the polymer/air and polymer/water interfaces of several model PDMS materials.<sup>41</sup> The results suggested that all the PDMS surfaces studied were mainly covered by methyl groups. Surface restructuring of the methyl groups has also been observed in water. Yurdumakan *et al.* used SFG to study the buried PDMS/polystyrene (PS) interface to elucidate the friction property at the interface.<sup>42</sup> They also studied the buried interfaces between oxidized PDMS or regular PDMS and SAMs. It was concluded that the enhanced ordering of PDMS can be induced by both the confinement at the interface and the template of the SAM methyl groups.<sup>43</sup> Ye *et al.*



applied SFG to study PDMS surface changes after various treatments, such as plasma and UV irradiation.<sup>44</sup> The chain conformation of a PDMS monolayer at the air/water interface has also been studied using SFG.<sup>45</sup> It was found that methyl groups of PDMS chains at the interface are disordered in the dilute regime, while two methyl groups on the repeating unit point to air asymmetrically with higher PDMS surface densities. Ye *et al.* studied surface structures of PDMS materials incorporated with biocides and other functionalities for marine antifouling and fouling-release coating applications. Surface restructuring behaviors of various PDMS materials have been followed in detail using SFG.<sup>46-48</sup> SFG has also been applied to study molecular interactions at buried polymer/silane interfaces,<sup>22, 49-51</sup> and various polymer/PDMS (with or without silane adhesion promoters) interfaces.<sup>52-53</sup>

The goal of this research is to use SFG as an analytical technique to extensively study the interfacial molecular structures of PDMS materials on various substrates, particularly polymer substrates. We will first develop a methodology to quantitatively calculate PDMS molecular orientations at buried interfaces based on polarization dependent SFG measurement. We are also interested in understanding the absolute orientations of PDMS methyl group at various interfaces and their relation with interfacial hydrophobicity. Furthermore, we want to use SFG to investigate the molecular behaviors of silane adhesion promoters at PDMS/polymer interfaces to understand silane adhesion promoting mechanisms at such interfaces. To obtain a general conclusion, we will use methoxysilanes and ethoxysilanes to improve PDMS' adhesion to poly(ethylene terephthalate) (PET). In order to correlate our interfacial molecular structure understanding to mechanical adhesion test, we developed a method to measure adhesion strength using polymer blocks adhered by PDMS adhesives. We will show that SFG is a powerful technique for studying buried interfacial molecular structures of adhesives. Continued success in the related research can help to depict

clearer physical pictures of adhesion mechanisms and provide knowledge that can help to develop better adhesion promoters for industry.

## **2.2 Molecular Orientation Determination of PDMS Material at Buried Interfaces**

First of all, we want to use SFG as a tool to quantitatively obtain the interfacial molecular orientation information at interfaces between PDMS and different substrates. PET is widely used in industry as a barrier material and as a substrate for microelectronic devices. Therefore, we will perform the SFG study at the PET/PDMS interface to understand PDMS' molecular behavior at such an interface. Furthermore, silicon is the most widely used substrate for electronics, which is usually covered by a layer of silicon dioxide. Therefore, we are also interested in studying the interface between PDMS and silicon dioxide, or silica.

### **2.2.1 Materials Used in the Research and Sample Preparation**

Fused silica substrates (right angle prisms) were obtained from Altos Photonics, Inc. They were cleaned overnight by placing in a concentrated sulfuric acid bath saturated with potassium dichromate at 60°C. These substrates were then rinsed using deionized water and dried with nitrogen gas before polymer deposition. In order to avoid spectral confusion, PET samples with aliphatic chain deuterated ( $d_4$ -PET) were used in the experiment, which was obtained from Polymer Source Inc. The  $d_4$ -PET was dissolved in 2-chlorophenol (Sigma Aldrich) to form a 1 wt% solution. The polymer thin films were then prepared by spin-coating the 1 wt% polymer solution on fused silica prisms at 2500 rpm. The spin coater was from Specialty Coating Systems (P-6000). Deuterated polystyrene ( $d_8$ -PS) and deuterated poly(methyl methacrylate) ( $d_8$ -PMMA) were also obtained from Polymer Source Inc. The procedure of making  $d_8$ -PS and  $d_8$ -PMMA samples were similar to that of  $d_4$ -PET thin film. The PDMS samples were prepared by using Sylgard 184 silicone elastomer kit, which was obtained from Dow Corning Corporation. The

Sylgard 184 silicone elastomer was mixed in 10:1 base/curing agent ratio using a vortex mixture. For cured interfaces, the samples were cured in the oven at 140 °C for 2 hours, and then stored at room temperature for 24 hours before use. Right angle silica prisms were purchased from Altos Photonics, Inc. They were placed in a concentrated sulfuric acid and potassium dichromate mixture overnight at 60°C to eliminate hydrocarbon contaminations. Then they were rinsed with deionized water and further cleaned in a home-built air plasma cleaner.

TiO<sub>2</sub> thin films used in the experiment were deposited on silica prisms. Before deposition, silica prisms were cleaned using the procedure previously mentioned. The deposition of a Ti thin film was carried out using electron beam physical vapor deposition (EnerJet Evaporator). The environment was oil-free and the pressure was lower than  $2 \times 10^{-6}$  Torr. The thickness of the deposited Ti film was ~50 nm and was monitored by a quartz crystal oscillator. The substrate was heated at 700°C for 4 hours to form a translucent layer of TiO<sub>2</sub> on fused silica.

In order to compare the interference of the TiO<sub>2</sub> non-resonant SFG signal with the SFG signal from the silica/PDMS interface to the interference of the TiO<sub>2</sub> non-resonant SFG signal with the SFG signal from the polymer/PDMS interface, some fused silica prisms with TiO<sub>2</sub> coating were selected and a thin layer (~50 nm) of silica was coated on the TiO<sub>2</sub> surface of each substrate. The procedure of coating silica on TiO<sub>2</sub> was similar to that of coating Ti on silica.

The experimental geometry used for this study is shown in Figure 2-1.

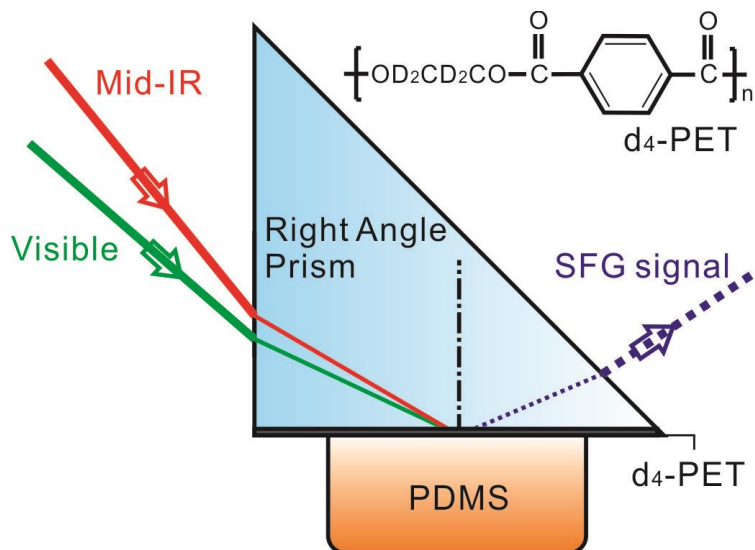


**Figure 2-1.** The near critical angle (NCA) geometry used in the experiment for interface studies. To clearly show the SFG reflection signal, the reflected mid-IR and visible beams were not plotted. The molecular formula of  $d_4$ -PET is displayed on the top right.

### 2.2.2 PDMS Methyl Group Orientation Calculation Method

In Chapter 1, we have introduced the method of using polarized SFG spectroscopy measurements to deduce molecular orientation information of a methyl at an interface. The method has been applied to investigate various methyl group behaviors at surfaces and interfaces *in situ*. However, we found that such a method is no longer valid for PDMS methyl group orientation calculation. This problem is caused by the different molecular arrangement in a PDMS molecule.

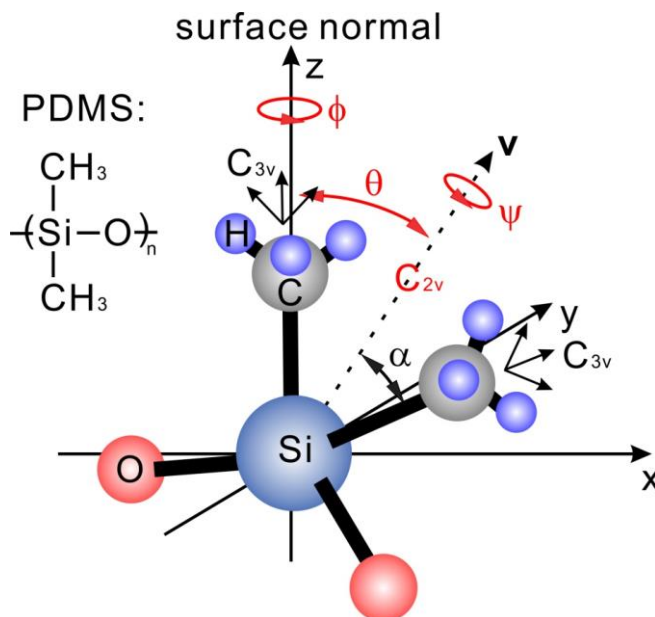


**Figure 2-2.** The molecular structure of PDMS, and the coordinate system chosen for orientation analysis. Each methyl group presents a  $C_{3v}$  symmetry. The entire  $\text{Si}(\text{CH}_3)_2$  group presents a  $C_{2v}$  symmetry.  $xyz$  coordinate demonstrates the lab frame.  $\theta$ ,  $\psi$ ,  $\phi$  are tilt angle, twist angle and azimuthal angle of vector  $v$  bisects  $\text{Si}(\text{CH}_3)_2$  group. The molecular formula of PDMS is displayed on the left.

In PDMS, even though the angles between various chemical bonds can be flexible,<sup>54</sup> the two neighboring methyl groups on average have a fixed bond angle of  $112^\circ$  (as shown in Figure 2-2). Therefore, the vibrational mode hyperpolarizabilities of the two individual methyl groups need to be combined in the molecular frame. For a  $\text{Si}(\text{CH}_3)_2$  group, the transformation between lab frame and molecular frame can be achieved using a united atom model for each methyl group.<sup>55</sup> The two methyl groups connected to the same Si atom are then considered to adopt a  $C_{2v}$  symmetry, while each methyl group still has a  $C_{3v}$  symmetry. A vector  $v$ , which bisects the two methyl groups, is used to describe the molecular orientation of these two methyl groups. The angle between the principle axis of each methyl group and the vector  $v$  is defined as angle  $\alpha$  ( $\alpha=56^\circ$ ). The tilt angle and twist angle which will be discussed in the paper is in reference to this vector  $v$ . After two

coordinate transformations, the second-order nonlinear optical susceptibility components of the Si(CH<sub>3</sub>)<sub>2</sub> group in PDMS can be expressed as:<sup>55</sup>

Symmetric stretch:

$$\chi_{yyz} = \chi_{xxz} = (N / 2\varepsilon_0)(\beta_{aac} - \beta_{ccc})\{(\cos \theta - \cos^3 \theta)[(5 + 3 \cos 2\psi)(\cos \alpha - \cos^3 \alpha) - 2 \cos \alpha] - 2 \cos \theta(\cos \alpha - \cos^3 \alpha)\} + (2N / \varepsilon_0)\beta_{aac} \cos \theta \cos \alpha \quad (2.1)$$

$$\chi_{yzy} = \chi_{zxx} = \chi_{xzx} = (N / 2\varepsilon_0)(\beta_{aac} - \beta_{ccc})[(\cos \theta - \cos^3 \theta)(5 + 3 \cos 2\psi)(\cos \alpha - \cos^3 \alpha) + 2 \cos \theta \cos \alpha(\cos^2 \theta + \cos^2 \alpha - 2)] \quad (2.2)$$

Asymmetric stretch:

$$\chi_{yyz} = \chi_{xxz} = (N / \varepsilon_0)\beta_{caa}\{-2 \cos \theta + 3(\cos \theta - \cos^3 \theta)(1 + \cos 2\psi)\}(\cos \alpha - \cos^3 \alpha) - 2(\cos \theta - \cos^3 \theta)\cos^3 \alpha \quad (2.3)$$

$$\chi_{yzy} = \chi_{zxx} = \chi_{xzx} = (N / \varepsilon_0)\beta_{caa}[3(\cos \theta - \cos^3 \theta)(\cos \alpha - \cos^3 \alpha)(1 + \cos 2\psi) + 2 \cos^3 \theta \cos^3 \alpha] \quad (2.4)$$

Here,  $N$  is the surface number density of detected functional groups,  $\varepsilon_0$  is the permittivity of free space.  $\beta_{aac}, \beta_{ccc}, \beta_{caa}$  are the hyperpolarizability components of the single methyl group C-H stretching modes.  $\chi_{yyz}, \chi_{xxz}, \chi_{yzy}, \chi_{zxx}, \chi_{xzx}$  are second order nonlinear optical susceptibility components of the C-H stretching modes for Si(CH<sub>3</sub>)<sub>2</sub> defined in the lab-fixed coordination system. Furthermore, it is assumed in equations (2.1)-(2.4) that the sample is isotropic in the x-y plane, and therefore the azimuthal angle  $\phi$  can be averaged. The angle  $\theta$  is the tilt angle of vector  $v$  of the entire Si(CH<sub>3</sub>)<sub>2</sub> group (vs. the surface normal),  $\psi$  is the twist angle of the same group.

The values of  $\beta_{aac}, \beta_{ccc}, \beta_{caa}$  can be obtained by calculation. It has been reported that the ratio of  $\beta_{aac} / \beta_{ccc}$  is in the range of 1.6-4.3 for a methyl group.<sup>19</sup> For a PDMS methyl group, the ratio  $\beta_{aac} / \beta_{ccc} = 2.3$  has been applied in previous publications<sup>56-57</sup> based on the bond additivity method.  $\beta_{aac} / \beta_{caa} \approx 1$  has also been reported for a methyl group.<sup>36</sup> In this research, we first provide numerical analysis based on equations (2.1)-(2.4) by assigning values

$\beta_{aac} : \beta_{ccc} : \beta_{caa} = 2.3:1:2.3$ ,  $\beta_{ccc} = 1$ . Calculated values of  $\chi_{yyz,s} \cdot \epsilon_0 / N$ ,  $\chi_{yyz,as} \cdot \epsilon_0 / N$ , and the ratios of  $\chi_{yyz,s} / \chi_{yyz,as}$  and  $\chi_{yyz,as} / \chi_{zy,as}$  were plotted as functions of tilt angle  $\theta$  and twist angle  $\psi$  (Figure 2-3). Taken equations (1.3) and (1.4) into consideration, it is able to deduce the possible range of the molecular orientation of the methyl groups in PDMS based on the SFG symmetric and asymmetric stretching signals detected using ssp and sps polarization combinations. Either the ratio of  $\chi_{yyz,s} / \chi_{yyz,as}$  or  $\chi_{yyz,as} / \chi_{zy,as}$  obtained from the experiment is possible to be used to define a range of angle  $\theta$  and  $\psi$ . In this research, we deduced both ratios and compared the possible orientation angle ranges assuming a  $\delta$ -orientation angle distribution. Although interfacial methyl groups may not adopt a  $\delta$ -orientation distribution, the  $\delta$ -distribution orientation angle deduced here can be considered to represent the average orientation of the methyl groups. The overlapping orientation angle region obtained by these two ratios was considered to be the likely molecular orientations that PDMS methyl groups tended to adopt. From Figures 2-3c and d we find that the value of  $\chi_{yyz,s} / \chi_{yyz,as}$  can be positive or negative due to different tilt angle and twist angle combinations. Positive values tend to hold at the right bottom corner, when tilt angle is big ( $>40^\circ$ ), and twist angle is small ( $<50^\circ$ ). On the other hand, when tilt angle is small ( $<40^\circ$ ) or twist angle is big ( $>50^\circ$ ),  $\chi_{yyz,s} / \chi_{yyz,as}$  will have negative values. For the values of  $\chi_{yyz,as} / \chi_{zy,as}$ , this trend is similar.

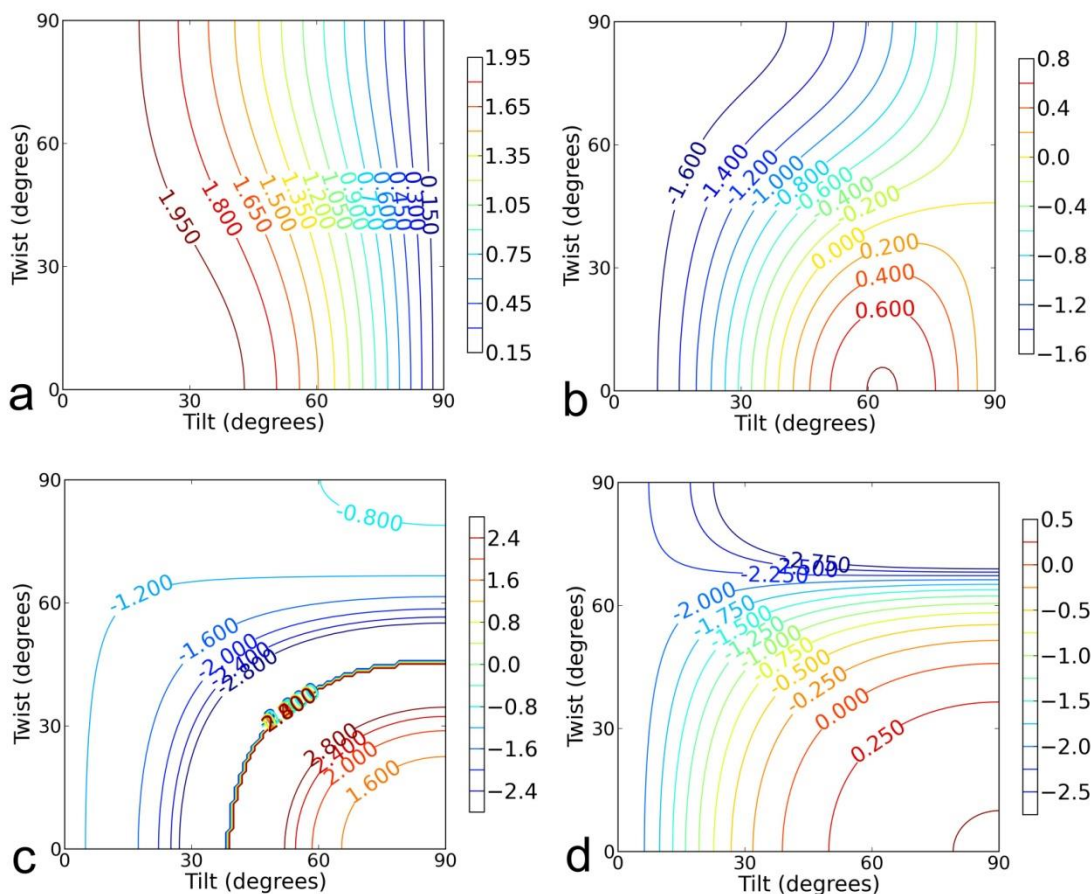


**Figure 2-3.** Calculated values of (a)  $\chi_{yyz,s} \cdot \varepsilon_0 / N$  and (b)  $\chi_{yyz,as} \cdot \varepsilon_0 / N$ , ratios of (c)  $\chi_{yyz,s} / \chi_{yyz,as}$  and (d)  $\chi_{yyz,as} / \chi_{zyz,as}$  are plotted as functions of tilt angle  $\theta$  and twist angle  $\psi$ , with the angle ranges between  $0^\circ$  and  $90^\circ$ . It was assumed that  $\beta_{aac} : \beta_{ccc} : \beta_{caa} = 2.3:1:2.3$  and  $\beta_{ccc} = 1$  based on the previous publications.

### 2.2.4 SFG Experimental Results

SFG was applied to study interfacial molecular structures of PDMS while in contact with  $d_4$ -PET and silica. The ssp SFG spectra collected from  $d_4$ -PET/PDMS interfaces are shown in Figures 2-4a and b. Use equation (1.2), both spectra can be fit to get the amplitude  $A_q$ , frequency  $\omega_q$ , and linewidth  $\Gamma_q$  of the vibrational modes. The spectral fitting results are listed in Table 2-1. All the SFG ssp spectra between  $2800 \text{ cm}^{-1}$  and  $3000 \text{ cm}^{-1}$  in the aliphatic C-H stretching frequency



range were dominated by two peaks. One peak was centered at  $2900\text{ cm}^{-1}$ , contributed by the symmetric C-H stretching mode of the Si-CH<sub>3</sub> group. The second peak was centered  $\sim 2962\text{ cm}^{-1}$ , generated by the asymmetric C-H stretching mode of the same group. These two strong signals in the SFG spectra indicate that PDMS methyl groups are ordered at the buried *d*<sub>4</sub>-PET/PDMS interfaces, regardless of curing or not. The PDMS methyl symmetric C-H stretching peak center was slightly red shifted from that detected at the air/PDMS interface<sup>45</sup> as well as that of the silica/PDMS interfaces which will be discussed below. Such a shift may be due to the interactions between PDMS methyl groups and the carbon oxygen double bonds in the PET substrate at the interface. At these *d*<sub>4</sub>-PET/PDMS interfaces, in addition to the PDMS methyl signals, SFG signals at around  $3100\text{ cm}^{-1}$  were also observed, showing that the *d*<sub>4</sub>-PET aromatic group was also ordered at the interfaces. We are not able to quantify the molecular orientation of the *d*<sub>4</sub>-PET aromatic ring because its vibrational signals from various modes cannot be clearly distinguished.

Compare the SFG spectra collected from the *d*<sub>4</sub>-PET/PDMS interfaces before and after curing PDMS, it was found that the SFG spectral features of the PDMS methyl symmetric and asymmetric C-H stretching modes were similar, even though the intensities of the two peaks for PDMS before and after curing were slightly different. The fitted ratios of  $\chi_{ssp,s} / \chi_{ssp,as}$  of PDMS methyl groups before and after curing were  $1.24 \pm 0.17$  and  $1.35 \pm 0.15$  (derived from Table 2-1), indicating that the PDMS methyl groups have a minor difference in orientation at the *d*<sub>4</sub>-PET/uncured PDMS and *d*<sub>4</sub>-PET/cured PDMS interfaces.

The SFG spectra presented in Figure 2-4 could not be fit using opposite signs for the symmetric and asymmetric C-H stretches, different from fitting the normal methyl symmetric and asymmetric peaks. Therefore, the two peaks were fit using the same sign, which suggested that the

two peaks have the same phase. For the SFG signals detected using the same polarization combination, we have

$$\chi_{ssp,s} / \chi_{ssp,as} = \chi_{yyz,s} / \chi_{yyz,as}$$

Therefore, the ratios of  $\chi_{yyz,s} / \chi_{yyz,as}$  at the  $d_4$ -PET/PDMS interface before and after curing were  $1.24 \pm 0.17$  and  $1.35 \pm 0.15$ , respectively.

SFG spectra were also collected in the sps polarization combination from the  $d_4$ -PET/PDMS interfaces before and after curing PDMS (Figures 2-4c and d). In sps spectra, only asymmetric C-H stretch at  $\sim 2960 \text{ cm}^{-1}$  was clearly resolved. From equation (1.4), such an sps SFG signal corresponds to the nonlinear optical susceptibility component  $\chi_{zy,as}$ . We can calculate from the values in Table 2-1 that at the  $d_4$ -PET/uncured PDMS interface:

$$\chi_{ssp,as} / \chi_{sps,as} = \pm 0.47 \pm 0.06$$

The different Fresnel coefficients at the  $d_4$ -PET/PDMS interfaces in the ssp and sps polarization combinations were calculated. From Appendix 2.2.9, we have

$$\chi_{eff,ssp} = 1.48 \cdot \chi_{yyz} \text{ and } \chi_{eff,sps} = 1.58 \cdot \chi_{zy}$$

$$\text{Therefore, } \chi_{yyz} / \chi_{zy} = 1.07 \cdot \chi_{eff,ssp} / \chi_{eff,sps}.$$

Using this relation, we can deduce at the  $d_4$ -PET/uncured PDMS interface:

$$\chi_{yyz,as} / \chi_{zy,as} = \pm 0.51 \pm 0.06.$$

We can also calculate from the values listed in Table 2-1 that at the  $d_4$ -PET/cured PDMS interface,

$$\chi_{ssp,as} / \chi_{sps,as} = \pm 0.47 \pm 0.05.$$

$$\text{Similarly, we can deduce } \chi_{yyz,as} / \chi_{zy,as} = \pm 0.51 \pm 0.05.$$

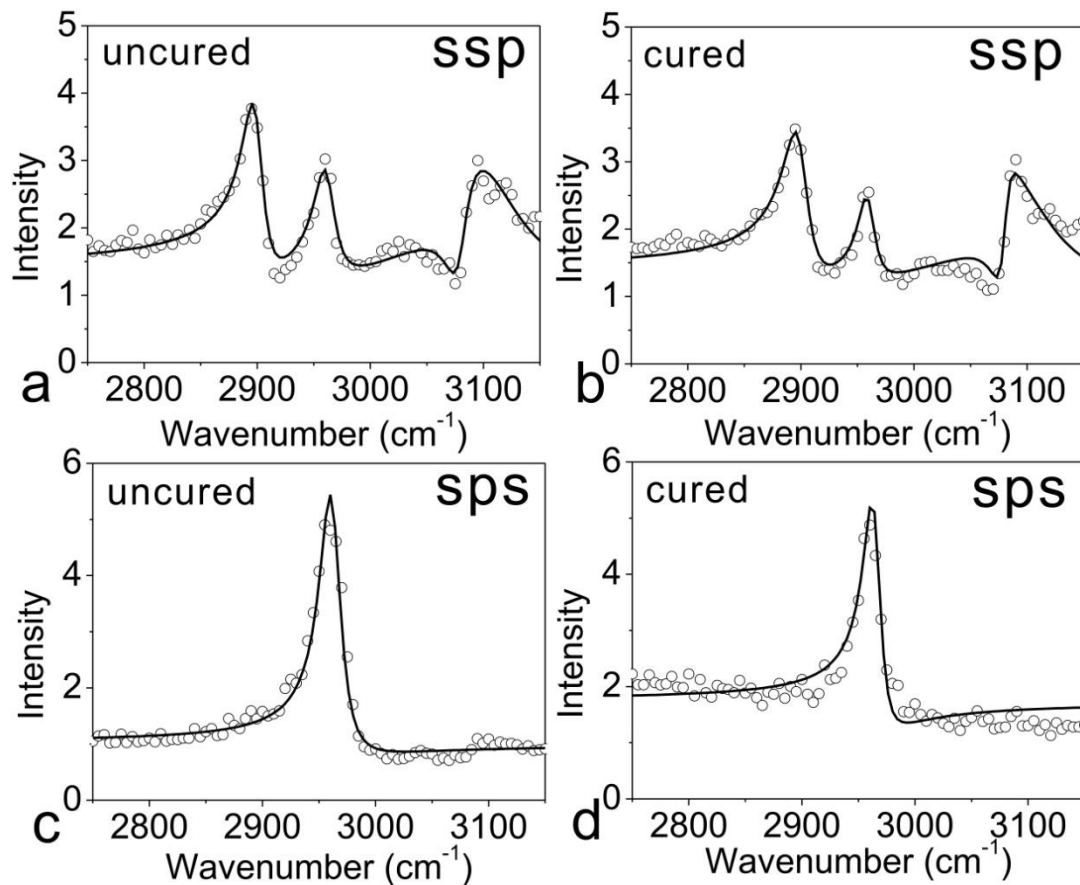


**Figure 2-4.** (a), (c) ssp and sps SFG spectra collected from the  $d_4$ -PET/PDMS interface before curing and (b), (d) after curing. Dots are measured data; lines are fitting results.

Interfaces	$\omega_q$ (cm $^{-1}$ )	$A_q$	$\Gamma_q$ (cm $^{-1}$ )	$ A_q/\Gamma_q $	Assignment
$d_4$ -PET/PDMS (uncured, ssp)	2900	13.7±0.9	11.2±0.8	1.22±0.12	Si-CH $_3$ (s)
	2962	11.3±0.7	11.5±0.8	0.98±0.09	Si-CH $_3$ (as)
$d_4$ -PET/PDMS (cured, ssp)	2900	15.6±1.0	13.4±0.6	1.16±0.09	Si-CH $_3$ (s)
	2960	7.7±0.5	9.0±0.5	0.86±0.07	Si-CH $_3$ (as)
$d_4$ -PET/PDMS (uncured, sps)	2962	23.8±0.9	11.5±0.8	2.07±0.16	Si-CH $_3$ (as)
$d_4$ -PET/PDMS (cured, sps)	2965	16.4±0.8	9.0±0.6	1.82±0.15	Si-CH $_3$ (as)

**Table 2-1.** Spectral fitting results for the SFG spectra shown in Figure 2-4.

SFG spectra from the silica/PDMS interface were collected before and after curing PDMS (Figure 2-5). Before curing, both the C-H symmetric and asymmetric stretching signals of Si-CH $_3$

could be detected in ssp polarization combination (Figure 2-5a), while in the sps spectrum, only the asymmetric stretching signal could be detected at around 2960 cm<sup>-1</sup> (Figure 2-5c). For the ssp spectrum, good fitting results could only be achieved when opposite amplitude signs for the symmetric and asymmetric C-H stretching signals were used. This suggests that at the silica/PDMS interface, the symmetric and asymmetric stretching modes of Si-CH<sub>3</sub> groups have different phases. The fitting results shown in Table 2-2 indicate that at silica/uncured PDMS interface:

$$\chi_{\text{yyz},s} / \chi_{\text{yyz},as} = -0.98 \pm 0.13$$

From the fitting results, we can also obtain

$$\chi_{\text{ssp},as} / \chi_{\text{sps},as} = \pm 2.66 \pm 0.30 \text{ at such an interface.}$$

The different Fresnel coefficients at the silica/PDMS interfaces in the ssp and sps SFG signals were calculated. From Appendix 2.2.9, we have

$$\chi_{\text{eff},ssp} = 1.31 \cdot \chi_{\text{yyz}} \text{ and } \chi_{\text{eff},sps} = 1.33 \cdot \chi_{\text{zyz}}$$

$$\text{Therefore, } \chi_{\text{yyz}} / \chi_{\text{zyz}} = 1.02 \cdot \chi_{\text{eff},ssp} / \chi_{\text{eff},sps} \cdot$$

Accordingly, at the silica/uncured PDMS interface,

$$\chi_{\text{yyz},as} / \chi_{\text{zyz},as} = \pm 2.71 \pm 0.31.$$

Fitting results from the SFG spectra collected from the silica/cured PDMS interface (Figures 2-5b and d, Table 2-2) show that

$$\chi_{\text{yyz},s} / \chi_{\text{yyz},as} = -1.53 \pm 0.21 \text{ and } \chi_{\text{ssp},as} / \chi_{\text{sps},as} = \pm 1.79 \pm 0.23$$

Considering the different Fresnel coefficients in the ssp and sps SFG signals, we can obtain

$$\chi_{\text{yyz},as} / \chi_{\text{zyz},as} = \pm 1.83 \pm 0.23.$$

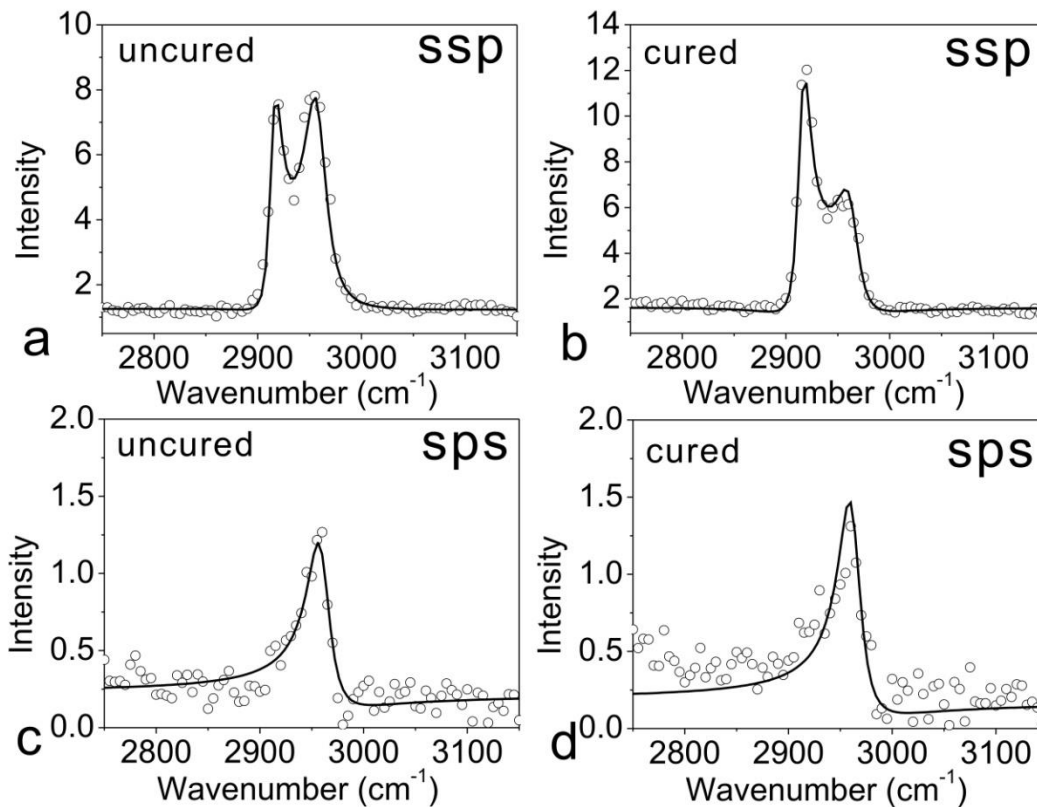


**Figure 2-5.** (a), (c) ssp and sps SFG spectra collected from the silica/PDMS interface before curing and (b), (d) after curing. Dots are measured data; lines are fitting results.

Interfaces	$\omega_q$ (cm <sup>-1</sup> )	$A_q$	$\Gamma_q$ (cm <sup>-1</sup> )	$ A_q/\Gamma_q $	Assignment
Silica/PDMS (uncured, ssp)	2915	17.2±0.8	6.9±0.7	2.49±0.28	Si-CH <sub>3</sub> (s)
Silica/PDMS (cured, ssp)	2958	-33.6±1.2	13.3±0.9	2.53±0.19	Si-CH <sub>3</sub> (as)
Silica/PDMS (uncured, sps)	2917	22.9±1.3	7.5±0.7	3.05±0.33	Si-CH <sub>3</sub> (s)
Silica/PDMS (cured, sps)	2964	-26.1±1.4	13.1±0.8	1.99±0.16	Si-CH <sub>3</sub> (as)
Silica/PDMS (uncured, ssp)	2960	12.7±0.7	13.3±0.9	0.95±0.08	Si-CH <sub>3</sub> (as)
Silica/PDMS (cured, sps)	2962	14.5±1.0	13.1±0.9	1.11±0.11	Si-CH <sub>3</sub> (as)

**Table 2-2.** Spectral Fitting results for the SFG spectra shown in Figure 2-5.

### 2.2.5 Deriving Molecular Orientation of PDMS Methyl Groups at Interfaces

The values of  $\chi_{yyz,s} / \chi_{yyz,as}$  and  $\chi_{yyz,as} / \chi_{zyz,as}$  obtained in the experiments were compared to the calculated map shown in Figures 2-3c and d to deduce the possible angle range of the PDMS

methyl group orientation. Considering the possible fitting errors and other experimental errors, a 20% error bar was included in the measured ratios for orientation analysis. The possible values for  $\theta$  and  $\psi$  of  $\text{Si}(\text{CH}_3)_2$  groups at the  $d_4$ -PET/PDMS interfaces were then plotted for each measurement and for both measurements (Figure 2-6). Figure 2-6a shows that at the  $d_4$ -PET/uncured PDMS interface, according to  $\chi_{yyz,s} / \chi_{yyz,as} = 1.24$  obtained above,  $\text{Si}(\text{CH}_3)_2$  groups tend to have a  $>75^\circ$  tilt angle, but a  $<15^\circ$  twist angle. Based on  $\chi_{yyz,as} / \chi_{yzy,as} = 0.51$ , it is deduced that the possible range shown in Figure 2-6b is larger. Possible values of tilt angles and twist angles are  $\theta > 70^\circ$ ,  $\psi < 20^\circ$ , respectively. The overlapping orientation angle region that satisfies both measurements is shown in Figure 2-6c, where the possible orientations for PDMS methyl groups are within the range of tilt angle  $>75^\circ$ , twist angle  $<15^\circ$ . Here  $\chi_{yyz,as} / \chi_{yzy,as} = 0.51$  rather than  $-0.51$  was chosen because the possible orientation angle range deduced from the negative value would not have any overlap with that obtained by  $\chi_{yyz,s} / \chi_{yyz,as} = 1.24$  (Appendix 2.2.9). According to equations (2.1)-(2.4), if methyl groups are completely lying down, i.e.  $\theta = 90^\circ$ ,  $\chi_{yyz,s} = \chi_{yyz,as} = \chi_{yzy,as} = 0$ , there should be no SFG signals detected in the ssp and sps polarization combinations. However, SFG signals in both polarization combinations were detected, which indicates that  $\theta > 75^\circ$  but  $\theta \neq 90^\circ$ . The tilt angles for PDMS methyl groups at the  $d_4$ -PET/uncured PDMS interface are large, but methyl groups are not completely lying down. At the same time, they tend to have very small twist angles at the interface.

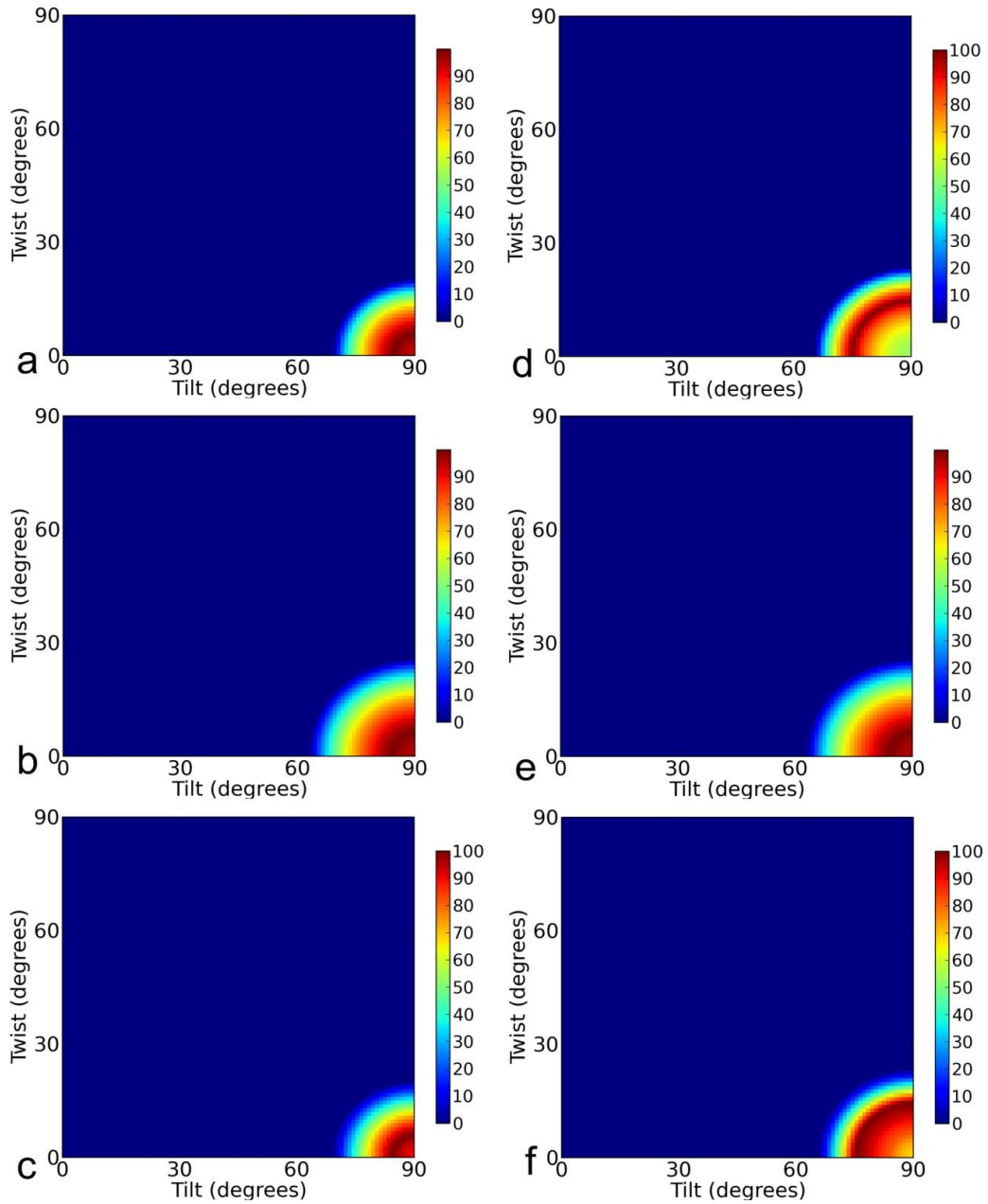


**Figure 2-6. Plot  $\chi_{yyz,s} / \chi_{yyz,as}$  and  $\chi_{yyz,as} / \chi_{yzy,as}$  values obtained from SFG experiment in Figure 2-4 to obtain: (a) Orientation angle range of  $\text{Si}(\text{CH}_3)_2$  at the  $d_4$ -PET/uncured PDMS interface using  $\chi_{yyz,s} / \chi_{yyz,as} = 1.24$  ; (b) Orientation angle range of  $\text{Si}(\text{CH}_3)_2$  at the  $d_4$ -PET/uncured PDMS interface using  $\chi_{yyz,as} / \chi_{yzy,as} = 0.51$  ; (d) Orientation angle range of  $\text{Si}(\text{CH}_3)_2$  at the  $d_4$ -PET/cured PDMS interface using  $\chi_{yyz,s} / \chi_{yyz,as} = 1.35$  ; (e) Orientation angle range of  $\text{Si}(\text{CH}_3)_2$  at the  $d_4$ -PET/cured PDMS interface using  $\chi_{yyz,as} / \chi_{yzy,as} = 0.51$  ; (c) Overlapping area of (a) and (b); (f) Overlapping area of (d) and (e). The error bar is 20%.**

Similarly, at the  $d_4$ -PET/cured PDMS interface, the possible orientation angle values derived by two different measurements ( $\chi_{yyz,s} / \chi_{yyz,as} = 1.35$  and  $\chi_{yyz,as} / \chi_{yzy,as} = 0.51$ ) are shown in Figures 2-6d and e. The overlapping area is shown in Figure 2-6f, which indicates a similar but slightly larger orientation angle range than that shown in Figure 2-6c. In the calculation,  $\chi_{yyz,as} / \chi_{yzy,as} = 0.51$  was used rather than  $\chi_{yyz,as} / \chi_{yzy,as} = -0.51$  also because only the positive value will lead to orientation angle range which can overlap with that obtained from the other measurement  $\chi_{yyz,s} / \chi_{yyz,as} = 1.35$  (Appendix 2.2.9). From Figure 2-6c, we can conclude that at the  $d_4$ -PET/cured PDMS interface, methyl groups tend to have big tilt angles ( $>70^\circ$ ) but do not completely lie down ( $\neq 90^\circ$ ). The twist angles for the methyl groups are small ( $<20^\circ$ ).

At the silica/uncured PDMS interface, the possible orientation angle range deduced based on  $\chi_{yyz,s} / \chi_{yyz,as} = -0.98 \pm 0.13$  and  $\chi_{yyz,as} / \chi_{yzy,as} = \pm 2.71 \pm 0.31$  are shown in Figures 2-7a and b, respectively. If the positive value of 2.71 was chosen, then there will be no possible orientation range satisfied (Appendix 2.2.9). Therefore,  $\chi_{yyz,as} / \chi_{yzy,as} = -2.71$  was used in calculation. The overlapping orientation angle range which satisfies both measurements is shown in Figure 2-7c. At the silica/PDMS interface, the possible methyl group tilt angles and twist angles covered a broad range. The range was quite different from that of methyl groups at the  $d_4$ -PET/PDMS interface, due to the different interfacial interactions. Here the twist angle tended to be bigger than  $60^\circ$ , which was much larger than that at the  $d_4$ -PET/PDMS interface. Similarly,  $\theta$  cannot be  $90^\circ$ . Otherwise, there would not be SFG signal detected.



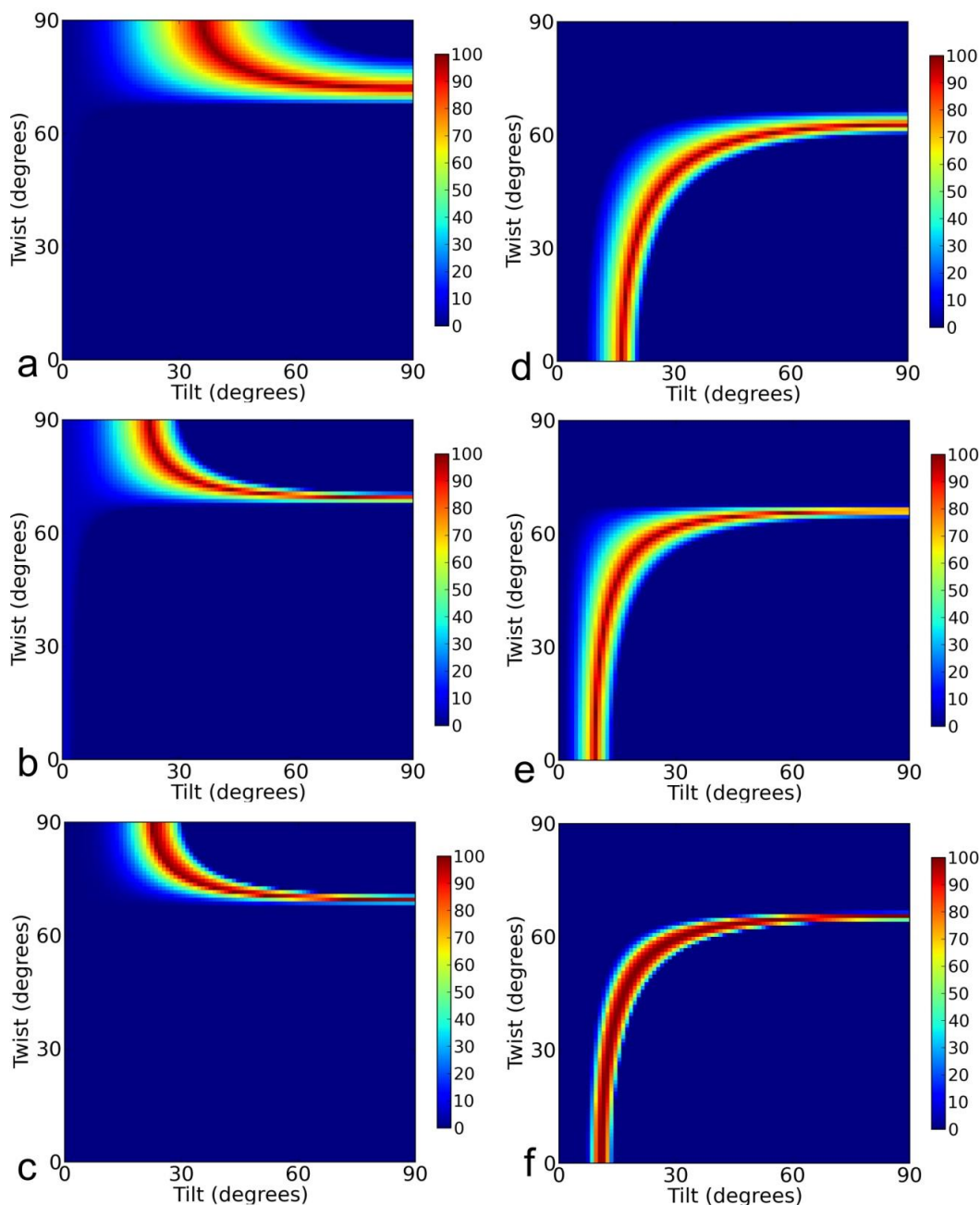


**Figure 2-7. Plot  $\chi_{yyz,s} / \chi_{yyz,as}$  and  $\chi_{yyz,as} / \chi_{zy,as}$  values obtained from SFG experiment in Figures 2-5 to obtain: (a) Orientation angle range of Si(CH<sub>3</sub>)<sub>2</sub> at the silica/uncured PDMS interface using  $\chi_{yyz,s} / \chi_{yyz,as} = -0.98$  ; (b) Orientation angle range of Si(CH<sub>3</sub>)<sub>2</sub> at the silica/uncured PDMS interface using  $\chi_{yyz,as} / \chi_{zy,as} = -2.71$  ; (d) Orientation angle range of Si(CH<sub>3</sub>)<sub>2</sub> at the silica/cured PDMS interface using  $\chi_{yyz,s} / \chi_{yyz,as} = -1.53$  ; (e) Orientation angle range of Si(CH<sub>3</sub>)<sub>2</sub> at the silica/cured PDMS interface using  $\chi_{yyz,as} / \chi_{zy,as} = -1.83$  ; (c) Overlapping area of (a) and (b); (f) Overlapping area of (d) and (e). The error bar is 20%.**

Fitting results from the SFG spectra collected from the silica/cured PDMS interface show that  $\chi_{yyz,s} / \chi_{yyz,as} = -1.53 \pm 0.21$  and  $\chi_{ssp,as} / \chi_{sps,as} = \pm 1.79 \pm 0.23$ . Considering the different Fresnel coefficients in the ssp and sps SFG signals, we obtained  $\chi_{yyz,as} / \chi_{zyz,as} = \pm 1.83 \pm 0.23$ . Similarly, the possibility that  $\chi_{yyz,as} / \chi_{zyz,as}$  being  $+1.83 \pm 0.23$  can be excluded (Appendix 2.2.9) and  $\chi_{yyz,as} / \chi_{zyz,as} = -1.83$  was used in calculation. The possible orientation angle range of methyl groups at the interface deduced from each measurement is shown in Figures 2-7d and e, respectively. The overlapping range which satisfies both measurements is shown in Figure 2-7f and can be considered as possible orientation angle range of methyl groups at the silica/PDMS interface after curing.

Figure 2-7 shows that the possible orientation angle ranges of PDMS methyl groups at silica/PDMS interfaces are broad. In order to narrow down the possible orientation ranges at such interfaces, the resonance strengths  $\chi_{yyz,s}$  and  $\chi_{yyz,as}$  of PDMS methyl groups at the  $d_4$ -PET/PDMS and silica/PDMS interfaces were also compared. From Figure 2-6 it was concluded that PDMS methyl groups tend to have big tilt angle between  $77^\circ$  and  $90^\circ$  and small twist angle between  $0^\circ$  and  $13^\circ$  (50% maximum) at the  $d_4$ -PET/PDMS interface before curing. This corresponds to the area of:

$$0 < \chi_{yyz,s,(uncured)PDMS/dPET} \cdot \epsilon_0 / N < 0.70 \text{ in Figure 2-3a.}$$

Possible values of  $\chi_{yyz,s,(uncured)PDMS/silica} \cdot \epsilon_0 / N$  at the PDMS/silica interfaces were obtained by comparing its symmetric C-H stretching resonance strength with that at the  $d_4$ -PET/uncured PDMS interface. Since different interfaces were studied, different Fresnel coefficients also need to be considered. According to the spectral fitting results, PDMS methyl group symmetric C-H

stretching signal detected from the silica/uncured PDMS interface was  $\chi_{ssp,s,(uncured)PDMS/Silica} = 2.49 \pm 0.28$  (Table 2.2, in arbitrary unit). At the  $d_4$ -PET/uncured PDMS interface, the methyl group C-H symmetric stretching signal strength was  $\chi_{ssp,s,(uncured)PDMS/dPET} = 1.22 \pm 0.12$  (in arbitrary unit). According to calculation, the Fresnel coefficients were different at the silica/PDMS and PET/PDMS interfaces (Appendix 2.2.9). Furthermore, compared to the silica/PDMS interface, IR and visible beams reaching the  $d_4$ -PET/PDMS interface were attenuated by silica/ $d_4$ -PET interface due to the reflection. Combining Fresnel coefficient and attenuation factor (Appendix 2.2.9):

$$\frac{\chi_{yyz,s,(uncured)PDMS/Silica}}{\chi_{yyz,s,(uncured)PDMS/dPET}} = 1.03 \frac{\chi_{ssp,s,(uncured)PDMS/Silica}}{\chi_{ssp,s,(uncured)PDMS/dPET}}.$$

Therefore, applying two measured values, we can obtain  $\frac{\chi_{yyz,s,(uncured)PDMS/Silica}}{\chi_{yyz,s,(uncured)PDMS/dPET}} = 2.10$ .

Since  $0 < \chi_{yyz,s,(uncured)PDMS/dPET} \cdot \epsilon_0 / N < 0.70$ , therefore we have:

$$0 < \chi_{yyz,s,(uncured)PDMS/Silica} \cdot \epsilon_0 / N < 1.47.$$

The possible orientation range with  $0 < \chi_{yyz,s,(uncured)PDMS/Silica} \cdot \epsilon_0 / N < 1.47$  in Figure 2-3a was overlapped with the range deduced in Figure 2-7c. The possible orientation angle range of methyl group at the silica/uncured PDMS interface is shown in Figure 2-8a and is narrowed to  $45^\circ \sim 90^\circ$  in tilt angle,  $70^\circ \sim 75^\circ$  in twist angle.

This analysis can be further validated by comparing the asymmetric C-H stretching signals. From Tables 2-1 and 2-2, the signal strengths of the asymmetric C-H stretching modes at the  $d_4$ -PET/uncured PDMS interface and the silica/uncured PDMS interface were  $0.98 \pm 0.09$  and  $2.53 \pm 0.19$  respectively (in arbitrary unit). Therefore, the signal strength ratio was:

$$\chi_{ssp,as,(uncured)PDMS/Silica} / \chi_{ssp,as,(uncured)PDMS/dPET} = -(2.53 / 0.98) = -2.58$$

The negative sign used here indicates that at these two interfaces, the asymmetric C-H stretches have different signs compared to the corresponding symmetric C-H stretches, as mentioned previously. We can further calculate the ratio:

$$\chi_{yyz,as,(uncured)PDMS/Silica} / \chi_{yyz,as,(uncured)PDMS/dPET} = 1.03 \times (-2.58) = -2.66$$

At the  $d_4$ -PET/uncured PDMS interface the methyl group tilt angle was determined to be between 77 and 90° and twist angle was between 0 and 13°, which corresponds to the area of  $0 < \chi_{yyz,as,(uncured)PDMS/dPET} \cdot \epsilon_0 / N < 0.57$  in Figure 2-3b. At the silica/uncured PDMS interface, the value  $\chi_{yyz,as,(uncured)PDMS/dPET} \cdot \epsilon_0 / N$  needs to be multiplied by the factor of -2.66, and thus  $-1.52 < \chi_{yyz,as,(uncured)PDMS/Silica} \cdot \epsilon_0 / N < 0$ . The corresponding range in Figure 2-3b was plotted together with possible orientations determined in Figure 2-7c and is shown as Figure 2-8b. The possible methyl group orientation at the silica/uncured PDMS interface is 35° <  $\theta$  < 90° in tilt angle, 70°~75° in twist angle. This is not very different from the result obtained by comparing the C-H symmetric stretching signals (Figure 2-8a), but with a slightly larger range. In summary, Figure 2-8a demonstrates the most possible orientation angle range of methyl groups at the silica/uncured PDMS interface.

The same analysis can also be applied to the silica/cured PDMS interface. From Tables 2-1 and 2-2 considering C-H symmetric mode:

$$\chi_{ssp,s,(cured)PDMS/Silica} / \chi_{ssp,s,(uncured)PDMS/dPET} = 3.05 / 1.22 = 2.50$$

Therefore, we can obtain:

$$\chi_{yyz,s,(cured)PDMS/Silica} / \chi_{yyz,s,(uncured)PDMS/dPET} = 1.03 \times 2.50 = 2.58$$

For  $d_4$ -PET/uncured PDMS interface,  $0 < \chi_{yyz,s,(uncured)PDMS/dPET} \cdot \epsilon_0 / N < 0.70$ . Therefore,  $0 < \chi_{yyz,s,(cured)PDMS/Silica} \cdot \epsilon_0 / N < 1.81$ , corresponds to range 0 to 1.81 in Figure 2-3a. The

overlapped area of Figure 2-3a (0 to 1.81) and Figure 2-7f is shown in Figure 2-8c. The results suggesting possible orientation range of methyl group at silica/cured PDMS interface can be narrowed down to tilt angle  $33^\circ \sim 90^\circ$ , twist angle  $58^\circ \sim 66^\circ$ .

Similarly, using the asymmetric C-H stretching mode:

$$\chi_{ssp,as,(cured)PDMS/Silica} / \chi_{ssp,as,(uncured)PDMS/dPET} = -(1.99 / 0.98) = -2.03$$

This further gives:

$$\chi_{yyz,as,(cured)PDMS/Silica} / \chi_{yyz,as,(uncured)PDMS/dPET} = 1.03 \times (-2.03) = -2.09$$

For the  $d_4$ -PET/uncured PDMS interface,  $0 < \chi_{yyz,as,(uncured)PDMS/dPET} \cdot \epsilon_0 / N < 0.57$ .

Therefore,  $-1.19 < \chi_{yyz,as,(cured)PDMS/Silica} \cdot \epsilon_0 / N < 0$ , corresponds to -1.19 to 0 in Figure 2-3b. The overlapped area of Figure 2-3b (0 to -1.19) and Figure 2-7f is shown in Figure 2-8d. The orientation ranges obtained in Figures 2-8c and d are quite similar, while the latter has a slightly smaller range, tilt angle  $45^\circ \sim 90^\circ$ , twist angle  $60^\circ \sim 66^\circ$ . This suggests that the methyl group's possible orientation range at the silica/cured PDMS interface is  $45^\circ \sim 90^\circ$  in tilt angle,  $60^\circ \sim 66^\circ$  in twist angle.

A single methyl group possesses a  $C_{3v}$  symmetry, therefore it is usually not necessary to consider the twist angle. In the above analysis, for a  $\text{Si}(\text{CH}_3)_2$  group, we considered both tilt and twist angles. Here we demonstrate that the consideration of twist angle is essential. Figure 2-9 shows the ratios of  $\chi_{yyz,s} / \chi_{yyz,as}$  and  $\chi_{yyz,as} / \chi_{zyz,as}$  as functions of the tilt angle  $\theta$  after averaging the twist angle from 0 to  $360^\circ$ . It shows that  $\chi_{yyz,s} / \chi_{yyz,as}$  cannot have a reasonable positive value for the tilt angle between 0 and  $90^\circ$ . From the experiment we obtained that  $\chi_{ssp,s} / \chi_{ssp,as} = \chi_{yyz,s} / \chi_{yyz,as} = 1.24$  and 1.35 respectively for PDMS methyl groups at the  $d_4$ -PET/PDMS interfaces before and after curing PDMS. These two values are both positive. This indicates that the twist angle of  $\text{Si}(\text{CH}_3)_2$  groups at the  $d_4$ -PET/PDMS interfaces cannot be

averaged.  $\text{Si}(\text{CH}_3)_2$  groups tend to adopt certain twist angles (e.g.  $<15^\circ$  at the  $d_4$ -PET/PDMS interfaces as discussed before) rather than adopt all possible twist angles from  $0$  to  $90^\circ$ .

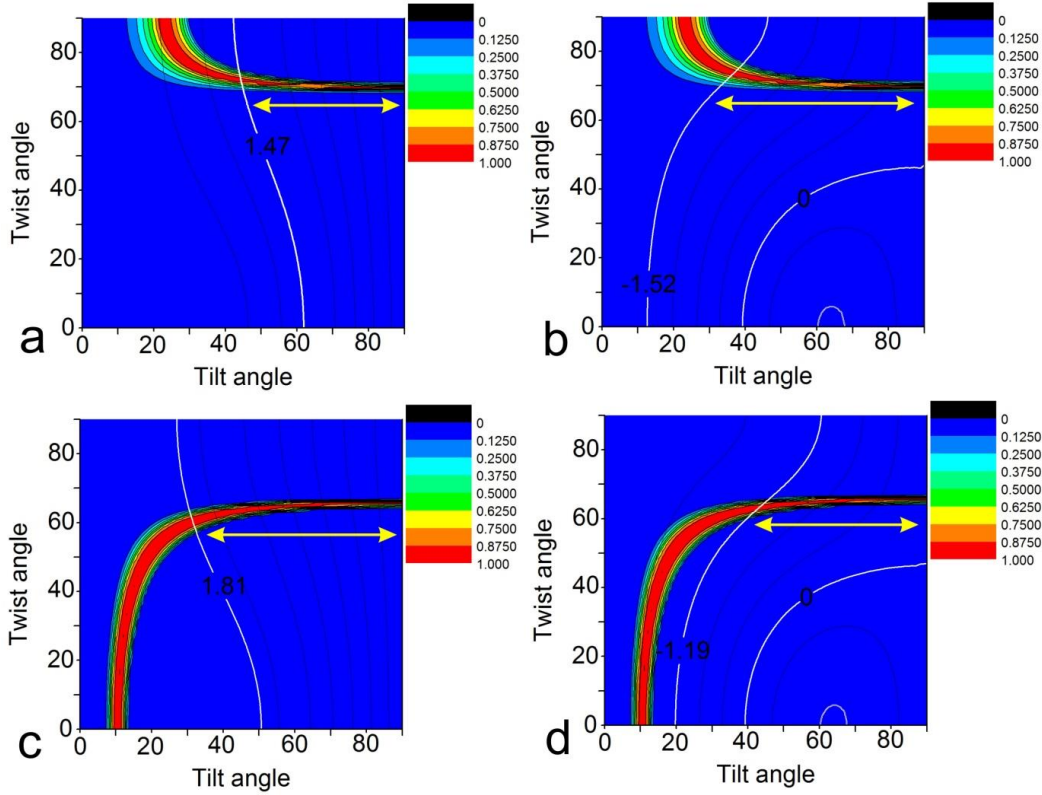


**Figure 2-8. Possible orientation angle range of  $\text{Si}(\text{CH}_3)_2$  group at the silica/uncured PDMS interface further determined using (a)  $\frac{\chi_{yyz,s,(uncured)PDMS/Silica}}{\chi_{yyz,s,(uncured)PDMS/dPET}}$  and (b)  $\frac{\chi_{yyz,as,(uncured)PDMS/Silica}}{\chi_{yyz,as,(uncured)PDMS/dPET}}$ ; Possible orientation angle range of  $\text{Si}(\text{CH}_3)_2$  group at the silica/cured PDMS interface further determined using (c)  $\frac{\chi_{yyz,s,(cured)PDMS/Silica}}{\chi_{yyz,s,(uncured)PDMS/dPET}}$  and (d)  $\frac{\chi_{yyz,as,(cured)PDMS/Silica}}{\chi_{yyz,as,(uncured)PDMS/dPET}}$ . For (a) and (c), possible angle ranges are from white curve to the right; for (b) and (d), possible ranges are between two white lines. Arrows are used to demonstrate the possible angle range in all figures.**

Similarly, at the silica/uncured PDMS interface, Figure 2-9 shows that the measured  $\chi_{yyz,s} / \chi_{yyz,as} = -0.98$  ratio is out of the possible range, indicating that at this interface, the twist angle for  $\text{Si}(\text{CH}_3)_2$  groups cannot be averaged. At the silica/cured PDMS interface, even though

both the measured  $\chi_{yyz,s} / \chi_{yyz,as} = -1.53$  and  $\chi_{yyz,as} / \chi_{zy,as} = -1.83$  (not shown in Figure 2-9) ratios fall on the corresponding curve after averaging the twist angle, but the possible tilt angles deduced from these two measurements are not the same, at  $\sim 28^\circ$  and  $\sim 18^\circ$ , respectively. We believe that this is also because the twist angles cannot be averaged.

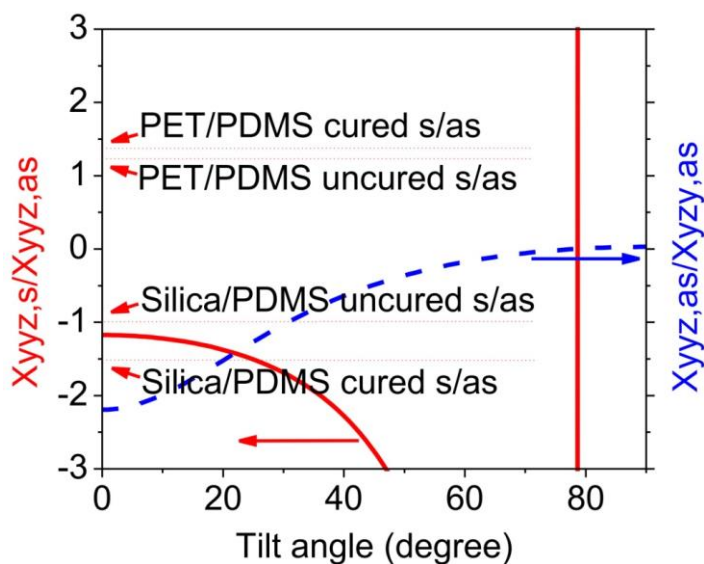


**Figure 2-9.**  $\chi_{yyz,s} / \chi_{yyz,as}$  (solid red line) and  $\chi_{yyz,as} / \chi_{zy,as}$  (broken blue line) as functions of tilt angle (the ratio values are obtained by averaging twist angle  $\psi$  from 0 to  $360^\circ$ ). The experimentally measured values are shown as dotted lines, and demonstrated by the red arrows.

### 2.2.6 A Method to Derive the Absolute Orientation of PDMS Methyl Groups at Interfaces

As we showed in Table 2-1, the best fitting results for ssp SFG spectra collected from the  $d_4$ -PET/PDMS interfaces were obtained when the strengths or amplitudes of the symmetric and asymmetric C-H stretching signals have the same sign. Differently, Table 2-2 shows that the best fitting results for ssp SFG spectra collected from the silica/PDMS interfaces were obtained when the amplitudes of the symmetric and asymmetric C-H stretching signals have different signs. To further confirm the spectral fitting results, silica prisms coated with a thin  $\text{TiO}_2$  film were used in

the experiment to provide non-resonant SFG signals. Such non-resonant signals can interfere with the SFG signals generated from the PDMS methyl groups at the interfaces to determine the signs (or phases) of the SFG signals.

Similar to the previous  $d_4$ -PET/PDMS interface, a  $d_4$ -PET film with a thickness of about 50 nm was spin cast on the  $\text{TiO}_2$  film (deposited on fused silica prism) at the spin speed of  $\sim 2500$  rpm and using a 2 wt%  $d_4$ -PET solution in 2-chlorophenol. Then the  $d_4$ -PET surface was contacted with PDMS and SFG spectra were collected from this interface. The SFG spectrum collected from the  $d_4$ -PET/PDMS interface before curing is shown in Figure 2-10a. Two peaks at  $\sim 2900$  and  $\sim 2960 \text{ cm}^{-1}$  were detected, both of which had positive amplitude relative to the non-resonant background. This demonstrated that these two peaks have the same phase (or their amplitudes have the same sign). After curing PDMS, the ssp SFG spectrum collected from the  $d_4$ -PET/cured PDMS interface is shown in Figure 2-10b, which leads to the similar conclusion that the peaks at  $\sim 2900$  and  $\sim 2960 \text{ cm}^{-1}$  have the same phase. Therefore, the results obtained with the help of a thin  $\text{TiO}_2$  film are compatible to those discussed previously, validating the previous fitting results.

A thin layer of  $\text{SiO}_2$  film with a thickness of 50 nm was also coated on the  $\text{TiO}_2$  film (deposited on a fused silica prism). SFG ssp spectra were then collected from the  $\text{SiO}_2$  (on  $\text{TiO}_2$ )/PDMS interface. Before curing PDMS, the detected SFG spectrum had one positive and one negative interference (at  $2905$  and  $2960 \text{ cm}^{-1}$ ) with the non-resonant SFG background generated from the  $\text{TiO}_2$  film (Figure 2-10c). This indicated that the symmetric and asymmetric C-H stretching signals of the PDMS methyl groups at the silica/PDMS interface have different phases (the amplitudes of which have different signs). After curing PDMS, the SFG ssp spectrum was also collected from the interface (Figure 2-10d), which indicates the different phases for the



symmetric and asymmetric C-H stretching signals of the methyl groups as well. These results also match the spectral fitting results discussed above.

Figure 2-10 shows that in all the SFG spectra, the C-H symmetric stretching signals interfered with the TiO<sub>2</sub> non-resonant SFG signal similarly (positive interference), which suggests that methyl groups at both *d*<sub>4</sub>-PET/PDMS and silica/PDMS interfaces before and after curing PDMS have the same absolute orientation. Since silica has a very hydrophilic surface, hydrophobic methyl groups may orient away from the silica surface (towards the bulk PDMS). The results further indicate that at the *d*<sub>4</sub>-PET/PDMS interface, the methyl groups may also orient away from the polymer surface. This is possible because C=O groups were detected on the PET surface,<sup>59</sup> showing that the PET surface can be hydrophilic. The PET surface is less hydrophilic compared to the silica surface. This may account for the methyl groups with larger tilt angles at the *d*<sub>4</sub>-PET/PDMS interface compared to that at the silica/PDMS interface.

To further confirm the conclusion regarding the absolute orientation of the methyl groups at the *d*<sub>4</sub>-PET/PDMS and silica/PDMS interfaces, the absolute orientations of PDMS methyl groups at hydrophobic surfaces were studied. *d*<sub>8</sub>-PS and *d*<sub>8</sub>-PMMA were used to make hydrophobic surfaces. About 50 nm thin films of *d*<sub>8</sub>-PS and *d*<sub>8</sub>-PMMA on TiO<sub>2</sub> films were prepared using spin coating. SFG ssp spectra were then collected from the *d*<sub>8</sub>-PS/PDMS interface and the *d*<sub>8</sub>-PMMA/PDMS interface before and after curing PDMS (Figure 2-11). The results show that the SFG signals detected from the C-H symmetric stretching modes of the PDMS methyl groups at the *d*<sub>8</sub>-PS/PDMS interface and *d*<sub>8</sub>-PMMA/PDMS interface interfere differently with the non-resonant SFG signal from the TiO<sub>2</sub> film compared to the *d*<sub>4</sub>-PET and silica cases discussed above. Figure 2-11 demonstrates that all the SFG signals from the PDMS methyl C-H symmetric stretches interfere negatively with the TiO<sub>2</sub> non-resonant background. This indicates that the

absolute orientations of the PDMS methyl groups at the  $d_8$ -PS/PDMS interface and the  $d_8$ -PMMA/PDMS interfaces are different (opposite) as compared to that at the  $d_4$ -PET/PDMS and silica/PDMS interfaces. This suggests that at the  $d_8$ -PS/PDMS and  $d_8$ -PMMA/PDMS interfaces, the methyl groups orient towards the polymer surfaces.

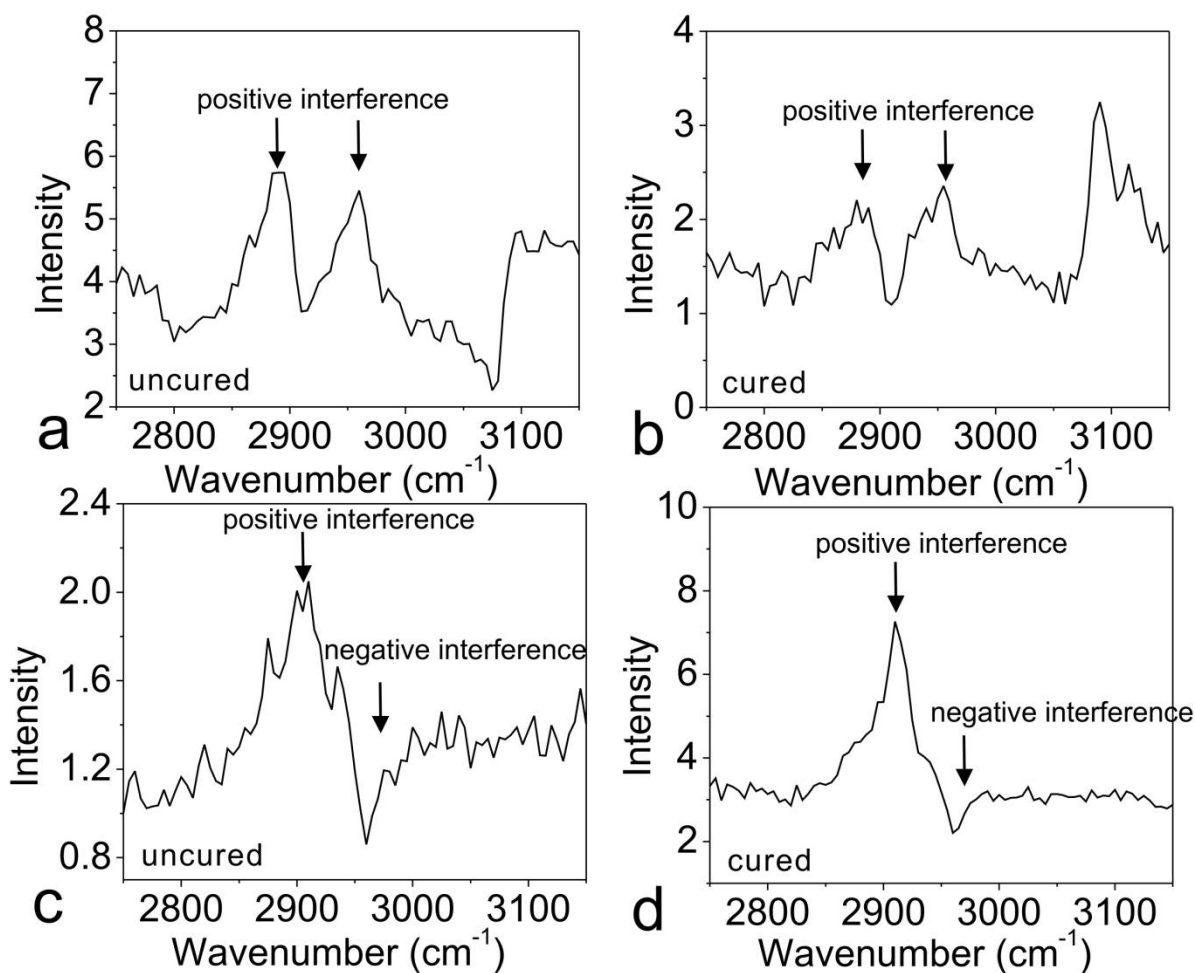


**Figure 2-10. SFG ssp spectra collected from the  $d_4$ -PET/PDMS interface ( $d_4$ -PET on a  $\text{TiO}_2$  layer): (a) before curing (b) after curing; SFG ssp spectra collected from the silica/PDMS interface (a thin layer of silica on a  $\text{TiO}_2$  layer): (c) before curing (d) after curing.**

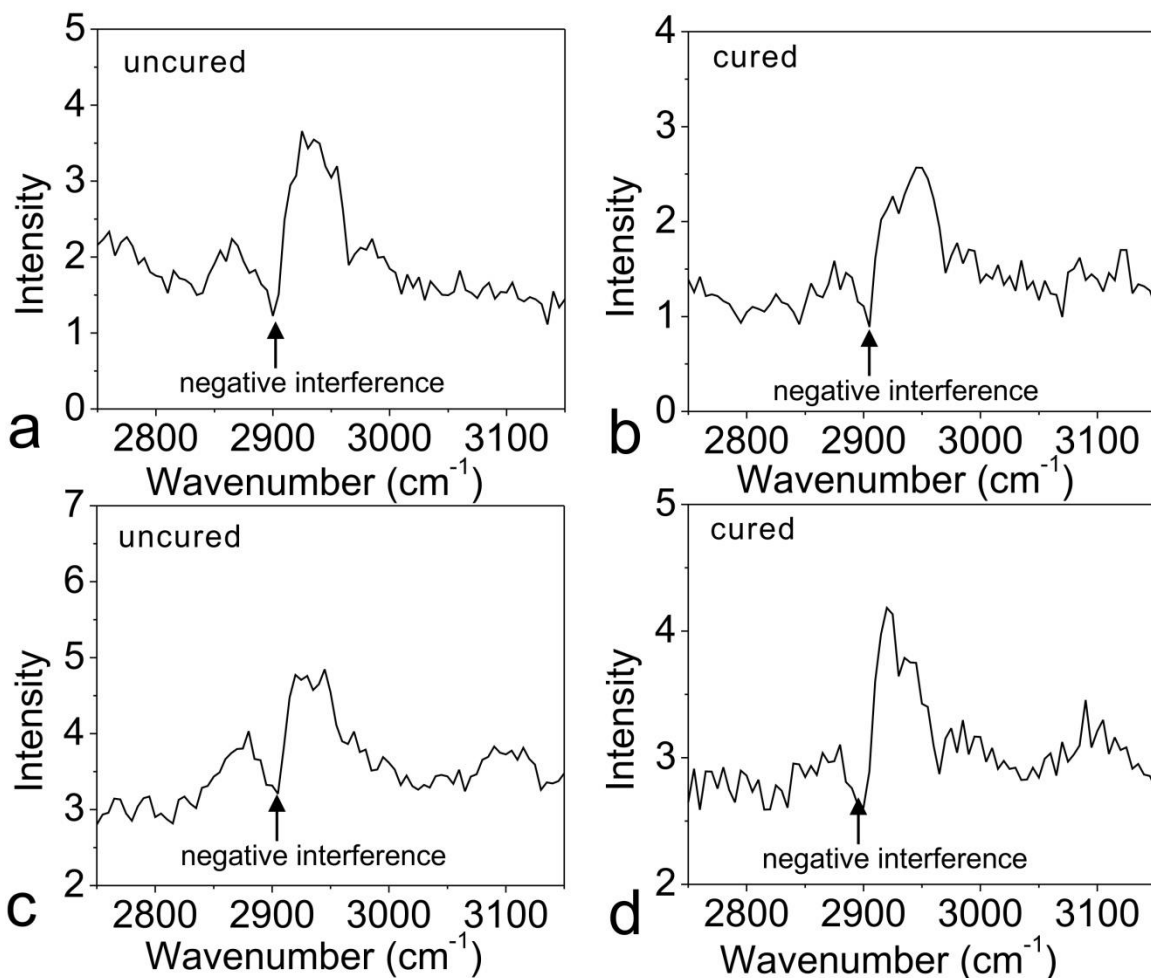


**Figure 2-11.** SFG ssp spectra collected from the *d*<sub>8</sub>-PS/PDMS interface (*d*<sub>8</sub>-PS on a TiO<sub>2</sub> layer): (a) before curing (b) after curing; SFG ssp spectra collected from the *d*<sub>8</sub>-PMMA/PDMS interface (*d*<sub>8</sub>-PMMA on a TiO<sub>2</sub> layer): (c) before curing (d) after curing.

## 2.2.7 Surface Hydrophobicity Studies and Their Relation to PDMS Interfacial Molecular Orientation

The different absolute orientations of PDMS methyl groups at buried interfaces can be explained according to the hydrophobicity of different surfaces. The water contact angles were measured on various surfaces which were used in this research to contact PDMS (Table 2-3). Silica had the smallest contact angle, while *d*<sub>4</sub>-PET had a slightly smaller contact angle than *d*<sub>8</sub>-PMMA, and *d*<sub>8</sub>-PS had the biggest contact angle. Therefore, the hydrophobic order of various surfaces is:

$d_8$ -PS >  $d_8$ -PMMA >  $d_4$ -PET > silica. From the previous discussion, PDMS methyl groups at the  $d_4$ -PET/PDMS and silica/PDMS interfaces both orient away from the contacting media and towards the PDMS bulk. This is understandable because at the silica/PDMS interface, due to the unfavorable interactions between the methyl groups and hydrophilic silica, the methyl groups orient away from the silica surface. At the  $d_4$ -PET/PDMS interface, the deduced orientation of the interfacial Si(CH<sub>3</sub>)<sub>2</sub> groups has large tilt angles (more or less lying down at the interface). This indicates that the hydrophobicity of the  $d_4$ -PET surface is on the margin of determining the net orientation of PDMS methyl group orienting away or towards the contacting medium. At the  $d_8$ -PMMA/PDMS and  $d_8$ -PS/PDMS interfaces, the polymer surface hydrophobicity increases. Therefore, the methyl groups have more favorable interactions with the polymer surfaces. This leads to the net orientation of methyl groups tilting towards the polymer substrates.

Material	$d_4$ -PET	Silica	$d_8$ -PMMA	$d_8$ -PS
Average contact angle	62.8±0.7	~0	65.2±0.6	88.3±0.7

**Table 2-3. Water contact angle measurement results of polymer and silica surfaces used in the experiment.**

### 2.2.8 Conclusion

In this study, we measured the molecular structures at the buried  $d_4$ -PET/PDMS and silica/PDMS interfaces. The results show that PDMS Si(CH<sub>3</sub>)<sub>2</sub> groups tend to have different orientations at different interfaces. At the  $d_4$ -PET/PDMS interface, PDMS Si(CH<sub>3</sub>)<sub>2</sub> groups tend to have large tilt angles (>70°) but small twist angles (<20°). The C-H symmetric and asymmetric stretching signals of PDMS methyl groups have the same phase. On the other hand, at the silica/PDMS interface, PDMS methyl groups tend to have a broader orientation angle range. Before and after curing PDMS, PDMS methyl groups orientation does not have a significant

change at the  $d_4$ -PET/PDMS interface (tilt angle  $>70^\circ$ ), while at the silica/PDMS interface, the twist angles changed about  $10^\circ$ . In this research we assumed a  $\delta$ -orientation distribution of methyl groups at interfaces. In reality, the  $\delta$ -distribution may not be accurate, but the deduced orientation angles should be sufficient to address the average orientation trend. We also conclude that it is necessary to consider the twist angles of PDMS methyl groups at buried interfaces. PDMS methyl groups do not have a random distribution of twist angles. With the help of the non-resonant SFG signals generated from a  $\text{TiO}_2$  thin film, it is confirmed that the methyl group symmetric and asymmetric stretching modes have the same phase at the  $d_4$ -PET/PDMS interface and have different phases at the silica/PDMS interface, both before and after curing. PDMS methyl groups tend to orient towards the PDMS bulk rather than towards the  $d_4$ -PET or silica substrates. Differently, when PDMS materials are in contact with hydrophobic surfaces, such as  $d_8$ -PS and  $d_8$ -PMMA, the PDMS methyl groups orient to the hydrophobic surfaces due to the favorable interactions at the interfaces.

### **2.2.9 Appendix**

#### **1. Fresnel Factors**

We calculated the Fresnel coefficient factors based on the parameters used in our experiment. A schematic of the experimental data collection geometry is shown in Figure 2-12.

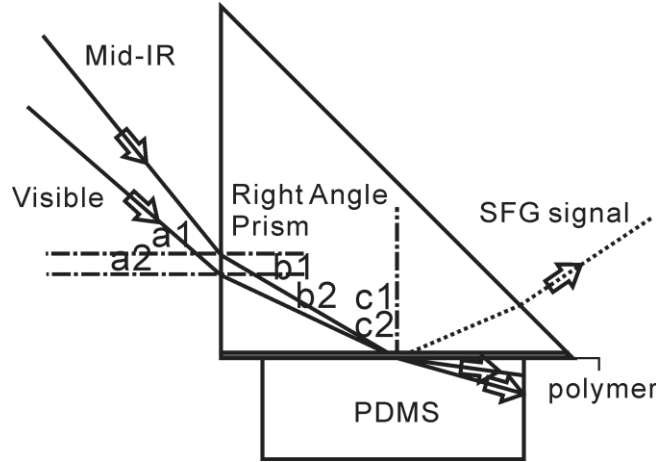


**Figure 2-12. The near total reflection geometry used in the SFG experiment and the angle definitions.**

The refractive index of air is 1.00 at all frequencies. The refractive indices of the silica prism are 1.41, 1.46, and 1.47 at  $2900\text{ cm}^{-1}$  (IR), 532 nm (visible), and 461 nm (signal), respectively. The refractive indices of PDMS are 1.37 (IR), 1.43(visible) and 1.43(signal). The refractive indices of PET are 1.47 (IR), 1.57 (visible) and 1.59 (signal).<sup>58</sup> The input angles of the visible and IR beams were  $60.0^\circ$  and  $57.0^\circ$  vs. the surface normal in the lab frame. Therefore, the incident angle of the input IR beam at the prism/air interface (angle a1) was  $33.0^\circ$ , while the incident angle of the input visible beam (angle a2) at the same interface was  $30.0^\circ$ .

(1) At the silica/PDMS interface:

We calculated the refractive angles for both the IR and visible beams inside the prism (angles b1 and b2), which were  $22.7^\circ$  and  $20.0^\circ$ , respectively. We then deduced that the incident angles of the two input beams at the silica/PDMS interface were  $67.3^\circ$  and  $70.0^\circ$  respectively.

We can use the following equations to calculate Fresnel coefficients:<sup>59</sup>

$$L_{yy}(\omega) = \frac{2n_1(\omega)\cos\theta}{n_1(\omega)\cos\theta + n_2(\omega)\cos\gamma}, \quad L_{zz}(\omega) = \frac{2n_2(\omega)\cos\theta}{n_1(\omega)\cos\gamma + n_2(\omega)\cos\theta} \left( \frac{n_1(\omega)}{n'(\omega)} \right)^2$$

where  $\theta$  is the incident angle at the interface, and  $\gamma$  is the refractive angle at the interface and can be calculated using  $\theta$  and refractive indices of both materials forming the interface.  $n'(\omega)$  is the refractive index of the interface, which can be approximated by averaging the refractive indices of the two materials forming the interface. At the silica/PDMS interface, the values of  $n'$  equal to 1.39 (IR), 1.445 (visible), 1.45 (signal), respectively.

Along with the following two equations,

$$\chi_{eff,ssp} = L_{yy}(\omega_{SF})L_{yy}(\omega_{vis})L_{zz}(\omega_{IR})\sin\theta_{i,IR} \cdot \chi_{yyz}$$

$$\chi_{eff,spz} = L_{yy}(\omega_{SF})L_{zz}(\omega_{vis})L_{yy}(\omega_{IR})\sin\theta_{i,vis} \cdot \chi_{zyz}$$

we calculated the effective Fresnel coefficients at the silica/PDMS interface to be:

$$\chi_{eff,ssp} = 1.31 \cdot \chi_{yyz}$$

$$\chi_{eff,spz} = 1.33 \cdot \chi_{zyz}$$

(2) At the  $d_4$ -PET/PDMS interface:

The  $d_4$ -PET layer was between the silica and PDMS. The IR and visible input beams at the  $d_4$ -PET/silica interface were still  $67.3^\circ$  and  $70.0^\circ$ , respectively. Passing through the  $d_4$ -PET film, the incident angles of IR and visible beams at the  $d_4$ -PET/PDMS interface can be calculated as  $54.4^\circ$  and  $59.0^\circ$ , respectively. At the  $d_4$ -PET/PDMS interface, the values of  $n'$  equal to 1.42 (IR), 1.50 (visible), 1.51 (signal), respectively. Similar to the silica/PDMS interface, we can calculate at the  $d_4$ -PET/PDMS interface:

$$\chi_{eff,ssp} = 1.48 \cdot \chi_{yyz}$$

$$\chi_{eff,spz} = 1.58 \cdot \chi_{zyz}$$

Compared to the silica/PDMS interface, IR and visible beams reaching the  $d_4$ -PET/PDMS interface were attenuated by the silica/ $d_4$ -PET interface due to the reflection. Similarly, the signal

generated from the  $d_4$ -PET/PDMS interface was also attenuated by silica/ $d_4$ -PET interface. Based on Snell's law, we can calculate that the transmission ratio for s polarized signal is 0.962, for s polarized visible beam is 0.957, for p polarized IR is 0.995. Therefore, the ssp polarization attenuation factor is  $A=0.962 \times 0.957 \times 0.995=0.915$ . This factor was used in the above discussion for narrowing the possible orientation angle range of PDMS methyl group at the silica interface.

In ssp polarization, we have:

$$\frac{A \cdot \chi_{ssp,PDMS/Silica}}{\chi_{ssp,PDMS/dPET}} = \frac{1.31 \cdot \chi_{yyz,PDMS/Silica}}{1.48 \cdot \chi_{yyz,PDMS/dPET}}$$

Therefore,

$$\frac{\chi_{yyz,PDMS/Silica}}{\chi_{yyz,PDMS/dPET}} = \frac{1.48 \cdot A}{1.31} \frac{\chi_{ssp,PDMS/Silica}}{\chi_{ssp,PDMS/dPET}} = \frac{1.48 \cdot 0.915}{1.31} \frac{\chi_{ssp,PDMS/Silica}}{\chi_{ssp,PDMS/dPET}} = 1.03 \frac{\chi_{ssp,PDMS/Silica}}{\chi_{ssp,PDMS/dPET}}$$

## 2. Possible Orientation Angle Ranges of PDMS Si(CH<sub>3</sub>)<sub>2</sub> Groups

At the  $d_4$ -PET/uncured PDMS interface, from the spectral fitting results and considering the Fresnel coefficients, we have

$$\chi_{yyz,s} / \chi_{yyz,as} = 1.24 \pm 0.17$$

$$\chi_{yyz,as} / \chi_{yzy,as} = \pm 0.51 \pm 0.06$$

The possible ranges of orientation angles for PDMS Si(CH<sub>3</sub>)<sub>2</sub> groups deduced using  $\chi_{yyz,s} / \chi_{yyz,as} = 1.24$  and  $\chi_{yyz,as} / \chi_{yzy,as} = -0.51$  are shown in Figure 2-13a and b, respectively. Figure 2-13c shows the overlapping area of the two ranges in Figure 2-13a and b. Clearly that if  $\chi_{yyz,as} / \chi_{yzy,as} = -0.51$ , no possible orientation angle for PDMS methyl groups satisfies both measured values. Therefore, we believe that  $\chi_{yyz,as} / \chi_{yzy,as} = 0.51 \pm 0.06$ .



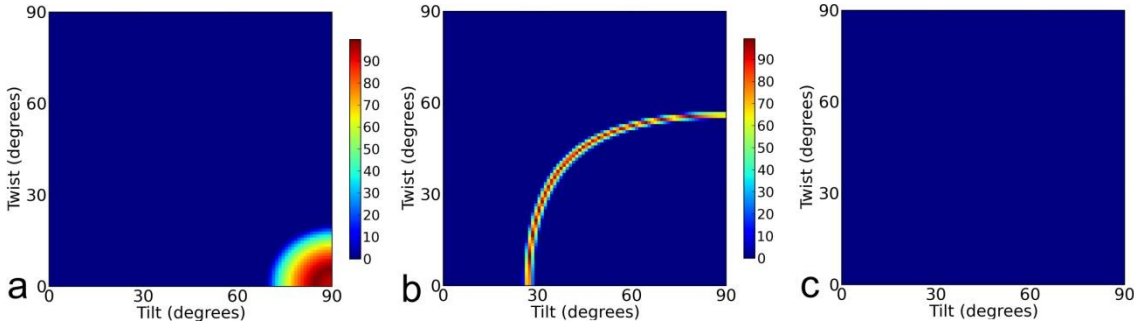


**Figure 2-13.** Plot  $\chi_{yyz,s} / \chi_{yyz,as}$  and  $\chi_{yyz,as} / \chi_{yzy,as}$  values obtained from SFG experiment in Figures 2-3c and d respectively to obtain: (a) Orientation angle range of Si(CH<sub>3</sub>)<sub>2</sub> group at the *d*<sub>4</sub>-PET/uncured PDMS interface using  $\chi_{yyz,s} / \chi_{yyz,as} = 1.24$ ; (b) Orientation angle range of Si(CH<sub>3</sub>)<sub>2</sub> group at the *d*<sub>4</sub>-PET/uncured PDMS interface using  $\chi_{yyz,as} / \chi_{yzy,as} = -0.51$ ; (c) Overlapping area of (a) and (b). No possible orientation angle range can be identified in (c). The error bar presented here is 20%.

Similarly, the orientation ranges deduced using  $\chi_{yyz,s} / \chi_{yyz,as} = 1.35$  and  $\chi_{yyz,as} / \chi_{yzy,as} = -0.51$  are shown in Figures 2-14a and b. The overlapping area is shown in Figure 2-14c, with no possible orientation range can be identified. Therefore, we believe that  $\chi_{yyz,as} / \chi_{yzy,as} = 0.51 \pm 0.05$  at the *d*<sub>4</sub>-PET/cured PDMS interface.

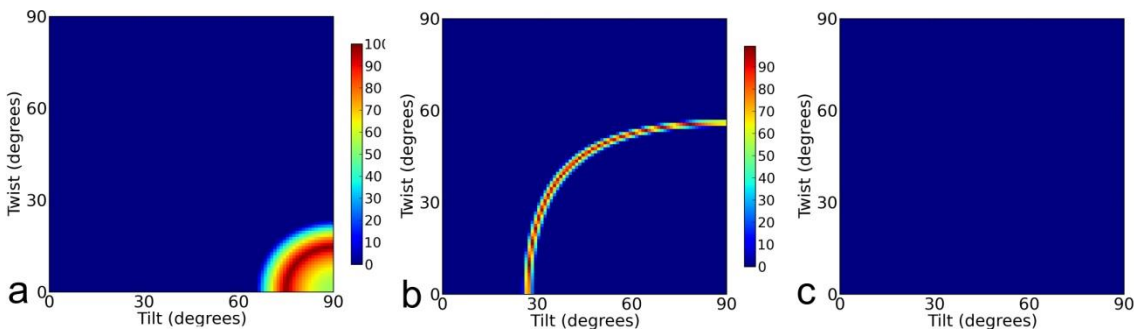


**Figure 2-14.** Plot  $\chi_{yyz,s} / \chi_{yyz,as}$  and  $\chi_{yyz,as} / \chi_{yzy,as}$  values obtained from SFG experiment in Figure 2-3c and d respectively to obtain: (a) Orientation angle range of Si(CH<sub>3</sub>)<sub>2</sub> group at the *d*<sub>4</sub>-PET/cured PDMS interface using  $\chi_{yyz,s} / \chi_{yyz,as} = 1.35$ ; (b) Orientation angle range of Si(CH<sub>3</sub>)<sub>2</sub> group at the *d*<sub>4</sub>-PET/cured PDMS interface using  $\chi_{yyz,as} / \chi_{yzy,as} = -0.51$ ; (c) Overlapping area of (a) and (b). No possible orientation angle range can be identified in (c). The error bar presented here is 20%

Similarly, we can obtain at the silica/uncured PDMS interface,  $\chi_{yyz,as} / \chi_{zy,as} = -2.71 \pm 0.31$  rather than  $2.71 \pm 0.31$ ; at the silica/cured PDMS interface,  $\chi_{yyz,as} / \chi_{zy,as} = -1.83 \pm 0.23$  rather than  $1.83 \pm 0.23$ . These results can be easily obtained because in Figure 2-3d, there's no possible orientation range satisfies  $\chi_{yyz,as} / \chi_{zy,as} > +1$ .

### 2.3 Mechanical Adhesion Test

We have systematically studied the PDMS molecular orientations at PET and silica interfaces. Next we will use SFG to investigate the interfacial behaviors of silane adhesion promoters at polymer/PDMS interfaces. We aim to correlate the different interfacial molecular structures to the different mechanical adhesion measurement results. Therefore, it is necessary to develop an adhesion measurement method for our study.

Based on the ASTM D3163 standard with some modifications, we carried out mechanical adhesion test of cured PDMS (Sylgard 184 silicone elastomer) adhere to PET blocks using an Instron 5544 mechanical testing instrument. The testing geometry in the experiment is 180 degree shear strength test (as shown in Figure 2-15). A PET sheet (Ertalyte) was cut into small pieces with the same size. The contact surface area of each PET test piece is  $30.0 \times 12.0 \text{ mm}^2$ . The PET surfaces were sanded and cleaned using ethanol before use. Two PET pieces were attached by using different PDMS silane (with or without MVS) mixtures and cured at  $140 \text{ }^\circ\text{C}$  for 120 minutes. Then the test pieces are stored at room temperature for 24 hours. The PDMS adhesive thickness is about 0.5 mm. The bonded PET pieces were pulled apart at the room temperature with the pulling speed of 1.3 mm/min while the shear strength was measured. The adhesion test data shown in this work with megaPascal (MPa) unit was calculated by dividing the break force by effective adhesion area. The break force was taken as the maximum force observed before a sudden decrease which

occurred due to the adhesive failure. In this experiment, all the failures we observed are at the interfaces of PET and silicone elastomer (adhesive failure), not in the silicone elastomer bulk (cohesive failure).

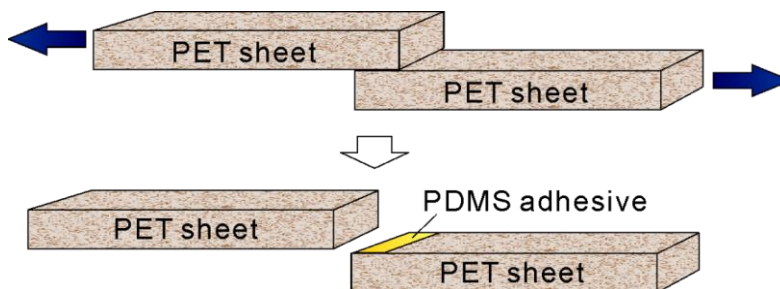


**Figure 2-15. Adhesion test geometry for shear strength test. The top panel shows two test pieces adhered together by PDMS adhesive; the bottom panel shows that after the 180 degree shear test, two test pieces were pulled apart.**

## **2.4 The Study of Methoxy-silane Adhesion Promoters at the PDMS/PET Interface**

### **2.4.1 Materials Used in the Research and Sample Preparation**

In this study, fused silica substrates were also used as sample support for SFG measurements. The cleaning procedures and  $d_4$ -PET sample preparation method were similar as described in section 2.2.1. The  $d_4$ -PET polymer thin films were prepared by spin coating its 2 wt% solution in 2-chlorophenyl at 2500 rpm on fused silica substrates. Silane (3-glycidoxypropyl) dimethyl-methoxysilane ( $\gamma$ -GPDMS) was ordered from Silar Laboratories. Silanes (3-glycidoxypropyl) trimethoxysilane ( $\gamma$ -GPS) and (3-glycidoxypropyl) methyl-dimethoxysilane ( $\gamma$ -GPMS), Methylvinylsiloxanol (MVS), and Sylgard 184 silicone elastomer kit were obtained from the Dow Corning Corporation.

The Sylgard 184 silicone elastomer was prepared by mixing the base and curing agent in a 10:1 ratio. To incorporate silanes into PDMS, 1.5 wt%  $\gamma$ -GPS, 3.0 wt% 1:1 (wt/wt)  $\gamma$ -GPS/MVS mixture, 1.5 wt%  $\gamma$ -GPMS, 3.0 wt% 1:1 (wt/wt)  $\gamma$ -GPMS/MVS mixture, 1.5 wt% ( $\gamma$ -GPDMS), 3.0

wt% 1:1 (wt/wt)  $\gamma$ -GPDMS/MVS mixture were mixed homogeneously using a vortex mixer (Vortex-Genie 2T, Scientific Industries Inc.) into the PDMS base before curing respectively. When MVS was added, a SiH-functional PDMS (6-3570, Dow Corning) was added to maintain a 1.5:1 Si-H/vinyl molar ratio. The 1:1 (wt/wt) silane/MVS mixtures were used because it was shown that the 1:1 (wt/wt)  $\gamma$ -GPS/MVS mixture can effectively enhance the adhesion between polymers and PDMS<sup>60-62</sup>. The curing of the silicone samples was carried out in an oven at 140°C for 120 minutes on *d*<sub>4</sub>-PET surfaces. The samples were then kept at room temperature for 24 hours before use.

Molecular formulas of the materials used in the experiments are shown in Figure 2-16.

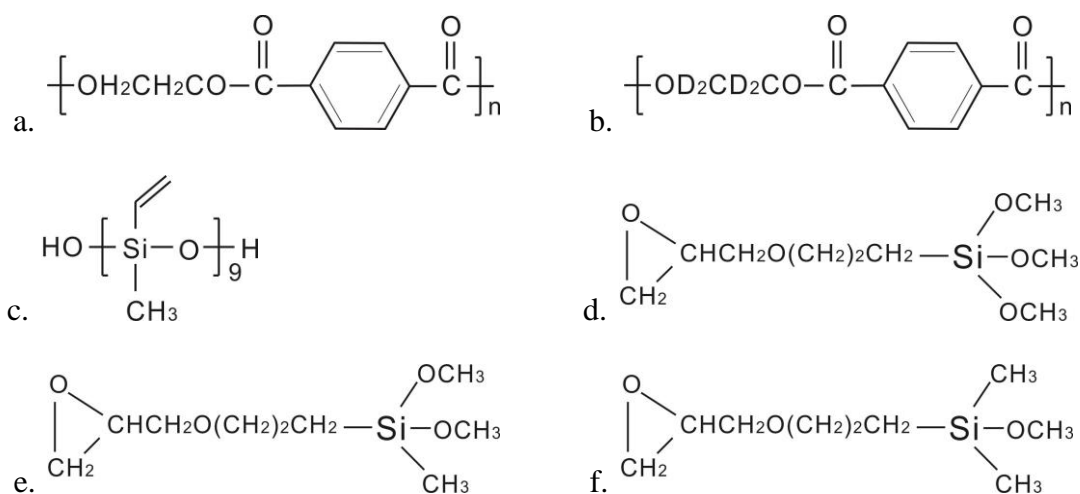


**Figure 2-16. Chemical structures of polymers and silanes employed in the study: (a) Poly(ethylene terephthalate) (PET); (b) PET with aliphatic chain deuterated (*d*<sub>4</sub>-PET); (c) Methylvinylsiloxanol (MVS); (d) (3-glycidoxypropyl) trimethoxysilane ( $\gamma$ -GPS); (e). (3-glycidoxypropyl) methyl-dimethoxysilane ( $\gamma$ -GPMS); (f) (3-glycidoxypropyl) dimethyl-methoxysilane ( $\gamma$ - GPDMS)**

#### 2.4.2 Interfaces between *d*<sub>4</sub>-PET and MVS or Silicone (Without Silanes)

To avoid overlapping signals from other compounds in the C-H stretching frequency range, deuterated *d*<sub>4</sub>-PET was used in the experiments. Therefore, no aliphatic SFG C-H stretching signal

(usually  $< 3000\text{ cm}^{-1}$ ) could be observed from  $d_4$ -PET. Our previous research indicated that on the  $d_4$ -PET surface in air, only an aromatic C-H stretching signal ( $> 3000\text{ cm}^{-1}$ ) was detected<sup>62</sup>. Here, we first studied the interfaces between  $d_4$ -PET and silicone elastomers before and after curing. In previous studies, no SFG signal could be observed from such interfaces<sup>63</sup>. In this experiment, the signal enhancement provided by the new experimental geometry revealed two peaks at  $\sim 2900$  and  $2965\text{ cm}^{-1}$  (from PDMS methyl symmetric and asymmetric stretches) (Figures 2-17a and b). Furthermore, after spectral fitting we found that the symmetric/asymmetric stretching signal strength ratios are different before and after curing (0.9 before curing, 1.1 after curing). This indicates that the PDMS methyl group orientation changed at the interface during the curing process. An aromatic C-H stretching signal at  $\sim 3085\text{ cm}^{-1}$  was also detected at the  $d_4$ -PET/silicone interfaces, showing that the  $d_4$ -PET phenyl groups are also ordered at these interfaces.

We also collected the ssp SFG spectrum from the  $d_4$ -PET/MVS interface (Figure 2-17c). Two peaks at  $2945$  and  $2970\text{ cm}^{-1}$  were detected. The  $2970\text{ cm}^{-1}$  signal is due to the asymmetric stretching mode of the Si-CH<sub>3</sub> group in MVS. The  $2945\text{ cm}^{-1}$  signal is unknown, which might be contributed by the Si-CH<sub>3</sub> group or other C-H groups in MVS. Nevertheless, the detection of SFG signal here indicated that methyl groups (and perhaps other C-H groups) in MVS can be ordered at the  $d_4$ -PET/MVS interface.

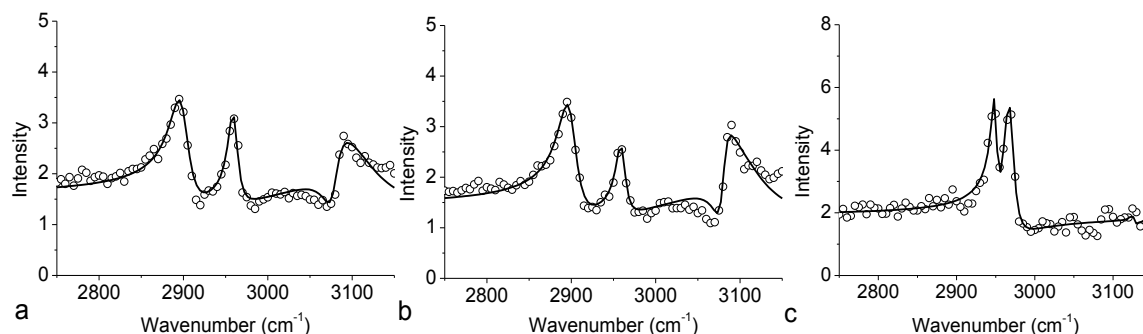


**Figure 2-17. SFG spectra collected from (a) the  $d_4$ -PET/uncured silicone interface, (b) the  $d_4$ -PET/cured silicone interface, (c) the  $d_4$ -PET/MVS interface. The dots are experimental data and the lines are fitting results.**

### 2.4.3 Interfaces between $d_4$ -PET and Silane or Silane-MVS Mixture

SFG spectroscopy was previously applied to study the interfaces between  $d_4$ -PET in contact with a variety of silanes and their mixtures with MVS<sup>62</sup>. When  $d_4$ -PET was in contact with  $\gamma$ -GPS, a weak signal of the methoxy headgroups on  $\gamma$ -GPS was observed from the  $d_4$ -PET/ $\gamma$ -GPS interface, while at the  $d_4$ -PET/ $\gamma$ -GPS:MVS mixture interface, a much stronger methoxy C-H stretching SFG signal was observed<sup>62</sup>.

We first reproduced the SFG results at the  $d_4$ -PET/ $\gamma$ -GPS and  $d_4$ -PET/ $\gamma$ -GPS:MVS mixture interfaces using the window geometry (Figure 2-18a). We then collected SFG spectra from the same interfaces using the near critical angle (NCA) geometry (Figure 2-1, Figure 2-18b). The spectra collected using different experimental geometries have similar features, but those collected using the NCA geometry exhibit stronger intensities, more spectral details, and better signal-to-noise ratios. In order to understand the effect of silane headgroups on interfacial silane behaviors, we also collected SFG spectra from the interfaces between  $d_4$ -PET and silanes with a variety of different headgroups:  $\gamma$ -GPMS,  $\gamma$ -GPDMS, and their mixtures with MVS. All of these SFG spectra are shown in Figure 2-18. Furthermore, we fitted all the spectra using Equation 1.2. As mentioned above, since this study focused on the effect of headgroups upon adhesion, we will only discuss

the SFG signal contributed by the headgroups (especially the methoxy peak at  $\sim 2840\text{ cm}^{-1}$ ). The assignments for other C-H signals are complicated, and therefore other functional group signals are not discussed in detail here. Further information and possible peak assignments are presented in the Appendix 2.4.9.

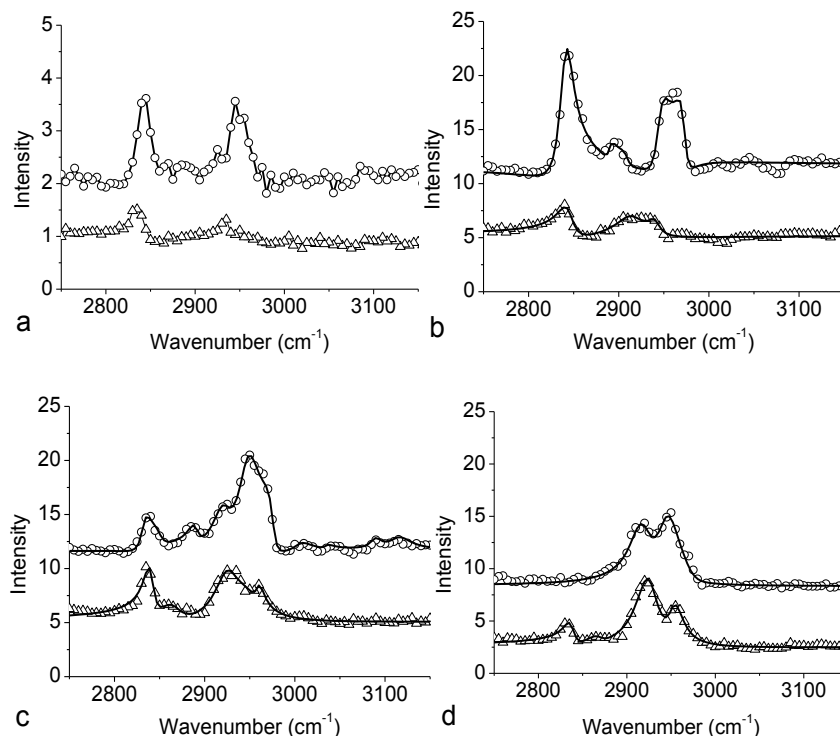


**Figure 2-18.** SFG spectra collected from (a) the  $d_4$ -PET/ $\gamma$ -GPS ( $\Delta$ ) and  $d_4$ -PET/ $\gamma$ -GPS:MVS interfaces ( $\circ$ ) using the window geometry, (b) the  $d_4$ -PET/ $\gamma$ -GPS ( $\Delta$ ) and  $d_4$ -PET/ $\gamma$ -GPS:MVS interfaces ( $\circ$ ) using the NCA geometry, (c) the  $d_4$ -PET/ $\gamma$ -GPMS ( $\Delta$ ) and  $d_4$ -PET/ $\gamma$ -GPMS:MVS interfaces ( $\circ$ ) using the NCA geometry, (d) the  $d_4$ -PET/ $\gamma$ -GPDMS ( $\Delta$ ) and  $d_4$ -PET/ $\gamma$ -GPDMS:MVS interfaces ( $\circ$ ) using the NCA geometry. For (b), (c), (d), the dots are experimental data and the lines are fitting results.

At the  $d_4$ -PET/ $\gamma$ -GPS interface, the peak centered at  $\sim 2840\text{ cm}^{-1}$  is assigned to the symmetric C-H stretch of the methoxy group. This indicates that at the interface, silane methoxy groups segregate with some order. Similar to our previous reports, at the  $d_4$ -PET/ $\gamma$ -GPS:MVS 1:1 mixture interface, the intensity of the  $2840\text{ cm}^{-1}$  peak increased greatly (Figures 2-18a and b).

According to the fitting results in the Appendix 2.4.9, the signal strength increased from 1.2 to 3.2 from the methoxy groups at the interface after MVS was introduced into the system. This shows that MVS greatly increases the ordering of  $\gamma$ -GPS methoxy groups at the  $d_4$ -PET/mixture interface.

A methoxy peak was also detected from  $\gamma$ -GPMS in the spectrum collected from the  $d_4$ -PET/ $\gamma$ -GPMS interface (Figure 2-18c). A  $\gamma$ -GPMS molecule has only two methoxy groups plus a methyl group. The SFG signal of the methyl headgroup, which is connected to the Si atom of the silane, should be observed at  $\sim 2910\text{ cm}^{-1}$  if they segregate with order at the interface. However, this peak is close to the methylene asymmetric stretching signal, and therefore the peak observed at about  $\sim 2920\text{ cm}^{-1}$  cannot be definitely assigned to the Si-CH<sub>3</sub> headgroup. The SFG signal intensity observed from the methoxy groups at the  $d_4$ -PET/ $\gamma$ -GPMS interface (signal strength 1.4) is not very different from that observed at the  $d_4$ -PET/ $\gamma$ -GPS interface (signal strength 1.2). In the SFG spectrum collected from the  $d_4$ -PET/ $\gamma$ -GPMS:MVS 1:1 mixture interface, the methoxy C-H symmetric stretch at  $\sim 2840\text{ cm}^{-1}$  can still be resolved. The spectral fitting results indicated that the signal strength grows from 1.4 to 1.7 after the introduction of MVS. This shows that the addition of MVS slightly enhanced the methoxy ordering of  $\gamma$ -GPMS at the interface.

At the  $d_4$ -PET/ $\gamma$ -GPDMS interface (Figure 2-18d), the SFG signal of the methoxy symmetric stretch at about  $2840\text{ cm}^{-1}$  could also be detected. As discussed above, the observed peak at  $2925\text{ cm}^{-1}$  may be contributed by the methylene asymmetric stretching and/or the methyl headgroup. Therefore, possibly the methyl headgroup also exhibits some order at the  $d_4$ -PET/ $\gamma$ -GPDMS interface. At the  $d_4$ -PET/ $\gamma$ -GPDMS:MVS 1:1 mixture interface, no SFG signal at  $\sim 2840\text{ cm}^{-1}$  was detected, indicating that the interfacial methoxy group is disordered by the addition of MVS. This is different from the  $\gamma$ -GPS and  $\gamma$ -GPMS cases discussed above. The C-H symmetric



stretching signal of the silane methyl headgroups at  $2918\text{ cm}^{-1}$  could be resolved. Again, this peak could overlap with peaks from the methylene groups, or even the Si-CH<sub>3</sub> groups in MVS.

The SFG results reported above demonstrate that silane methoxy headgroups exhibit some order at the *d*<sub>4</sub>-PET/ $\gamma$ -GPS, *d*<sub>4</sub>-PET/ $\gamma$ -GPMS and *d*<sub>4</sub>-PET/ $\gamma$ -GPDMS interfaces. The addition of MVS to the first two silanes enhanced the interfacial ordering of the methoxy groups. In contrast, the addition of MVS disordered the methoxy groups at the *d*<sub>4</sub>-PET/ $\gamma$ -GPDMS (with MVS) interface.

#### **2.4.4 Interfaces between *d*<sub>4</sub>-PET and Uncured Silicone Mixed with Silane or Silane-MVS**

##### **Mixture**

SFG spectra were collected from several *d*<sub>4</sub>-PET/uncured silicone interfaces, with PDMS silicone mixed with silane or silane+MVS. Figure 2-19a shows the SFG spectra collected from the *d*<sub>4</sub>-PET/uncured silicone (mixed with  $\gamma$ -GPS with and without MVS) interfaces. In the absence of MVS, the ordering of the silane methoxy group at the interface could be inferred by the observed signal at  $\sim 2840\text{ cm}^{-1}$ . With MVS, the methoxy groups and the backbone still adopt some order at the interface. The strength of the methoxy signal at  $\sim 2840\text{ cm}^{-1}$  increased only slightly after the addition of MVS (from 1.3 to 1.7). This is different from the situation where *d*<sub>4</sub>-PET was in contact with  $\gamma$ -GPS alone or with a  $\gamma$ -GPS:MVS mixture, in which the addition of MVS greatly enhanced the methoxy interfacial order. The results indicate that uncured PDMS influences methoxy ordering at the *d*<sub>4</sub>-PET interface.

At the *d*<sub>4</sub>-PET/uncured silicone (mixed with  $\gamma$ -GPMS, or with  $\gamma$ -GPMS:MVS) interface, the  $2840\text{ cm}^{-1}$  peak was again observed, indicating ordering of the silane methoxy headgroups (Figure 2-19b). The fitting results indicate that the signal strength of this peak is very similar before and after the addition of MVS, at 1.0 and 1.2 respectively. This indicates that the interfacial

segregation and/or interfacial orientation of the methoxy headgroups may only slightly change after the addition of MVS.

Figure 2-19c shows the SFG spectra collected from the  $d_4$ -PET/uncured silicone (mixed with  $\gamma$ -GPDMS with and without MVS) interfaces. With only silane in silicone, weak methoxy symmetric stretching signals can be observed at  $\sim 2840\text{ cm}^{-1}$ . This shows that methoxy headgroups adopt some order at the interface. With MVS and silane in silicone, these signals disappear, suggesting that the methoxy groups are no longer ordered.

Furthermore, in all of the samples that incorporate uncured silicone, signals at  $\sim 3080\text{ cm}^{-1}$  provide evidence that phenyl groups in  $d_4$ -PET adopt some order at the interface. This is different from the situations without the uncured silicone. At the  $d_4$ -PET/uncured silicone interfaces for all the three silanes, the methoxy signal strengths are similar, at 1.3, 1.0, and 1.0 respectively. However, when mixed with MVS, the methoxy interfacial segregation and/or interfacial ordering increased slightly for  $\gamma$ -GPS, remained more or less the same for  $\gamma$ -GPMS, and decreased for  $\gamma$ -GPDMS.

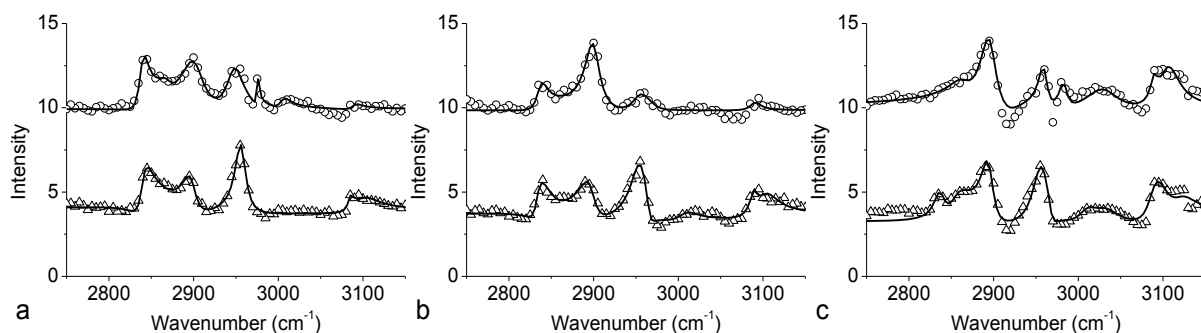


**Figure 2-19. SFG spectra collected from the interfaces between  $d_4$ -PET and uncured silicones mixed with (a)  $\gamma$ -GPS ( $\Delta$ ) and  $\gamma$ -GPS:MVS ( $\circ$ ), (b)  $\gamma$ -GPMS ( $\Delta$ ) and  $\gamma$ -GPMS:MVS ( $\circ$ ), (c)  $\gamma$ -GPDMS ( $\Delta$ ) and  $\gamma$ -GPDMS:MVS ( $\circ$ ). The dots are experimental data and the lines are fitting results.**

## 2.4.5 Interfaces between $d_4$ -PET and Cured Silicone Mixed with Silane or Silane-MVS

### Mixture

We cured all the samples investigated above in a convection oven for 120 minutes at 140 °C, and kept the samples at room temperature for 24 hours. We then collected SFG spectra from the interfaces of all the cured samples. In the spectrum collected from the  $d_4$ -PET/cured silicone interface with 1.5%  $\gamma$ -GPS (Figure 2-20a), a peak at  $\sim 2840\text{ cm}^{-1}$  was observed, indicating that the  $\gamma$ -GPS methoxy groups were segregated to and ordered at the polymer interface. The intensity of the  $\gamma$ -GPS methoxy peak was weaker after the addition of MVS, which was opposite to the relative intensities observed in the spectra collected when  $d_4$ -PET in contact with silane or the uncured silicone (with or without MVS). Before and after the addition of MVS, the signal strengths are 1.4 and 1.1, respectively. Compared to the uncured silicone cases, the signal strength of the methoxy groups at the interface with  $\gamma$ -GPS is similar, at 1.3 and 1.4 respectively. However, for the  $\gamma$ -GPS with MVS, the signal decreased substantially from 1.7 to 1.1. As we will further discuss in the next section, the  $d_4$ -PET/cured silicone (with  $\gamma$ -GPS and MVS) interface has the best adhesion. The methoxy SFG signal decrease may be due to the high cure temperature of 140 °C, which may induce a chemical reaction or diffusion of the silane at the polymer interface. The loss of methoxy signal upon curing suggests that the methoxy headgroups might play a role in interfacial adhesion through chemical reactions or interfacial diffusion.

SFG spectra were collected from the  $d_4$ -PET/cured silicone interfaces with silicone mixed with  $\gamma$ -GPMS (1.5 %) and  $\gamma$ -GPMS:MVS mixture (3.0 %), shown in Figure 2-20b. In both cases the peak at  $\sim 2840\text{ cm}^{-1}$  was observed. The fitting results indicated that the methoxy signal strengths are about the same, at 0.8 and 0.7 respectively. As with  $\gamma$ -GPS, the fitted signal strength of the interfacial methoxy groups of  $\gamma$ -GPMS before and after curing the silicone is similar, at 1.0 and

0.8 respectively. After the addition of MVS, the signal strength decreased from 1.2 (before curing) to 0.7 (after curing), which suggests that adhesion strength may be related to interfacial chemical reactions or interfacial diffusion of the methoxy groups due to curing. SFG spectra were also collected from the  $d_4$ -PET/cured silicone interfaces with silicone mixed with  $\gamma$ -GPDMS (1.5 %), or  $\gamma$ -GPDMS:MVS mixture (3.0 %). These spectra are displayed in Figure 2-20c. No methoxy signals were detected at either interface, which is different from the  $\gamma$ -GPS and  $\gamma$ -GPMS situations.

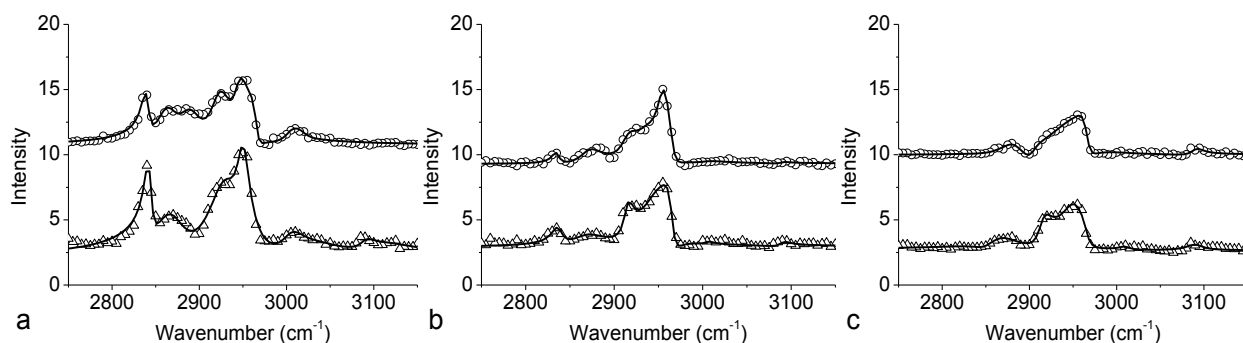


**Figure 2-20. SFG spectra collected from the interfaces between  $d_4$ -PET and cured silicone with (a)  $\gamma$ -GPS ( $\Delta$ ) and  $\gamma$ -GPS:MVS ( $\circ$ ), (b)  $\gamma$ -GPMS ( $\Delta$ ) and  $\gamma$ -GPMS:MVS ( $\circ$ ), and (c)  $\gamma$ -GPDMS ( $\Delta$ ) and  $\gamma$ -GPDMS:MVS ( $\circ$ ). The dots are experimental data and the lines are fitting results.**

#### 2.4.6 Mechanical Adhesion Test Results

To correlate the SFG results on buried interfaces to polymer adhesion, adhesion strength was measured using shear testing. The method used to perform the test is demonstrated in section 2.3. The forces to break the interfaces of the samples were measured in the experiment to compare the adhesion strengths at different interfaces. All samples were monitored to exclude erroneous results due to defects (e.g., bubbling). The adhesion strength was calculated by dividing the measured breaking force by the contact area. Four samples were prepared for each adhesive mixture in every adhesion experiment, and the adhesion experiment was repeated several times.

The shear testing results (Figure 2-21) show that pure silicone only has weak adhesion to PET (<1 MPa). The addition of  $\gamma$ -GPDMS by itself, or mixed with MVS, does not increase the adhesion between the adhesive and PET (<1 MPa). In contrast, adding epoxy silanes  $\gamma$ -GPS and  $\gamma$ -GPMS to silicone increases the adhesion strength between silicone and PET (1-3 MPa). The use of either the  $\gamma$ -GPS:MVS mixture or the  $\gamma$ -GPMS:MVS mixture in silicone leads to much stronger adhesion to PET (3-5 MPa). Additionally, the adhesion failure for all samples except PDMS  $\gamma$ -GPS:MVS mixture and PDMS  $\gamma$ -GPMS:MVS mixture happened at polymer/adhesive interfaces. There was no bulk failure for these adhesive samples. For the PDMS  $\gamma$ -GPS:MVS mixture and PDMS  $\gamma$ -GPMS:MVS mixture, both cohesive and adhesive failures were observed.

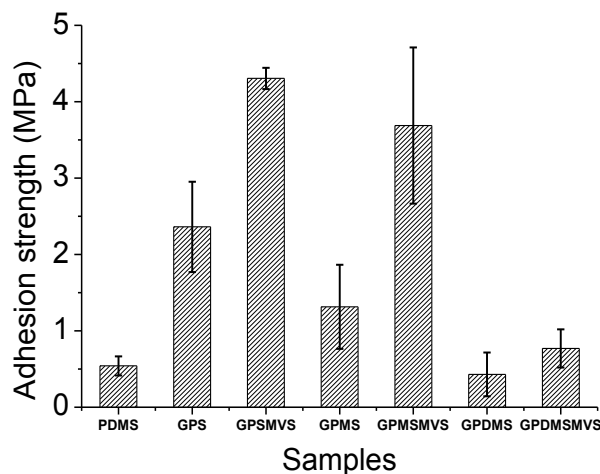


**Figure 2-21. The adhesion test results (using 180 degree shear test). Strength=Force/Contact area.**

#### 2.4.7 The Relation between Interfacial Molecular Ordering and Adhesion

Figure 2-21 shows that the addition of  $\gamma$ -GPS alone and with MVS or  $\gamma$ -GPMS alone and with MVS greatly enhanced the adhesion of silicone to PET. The relative improvement in adhesion attributed to the addition of silanes has the following hierarchy:  $\gamma$ -GPS (three methoxy headgroups) >  $\gamma$ -GPMS (two methoxy headgroups) >  $\gamma$ -GPDMS (only one methoxy headgroup). Similarly, the

addition of  $\gamma$ -GPS and MVS improves adhesion greater than the addition of  $\gamma$ -GPMS and MVS, which in turn improves the adhesion more than the addition of  $\gamma$ -GPDMS and MVS into silicone. This clearly shows that the methoxy headgroups play an important role in adhesion. The more methoxy groups a silane has, the stronger the adhesion. Also the mixing of MVS with silane greatly enhanced the adhesion between PET and PDMS silicone.

Our adhesion testing results can be correlated to the SFG results quite well. The SFG data indicated that at the PET/cured silicone interfaces, when  $\gamma$ -GPS (with or without MVS) and  $\gamma$ -GPMS (with or without MVS) were used, interfacial segregation and ordering of methoxy headgroups could be observed, leading to strong adhesion. When  $\gamma$ -GPDMS (with or without MVS) was used, no interfacial segregation and/or ordering of methoxy headgroups could be detected from the PET/cured silicone interfaces, and only weak adhesion was observed. Furthermore, the signal strength decreased substantially after the silicone was cured in the case of the two samples with the strongest adhesion ( $\gamma$ -GPS with MVS and  $\gamma$ -GPMS with MVS). Here, we believe that the signal strength decrease is related to interfacial chemical reactions and/or diffusion processes that could lead to stronger adhesion. For example, there may be a chemical reaction between the PET hydroxyl end groups and silane methoxy headgroups,<sup>64</sup> which can be studied in the future by using samples of PET with different molecular weights. Interfacial diffusion can also be tested, using methods developed previously.<sup>65-67</sup> The addition of the  $\gamma$ -GPS:MVS mixture to silicone leads to the strongest ordering of methoxy groups at the PET/uncured silicone interface, and the largest decrease in signal after the silicone curing. This suggests that this sample is subject to a large amount of interfacial chemical reaction and/or interfacial diffusion, which is correlated to observations of the strongest adhesion at the PET/silicone interface of the samples studied here.

## 2.4.8 Conclusion

This research focused on the effect of silane headgroups, especially, the methoxy headgroups on silane interfacial structures at the PET/silane, PET/silane-MVS mixture, PET/uncured silicone (with silane or silane-MVS mixture), and PET/cured silicone (with silane or silane-MVS mixture) interfaces. We showed that silanes with different headgroups can behave differently at various interfaces. For  $\gamma$ -GPS,  $\gamma$ -GPMS and  $\gamma$ -GPDMS, methoxy headgroups tend to order at the polymer/silane interfaces. MVS greatly increased the methoxy group ordering in  $\gamma$ -GPS at the interface, slightly affected the interfacial methoxy order in  $\gamma$ -GPMS, and disordered the interfacial methoxy groups in  $\gamma$ -GPDMS.

Uncured silicone affected the methoxy interfacial segregation and/or order at the interfaces. At the  $d_4$ -PET/uncured silicone interfaces for all the three silanes, the methoxy signal strengths are similar, at 1.3, 1.0, and 1.0 respectively. However, when mixing with MVS, the methoxy order increased slightly for  $\gamma$ -GPS, remained more or less the same for  $\gamma$ -GPMS, and decreased for  $\gamma$ -GPDMS.

At the  $d_4$ -PET/cured silicone interfaces, the SFG signal detected from the methoxy groups was stronger for the addition of  $\gamma$ -GPS alone to silicone compared to the addition of  $\gamma$ -GPS:MVS mixture to silicone, while it was similar for the addition of  $\gamma$ -GPMS alone and the addition of the  $\gamma$ -GPMS:MVS mixture. At the  $d_4$ -PET/cured silicone interface, no methoxy SFG signal was detected when either adding  $\gamma$ -GPDMS alone or adding the  $\gamma$ -GPDMS:MVS mixture to silicone.

A range of methoxy group interfacial segregation and ordering behaviors was observed, which was correlated to measurements of adhesion strengths. Strong adhesion was detected at the PET/cured PDMS interfaces when  $\gamma$ -GPS (with or without MVS) and  $\gamma$ -GPMS (with or without MVS) were used, because of the interfacial segregation and ordering of methoxy headgroups

before and after curing. The methoxy SFG signal strength decreased substantially after the silicone was cured when using silicone with either  $\gamma$ -GPS with MVS or  $\gamma$ -GPMS with MVS, and these two samples had the highest adhesive strength of those studied. We therefore believe that stronger adhesion is related to (1) the interfacial segregation and ordering of methoxy groups at PET/uncured and cured silicone interfaces, and (2) the methoxy SFG signal strength decrease during the curing process (which could be related to interfacial chemical reactions and/or diffusion). The second hypothesis will be further studied in section 2.5.

#### 2.4.9 Appendix

Fitting parameters used in the experiments are listed below:

Material	$\omega_q$ (cm <sup>-1</sup> )	$ A_{q,ssp} $	$\Gamma_q$ (cm <sup>-1</sup> )	$ A_{q,ssp} / \Gamma_q $	Assignment
Silicone uncured	2900	13.8	12.4	1.1	-SiCH <sub>3</sub> (s)
	2960	8.3	6.9	1.2	-SiCH <sub>3</sub> (as)
Silicone cured	2913	27.0	7.6	3.5	-SiCH <sub>3</sub> (s)
	2963	15.0	4.7	3.2	-SiCH <sub>3</sub> (as)
MVS	2950	4.6	4.3	1.1	unknown
	2968	15.0	8.0	1.9	-SiCH <sub>3</sub> (as)

**Table 2-4. Fitting results for Figure 2-17.**



Material	$\omega_q$ (cm <sup>-1</sup> )	$ A_{q,ssp} $	$\Gamma_q$ (cm <sup>-1</sup> )	$ A_{q,ssp} / \Gamma_q $	Assignment
GPS	2840	10.0	7.5	1.3	-OCH <sub>3</sub> (s)
	2860	12.7	27.5	0.5	-CH <sub>2</sub> (s)
	2898	10.2	9.5	1.1	Si-CH <sub>3</sub> (s)
	2956	19.5	8.2	2.4	-OCH <sub>3</sub> (Fermi and/or as)
	2960	4.0	8.7	0.5	SiCH <sub>3</sub> and/or OCH <sub>3</sub> (as)
GPSMVS	2839	11.0	6.5	1.7	-OCH <sub>3</sub> (s)
	2870	2.7	9.0	0.3	-CH <sub>2</sub> (s)
	2902	24.7	16.6	1.5	Si-CH <sub>3</sub> (s)
	2948	16.9	12.6	1.3	-OCH <sub>3</sub> (Fermi and/or as)
GPMS	2975	1.3	1.5	0.9	SiCH <sub>3</sub> and/or OCH <sub>3</sub> (as)
	2834	6.5	6.8	1.0	-OCH <sub>3</sub> (s)
	2850	4.3	15.0	0.3	-CH <sub>2</sub> (s)
	2897	11.4	10.9	1.0	Si-CH <sub>3</sub> (s)
	2955	29.2	13.2	2.2	-OCH <sub>3</sub> (Fermi and/or as)
GPMSMVS	2965	8.7	6.2	1.4	SiCH <sub>3</sub> and/or OCH <sub>3</sub> (as)
	2837	9.0	7.4	1.2	-OCH <sub>3</sub> (s)
	2900	20.7	10.7	1.9	Si-CH <sub>3</sub> (s)
	2953	12.9	13.2	1.0	-OCH <sub>3</sub> (Fermi and/or as)
GPDMS	2970	8.0	17.5	0.5	SiCH <sub>3</sub> and/or OCH <sub>3</sub> (as)
	2837	7.5	7.8	1.0	-OCH <sub>3</sub> (s)
	2857	17.0	14.9	1.1	-CH <sub>2</sub> (s)
	2895	15.2	8.4	1.8	Si-CH <sub>3</sub> (s)
	2955	26.3	13.3	2.0	-OCH <sub>3</sub> (Fermi and/or as)
GPDMSMVS	2967	8.6	7.4	1.2	SiCH <sub>3</sub> and/or OCH <sub>3</sub> (as)
	2865	6.5	15.0	0.4	-CH <sub>2</sub> (s)
	2896	21.6	11.3	1.9	Si-CH <sub>3</sub> (s)
	2920	4.5	14.8	0.3	-CH <sub>2</sub> (as)
	2960	7.4	6.1	1.2	Si-CH <sub>3</sub> (as)
	2983	4.8	5.5	0.9	Si-CH <sub>3</sub> (as) (Interference)

**Table 2-5. Fitting results for Figure 2-18.**

Material	$\omega_q$ (cm <sup>-1</sup> )	$ A_{q,ssp} $	$\Gamma_q$ (cm <sup>-1</sup> )	$ A_{q,ssp} / \Gamma_q $	Assignment
GPS	2845	13.3	10.8	1.2	-OCH <sub>3</sub> (s)
	2915	30.9	19.4	1.6	-CH <sub>2</sub> (as)
	2940	15.2	7.9	1.9	-OCH <sub>3</sub> (Fermi and/or as)
GPS/MVS	2840	30.3	9.5	3.2	-OCH <sub>3</sub> (s)
	2890	2.0	4.4	0.5	unknown
	2910	2.7	6.6	0.4	Si-CH <sub>3</sub> (s)
	2945	15.4	8.9	1.7	-OCH <sub>3</sub> (Fermi and/or as)
GPMS	2972	10.0	6.3	1.6	SiCH <sub>3</sub> and/or OCH <sub>3</sub> (as)
	2841	9.9	6.8	1.4	-OCH <sub>3</sub> (s)
	2865	13.3	16.1	0.8	-CH <sub>2</sub> (s)
	2926	25.6	16.5	1.6	-CH <sub>2</sub> (as)
	2945	18.5	19.5	0.9	-OCH <sub>3</sub> (Fermi and/or as)
GPMSMVS	2960	3.5	5.7	0.6	SiCH <sub>3</sub> and/or OCH <sub>3</sub> (as)
	2840	11.9	7.1	1.7	-OCH <sub>3</sub> (s)
	2850	4.2	8.4	0.5	-CH <sub>2</sub> (s)
	2890	5.0	7.0	0.7	unknown
	2921	15.8	13.0	1.2	-CH <sub>2</sub> (as)
GPDMS	2947	39.5	15.0	2.6	-OCH <sub>3</sub> (Fermi and/or as)
	2975	15.0	7.2	2.1	SiCH <sub>3</sub> and/or OCH <sub>3</sub> (as)
	2838	6.7	7.2	0.9	-OCH <sub>3</sub> (s)
	2867	3.7	10.2	0.4	-CH <sub>2</sub> (s)
	2925	35.9	15.6	2.3	-CH <sub>2</sub> (as)
GPDMSMVS	2953	13.5	10.3	1.3	-OCH <sub>3</sub> (Fermi and/or as)
	2918	20.8	13.1	1.6	Si-CH <sub>3</sub> (s) (MVS)
	2945	16.8	10.0	1.7	-OCH <sub>3</sub> (Fermi and/or as)
	2974	10.0	8.9	1.1	SiCH <sub>3</sub> and/or OCH <sub>3</sub> (as) Si-CH <sub>3</sub> (as) (silane, MVS)

**Table 2-6. Fitting results for Figure 2-19.**

Material	$\omega_q$ (cm <sup>-1</sup> )	$ A_{q,ssp} $	$\Gamma_q$ (cm <sup>-1</sup> )	$ A_{q,ssp} / \Gamma_q $	Assignment
GPS	2843	6.7	4.9	1.4	-OCH <sub>3</sub> (s)
	2870	28.5	23.6	1.2	-CH <sub>2</sub> (s)
	2930	41.0	23.0	1.8	-CH <sub>2</sub> (as)
	2950	14.6	9.3	1.6	-OCH <sub>3</sub> (Fermi and/or as)
GPSMVS	2840	5.7	5.2	1.1	-OCH <sub>3</sub> (s)
	2865	15.2	15.0	1.0	-CH <sub>2</sub> (s)
	2890	18.0	17.0	1.1	Si-CH <sub>3</sub> (s)
	2923	22.5	15.0	1.5	-CH <sub>2</sub> (as)
	2945	11.2	9.8	1.1	-OCH <sub>3</sub> (Fermi and/or as)
GPMS	2965	6.8	5.6	1.2	SiCH <sub>3</sub> and/or OCH <sub>3</sub> (as)
	2837	5.7	7.5	0.8	-OCH <sub>3</sub> (s)
	2870	18.5	23.7	0.8	CH <sub>2</sub> (s)
	2915	18.0	6.5	0.8	Si-CH <sub>3</sub> (s)
	2947	56.7	24.3	2.3	-OCH <sub>3</sub> (Fermi and/or as)
GPMSMVS	2965	18.0	6.7	2.7	SiCH <sub>3</sub> and/or OCH <sub>3</sub> (as)
	2835	3.6	5.0	0.7	-OCH <sub>3</sub> (s)
	2871	15.7	15.0	1.0	CH <sub>2</sub> (s)
	2915	22.5	11.5	2.0	Si-CH <sub>3</sub> (s)
	2940	15.7	15.0	1.0	-OCH <sub>3</sub> (Fermi and/or as)
GPDMS	2955	25.6	10.7	2.4	SiCH <sub>3</sub> and/or OCH <sub>3</sub> (as)
	2965	14.0	8.3	1.7	SiCH <sub>3</sub> and/or OCH <sub>3</sub> (as)
	2856	10.0	18.0	0.6	CH <sub>2</sub> (s) (silane)
	2870	41.9	32.9	1.3	unknown
	2915	20.4	9.1	2.2	Si-CH <sub>3</sub> (s)
GPDMSMVS	2951	42.1	17.3	2.4	Si-CH <sub>3</sub> (as)
	2965	21.5	8.6	2.5	Si-CH <sub>3</sub> (as)
	2860	4.3	21.3	0.2	CH <sub>2</sub> (s) (silane)
	2883	9.5	13.5	0.7	unknown
	2902	8.0	9.3	0.9	Si-CH <sub>3</sub> (s)
	2945	58.9	33.4	1.8	Si-CH <sub>3</sub> (as)
	2965	17.0	7.2	2.4	Si-CH <sub>3</sub> (as)

**Table 2-7. Fitting results for Figure 2-20**

## 2.5 Ethoxy-silane Adhesion Promoters at the PDMS/PET Interface

In the previous section we systematically studied methoxy-silane behaviors at the PDMS/PET interface. It was found that silane methoxy headgroups are involved in interfacial chemical reaction or randomization, decreasing their SFG signals generated at the interfaces. Such signal decrease can be correlated to the improved adhesion. MVS molecules can further facilitate such SFG signal decreases, leading to stronger adhesion at interfaces. We also found that the silane with higher number of methoxy headgroups tends to exhibit stronger adhesion promotion effect.

Besides methoxy silanes (with methoxy headgroups), chloride silanes (with chloride headgroups) have also been used as adhesion promoters. The disadvantage of methoxy-silanes and chloride silanes is that in the adhesion promoting process, they tend to release harmful methanol or corrosive hydrochloric acid, respectively.<sup>10</sup> To reduce negative environmental impact, silanes with ethoxy headgroups (ethoxy silanes) are used as adhesion promoters. In the adhesion promoting reaction, ethoxy silanes tend to release harmless ethanol molecules.<sup>68</sup> In the following research, we studied three epoxy silanes with the same backbone and endgroup, but different headgroups at the buried interfaces between PDMS and PET. The following work can also generalize the conclusion we obtained from section 2.4.

### 2.5.1 Materials Used in the Research and Sample Preparation

The (3-glycidoxypropyl) triethoxysilane ( $\gamma$ -GPES), (3-glycidoxypropyl) methyl-diethoxysilane ( $\gamma$ -GPDES), (3-glycidoxypropyl) dimethyl-ethoxysilane ( $\gamma$ -GPDMS) were purchased from Sigma Aldrich. The silane molecular formulas are shown in Figure 2-22. The Sylgard 184 silicone elastomer was again prepared by mixing the base and the curing agent with a 10:1 ratio. To incorporate silanes into PDMS, 1.5 wt%  $\gamma$ -GPES, 3.0 wt% 1:1 (wt/wt)  $\gamma$ -GPES/MVS mixture, 1.5 wt%  $\gamma$ -GPDES, 3.0 wt% 1:1 (wt/wt)  $\gamma$ -GPDES/MVS mixture, 1.5 wt%

$\gamma$ -GPDMES, 3.0 wt% 1:1 (wt/wt)  $\gamma$ -GPDMES/MVS mixture were mixed homogeneously using a vortex mixer into the silicone mixture before curing respectively. When MVS was added, a SiH-functional PDMS was added to maintain a 1.5:1 SiH/vinyl molar ratio. The  $d_4$ -PET film preparation, the PDMS curing condition, and the substrate cleaning produces are the same as those mentioned in the previous sections and will not be repeated here.

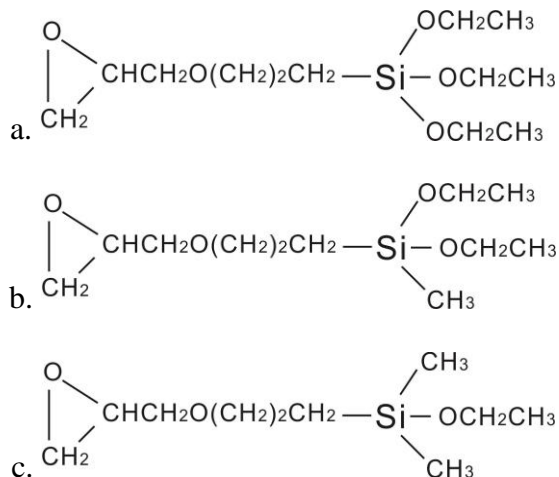


**Figure 2-22. Chemical structures of silanes employed in the study: a. (3-glycidoxypropyl) triethoxysilane ( $\gamma$ -GPES); b. (3-glycidoxypropyl) methyl-diethoxysilane ( $\gamma$ -GPDES); c. (3-glycidoxypropyl) dimethyl-ethoxysilane ( $\gamma$ - GPDMES) .**

### 2.5.2 Mechanical Adhesion Test

The adhesion test results for PDMS and PDMS silane mixtures with and without MVS adhere to PET using the 180 degree shear test are shown in Figure 2-23. In the tests, five samples were prepared for each type, and therefore each experiment was reproduced five times. The results with error bars shown in Figure 2-23 are the averaged values with the standard deviations. Figure 2-23 shows clearly that silanes with different ethoxy headgroups exhibit different adhesion promotion behavior when incorporated into PDMS. Compared to PDMS alone, the  $\gamma$ -GPES tends to increase the adhesion to PET,  $\gamma$ -GPDES does not significantly alter the adhesion,  $\gamma$ -GPDMES tends to decrease the adhesion. When MVS was added to the mixture together with silanes, all

samples show substantially increased adhesion strength, while the measured strengths are  $\gamma$ -GPES:MVS >  $\gamma$ -GPDES:MVS >  $\gamma$ -GPDMS:MVS. These results indicate that silane ethoxy headgroups tend to improve the interfacial adhesion between PET and PDMS. The more ethoxy group the silane has, the stronger adhesion its mixture with PDMS tends to have. It also shows that MVS can greatly improve the adhesion of silane PDMS mixtures to PET.

However, it is still unclear at the molecular level how silane headgroup can affect the adhesion and why MVS improves the adhesion. Silanes are mixed in the PDMS with very small fractions, whether they can segregate to the PET/PDMS interface is unknown. If they do segregate to the interface, it is still unknown whether they exhibit interfacial order. It is well known that on a silica substrate where hydroxyl groups are present, ethoxy-silanes can interact with the substrate through a chemical reaction. Ethoxy headgroup reacts with the hydroxyl group to release an ethanol molecule while the rest of the silane molecule directly binds to the silica substrate to improve adhesion. However, it is not known whether ethoxy-silanes will have a similar reaction with polymer (e.g., PET) surfaces and whether ethoxy headgroups can play a role to improve adhesion to polymer surfaces. Silane headgroups may also cross-linked at the PET substrate surface through reaction with water molecule adsorbed in air.<sup>8, 10, 69</sup> MVS has hydroxyl groups which may play a role for improving silane headgroup reaction at the substrate surface to form cross-linking. In order to have a further understanding on the molecular behavior of interfacial silanes and MVS, SFG was applied to investigate the buried PET/PDMS interfaces.

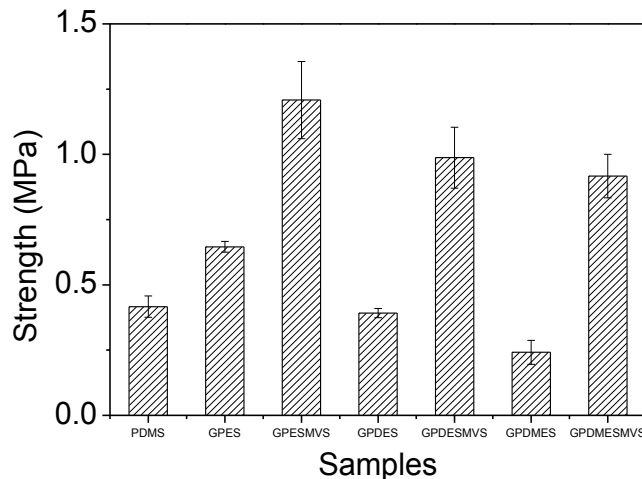


**Figure 2-23. Adhesion test results of ethoxy-silane incorporated in PDMS adhesives. Samples from left to right: PDMS,  $\gamma$ -GPES,  $\gamma$ -GPES:MVS,  $\gamma$ -GPDES,  $\gamma$ -GPDES:MVS,  $\gamma$ -GPDMS,  $\gamma$ -GPDMS:MVS. Only a very small amount of silane or silane:MVS mixture was added to PDMS here.**

### 2.5.3 SFG Experimental Results on $d_4$ -PET and Silane or Silane-MVS Mixture Interfaces

SFG spectra collected from various  $d_4$ -PET/silane and  $d_4$ -PET/silane:MVS mixture interfaces are shown in Figure 2-24. At the  $d_4$ -PET/ $\gamma$ -GPES interface, three peaks can be resolved at 2865, 2925 and 2975  $\text{cm}^{-1}$ , which can be assigned to the methylene symmetric and asymmetric C-H stretches, and the methyl (in ethoxy group) asymmetric C-H stretch, respectively. The peak at 2925  $\text{cm}^{-1}$  may also have some contribution from the silane methyl Fermi resonance. However, since the peak center is slightly lower and no methyl symmetric stretching signal can be observed, it is more likely that this peak is only or mainly contributed from the methylene asymmetric stretch. This indicates that both methylene and methyl groups in the silane molecule exhibit some order at the interface. At the  $d_4$ -PET/ $\gamma$ -GPES:MVS mixture interface, the Fermi resonance signal intensity from the methyl group (in the silane ethoxy headgroup) increased greatly at 2935  $\text{cm}^{-1}$ . In addition to the asymmetric methyl stretching signal at 2972  $\text{cm}^{-1}$ , another peak at around 2894  $\text{cm}^{-1}$  was also observed and assigned to the methyl (in ethoxy) symmetric C-H stretch in silane. These results

show that without MVS, silane headgroup tends to adopt some order at the  $d_4$ -PET interface. The stronger asymmetric C-H stretching signal indicates that the methyl groups in the ethoxy headgroup tilt more towards the surface.<sup>38</sup> The addition of MVS into the silane enhanced the ordering of silane methyl group (in the ethoxy headgroup) at the interface. The strong symmetric/Fermi resonance signals indicate that after the addition of MVS, the methyl groups in ethoxy groups tend to stand up more at the interface.<sup>38</sup>

In the SFG spectrum collected from the  $d_4$ -PET/ $\gamma$ -GPDES interface, methyl group signal at 2890, 2935 and 2975  $\text{cm}^{-1}$  can also be detected. This shows that the silane headgroup adopts some order at the interface. After the addition of MVS to the silane, similar spectral features can be detected with stronger intensity.  $\gamma$ -GPDES has only two ethoxy headgroups, the methyl (in the ethoxy headgroup) symmetric stretch is weaker as compared to  $\gamma$ -GPES which has three ethoxy headgroups.

In the SFG spectrum collected from the  $d_4$ -PET/ $\gamma$ -GPDMEs interface, the broad peak between 2900 and 2960  $\text{cm}^{-1}$  should be contributed from the C-H stretching signals from the methyl headgroup ( $\text{Si-CH}_3$ ) and ethoxy head groups ( $\text{Si-OCH}_2\text{CH}_3$ ) of  $\gamma$ -GPDMEs. After adding MVS to the silane, SFG spectrum collected from the  $d_4$ -PET/ $\gamma$ -GPDMEs:MVS mixture interface shows three weak peaks, which is quite similar to the spectrum detected from the interface between pure MVS and  $d_4$ -PET.<sup>70</sup> The addition of MVS tends to decrease the coverage and/or order of  $\gamma$ -GPDMEs silane headgroups at the PET interface.

These results show that MVS has different effects on the interactions between different silanes and  $d_4$ -PET. The addition of MVS increases the headgroup order at the  $d_4$ -PET/silane interfaces for  $\gamma$ -GPES and  $\gamma$ -GPDES silanes, but decreases the methyl headgroup order at the  $\gamma$ -GPDMEs/ $d_4$ -PET interface. To better understand the impact of silane and MVS on adhesion



promoting, it is necessary to incorporate them to PDMS and study the structures at the PDMS/ $d_4$ -PET interfaces.

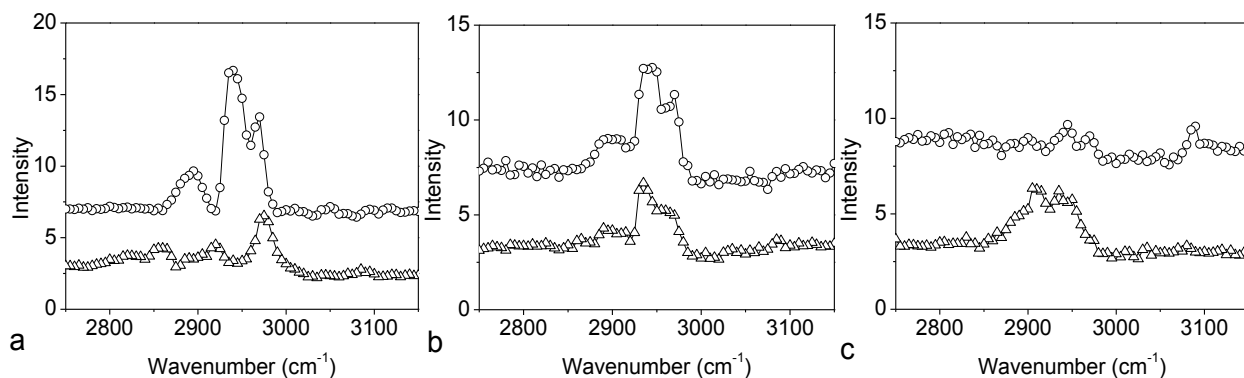


**Figure 2-24.** SFG ssp spectra of (a)  $d_4$ -PET/ $\gamma$ -GPES (bottom) and  $d_4$ -PET/ $\gamma$ -GPES:MVS mixture interfaces (top) (b)  $d_4$ -PET/ $\gamma$ -GPDES (bottom) and  $d_4$ -PET/ $\gamma$ -GPDES:MVS mixture interfaces (top) (c)  $d_4$ -PET/ $\gamma$ -GPDMES (bottom) and  $d_4$ -PET/ $\gamma$ -GPDMES:MVS mixture interfaces (top).

#### 2.5.4 Silane Incorporated into PDMS

It was shown in the previous section that at  $d_4$ -PET/uncured PDMS interface, only two weak peaks from Si-CH<sub>3</sub> symmetric and asymmetric modes at 2900 and 2960 cm<sup>-1</sup> can be observed.<sup>70</sup> Here, SFG spectra were collected from  $d_4$ -PET/uncured PDMS interfaces when silane and silane:MVS mixtures were incorporated into PDMS. In order to quantitatively compare the silane ordering at interfaces, all SFG spectra shown in Figure 2-25 were fit using equation (1.2). The detailed fitting parameters are listed in Table 2-8.

At the  $d_4$ -PET/uncured PDMS  $\gamma$ -GPES mixture interface (Figure 2-25a), strong peaks at 2893, 2930, and 2965 cm<sup>-1</sup> were detected, which can be assigned to the C-H symmetric stretching, Fermi resonance, and asymmetric stretching of methyl groups in ethoxy headgroups. The peak at 2893 and 2965 cm<sup>-1</sup> may also have contribution from the methyl symmetric (at 2900 cm<sup>-1</sup>) and asymmetric (at 2960 cm<sup>-1</sup>) stretching signal of Si-CH<sub>3</sub> in PDMS. Compared to the  $d_4$ -PET/ $\gamma$ -GPES

interface, the stronger SFG signals (especially the Fermi resonance signal which does not contain possible contributions from PDMS) indicated that uncured PDMS induced silane headgroups to be more ordered at the interface. SFG spectrum was also collected from the *d*<sub>4</sub>-PET/uncured PDMS  $\gamma$ -GPES:MVS mixture interface (Figure 2-25a). In this spectrum, the 2898 cm<sup>-1</sup> signal could be assigned to the contribution from Si-CH<sub>3</sub> in PDMS and/or MVS. It might also have small contribution from the ethoxy methyl groups. Compared to the spectrum detected from the *d*<sub>4</sub>-PET/uncured PDMS  $\gamma$ -GPES mixture interface, this symmetric C-H stretching contribution increased (signal strength from 1.52 to 2.31). However, both Fermi resonance and asymmetric C-H stretching peaks became weaker (signal strength from 1.85 and 1.33 to 1.04 and 0.51). Since the increased signal is not mainly contributed from the ethoxy methyl groups, but the decreased signals are mainly generated from the ethoxy methyl groups, we believe that the presence of MVS reduces  $\gamma$ -GPES ethoxy headgroup ordering at *d*<sub>4</sub>-PET/uncured PDMS interface.

At the *d*<sub>4</sub>-PET/uncured PDMS  $\gamma$ -GPDES mixture interface (Figure 2-25b), three peaks of the methyl group can also be detected at 2892, 2931 and 2964 cm<sup>-1</sup>, from ethoxy headgroups. The 2892 and 2964 cm<sup>-1</sup> signal may also contain contribution from the PDMS Si-CH<sub>3</sub> symmetric and asymmetric stretching. The 2931 cm<sup>-1</sup> Fermi resonance signal is clearly weaker compared to the *d*<sub>4</sub>-PET/uncured PDMS  $\gamma$ -GPES interface case (signal strength of 0.90 compared to 1.85). After the addition of MVS to the system, SFG spectrum at the interface (Figure 2-25b) shows only a strong peak at 2898 cm<sup>-1</sup> (signal strength 2.17), which could be mainly from Si-CH<sub>3</sub> in PDMS or MVS. As the *d*<sub>4</sub>-PET/uncured PDMS with  $\gamma$ -GPES interface discussed above, here the addition of MVS reduces the ethoxy group interfacial segregation/ordering.

SFG spectrum collected from the *d*<sub>4</sub>-PET/uncured PDMS  $\gamma$ -GPDMS mixture interface (Figure 2-25c) has two major peaks at 2893 and 2960 cm<sup>-1</sup>, due to the C-H symmetric and

asymmetric stretching signals of the methyl groups in the ethoxy headgroups. They may also contain some small contributions of the PDMS Si-CH<sub>3</sub> symmetric and asymmetric stretching. This is different from the spectrum detected from the *d*<sub>4</sub>-PET/ $\gamma$ -GPDMS interface, indicating that the uncured PDMS influences the interfacial structure of  $\gamma$ -GPDMS. After the addition of MVS to the mixture (Figure 2-25c), SFG spectrum at the interface has a strong peak at 2898 cm<sup>-1</sup> (signal strength 2.13), which may be due to the Si-CH<sub>3</sub> group in MVS and PDMS.

In all the spectra shown in Figure 2-25, the C-H stretching signal from the phenyl ring in *d*<sub>4</sub>-PET can be seen (~3100 cm<sup>-1</sup>). Since the peak at ~2890 and ~2960 cm<sup>-1</sup> may have some contribution from PDMS and MVS, it is difficult to quantitatively compare such peaks in Table 2-8. However, silane headgroup ordering can be compared using the Fermi resonance peak at ~2930 cm<sup>-1</sup>, which can only be contributed from the ethoxy methyl group. The spectral fitting results for the peak ~2930 cm<sup>-1</sup> shown in Table 2-8 demonstrate that the ethoxy headgroups in the ethoxy silane tend to order at the interfaces between *d*<sub>4</sub>-PET and uncured PDMS. The addition of MVS greatly reduced interfacial segregation/order of these ethoxy headgroups at the *d*<sub>4</sub>-PET/uncured PDMS interfaces. The results indicate clearly that PDMS can affect the interfacial structures of silanes and silane:MVS mixtures. MVS also has different effects on silane adhesion promoters at *d*<sub>4</sub>-PET/PDMS interfaces. It tends to decrease the silane ethoxy headgroup ordering at such interfaces, which may be due to some interfacial chemical reaction or entanglement.

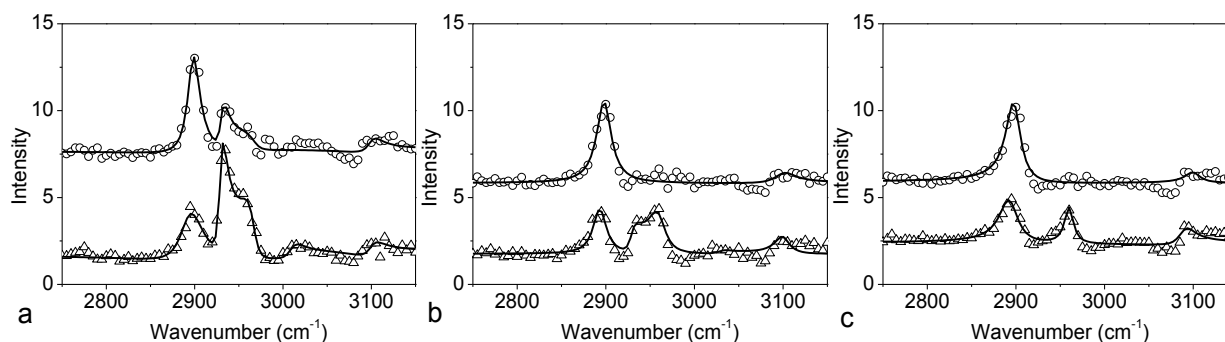


**Figure 2-25.** SFG spectra of (a)  $\gamma$ -GPES (bottom) and  $\gamma$ -GPES:MVS (top) (b)  $\gamma$ -GPDES (bottom) and  $\gamma$ -GPDES:MVS (top) (c)  $\gamma$ -GPDMES (bottom) and  $\gamma$ -GPDMES:MVS (top) at  $d_4$ -PET/uncured PDMS interfaces under ssp polarization combination. The dots are experimental data and the lines are fitting results.

Material (uncured)	$\omega_q$ (cm <sup>-1</sup> )	$A_{q,ssp}$	$\Gamma_q$ (cm <sup>-1</sup> )	$ A_{q,ssp} / \Gamma_q $	Assignment
$\gamma$ -GPES	2893	23.5±1.0	15.5±0.9	1.52±0.11	-CH <sub>3</sub> (s)
	2930	10.0±0.6	5.4±0.4	1.85±0.18	-CH <sub>3</sub> (s) Fermi
	2965	-13.0±0.7	9.8±0.4	1.33±0.09	-CH <sub>3</sub> (as)
$\gamma$ -GPESMVS	2898	19.6±1.0	8.5±0.5	2.31±0.18	-CH <sub>3</sub> (s)
	2931	5.7±0.5	5.5±0.4	1.04±0.12	-CH <sub>3</sub> (s) Fermi
	2966	-6.5±0.4	12.8±1.0	0.51±0.05	-CH <sub>3</sub> (as)
$\gamma$ -GPDES	2893	14.5±1.5	9.0±1.2	1.61±0.27	-CH <sub>3</sub> (s)
	2931	7.0±1.0	7.8±0.7	0.90±0.15	-CH <sub>3</sub> (s) Fermi
	2964	-18.4±0.9	11.8±0.5	1.56±0.10	-CH <sub>3</sub> (as)
$\gamma$ -GPDESMVS	2898	21.7±1.2	10.0±0.7	2.17±0.19	-CH <sub>3</sub> (s)
$\gamma$ -GPDMES	2893	20.5±1.7	12.8±1.3	1.60±0.21	-CH <sub>3</sub> (s)
	2960	-9.0±0.8	6.0±0.3	1.50±0.15	-CH <sub>3</sub> (as)
$\gamma$ -GPDMESMVS	2898	21.7±1.6	10.2±0.9	2.13±0.24	-CH <sub>3</sub> (s)

**Table 2-8.** Fitting results of Figure 2-25.

SFG was also used to study on interfaces of  $d_4$ -PET/cured PDMS mixed with silanes or silane:MVS mixtures. SFG spectra were collected from the  $d_4$ -PET/cured PDMS mixed with silane or silane:MVS mixture interfaces and were fit (Figure 2-26). The detailed fitting parameters are listed in Table 2-9. SFG spectrum collected from the  $d_4$ -PET/PDMS  $\gamma$ -GPES mixture interface after curing (Figure 2-26a) shows a very strong methyl headgroup Fermi resonance peak at 2930 cm<sup>-1</sup> (signal strength 4.68). Weak peak at 2890 cm<sup>-1</sup> was also observed (signal strength 1.31),

attribute to the symmetric C-H stretches of methyl group (in ethoxy headgroup) and possibly methyl groups in PDMS. The methyl asymmetric stretch exhibits a shoulder at  $2965\text{ cm}^{-1}$  in the spectrum. This indicates that methyl groups in ethoxy headgroups are quite ordered at the interface. After the addition of MVS to the system, SFG spectrum collected from the  $d_4$ -PET/cured PDMS  $\gamma$ -GPES:MVS mixture interface (Figure 2-26a) showed that the intensity of the peak at  $2930\text{ cm}^{-1}$  decreased (signal strength from 4.68 to 2.55). Therefore, the addition of MVS changed the silane headgroups at the cured PDMS interfaces and decreased silane headgroup orders.

The SFG spectrum collected from the  $d_4$ -PET/cured PDMS  $\gamma$ -GPDES mixture interface (Figure 2-26b) has three methyl peaks at 2890, 2930, and  $2964\text{ cm}^{-1}$ , from ethoxy headgroups. Peaks at 2890 and  $2964\text{ cm}^{-1}$  may also have contribution from PDMS methyl group. At this interface, silane headgroups also show some order at the interfaces similar to the  $\gamma$ -GPES case discussed above. After the addition of MVS to the mixture (Figure 2-26b), the SFG spectrum has similar features, but signal strengths are different (signal strengths changed from 0.91, 2.53, 2.24 to 1.42, 1.42, 1.61 respectively). Compared to the  $\gamma$ -GPES case, the SFG signal intensities are weaker. Silane headgroup order decrease after adding MVS was still observed by comparing peaks at  $2930\text{ cm}^{-1}$ .

At the  $d_4$ -PET/cured PDMS  $\gamma$ -GPDMS mixture interface after curing (Figure 2-26c), three methyl peaks in ethoxy headgroups were also detected. PDMS may also contribute to methyl symmetric and asymmetric signals at 2890 and  $2964\text{ cm}^{-1}$ . Silane headgroups also have some order at the interfaces similar to the other two cases. After the addition of MVS to the mixture (Figure 2-26c), the SFG spectrum has similar features, but signals change intensities (from 0.32, 1.58, 1.80 to 1.21, 0.82, 1.39), similar to other two cases. Comparing  $2930\text{ cm}^{-1}$  Fermi resonance peak from methyl headgroup, MVS also decreased the order of methyl functional groups at the  $d_4$ -PET/cured

PDMS  $\gamma$ -GPDMES mixture interfaces, but such a change is smaller compared to the other two cases.

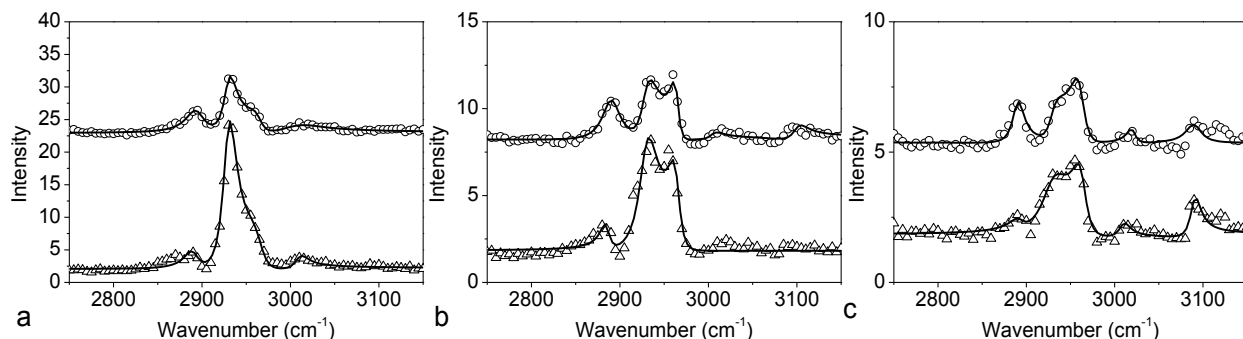


**Figure 2-26. SFG spectra of (a)  $\gamma$ -GPES (bottom) and  $\gamma$ -GPES:MVS (top) (b)  $\gamma$ -GPDES (bottom) and  $\gamma$ -GPDES:MVS (top) (c)  $\gamma$ -GPDMES (bottom) and  $\gamma$ -GPDMES:MVS (top) at  $d_4$ -PET/cured PDMS interfaces under ssp polarization combination. The dots are experimental data and the lines are fitting results.**

Material (cured)	$\omega_q$ (cm <sup>-1</sup> )	$ A_{q,ssp} $	$\Gamma_q$ (cm <sup>-1</sup> )	$ A_{q,ssp} / \Gamma_q $	Assignment
$\gamma$ -GPES	2890	13.2±1.2	10.1±1.0	1.31±0.18	-CH <sub>3</sub> (s)
	2930	44.9±0.9	9.6±0.2	4.68±0.14	-CH <sub>3</sub> (Fermi)
	2965	-26.0±1.0	12.8±0.7	2.03±0.14	-CH <sub>3</sub> (as)
	3010	12.9±1.8	9.4±2.0	1.37±0.35	-epoxy
$\gamma$ -GPESMVS	2893	21.0±1.9	13.1±1.2	1.60±0.21	-CH <sub>3</sub> (s)
	2930	23.7±1.0	9.3±0.4	2.55±0.15	-CH <sub>3</sub> (Fermi)
	2964	-20.3±1.3	10.1±0.5	2.01±0.16	-CH <sub>3</sub> (as)
	3005	31.6±3.0	29.9±3.5	1.06±0.16	-epoxy
$\gamma$ -GPDES	2885	5.8±0.9	6.4±1.2	0.91±0.22	-CH <sub>3</sub> (s)
	2930	32.7±1.6	12.9±0.8	2.53±0.20	-CH <sub>3</sub> (Fermi)
	2964	-17.9±1.2	8.0±0.2	2.24±0.16	-CH <sub>3</sub> (as)
$\gamma$ -GPDESMVS	2890	17.9±1.5	12.6±1.3	1.42±0.19	-CH <sub>3</sub> (s)
	2930	15.3±1.7	10.8±1.1	1.42±0.21	-CH <sub>3</sub> (Fermi)
	2964	-9.0±0.8	5.6±0.3	1.61±0.17	-CH <sub>3</sub> (as)
$\gamma$ -GPDMES	3005	3.7±1.5	8.5±5.0	0.44±0.31	-epoxy
	2893	3.1±0.8	9.8±2.0	0.32±0.10	-CH <sub>3</sub> (s)
	2930	29.3±1.4	18.6±1.0	1.58±0.11	-CH <sub>3</sub> (Fermi)
	2963	-17.6±0.9	9.8±0.3	1.80±0.11	-CH <sub>3</sub> (as)
$\gamma$ -GPDMESMVS	3010	-5.4±0.2	8.0±0.4	0.68±0.04	-epoxy
	2890	9.8±1.1	8.1±1.1	1.21±0.21	-CH <sub>3</sub> (s)
	2930	8.9±1.0	10.8±1.2	0.82±0.13	-CH <sub>3</sub> (Fermi)
	2961	-13.1±1.2	9.4±0.4	1.39±0.14	-CH <sub>3</sub> (as)
	3010	-3.9±0.6	6.0±1.1	0.65±0.16	-epoxy

**Table 2-9. Fitting results of Figure 2-26.**

## 2.5.5 The Relation between Interfacial Molecular Ordering and Adhesion

For comparison purpose, Table 2-10 summarizes the fitting results of the SFG signals contributed by the symmetric methyl stretching, Fermi resonance, and the asymmetric methyl stretching, as well as the sum of all the above three SFG signals detected from the uncured and cured samples. As discussed above, the methyl group Fermi resonance signal at  $2930\text{ cm}^{-1}$  does not have contributions from PDMS and MVS. Therefore, in order to quantitatively compare silane methyl headgroup ordering at different interfaces, we will compare Fermi resonance signals for all the cases. By using the detailed data analysis, we hope to understand the effects of the curing process and the addition of MVS on adhesion. To correlate SFG results to adhesion data, we list the signal strength differences of the Fermi resonance peaks and the adhesion testing data in Table 2-11.

	Symmetric(s)	Fermi(F)	Asymmetric(as)	(s)+(F)+(as)
$\gamma$ -GPES (uncured)	1.52±0.11	1.85±0.18	1.33±0.09	4.70±0.23
$\gamma$ -GPES (cured)	1.31±0.18	4.68±0.14	2.03±0.14	8.02±0.27
$\gamma$ -GPESMVS (uncured)	2.31±0.18	1.04±0.12	0.51±0.05	3.86±0.22
$\gamma$ -GPESMVS(cured)	1.60±0.21	2.55±0.15	2.01±0.16	6.16±0.30
$\gamma$ -GPDES (uncured)	1.61±0.27	0.90±0.15	1.56±0.10	4.07±0.32
$\gamma$ -GPDES (cured)	0.91±0.22	2.53±0.20	2.24±0.16	5.68±0.34
$\gamma$ -GPDESMVS (uncured)	2.17±0.19			2.17±0.19
$\gamma$ -GPDESMVS (cured)	1.42±0.19	1.42±0.21	1.61±0.17	4.45±0.33
$\gamma$ -GPDMS (uncured)	1.60±0.21		1.50±0.15	3.10±0.26
$\gamma$ -GPDMS (cured)	0.32±0.10	1.58±0.11	1.80±0.11	3.70±0.18
$\gamma$ -GPDMSMVS (uncured)	2.13±0.24			2.13±0.24
$\gamma$ -GPDMSVMS (cured)	1.21±0.21	0.82±0.13	1.39±0.14	3.42±0.28

**Table 2-10. Fitting result summary from Tables 2-8 and 2-9.**

Variable	Silanes	Signal strength difference (Fermi resonance)	Adhesion strength
Curing (cured)-(uncured)	$\gamma$ -GPES	4.68-1.85=2.83	0.64±0.02MPa
	$\gamma$ -GPDES	2.53-0.90=1.63	0.39±0.02MPa
	$\gamma$ -GPDMES	1.58-0.00=1.58	0.24±0.05MPa
	$\gamma$ -GPES+MVS	2.55-1.04=1.51	1.21±0.15MPa
	$\gamma$ -GPDES+MVS	1.42-0.00=1.42	0.99±0.12MPa
	$\gamma$ -GPDMES+MVS	0.82-0.00=0.82	0.92±0.08MPa
MVS (without MVS)-(with MVS) after curing	$\gamma$ -GPES	4.68-2.55=2.13	1.21±0.15MPa
	$\gamma$ -GPDES	2.53-1.42=1.11	0.99±0.12MPa
	$\gamma$ -GPDMES	1.58-0.82=0.76	0.92±0.08MPa

**Table 2-11. Fermi resonance signal strength differences for silane headgroup methyl before and after curing PDMS, as well as with and without the addition of MVS. The related adhesion strengths are shown in the right column.**

Table 2-11 shows that the curing process tends to increase the silane methyl headgroup order at all the interfaces. If we only compare the results of the silane-PDMS mixtures without MVS, the SFG Fermi resonance signals from silane methyl headgroup of  $\gamma$ -GPES-PDMS mixture before and after curing exhibit the biggest intensity change. This SFG signal intensity change is 4.68-1.85=2.83. For the  $\gamma$ -GPDES-PDMS mixture sample before and after curing, the SFG intensity change is 2.53-0.90=1.63, which is smaller than the previous  $\gamma$ -GPES-PDMS mixture case. For the  $\gamma$ -GPDMES-PDMS mixture, the SFG Fermi resonance signal intensity (at 2930 cm<sup>-1</sup>) before curing is 0, after curing is 1.58. Therefore, the difference is 1.58-0=1.58, which is the smallest among all the three cases. If we characterize the interfacial methyl ordering using the SFG signal strength of the methyl Fermi resonance signal, we can see that the more ethoxy headgroup the silane has, the stronger order it tends to have at the PET/uncured PDMS and PET/cured PDMS interfaces. In addition, the above discussion shows that the increases of the methyl interfacial



ordering after curing PDMS follow the same trend. The adhesion results indicated that the  $\gamma$ -GPES-PDMS mixture tends to increase the adhesion of PDMS to PET, the  $\gamma$ -GPDES-PDMS mixture sample has similar adhesion as PDMS to PET, and the  $\gamma$ -GPDMEs-PDMS mixture has weaker adhesion to PET than PDMS alone. Therefore, we believe that the ethoxy silane methyl headgroup ordering at the interfaces between PDMS-silane mixture and PET is related to adhesion. The improved adhesion is associated with better headgroup ordering or/and ordering change.

The addition of small amount of MVS to the PDMS-silane mixtures greatly changed the molecular structures at the interfaces. SFG signals of the ethoxy methyl group at the PET/uncured PDMS interfaces decreased for all the three silane cases. However, after curing PDMS, the ethoxy methyl group signals for all the three samples increased comparing to before curing, similar to PDMS-silane mixture (without MVS) cases. After the curing process, the SFG methyl Fermi resonance signal strength change for the  $\gamma$ -GPES:MVS-PDMS mixture sample is  $2.55-1.04=1.51$ , which is the biggest among the three samples (with MVS). The change for the  $\gamma$ -GPDES:MVS-PDMS mixture sample is  $1.42-0=1.42$ , which is smaller than the previous case. For the  $\gamma$ -GPDMEs:MVS-PDMS mixture, the change is  $0.82-0=0.82$ , which is the smallest. The above observations are similar to those discussed previously before the introduction of MVS to the samples. Again, the results indicate that the more ethoxy headgroups the silane has, the more order ethoxy methyl group tends to have after curing, the larger ethoxy methyl ordering increase during the curing process.  $\gamma$ -GPES:MVS-PDMS mixture sample has the strongest adhesion to PET, which is stronger than the  $\gamma$ -GPDES:MVS-PDMS sample, which in turn is stronger than the  $\gamma$ -GPDMEs:MVS-PDMS mixture sample. Correlated to the SFG results, this again indicates that the silane headgroup ordering at the interfaces is related to adhesion. The better adhesion is also associated with better headgroup ordering or/and ordering change.

The curing process is a complicated chemical process that may involve multiple mechanisms. Although we find that the curing process can increase the order of silane methyl groups in ethoxy headgroup at the interfaces, it is still not clear if headgroup ordering at the interface directly resulted in good adhesion, or the ordering is essential for some other mechanisms that eventually lead to good adhesion. Furthermore, the above observation cannot explain why MVS can greatly improve PDMS adhesion to PET while the samples with the addition of MVS exhibit weaker silane headgroup order at the interfaces. According to our previous publication on methoxy silane adhesion promoter,<sup>70</sup> the strong adhesion is related to the chemical reaction involving the silane methoxy headgroups at the interface. Therefore, it is necessary for silane methoxy headgroups to segregate to and order at the interface between PET and PDMS to have the interfacial chemical reaction for strong adhesion. It is the interfacial chemical reaction that leads to the decrease of SFG signals generated from the silane methoxy headgroup, resulting in strong adhesion. Therefore, the larger decrease of the SFG signals from methoxy groups after curing PDMS lead to stronger adhesion. However, this was opposite to what we observed in this study.

In this study, we have not observed methyl (in ethoxy headgroup) signal decrease after curing. Instead, such signals were found to increase after curing for ethoxy silanes. First of all, we observed that methyl groups (in ethoxy headgroup) of silanes with more ethoxy headgroups tend to order more at the PET/PDMS interface compared to those of silanes with less ethoxy headgroups. The stronger ethoxy ordering very likely involves more headgroup reaction at the interface. Therefore, the silane ordering is essential for good interfacial adhesion but not directly results in strong adhesion, since the interfacial reaction (which leads to the ethoxy signal decrease) is directly related to interfacial adhesion. Here when silanes were incorporated with PDMS without MVS, all

samples showed headgroup ordering at the interface, but only  $\gamma$ -GPES improved the adhesion.  $\gamma$ -GPDES did not significantly improve adhesion although headgroups are ordered at the interface, while  $\gamma$ -GPDMS decreased the adhesion. Such results show that even though silane interfacial ordering provides headgroups needed for interfacial chemical reaction for strong adhesion, methyl ordering itself is not directly related to adhesion. With the addition of MVS into the system, methyl (in ethoxy group) signal decrease was not observed in this experiment. Instead, such signals increased for different systems with different increase amounts. This can be explained by different reactivity properties of ethoxysilanes and methoxysilanes. Curing can lead to more interfacial segregated silane headgroups, this will lead to SFG methyl signal increase. At the same time, curing can induce interfacial reactions involving silane headgroups, decreasing SFG methyl signals. These two effects may occur simultaneously in the curing process. For the methoxy silanes in previous study,<sup>70</sup> the silane headgroup reactivity is high and therefore the interfacial methoxy groups decreased in number, resulting in SFG headgroup signal decrease after curing. It was well known that ethoxy silanes reactivity is much less than methoxy silanes.<sup>10</sup> Accordingly, the interfacial reaction related headgroup signal decrease is less, resulting in total headgroup signal increase for ethoxysilanes compare to decrease for methoxysilanes. Less methyl SFG signal increase when MVS is coupled in the system indicates more chemical reactions involved, resulting in stronger adhesion.

Table 2-11 shows that with the addition of MVS to PDMS, the SFG methyl signal increase is smaller compared to the cases without MVS. Before and after curing, for the  $\gamma$ -GPES:MVS case, SFG signal strength change is  $2.55-1.04=1.51$ , which is smaller compared to the  $\gamma$ -GPES case, which is  $4.68-1.85=2.83$ . For the  $\gamma$ -GPDES:MVS case, SFG signal strength change is  $1.42-0=1.42$ , which is smaller compared to the  $\gamma$ -GPDES case:  $2.53-0.90=1.63$ . For the  $\gamma$ -GPDMS:MVS case,

the SFG signal change is  $0.82-0=0.82$ , which is also smaller compared to  $1.58-0=1.58$  for  $\gamma$ -GPDMS without the addition of MVS. Such a difference likely indicates that MVS may have further induced chemical reaction of silane headgroup at the PET/PDMS interface and provides improved adhesion strength. The adhesion results shown in Figure 2-23 indicate that  $\gamma$ -GPES:MVS mixture results in the strongest adhesion at the PET/PDMS interface, while  $\gamma$ -GPDES:MVS mixture is the second, and the  $\gamma$ -GPDMS:MVS mixture leads to the weakest adhesion. But overall all the three mixtures have stronger adhesion than PDMS itself or PDMS incorporated with silane alone. Considering all three samples with MVS, the bigger the difference in SFG headgroup signal before and after curing, the greater the adhesion the sample tends to have. The overall effect of MVS can also be compared only using the cured samples. Signal difference between  $\gamma$ -GPES and  $\gamma$ -GPES:MVS is  $4.68-2.55=2.13$ , between  $\gamma$ -GPDES and  $\gamma$ -GPDES:MVS is  $2.53-1.42=1.11$ , and between  $\gamma$ -GPDMS and  $\gamma$ -GPDMS:MVS is  $1.58-0.82=0.76$ . It was shown that only consider the presence and absence of MVS, the bigger signal difference also indicates the stronger the adhesion strength.

In the above discussion, we only considered the silane headgroup methyl Fermi resonance signal at  $2930\text{ cm}^{-1}$ . This can avoid the possible complication caused by the symmetric and asymmetric C-H stretching signals contributed from Si-CH<sub>3</sub> groups in PDMS and MVS at  $\sim 2900$  and  $\sim 2960\text{ cm}^{-1}$ . However, even if we take all three peaks into consideration, as shown in Table 2-10 (s)+(F)+(as), similar results can also be obtained. This indicates that possibly the contributions of PDMS and MVS are small or are similar for different samples.

The above discussion indicates that ethoxy-silane headgroups tend to order at the interface between PET and PDMS, which is a key factor for the adhesion. Silane headgroups can be involved in adhesion at the PET/PDMS interface similar to that at the silica/PDMS interface. Interfacial

chemical reaction and entanglement that decrease the interfacial headgroup ordering (leading to the SFG signal decrease of the headgroups) can provide strong adhesion.

### **2.5.6 Conclusion**

In this work we focused on the study of environmental friendly ethoxy-silanes. We compared three ethoxy-silanes:  $\gamma$ -GPES,  $\gamma$ -GPDES,  $\gamma$ -GPDMS and these silane MVS 1:1 mixtures at the interfaces between silane or silane:MVS and PET, between uncured PDMS and PET and between cured PDMS and PET. We find that different silanes tend to have different interfacial structures at the interfaces with PET. MVS can change the interfacial molecular interactions of silanes. We also find that addition of small amount of silane to PDMS can alter the interfacial molecular structures between PDMS and PET. The results show that silane headgroup order plays an important role in adhesion. The decrease of SFG headgroup signal indicates chemical reaction and disordering of such groups at the interfaces, which is related to improved adhesion. MVS tends to decrease the order of methyl group at the interfaces, which lead to much stronger adhesion. Together with previous publications, we demonstrated that silane headgroups greatly impact interfacial adhesion between PET and silicone elastomer.

### **2.6 Overall Summary**

Because of the wide applications of silicone adhesives, it is important to study adhesion mechanisms of silicone elastomers to polymers. Adhesion properties are believed to be directly related to the molecular structures at the adhesive/substrate interfaces. In this research, SFG vibrational spectroscopy has been used to investigate interfacial molecular structures between PDMS materials and various substrates.

We first deduced the molecular orientations of PDMS methyl groups at PDMS/PET and PDMS/silica interfaces. Absolute molecular orientations could also be obtained using the signal

interference patterns from PDMS methyl interfacial signal and the nonresonant signal generated by a TiO<sub>2</sub> film. The interfacial molecular orientations could be correlated to the substrate surface hydrophobicities.

Silane adhesion promoters are widely used to enhance PDMS adhesion to various substrates. In this work we investigated the methoxy-silane and ethoxy-silane molecular behaviors at PDMS/PET interfaces. We found that silane methoxy or ethoxy headgroups tend to order at such interfaces and were likely involved in some interfacial chemical reactions or interfacial entanglements, which promote the adhesion strength.

We developed SFG into a powerful, non-destructive tool to study the molecular mechanisms of silicone adhesion with polymer materials. The molecular level understanding on polymer/adhesive interfacial structures helps to design and develop adhesion promoters and polymer adhesives with improved performance.

## 2.7 References

1. Kinloch, A. J., *Adhesion and adhesives : science and technology*. Chapman and Hall: London, U.K. ; New York, U.S., 1987; p x, 441 p.
2. Yacobi, B. G.; Martin, S.; Davis, K.; Hudson, A.; Hubert, M., *J. Appl. Phys.* **2002**, *91*, 6227-6262.
3. Mittal, K. L., *Polymer surface modification: relevance to adhesion*. VSP: 2004.
4. Yacobi, B. G.; Martin, S.; Davis, K.; Hudson, A.; Hubert, M., *J. Appl. Phys.* **2002**, *91*, 6227-6262.
5. Mine, K.; Nishio, M.; Sumimura, S. Heat curable organopolysiloxane compositions containing adhesion additives. U.S. Patent 4033924, Jul 5, 1977.
6. Schulz, J. R. Self-adhering silicone compositions and preparations thereof. U.S. Patent 4087585, May 2, 1978.
7. Mittal, K. L., *Pure Appl. Chem.* **1980**, *52*, 1295-1305.
8. Plueddemann, E. P., *Silane coupling agents*. Springer: 1982.
9. Sathyanarayana, M. N.; Yaseen, M., *Prog. Org. Coat.* **1995**, *26*, 275-313.
10. Hermanson, G. T., *Bioconjugate techniques*. Academic press: 1996.
11. Gray, T. E.; Lutz, M. A. Curable organopolysiloxane compositions with improved adhesion. U.S. Patent 5595826, Jan 21, 1997.
12. Feresenbet, E.; Raghavan, D.; Holmes, G. A., *J. Adhesion* **2003**, *79*, 643-665.
13. Brown, H. R., *Science* **1994**, *263*, 1411-1413.
14. Dai, C. A.; Dair, B. J.; Dai, K. H.; Ober, C. K.; Kramer, E. J.; Hui, C. Y.; Jelinski, L. W., *Phys. Rev. Lett.* **1994**, *73*, 2472-2475.
15. Edgcombe, B. D.; Stein, J. A.; Fréchet, J. M. J.; Xu, Z.; Kramer, E. J., *Macromolecules* **1998**, *31*, 1292-1304.
16. Schulze, J. S.; Moon, B.; Lodge, T. P.; Macosko, C. W., *Macromolecules* **2001**, *34*, 200-205.
17. Shen, Y. R., *The principles of nonlinear optics*. J. Wiley: New York, 1984; p xii, 563 p.
18. Shen, Y. R., *Nature* **1989**, *337*, 519-525.
19. Zhuang, X.; Miranda, P.; Kim, D.; Shen, Y. R., *Phys. Rev. B* **1999**, *59*, 12632-12640.
20. Chen, Z.; Shen, Y. R.; Somorjai, G. A., *Annu. Rev. Phys. Chem.* **2002**, *53*, 437-465.
21. Chen, C. Y.; Wang, J.; Even, M. A.; Chen, Z., *Macromolecules* **2002**, *35*, 8093-8097.
22. Loch, C. L.; Ahn, D.; Chen, C.; Chen, Z., *J. Adhesion* **2005**, *81*, 319-345.
23. Kweskin, S. J.; Komvopoulos, K.; Somorjai, G. A., *Langmuir* **2005**, *21*, 3647-3652.
24. Moad, A. J.; Simpson, G. J., *J. Phys. Chem. A* **2005**, *109*, 1316-1323.
25. Chen, Z., *Polym. Int.* **2007**, *56*, 577-587.
26. Fourkas, J. T.; Walker, R. A.; Can, S. Z.; Gershgoren, E., *J. Phys. Chem. C* **2007**, *111*, 8902-8915.
27. Buch, V.; Tarbuck, T.; Richmond, G. L.; Groenzin, H.; Li, I.; Shultz, M. J., *J. Chem. Phys.* **2007**, *127*, 204710.
28. Lu, X. L.; Shephard, N.; Han, J. L.; Xue, G.; Chen, Z., *Macromolecules* **2008**, *41*, 8770-8777.
29. Baldelli, S., *Acc. Chem. Res.* **2008**, *41*, 421-431.
30. Sovago, M.; Vartiainen, E.; Bonn, M., *J. Chem. Phys.* **2009**, *131*, 161107.
31. Geiger, F. M., *Annu. Rev. Phys. Chem.* **2009**, *60*, 61-83.
32. Chen, Z., *Prog. Polym. Sci.* **2010**, *35*, 1376-1402.

33. Lu, X. L.; Clarke, M. L.; Li, D. W.; Wang, X. P.; Xue, G.; Chen, Z., *J. Phys. Chem. C* **2011**, *115*, 13759-13767.
34. Zhang, C.; Shephard, N. E.; Rhodes, S. M.; Chen, Z., *Langmuir* **2012**, *28*, 6052-6059.
35. Hirose, C.; Akamatsu, N.; Domen, K., *Appl. Spectrosc.* **1992**, *46*, 1051-1072.
36. Hirose, C.; Akamatsu, N.; Domen, K., *J. Chem. Phys.* **1992**, *96*, 997-1004.
37. Gautam, K. S.; Schwab, A. D.; Dhinojwala, A.; Zhang, D.; Dougal, S. M.; Yeganeh, M. S., *Phys. Rev. Lett.* **2000**, *85*, 3854-3857.
38. Wang, J.; Chen, C.; Buck, S. M.; Chen, Z., *J. Phys. Chem. B* **2001**, *105*, 12118-12125.
39. Wang, J.; Lee, S. H.; Chen, Z., *J. Phys. Chem. B* **2008**, *112*, 2281-2290.
40. Zhang, D.; Ward, R. S.; Shen, Y. R.; Somorjai, G. A., *J. Phys. Chem. B* **1997**, *101*, 9060-9064.
41. Chen, C.; Wang, J.; Chen, Z., *Langmuir* **2004**, *20*, 10186-10193.
42. Yurdumakan, B.; Nanjundiah, K.; Dhinojwala, A., *J. Phys. Chem. C* **2007**, *111*, 960-965.
43. Yurdumakan, B.; Harp, G. P.; Tsige, M.; Dhinojwala, A., *Langmuir* **2005**, *21*, 10316-10319.
44. Ye, H.; Gu, Z.; Gracias, D. H., *Langmuir* **2006**, *22*, 1863-1868.
45. Kim, C.; Gurau, M. C.; Cremer, P. S.; Yu, H., *Langmuir* **2008**, *24*, 10155-10160.
46. Ye, S.; McClelland, A.; Majumdar, P.; Stafslie, S. J.; Daniels, J.; Chisholm, B.; Chen, Z., *Langmuir* **2008**, *24*, 9686-9694.
47. Ye, S.; Majumdar, P.; Chisholm, B.; Stafslie, S.; Chen, Z., *Langmuir* **2010**, *26*, 16455-16462.
48. Shi, Q.; Ye, S.; Spanninga, S. A.; Su, Y.; Jiang, Z.; Chen, Z., *Soft Mat.* **2009**, *5*, 3487-3494.
49. Chen, C. Y.; Loch, C. L.; Wang, J.; Chen, Z., *J. Phys. Chem. B* **2003**, *107*, 10440-10445.
50. Loch, C. L.; Ahn, D.; Chen, Z., *J. Phys. Chem. B* **2006**, *110*, 914-918.
51. Loch, C. L.; Ahn, D.; Vazquez, A. V.; Chen, Z., *J. Colloid Interface Sci.* **2007**, *308*, 170-175.
52. Vazquez, A. V.; Shephard, N. E.; Steinecker, C. L.; Ahn, D.; Spanninga, S.; Chen, Z., *J. Colloid Interface Sci.* **2009**, *331*, 408-416.
53. Vázquez, A. V.; Boughton, A. P.; Shephard, N. E.; Rhodes, S. M.; Chen, Z., *Appl. Mater. Interfaces* **2010**, *2*, 96-103.
54. Zheng, P.; McCarthy, T. J., *Langmuir* **2010**, *26*, 18585-18590.
55. Kataoka, S.; Cremer, P. S., *J. Am. Chem. Soc.* **2006**, *128*, 5516-5522.
56. Harp, G. P.; Rangwalla, H.; Yeganeh, M. S.; Dhinojwala, A., *J. Am. Chem. Soc.* **2003**, *125*, 11283-11290.
57. Rao, A.; Rangwalla, H.; Varshney, V.; Dhinojwala, A., *Langmuir* **2004**, *20*, 7183-7188.
58. <http://refractiveindex.info/>.
59. Zhuang, X.; Miranda, P.; Kim, D.; Shen, Y., *Phys. Rev. B* **1999**, *59*, 12632-12640.
60. Mine, K.; Nishio, M.; Sumimura, S. Heat curable organopolysiloxane compositions containing adhesion additives. 4033924, July 5, 1977.
61. Schulz, J. R. Self-adhering silicone compositions and preparations thereof. May 2, 1978.
62. Loch, C. L.; Ahn, D.; Chen, Z., *J. Phys. Chem. B* **2006**, *110*, 914-918.
63. Vázquez, A. V.; Shephard, N. E.; Steinecker, C. L.; Ahn, D.; Spanninga, S.; Chen, Z., *J. Colloid Interface Sci.* **2009**, *331*, 408-416.
64. Xue, G.; Koenig, J. L.; Wheeler, D. D.; Ishida, H., *J. Appl. Polym. Sci.* **1983**, *28*, 2633-2646.
65. Chen, C.; Wang, J.; Chen, Z., *Langmuir* **2004**, *20*, 10186-10193.



66. Loch, C. L.; Ahn, D. C.; Vazquez, A. V.; Chen, Z., *Journal of Colloid and Interface Science* **2007**, *308*, 170-175.
67. Chen, C. Y.; Wang, J.; Loch, C. L.; Ahn, D.; Chen, Z., *Journal of the American Chemical Society* **2004**, *126*, 1174-1179.
68. Blumel, J., *J. Am. Chem. Soc.* **1995**, *117*, 2112-2113.
69. Witucki, G. L., *J. Coating. Technol.* **1993**, *65*, 57-60.
70. Zhang, C.; Shephard, N. E.; Rhodes, S. M.; Chen, Z., *Langmuir* **2012**, *28*, 6052-6059.

## CHAPTER 3

# MOLECULAR LEVEL UNDERSTANDING ON BURIED EPOXY ADHESIVE INTERFACES

### 3.1 Motivation

The microelectronic industry has advanced rapidly in the last several decades, especially with the invention of and continuous improvements on integrated circuits (IC). The use of flip-chip technology is crucial for the fast development of IC.<sup>1-2</sup> In flip-chip packing, the active side of IC is facing down and connected to the substrate by solder joints. In the early days of flip-chip technology, when IC chips were connected to ceramic substrates, thermal expansion mismatch was not a significant problem due to the small difference in thermal expansion coefficients (TEC) of substrate and die. Later when organic substrates such as polyimide (PI) and poly(ethylene terephthalate) (PET) were used as substrates, significant thermal stress was generated because of the TEC mismatch between the organic substrate and the silicon die.<sup>3</sup> This stress may lead to interfacial fatigue and delamination, causing failure of the device. Therefore, underfill materials were introduced to improve fatigue endurance.<sup>4</sup> In flip-chip technology, underfill resin is used to connect the IC to the substrate through solder joints. Underfill resin is usually dispensed after soldering a chip directly onto the printed circuit board (PCB).<sup>4</sup> After the underfilling, the assembly is heated to cure the underfill resin. The underfill provides both thermo-mechanical and environmental protection of the flip-chip assembly, and makes it stiffer. Therefore, the success of flip-chip technology highly relies on the performance of the underfill materials. Underfill materials are required to possess beneficial characteristics such as good adhesion, high glass transition

temperature, and good modulus. Bisphenol-type epoxy resins are most widely used underfill materials<sup>5</sup> while silane molecules are often used in the formulations as adhesion promoters.<sup>6-7</sup>

The delamination between die and underfill or between substrate and underfill may lead to cracking of the interconnection, or moisture diffusion through the delaminated area, resulting in the failure of the device.<sup>8-9</sup> Therefore, underfill adhesion is important for the reliability of the flip-chip assembly, which has been extensively studied. However, almost all the experimental studies up to date focused on a macroscopic understanding and have not examined molecular structures of the buried interfaces involving underfill materials *in situ*. Similarly, most simulations only lead to macroscopic understanding of these interfaces.

Adhesion is a complex and multidisciplinary subject.<sup>7, 10-13</sup> In addition to the bulk contributions from the viscoelastic properties of the adhesive, which will be maintained more or less constant in our studies, there exist a number of mechanisms that may contribute to adhesion including interfacial segregation and alignment, interfacial hydrogen and chemical bonding, interfacial diffusion, electrostatic attraction, and mechanical interlocking.<sup>14</sup> As the added silanes in this study have a relatively small impact on the bulk properties at the concentrations used (~1.5%), it is reasonable to expect that adhesion promotion is primarily through interface modification. For interfaces with strong adhesion, it is likely that some strong interactions are operative, perhaps in concert with inter-diffusion of certain species.

Adhesion mechanisms largely depend on the molecular interfacial structures and molecular interfacial interactions. Unfortunately, it is very challenging to investigate molecular structures of interfaces due to the lack of appropriate analytical techniques. It is also difficult to investigate buried interfaces *in situ*. The traditional way to examine a buried interface is to break the interface and examine the two resulting surfaces to extrapolate the molecular structure at the originally

buried interface. But such a process may destroy the original interfacial structure especially for the interfaces with good adhesion. Therefore, a technique which can study buried interfaces *in situ* at the molecular level is needed.

SFG vibrational spectroscopy has been applied to study surfaces and buried interfaces at the molecular level *in situ*.<sup>15-27</sup> As shown in the previous chapter, SFG has been used to examine buried interfaces between polymers and PDMS adhesives. The goal of this work is to use SFG as an analytical tool to investigate buried interfaces between epoxy (or epoxy-silane mixture) materials used in packaging and polymers. More specially, we want to understand the interfacial molecular structures of epoxy materials and their relation to adhesion. We will perform the study on model epoxies such as bisphenol-A diglycidyl ether (BADGE) and we will also investigate commercial epoxies. For the substrate, we are particularly interested in PET, since it is widely used as substrate for electronic devices. Adhesion testing experiments will be performed to measure the adhesion strengths between epoxies and polymers. The adhesion measurement data can be interpreted by the molecular structures of the buried interfaces deduced from the SFG results. This research is a fundamental step forward to understand the structure-function relationship at interfaces for packaging materials in microelectronic devices. The continuous success in such studies will ultimately lead to the design and development of underfills with improved performances.

### **3.2 Epoxy Curing Chemistry**

Epoxy resins (either pre-polymers with low molecular weight or polymers with higher molecular weight) usually have at least two epoxide groups in one molecule, which sometimes also referred to as glycidyl groups. Generally, they have poor mechanical properties and chemical resistance before curing. Epoxy curing process is a chemical reaction in which the epoxide groups

react with functional groups in the curing agent (hardener) to form a three dimensional crosslinking network which usually possessing good heat and chemical stability and good mechanical strength. Amines are most widely used curing agents for epoxy resins. A primary amine reacts with an epoxide group in epoxy through an addition reaction and produces a hydroxyl group and a secondary amine group. The secondary amine group can further react with an additional epoxy molecule in the system.<sup>28-29</sup> An example of epoxy curing process is shown in Figure 3-1. Although the details of the epoxy curing chemistry are well understood, the molecular adhesion mechanisms of epoxy-amine system to various other materials remain unclear. It is necessary to obtain in-depth understanding of adhesion mechanism at interfaces between substrate materials and epoxy-amine mixture because the failure at such interfaces (adhesive failure) is a general and problematic issue in electronic industry. Such interfacial studies can help to establish further insight in interfacial chemistry and can also potentially help to develop adhesives with better performance for many applications.

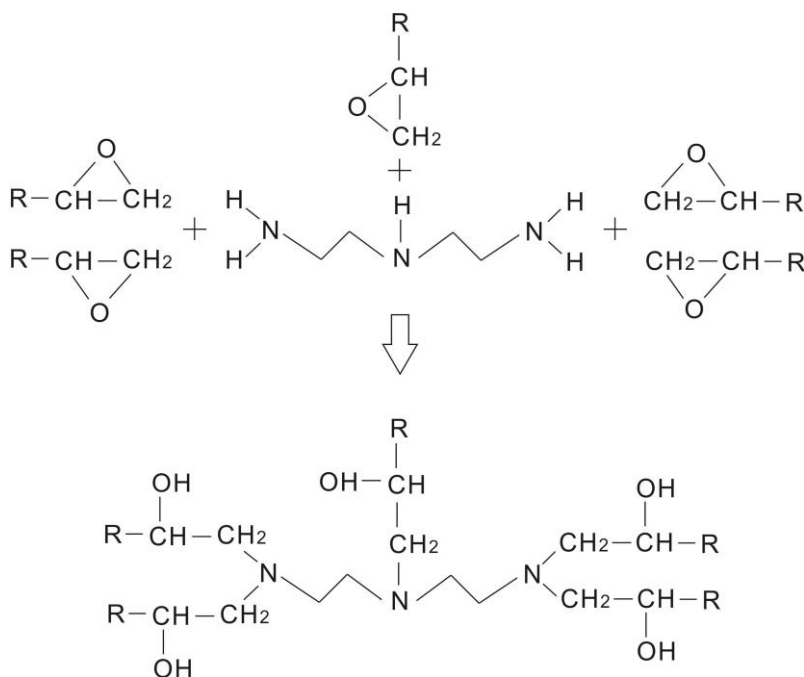


**Figure 3-1 Epoxy curing chemistry based on diethylenetriamine.**

### 3.3 Interfacial Molecular Ordering and Its Relation to Adhesion

#### 3.3.1 The Epoxy Systems and Sample Preparation

Fused silica right angle prisms were obtained from Altos Photonics, Inc. and used as solid supports for depositing polymer films. Silica prisms were cleaned using the method mentioned in Chapter 2. Aliphatic chain deuterated  $d_4$ -PET was purchased from Polymer Science Inc. The  $d_4$ -PET films were again prepared by spin coating the 2 wt% solution in 2-chlorophenol on the silica prisms at 2500 rpm. The deuterated polystyrene ( $d_8$ -PS) was also obtained from Polymer Science Inc. and the  $d_8$ -PS films were prepared using the same method as the  $d_4$ -PET films. The solvent used to dissolve  $d_8$ -PS was chloroform.

In this study, BADGE was purchased from Sigma-Aldrich. The BADGE samples were cured with diethylenetriamine (DETA) (from Sigma-Aldrich) as curing agent (hardener). Four silanes: (3-glycidoxypropyl) trimethoxysilane ( $\gamma$ -GPS), (3-Aminopropyl)trimethoxysilane (ATMS), Octadecyltrimethoxysilane (OTMS(18C)), and Octyltrimethoxysilane (OTMS(8C)) were purchased from Sigma-Aldrich and 1.5 wt% each silane was added to a BADGE sample in each experiment. BADGE epoxies with or without silane added were mixed with DETA and cured in an oven at 50 °C for 4 hours. Commercial epoxy resins 3302 (CE3302, transparent and colorless) and 3006 (CE3006, black) were obtained from Epoxies Etc. The main component of both commercial epoxy bases is bisphenol-A-(epichlorhydrin) epoxy resin, producing BADGE in the curing process. Small amounts of bis(1,2,2,6,6-pentamethyl-4 piperidiny)sebacate and 4-nonylphenol are present in CE3302. The curing agent (hardener) for CE3302 is polyoxypropylenediamine mixed with small amount of 4-nonylphenol. The mixing ratio for resin and hardener is 2:1 by weight. The curing for CE3302 took 2 hours at 52°C. CE3006 contains carbon black with substantial amount of calcium carbonate, small amount of oxirane, mono[(C12-

14-alkyloxy)methyl] and 4-nonylphenol. The hardener for CE3006 includes mainly calcium carbonate, polyaminoamide, small amount of tetraethylenepentamine, and benzyl alcohol. The mixing ratio for resin and hardener is 1:1 by weight. The curing for CE3006 took 1 hour at 100°C. All samples were mixed using a vortex mixer (Vortex-Genie 2T, Scientific Industries Inc.) before curing.

Molecular structures of the major materials discussed above which were used in the experiments are shown in Figure 3-2.

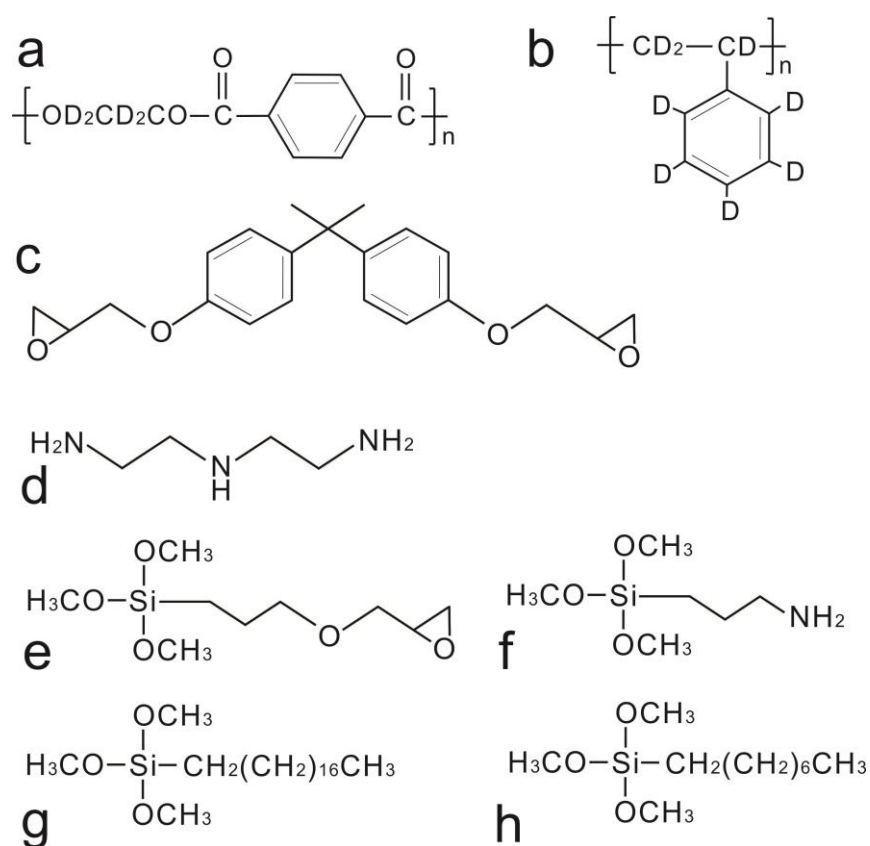


**Figure 3-2. Chemicals used in the experiment: (a) Poly(ethylene terephthalate) with aliphatic chain deuterated ( $d_4$ -PET) (b) Deuterated polystyrene ( $d_8$ -PS) (c) bisphenol A diglycidyl ether (BADGE); (d) diethylenetriamine (DETA); (e) (3-glycidoxypropyl) trimethoxysilane ( $\gamma$ -GPS); (f) (3-Aminopropyl)trimethoxysilane (ATMS); (g) Octadecyltrimethoxysilane (OTMS(18C)); (h) Octyltrimethoxysilane (OTMS(8C))**

### 3.3.2 SFG Experimental Results of a Model Epoxy in Contact with PET

We first collected SFG spectrum from the BADGE epoxy/ $d_4$ -PET interface without the addition of the curing agent DETA (Figure 3-3). Two peaks at  $2870\text{ cm}^{-1}$  and  $2930\text{ cm}^{-1}$  were detected in the spectrum which can be assigned to the methyl group symmetric C-H stretching mode and Fermi resonance in BADGE. This indicates that the BADGE methyl groups were ordered at this interface. A weak and broad peak at around  $3000\text{ cm}^{-1}$  was also observed, which is contributed from the BADGE epoxy ring. Another weak spectral feature detected at around  $3100\text{ cm}^{-1}$  should be contributed by the aromatic C-H stretching modes from the phenyl group in  $d_4$ -PET. This shows that the phenyl ring in  $d_4$ -PET also presents with some order at the BADGE/ $d_4$ -PET interface.

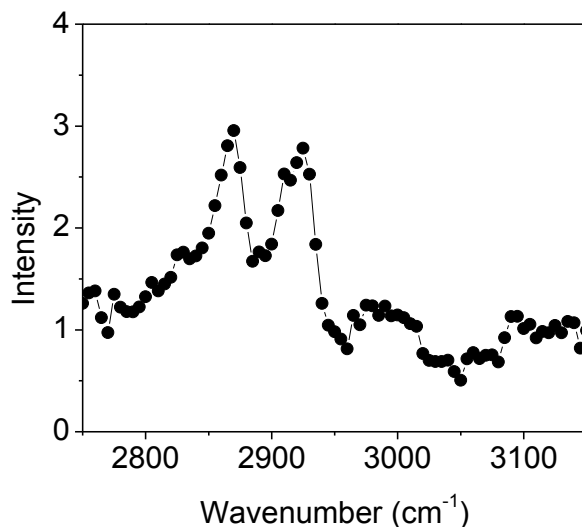


**Figure 3-3. SFG spectrum collected from the BADGE (without the curing agent DETA)/ $d_4$ -PET interface.**

We then collected SFG spectra of BADGE and different BADGE silane mixtures in contact with  $d_4$ -PET before and after curing with the addition of the curing agent DETA. We mixed BADGE with the curing agent DETA to form a homogeneous mixture, and contacted the mixture with spin coated  $d_4$ -PET thin film. SFG spectra were collected from the BADGE/ $d_4$ -PET interface



(Figure 3-4a). Before curing, a weak and broad peak at  $\sim 2950\text{ cm}^{-1}$  could be resolved, may due to the Fermi resonance of the BADGE methyl group, indicating that BADGE methyl groups may adopt some order at the interface. It is interesting to observe that this spectrum is markedly different from that shown in Figure 3-3; the overall SFG C-H stretching signal decreased greatly compared to the case before the addition of the curing agent. This demonstrates that the addition of the curing agent changed the interfacial structure substantially. Some of the curing agent molecules can segregate to the interface to disorder the interfacial BADGE molecules. Since the curing agent itself has a symmetric structure, it should generate no SFG C-H stretching signals. After curing, almost no signal can be detected, indicating that the curing process disordered the BADGE methyl groups at the interface.

After we studied the BADGE/ $d_4$ -PET interface before and after curing, we added small amounts (1.5 wt%) of four different silanes to mix with BADGE and DETA homogeneously before curing. We studied the mixture using SFG in C-H spectral range ( $2750\text{-}3150\text{ cm}^{-1}$ ). Similar spectral features were observed from the interfaces before curing when different silanes including  $\gamma$ -GPS, ATMS, OTMS (18C) and OTMS (8C) were added to the systems. The SFG signals were all weak and showed two weak peaks at  $\sim 2850\text{ cm}^{-1}$  and  $\sim 2950\text{ cm}^{-1}$  in C-H range, due to the methylene symmetric C-H stretching and methyl Fermi resonance. This shows that the addition of small amount (1.5 wt%) of various silanes does not substantially influence the interfacial structure before curing.

The samples were then cured at  $50\text{ }^\circ\text{C}$  for four hours. SFG spectra collected from the above interfaces in C-H stretching frequency range after curing are substantially different. No SFG signal in the C-H stretching frequency region was detected from the interfaces between  $d_4$ -PET and BADGE mixed with  $\gamma$ -GPS and ATMS respectively. We believe that  $\gamma$ -GPS and ATMS can

segregate to the interface. The disappearance of the SFG signals from these two interfaces may be due to the disordering of the interfacial silanes and/or the interfacial diffusion of silanes across the interface and the interface was not distinct anymore (Figures 3-4b and c). It has been shown extensively that interfacial diffusion can lead to the enhancement of adhesion.<sup>30-33</sup> Differently, the SFG spectrum collected from the BADGE (with 1.5 wt% OTMS(18C))/*d*<sub>4</sub>-PET interface after curing exhibits two strong peaks at 2880 cm<sup>-1</sup> and 2940 cm<sup>-1</sup> respectively (Figure 3-4d). These two peaks are assigned to the methyl endgroup C-H symmetric stretching and Fermi resonance in OTMS. This indicates that after curing, OTMS endgroups became ordered at the BADGE/*d*<sub>4</sub>-PET interface. The largest differences among  $\gamma$ -GPS, ATMS, and OTMS (18C) are that they have different endgroups, as epoxy, amino, and methyl groups respectively. Therefore the silane endgroups greatly impact the interfacial structures between BADGE (mixed with 1.5 wt% silane) and *d*<sub>4</sub>-PET.

We also collected SFG spectrum from the interface between *d*<sub>4</sub>-PET and BADGE mixed with 1.5 wt% OTMS(8C) after curing. The silane OTMS(8C) has a shorter chain than OTMS(18C). SFG spectrum collected from this interface is markedly different from the case when OTMS(18C) was added (Figure 3-4e). Only very weak signal was observed in the spectrum. This means at the interface of epoxy and PET, OTMS(8C) does not have strong order. This also demonstrates that the silane chain length impacts the interfacial structure. If the disappearance of signal is caused by the silane interfacial diffusion, then perhaps the shorter silane molecules can diffuse into the polymer matrix easier.

All four types of silanes studied here are methoxy silanes which have methoxy head groups. The C-H symmetric stretching signal of a methoxy group is centered at 2845 cm<sup>-1</sup>, which was not observed in the experiment using SFG. This indicates that the methoxy head groups are not ordered

at the interfaces. Moreover, all four types of silanes have backbones, which are composed of methylene groups. The C-H symmetric and asymmetric stretching signals of methylene groups are at  $2850\text{ cm}^{-1}$  and  $2920\text{ cm}^{-1}$  respectively, which were not observed either after curing.

For end group effect, both OTMS molecules (with different chain lengths) have methyl end groups, but only OTMS (18C) shows significant methyl C-H signal at the interface after curing. This means that OTMS (18C) methyl end group tends to adopt some order at the interface after curing, while OTMS (8C) molecules at the interface tend to have disordered methyl end groups. The  $\gamma$ -GPS' end group is an epoxy ring, which should generate SFG signal at  $3000\text{ cm}^{-1}$  when ordered. We did not observe any SFG signal at the interface. This is reasonable because such groups can react with N-H groups in amine. For ATMS, the end group has N-H bonds, which should contribute a peak at  $3300\text{ cm}^{-1}$  when adopting some order. We collected SFG spectra from the BADGE/*d*<sub>4</sub>-PET interfaces before and after curing in the N-H stretching frequency range ( $3100\text{-}3600\text{ cm}^{-1}$ ). The results are shown in Figure 3-5. Before curing, N-H stretching signal at  $3300\text{ cm}^{-1}$  can be observed, contributed by the ATMS -NH<sub>2</sub> end group or N-H groups in DETA. After curing, such N-H stretching signal disappeared. This indicates that ATMS -NH<sub>2</sub> end groups or N-H groups in DETA tend to adopt some order at BADGE/*d*<sub>4</sub>-PET interface before curing. N-H groups tend to form hydrogen bonding with PET,<sup>34</sup> which may lead to the ordering of N-H groups at the interface. In the curing process, N-H groups tend to react with epoxide groups in the epoxy. Therefore, after curing no N-H signal could be detected. For all the four types of silanes studied here, only methyl end groups in OTMS(18C) are strongly ordered at the interface after curing.

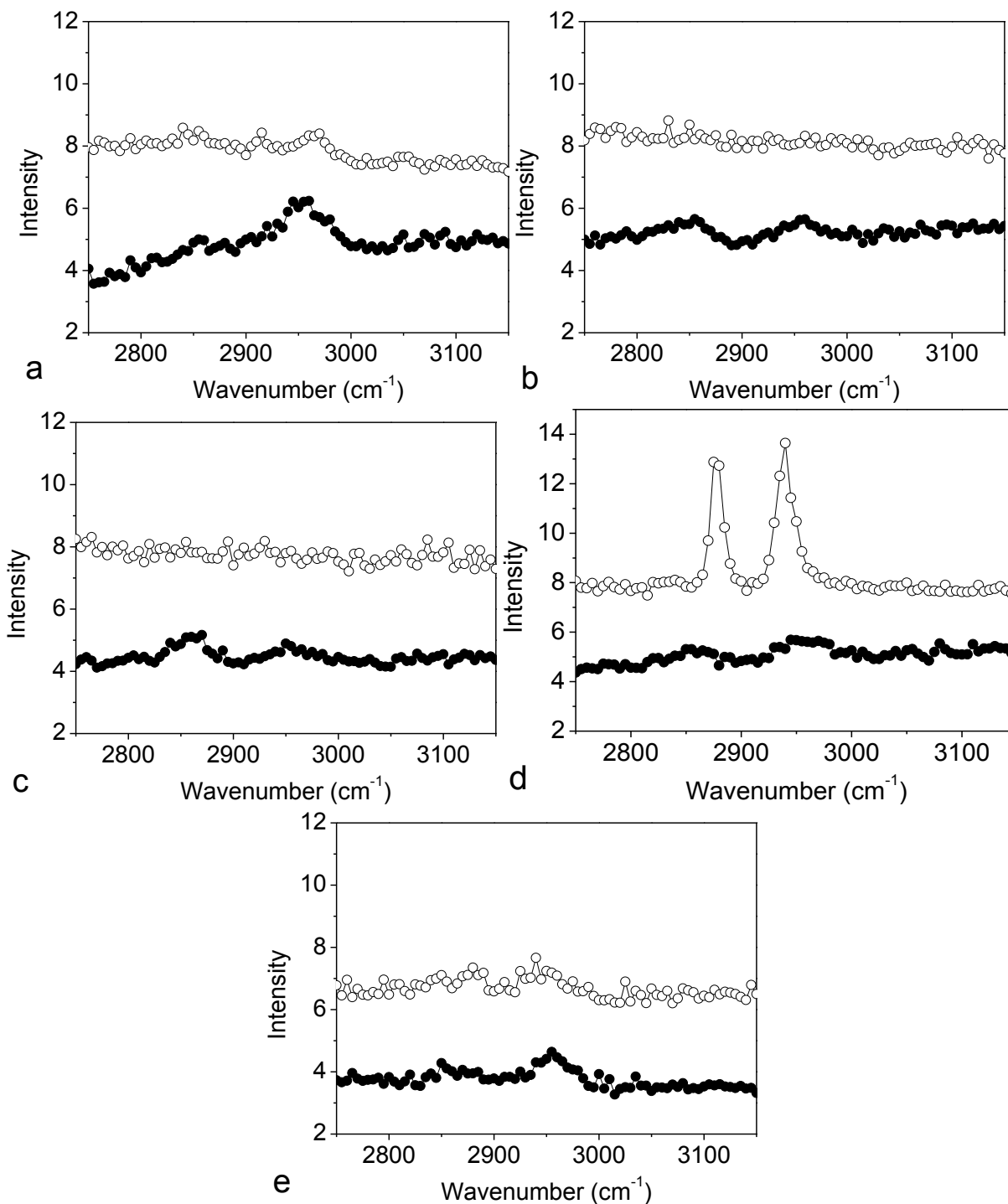


**Figure 3-4.** SFG spectra collected from (a) BADGE/ $d_4$ -PET interface; (b) BADGE+DETA+ $\gamma$ -GPS/ $d_4$ -PET interface; (c) BADGE+DETA+ATMS/ $d_4$ -PET interface; (d) BADGE+DETA+OTMS(18C)/ $d_4$ -PET interface; (e) BADGE+DETA+OTMS(8C)/ $d_4$ -PET interface. Closed dots: spectra collected before curing. Open dots: spectra collected after curing. The spectral range is from 2750 to 3150  $\text{cm}^{-1}$ .

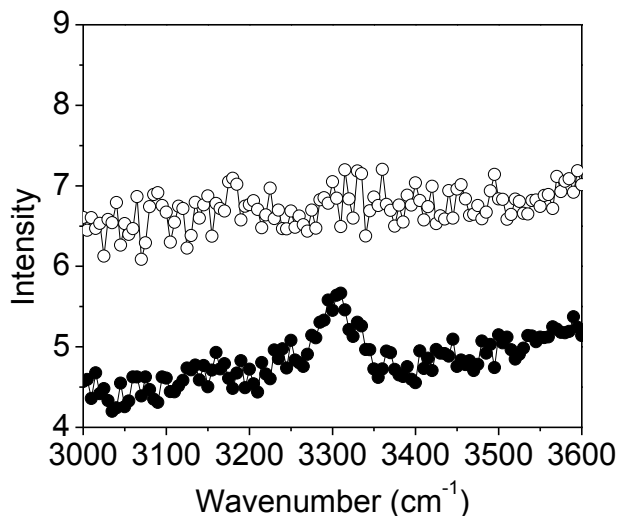


**Figure 3-5. SFG spectra collected from the BADGE+DETA+ATMS/ $d_4$ -PET interface. Bottom spectrum: before curing; top spectrum: after curing. The spectral range is from 3000 to 3600  $\text{cm}^{-1}$ .**

### 3.3.3 Interfacial Molecular Ordering and Its Relation to Adhesion

The adhesion testing experiments were carried out after curing the various interfaces (Figure 3-6). All these samples are only slightly different in bulk content: four samples have only 1.5 wt% of different silanes in the system while the fifth sample does not contain any silane. The adhesion testing results indicated clearly that the small amounts of silane incorporated into the epoxy mixtures can alter the adhesion properties. The addition of  $\gamma$ -GPS, ATMS, and OTMS(8C) to BADGE slightly increased the adhesion to  $d_4$ -PET while the addition of OTMS(18C) strongly decreased the adhesion. The adhesion data can be well correlated to the SFG measurements. Only the SFG spectrum collected from the interface after the addition of OTMS(18C) shows large methyl signal, indicating silane methyl endgroup order at the interface, which leads to weak adhesion. Almost no SFG signal could be detected from the cured interfaces after the additions of  $\gamma$ -GPS, ATMS, and OTMS(8C) into BADGE, indicating that these interfaces have disordered molecular structures. The interfacial disordered structure is caused by the randomization of the

molecules at the interface or interfacial diffusion, both of which can enable more entanglements of various molecular chains, resulting in stronger adhesion at the interface. We believe that the methyl ordering at the interface leads to weak adhesion because methyl groups cannot form stronger interactions than Van der Waals interactions.

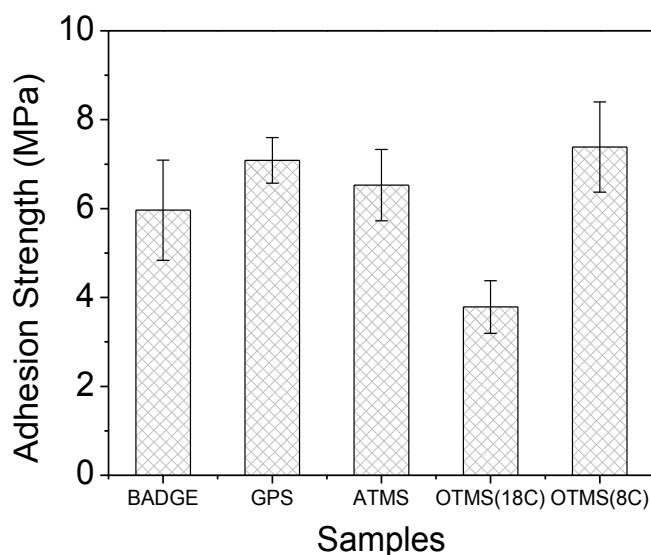


**Figure 3-6. Adhesion testing results of model epoxy BADGE and BADGE silane mixtures to PET after curing. Adhesion strength = Maximum adhesion force/contact area.**

### 3.3.5 SFG Experimental Results of Commercial Epoxy Materials in Contact with Polymers

We extended our research from model epoxy BADGE to commercial epoxies. We investigated two commercial underfill epoxies CE3302 and CE3006 which have the same BADGE main component. We first collected SFG spectra from the  $d_4$ -PET/CE3302 interfaces (Figure 3-7a). Without the curing agent, the detected SFG spectrum shows similar features compared to that detected from the BADGE/ $d_4$ -PET interface. Two peaks at  $2870\text{ cm}^{-1}$  and  $2930\text{ cm}^{-1}$  were detected, which are contributed by the methyl groups in the epoxy. After adding the curing agent to CE3302, the detected SFG spectrum from this interface did not change substantially, which is different from the model epoxy BADGE case reported above. Perhaps here the ordered methyl groups at the

interface are those from the other components in CE3302 such as bis(1,2,2,6,6-pentamethyl-4-piperidinyl)sebacate and 4-nonylphenol, which do not exist in the model BADGE epoxy. After curing, the strong methyl group symmetric C-H stretch in the SFG spectrum disappeared, while only a weak methyl asymmetric C-H stretching signal was detected. This is similar to the model BADGE case reported above.

We also collected SFG spectra from the *d*<sub>8</sub>-PS/CE3302 interfaces. As shown in Figure 3-7b, pure CE3302 base does not exhibit methyl group ordering at the interface with *d*<sub>8</sub>-PS. This indicates that CE3302 can have different interfacial molecular structures while in contact with different polymers, due to different molecular interactions. After the addition of the curing agent, methyl groups started to order at the *d*<sub>8</sub>-PS/CE3302 interface, similar to the *d*<sub>4</sub>-PET case. After curing, different from the *d*<sub>4</sub>-PET case, strong methyl group signals were detected at 2875 and 2935 cm<sup>-1</sup>. This means that the methyl groups are very ordered at the interface with *d*<sub>8</sub>-PS. According to the SFG and adhesion studies on the model epoxy BADGE reported above, we know that the disappearance of the SFG signals usually leads to strong adhesion, and methyl group interfacial ordering usually leads to weak adhesion. Therefore we can predict that the cured PET/CE3302 interface should have stronger adhesion, while the cured PS/CE3302 interface should have weaker adhesion. This was proved by the data acquired from the adhesion testing experiments. The adhesion testing results are shown in Figure 3-8. Clearly CE3302 has much stronger adhesion to PET compared to PS.

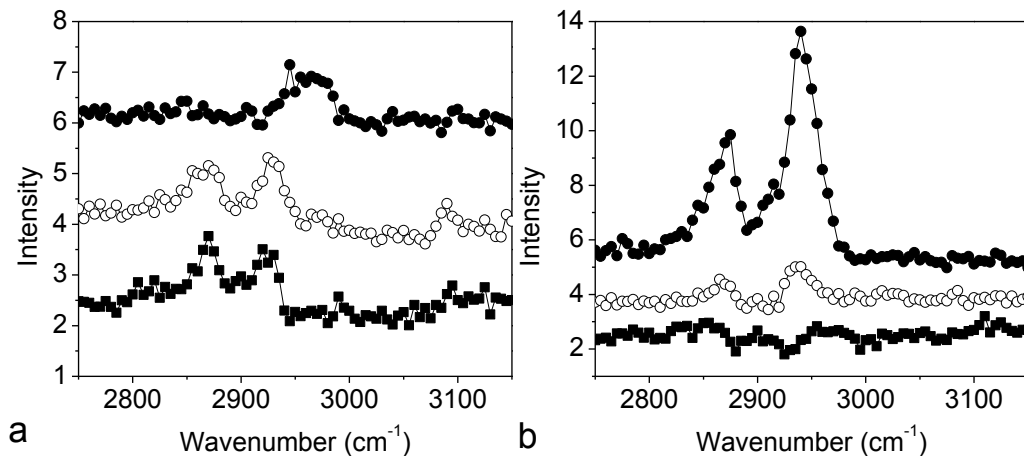


**Figure 3-7. SFG spectra collected from (a) the CE3302/*d*<sub>4</sub>-PET interface; (b) the CE3302/*d*<sub>8</sub>-PS interface. From the top to the bottom: SFG spectra from interfaces of the cured sample, the uncured sample, and the epoxy base without hardener.**

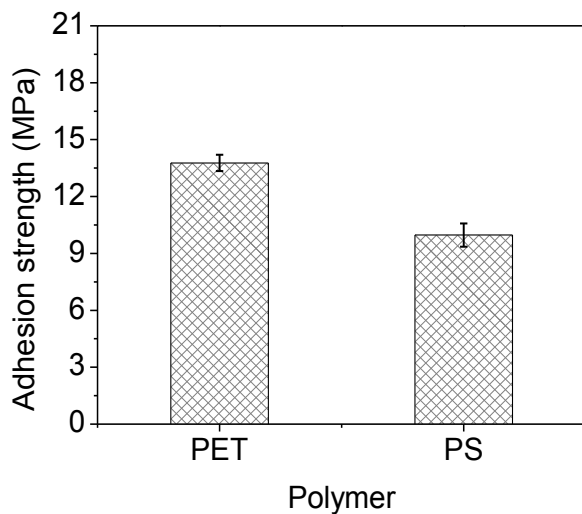


**Figure 3-8. Adhesion testing results of commercial epoxy 3302 to PET and PS.**

In addition to CE3302, we studied another commercial epoxy CE3006, which is a black epoxy due to its carbon black ingredient. We first collected the SFG spectrum from the *d*<sub>4</sub>-PET/CE3006 interface before the addition of the curing agent. Broad peaks at 2930 and 2960 cm<sup>-1</sup> were detected (Figure 3-9a), which were assigned to the methyl groups in epoxy. This spectrum is different from those collected from the *d*<sub>4</sub>-PET/pure BADGE interface and the *d*<sub>4</sub>-PET/CE3302 (without hardner) interface cases. This means that the carbonate ingredient in the sample could



affect the interfacial structure. After adding the curing agent, in addition to the methyl signals, SFG signal from methylene groups could also be detected at  $2850\text{ cm}^{-1}$ . However, after curing, no SFG signal could be detected from the interface, indicating the interfacial diffusion and/or interfacial disordering (Figure 3-9a). We then studied the  $d_8$ -PS/CE3006 interfaces. Before the addition of the curing agent, methyl groups are ordered at the interface, evidenced by the observed methyl symmetric and asymmetric stretching signals at  $2880$  and  $2960\text{ cm}^{-1}$ , respectively (Figure 3-9b). Another peak at  $2920\text{ cm}^{-1}$  could also be observed, indicating that methylene groups also adopt some order at the interface. After the addition of the hardener or curing agent, methyl groups are still ordered at the interface. After curing, much stronger SFG signals were detected at  $2850$ ,  $2880$ ,  $2920$ ,  $2940$ , and  $2960\text{ cm}^{-1}$ , showing that both methyl and methylene groups are highly ordered at the interface (Figure 3-9b). From SFG studies, we can again predict that the PET/CE3006 interface has stronger adhesion while the PS/CE3006 interface has weaker adhesion. The adhesion testing results again proved this prediction, as shown in Figure 3-10.

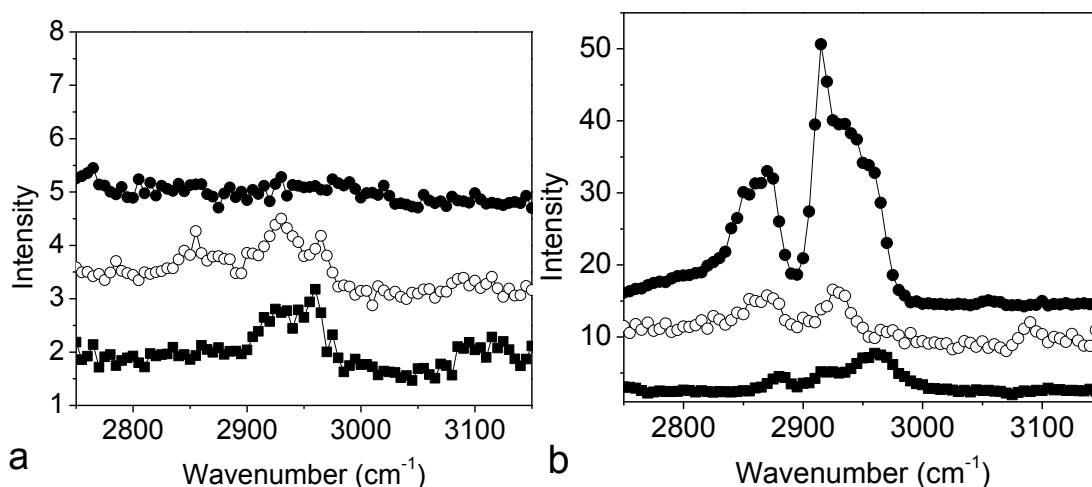


**Figure 3-9. SFG spectra collected from (a) the CE3006/ $d_4$ -PET interface; (b) the CE3006/ $d_8$ -PS. From the top to the bottom: SFG spectra from interfaces of the cured sample, the uncured sample, and the epoxy base without hardener. For spectrum in the middle of (b), it is multiplied by a factor of five.**

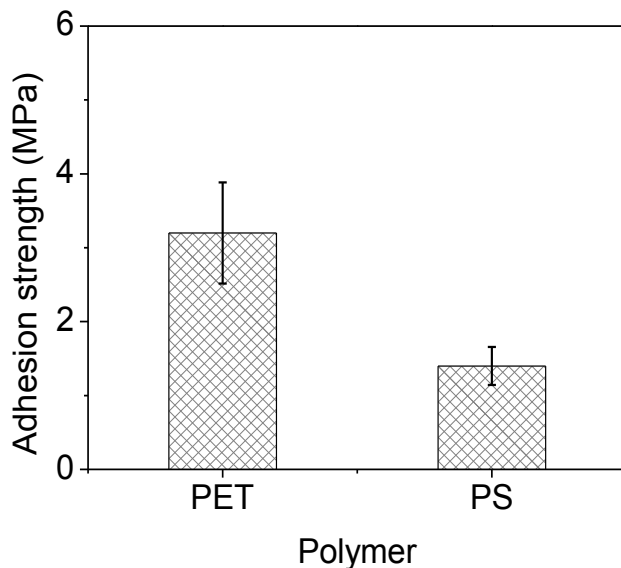


**Figure 3-10. Adhesion testing results of CE3006 to PET and PS.**

### 3.3.7 Conclusion

In this study, we demonstrated that SFG is a powerful technique to investigate molecular structures of buried interfaces *in situ* between polymers and underfill materials. A model epoxy and two commercial epoxy resins were investigated. In the model epoxy study, small amounts of different silanes (1.5 wt%) were added to the epoxy, which substantially influenced the polymer/epoxy interfacial structures and interfacial adhesion. Both silane endgroups and chain length play roles in silane behaviors at the buried interfaces. Silanes with epoxy end group, amino end group, and short chains methyl endgroup may segregate but disorder at the interface, together with the disorder of epoxy, provide strong adhesion. The long chain silane with methyl end group exhibits methyl ordering at the interface, reducing adhesion. This conclusion was supported by SFG studies on two commercial epoxy resins. SFG studies indicate that the molecular disorder may occur from both commercial resins while in contact with PET after curing, and strong adhesion was measured. Methyl group ordering at the interface was observed for these two

commercial epoxies while in contact with PS after curing, and weak adhesion was measured. We have demonstrated that SFG is a powerful tool to elucidate molecular mechanisms for adhesion at buried interfaces.

In the following study, we will perform ATR-FTIR spectroscopy together with SFG spectroscopy to further investigate the adhesion mechanism between model epoxy systems and PET substrate.

### **3.4 Adhesion Mechanism between Epoxy and PET**

In this section, further investigations on the epoxy-amine/PET adhesion mechanism were performed. Two model epoxies were cured on PET film surface using a model amine. We used SFG to reveal the molecular structures at the buried interfaces. Additionally, we applied ATR-FTIR to examine the interactions between the PET film and epoxies and/or amines. Although ATR-FTIR is not intrinsically interfacial selective, it could still help to provide a more complete picture of the adhesion mechanism through monitoring the interactions of epoxy and/or amine with PET. It was also used to monitor the existence of the remaining PET film before and after curing the epoxy-amine as well as after breaking the cured epoxy-amine/PET interface. Furthermore, reactive and nonreactive silanes were incorporated into the two epoxy-amines to study their effects on interfacial molecular structure and adhesion. We aim to provide an in-depth understanding on the molecular behaviors at the interface between epoxy-amine and PET substrate. The corresponding adhesion mechanism was proposed based on our observations and analysis.

The amine/PET and epoxy/PET interfaces were examined followed by the investigation of the epoxy-amine/PET interfaces. Additionally, silane molecules were incorporated into the epoxy-amine mixtures and their interfaces with PET were studied. All SFG spectra in this research were

collected using the polarization combination of ssp, which usually gives the strongest SFG signal from the interface. Unpolarized IR beam was used for the ATR-FTIR study.

### 3.4.1 Materials and Experimental Methods

Silica substrates and the cleaning procedures were the same as previously mentioned. The silicon prisms were obtained from Chengdu-yasi optoelectronics (Chengdu, China) for ATR-FTIR experiments. The cleaning procedures for silicon prisms were similar as that of the silica ones. CaF<sub>2</sub> right angle prisms were purchased from Altos Photonics, and was cleaned using toluene and ethanol, and was further etched using the Plasma cleaner. The *d*<sub>4</sub>-PET thin film deposition was also similar as before.

(1,4-butanediol)diglycidyl ether (BDDGE) and (1,4-cyclohexanedimethanol)diglycidyl ether (CDDGE) were purchased from Sigma Aldrich. The two epoxies were cured using DETA, which was also obtained from Sigma Aldrich. The epoxy amine ratio used in the experiment was calculated considering that each epoxide ring reacts with one amino-hydrogen atom. An additional 10 wt% amine was used in the epoxy-amine mixture taking into account of the amine evaporation. The epoxy and amine were mixed using a vortex mixer and sealed in a glass vial for 1 hr before use. The epoxy curing was carried out in an oven at 50 °C for two hours. Then the samples were stored at the room temperature for 12 hr. In the mechanical adhesion test, two PET blocks were adhered together using epoxy-amine mixtures with and without silanes. In the contact angle measurement, cured epoxy-amine mixture on substrate was peeled off to obtain the resulting surface for study. All silanes used in this experiment were purchased from Sigma Aldrich, including  $\gamma$ -GPS, ATMS and OTMS(18C) (OTMS). Silanes were incorporated into the epoxy-amine mixtures at 1.5 wt%. The mixtures were also well mixed and stored for 1 hr before use.

Chemical structures of BDDGE and CDDGE are shown in Figure 3-11.

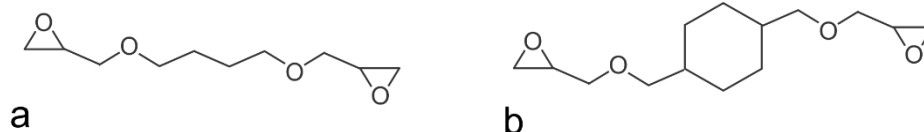


**Figure 3-11. Chemical structures of (a) (1,4-butanediol)diglycidyl ether (BDDGE) and (b) (1,4-cyclohexanedimethanol)diglycidyl ether (CDDGE).**

SFG experimental geometry used in this study is shown in Figure 3-12a, which is similar to that presented in the previous chapters and will not be repeated in detail here. The ATR-FTIR experiment was carried out using a Nicolet 6700 FTIR spectrometer (Thermo scientific Inc.). The sample chamber was purged with nitrogen gas to reduce the water vapor and carbon dioxide IR absorption. The experimental geometry used for ATR-FTIR experiment in this work is shown in Figure 3-12b.

Water contact angle measurements were performed using a commercial contact angle goniometer (KSV Cam 101) to study the hydrophobicity changes of the fractured PET/epoxy-amine interfaces after curing. Ultrapure water (Milli-Q water 18.2 M $\Omega$ ·cm) was used in the measurements.

The mechanical adhesion test method is also similar to that presented in Chapter 2. We used epoxy-amine mixtures here to glue two test pieces together, instead of using PDMS.

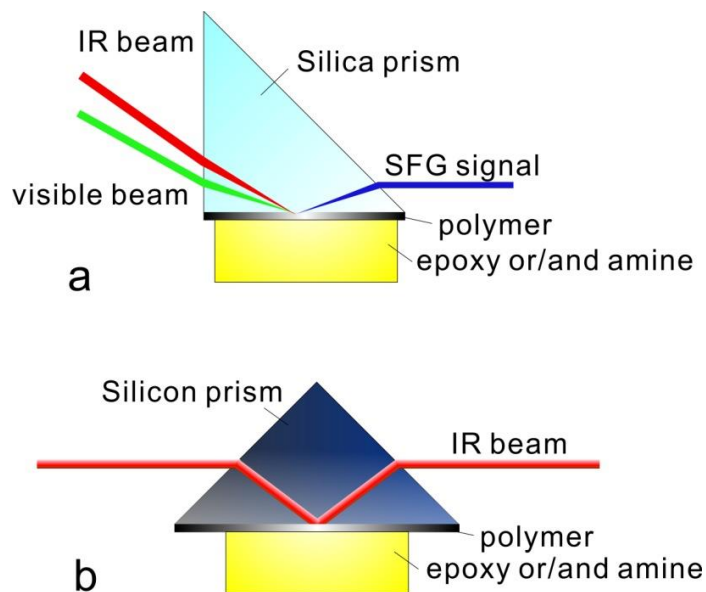


**Figure 3-12. Experimental geometries of (a) SFG spectroscopy and (b) ATR-FTIR spectroscopy.**

### 3.4.2 Epoxy/PET Interface

The ATR-FTIR spectra of the PET thin film on silicon substrate are shown in Figure 3-13 (black). A strong IR absorption at  $1722\text{ cm}^{-1}$  was observed and could be assigned to the C=O stretching vibration. Weak C-H stretching vibrational peaks could also be observed in the frequency range of  $2800\text{-}3100\text{ cm}^{-1}$ . No C=O vibration was found in other compounds used in the study such as epoxy (Figure 3-14), or amine. Therefore, the peak at  $1722\text{ cm}^{-1}$  could be used to monitor the change and the existence of the PET film. When the PET film contacted BDDGE epoxy, stronger C-H signal was observed due to the contribution from BDDGE in the IR penetration depth range (Figure 3-13a, red). Furthermore, the C=O peak intensity from PET decreased. Since no specific chemical reaction was expected between PET and BDDGE, the decrease of the PET signal was attributed to the solvation of PET by BDDGE (the dissolved PET diffused out of the IR penetration depth and could not be detected by ATR-FTIR). An interphase region with the presence of both PET and BDDGE could be formed after their contact. Although

BDDGE could dissolve part of the PET film, PET feature still remained and the spectrum was stable. After 2 hr's contact, we removed BDDGE and washed the PET surface using acetone and water (PET cannot be dissolved in acetone). After washing and drying the PET surface (film), the ATR-FTIR spectrum from the remaining film was collected and is shown in Figure 3-13a (blue). Almost no C-H stretching signal could be observed and weaker C=O stretching signal was detected (weaker than the original PET film). This means that BDDGE was washed away and it dissolved part of the PET film, but a thinner PET film still remained on the silicon substrate surface. A similar study was also carried out for the CDDGE-PET interaction. The difference between the two cases was that the contacting of CDDGE with PET showed little change of the PET C=O signal at the interface as well as after washing the CDDGE off from the surface (as shown in Figure 3-13b), indicating a less dissolution of PET by CDDGE. We placed PET pellets in pure BDDGE and CDDGE for a week at the room temperature respectively. The significant solvation of PET by BDDGE was observed while the solvation of PET by CDDGE was not as significant.

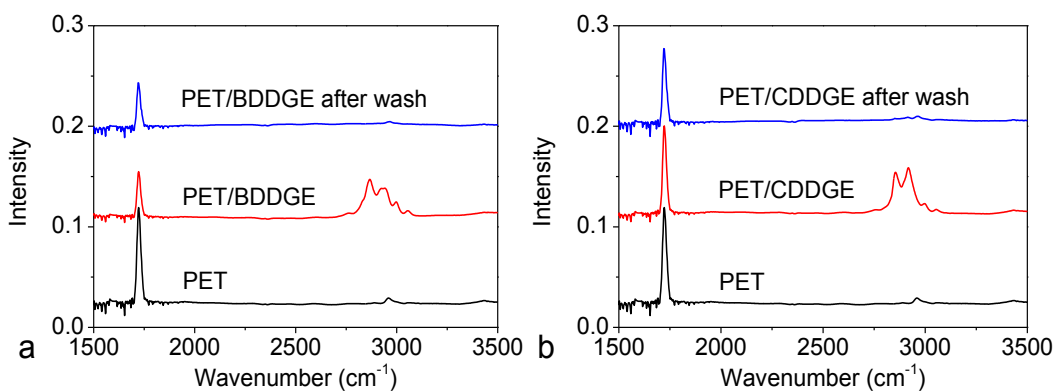


**Figure 3-13. ATR-FTIR spectra of (a) PET (black), PET contacting BDDGE epoxy (red), PET washed using acetone and water after contacting BDDGE epoxy for 2 hr (blue). (b) PET (black), PET contacting CDDGE epoxy (red), PET washed using acetone and water after contacting CDDGE epoxy for 2 hr (blue).**

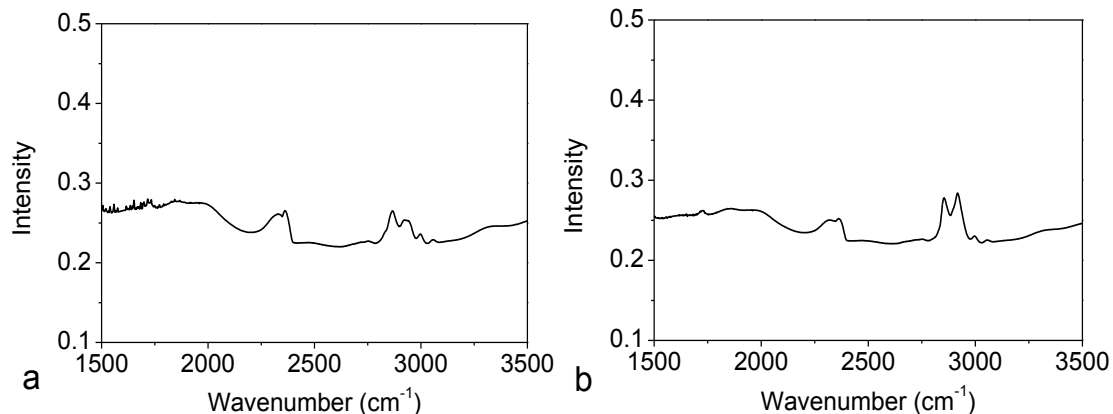


**Figure 3-14 ATR-FTIR spectra of (a) BDDGE and (b) CDDGE epoxy in contact with silicon substrate; No signal at 1722  $\text{cm}^{-1}$  can be detected.**

SFG spectra of PET and  $d_4$ -PET in air have been published previously.<sup>35-36</sup> For PET, both aliphatic and aromatic C-H stretching signals at 2960 and 3075  $\text{cm}^{-1}$  were observed. For  $d_4$ -PET, only aromatic C-H stretching signal at 3075  $\text{cm}^{-1}$  was detected.<sup>35-36</sup> PET surface in air also generate strong SFG signal from C=O stretching centered at 1725  $\text{cm}^{-1}$ .<sup>35</sup> Such published results were reproduced in this work.

Since epoxies tend to dissolve PET films, it is highly possible that epoxy molecules can diffuse into the films. SFG can be used to study such possible diffusions: If epoxy molecules diffuse into a PET film, they will further aggregate at the PET/prism substrate interface, generating SFG signal; however, because of the PET solvation and epoxy diffusion, there should be no sharp boundary between PET and epoxy, likely generating no SFG signal. In order to monitor the behavior of interfacial epoxies without spectral interference with PET, we used  $d_4$ -PET in the following SFG experiments. Additionally, different prism substrates were used including  $\text{CaF}_2$  and silica, because the diffused epoxy may have different structures while in contact with different substrates, which can be used to confirm the epoxy diffusion behavior.

The interfacial SFG signal from a BDDGE/blank  $\text{CaF}_2$  prism interface was first collected



as shown in Figure 3-15a (filled square). The peaks centered at around 2850 and 2950  $\text{cm}^{-1}$  were contributed by various methylene groups in the epoxy molecule; the peak at around 3000  $\text{cm}^{-1}$  signal could be assigned to the C-H group in the epoxide ring.<sup>37</sup> The SFG spectrum collected from the BDDGE/*d*<sub>4</sub>-PET (on CaF<sub>2</sub>) interface is shown in Figure 3-15a (open circle). It is very similar to the previous spectrum collected from the BDDGE/blank CaF<sub>2</sub> interface. This indicates that very likely epoxy molecules diffused into the *d*<sub>4</sub>-PET film and segregated at the *d*<sub>4</sub>-PET/prism interfacial area, generating similar SFG spectrum as that from the epoxy/blank prism (without *d*<sub>4</sub>-PET) interface. Although the *d*<sub>4</sub>-PET aromatic groups are ordered on the surface in air,<sup>35</sup> no substantial ordering of such groups can be detected at the BDDGE/*d*<sub>4</sub>-PET interface. This may also because the epoxy diffusion to the CaF<sub>2</sub> interface.

To further confirm the BDDGE diffusion through PET, we used a silica prism as a solid support to perform the SFG experiment. SFG spectrum collected from the BDDGE/blank silica prism interface is quite different from that at BDDGE/blank CaF<sub>2</sub> prism, as shown in Figure 3-15b (filled squares). The epoxy ring peak at 3000  $\text{cm}^{-1}$  became stronger while other peaks decreased in weaker intensity. Interestingly, the SFG spectrum collected from the BDDGE/*d*<sub>4</sub>-PET (on silica) interface is quite similar to that detected from the BDDGE/silica prism interface, but very different from that from the BDDGE/*d*<sub>4</sub>-PET (on CaF<sub>2</sub> prism) interface. Different signals from BDDGE in contact with *d*<sub>4</sub>-PET on different prisms and similar SFG spectrum detected from the interface between BDDGE and the same prism with and without *d*<sub>4</sub>-PET demonstrate the diffusion of BDDGE through the PET film and aggregation of BDDGE at the original PET/prism interface. Additionally, although *d*<sub>4</sub>-PET surface generates strong C=O SFG signal in air, when contacted with BDDGE, the C=O peak at 1725  $\text{cm}^{-1}$  disappeared, indicating the loss of order from the PET surface after contacting epoxy. This indicates that the *d*<sub>4</sub>-PET/BDDGE interphase area should have

no sharp boundary, generating no SFG signal.

A similar study was performed on the CDDGE epoxy. As shown in Figures 3-15c and 3-15d, SFG spectra collected from the CDDGE/substrate interface are quite similar for the same substrate (CaF<sub>2</sub> or silica) with and without *d*<sub>4</sub>-PET deposited; but for different substrates, SFG spectra collected from the epoxy/*d*<sub>4</sub>-PET (on substrate) interfaces are very different. These observations indicate that although the PET film solvation effect of CDDGE was much weaker as compared to BDDGE (as shown in the above discussed ATR-FTIR results), CDDGE molecules could still diffuse into the PET film. Again, the CDDGE/*d*<sub>4</sub>-PET interphase area likely generates no SFG signal.

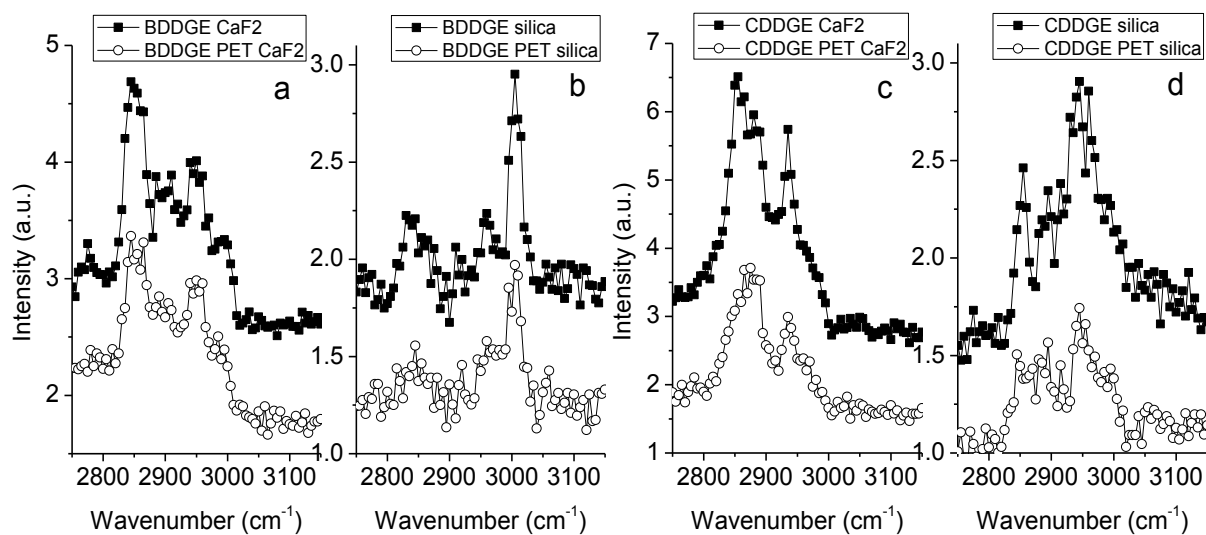


**Figure 3-15. SFG spectra collected from (a) BDDGE/blank CaF<sub>2</sub> interface (black square) and BDDGE/*d*<sub>4</sub>-PET (deposited on CaF<sub>2</sub>) interface (open circle); (b) BDDGE/blank silica interface (black square) and BDDGE/*d*<sub>4</sub>-PET (deposited on silica) interface (open circle); (c) CDDGE/blank CaF<sub>2</sub> interface (black square) and CDDGE/*d*<sub>4</sub>-PET (deposited on CaF<sub>2</sub>) interface (open circle); (d) CDDGE/blank silica interface (black square) and CDDGE/*d*<sub>4</sub>-PET (deposited on silica) interface (open circle).**

### 3.4.3 Amine/PET Interface

ATR-FTIR study was also carried out to understand PET-amine interactions. After contacting DETA with PET film deposited on a silicon prism, strong C-H and N-H stretching vibration peaks were detected but little change of PET C=O signal was seen in the IR spectrum (Figure 3-16a, red). Time dependent ATR-FTIR study showed that PET signal at the PET/DETA interface decreased only slightly over time, as shown in Figure 3-16b. It has been reported that DETA can react with PET by breaking the chemical bonds in polymer backbone and grafting N-H and O-H groups to the polymer.<sup>38-40</sup> Therefore, such signal change might be mainly caused by the reaction between PET and DETA. This reaction process might only slightly decrease the C=O signal at  $1722\text{ cm}^{-1}$  during contact but made the film much easier to be removed by breaking the polymer backbone. We removed the DETA after the contact and washed the PET surface using water (the contacting time was 40 min). The PET C=O ATR-IR signal showed a significant decrease (Figure 3-16a, blue). This PET signal decreasing behavior was quite different from the solvation behavior caused by contacting PET with epoxy (Figure 3-13). In this case, a substantial amount of PET polymers were broken into smaller parts and removed from the surface in the washing process. However, the PET C=O feature still remained after washing, indicating that some PET molecules still remained on the substrate. After washing away the DETA using water, no amine spectral feature could be detected in the ATR-FTIR spectrum (Figure 3-16a, blue). This is because only a small amount of amine might have diffused into and remained in the PET matrix after washing. Furthermore, although the chemical reaction could graft N-H and O-H groups to the polymer, the polymer film was too thin and the product was too little to be detected by ATR-FTIR. From these results, we found that very likely a large amount of PET molecules reacted with DETA (after washing the surface, PET signal greatly decreased) with little disturbance of the PET

film (if only contacted DETA with PET without washing, little signal decrease was observed). It is likely that DETA can diffuse into the PET film and react with PET in the bulk.

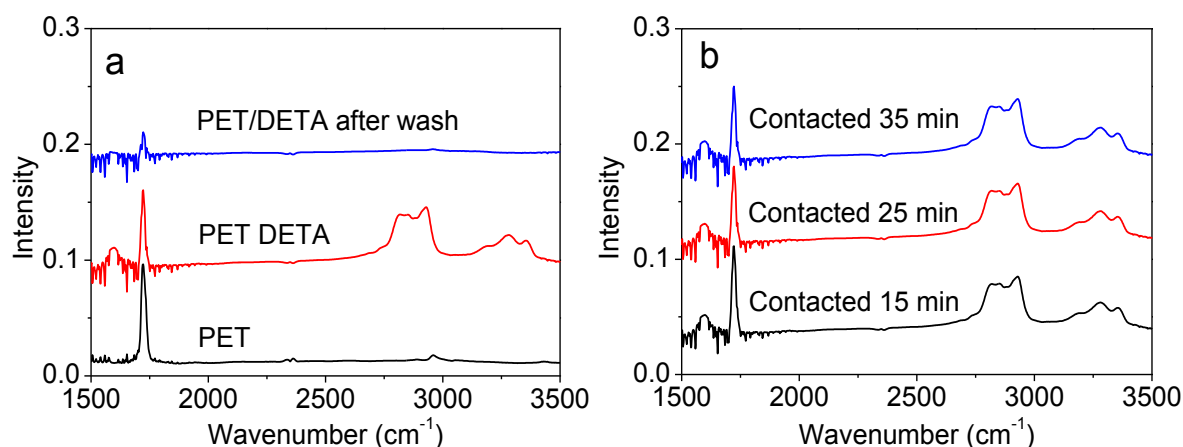


**Figure 3-16. (a) ATR-FTIR spectra of PET (black), PET contacting DETA (red), PET film after contacting DETA for 40 min and washed by water (blue); (b) Time dependent ATR-FTIR spectra of PET in contact with DETA.**

The diffusion of DETA into PET film can be confirmed by SFG study. We compared the SFG spectra collected from the DETA/CaF<sub>2</sub> prism, DETA/*d*<sub>4</sub>-PET (on CaF<sub>2</sub> prism), DETA/silica prism, DETA/*d*<sub>4</sub>-PET (on silica prism) interfaces, as shown in Figure 3-17. All spectra contain three peaks. The peaks around 2820-2850 cm<sup>-1</sup> and 2930-2960 cm<sup>-1</sup> are assigned to the C-H symmetric and asymmetric vibrational stretching of the N-CH<sub>2</sub> group in DETA respectively. The peak centered at 3300 cm<sup>-1</sup> is contributed by the N-H stretching in DETA. However, the relative intensities of these three peaks can be similar or different in different spectra: they are similar when collected from the same prism substrate (regardless of having *d*<sub>4</sub>-PET or not) and are quite different when collected from interfaces of *d*<sub>4</sub>-PET on different prism substrates. Similar to the previous epoxy diffusion study, here we conclude that DETA can diffuse into *d*<sub>4</sub>-PET, generating SFG signal from the *d*<sub>4</sub>-PET/prism interfaces. No SFG signal was generated from the *d*<sub>4</sub>-PET/DETA interphase, because the chemical reaction between the PET and DETA results in no clear boundary. No SFG C=O stretching peak was detected after contacting DETA with *d*<sub>4</sub>-PET, indicating the loss of order

of these C=O groups due to the chemical reaction and diffusion.

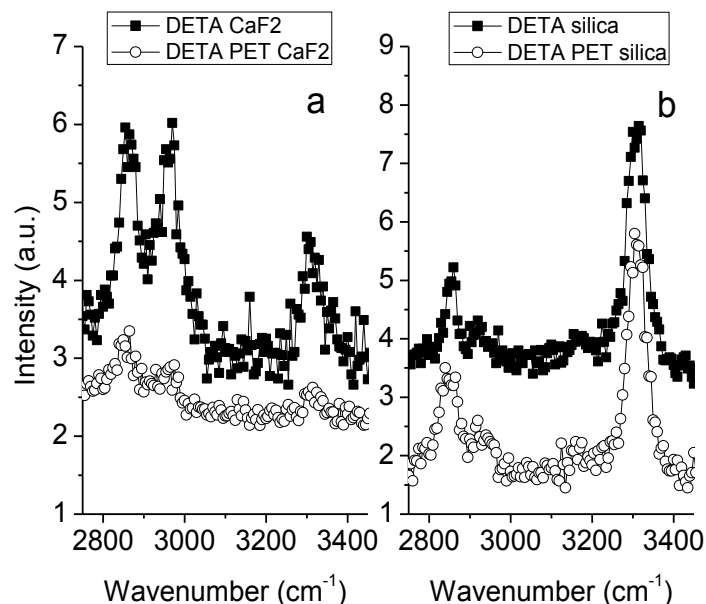


**Figure 3-17.** SFG spectra collected from (a) DETA/CaF<sub>2</sub> interface (black square) and DETA/*d*<sub>4</sub>-PET (deposited on CaF<sub>2</sub>) interface (open circle); (b) DETA/silica interface (black square) and DETA/*d*<sub>4</sub>-PET (deposited on silica) interface (open circle)

The amine diffusion can be further verified by the interactions of DETA molecules with a silane self-assembled monolayer grown on a silica substrate.

#### 3.4.4 Amine Diffusion into PET

A self-assembled monolayer (SAM) of Octadecyltrichlorosilane (OTCS) was grown on a silica substrate by placing the silica prism in a 1 mM OTCS solution in toluene overnight at room temperature. Before use, the SAM prisms were taken out and rinsed using toluene and dried with nitrogen gas. Deuterated polystyrene (*d*<sub>8</sub>-PS) was obtained from Polymer Source Inc. It was dissolved in toluene to form a 5 wt% solution. When *d*<sub>8</sub>-PS was spin-coated on the OTCS SAM, 1500 rpm spin speed was used. PET was further coated on the *d*<sub>8</sub>-PS using 4000 rpm spin speed.

In order to study amine diffusion into PET film, we designed the following experiments using SFG and ATR-FTIR spectroscopies. Basically, we used the interaction between an OTCS SAM and DETA to monitor the DETA diffusion.

SFG signal of the OTCS SAM grown on a silica prism was collected in the C-H range and is shown in Figure 3-18a (black square). Three peaks at 2850, 2875, and 2940  $\text{cm}^{-1}$  could be resolved, attributed from symmetric C-H stretching in methylene ( $\text{CH}_2$ ), symmetric C-H stretching in methyl ( $\text{CH}_3$ ), and Fermi resonance of methyl group, respectively. After contacting DETA, time dependent SFG signal changes monitored at 2875 and 2940  $\text{cm}^{-1}$  showed signal intensities decreased over time (Figure 3-18b). Such signal decrease was due to the disruption of OTCS SAM methyl endgroup ordering by DETA molecules. SFG spectrum was collected after signal stabilization and is shown in Figure 3-18a (red circle). Almost no resolvable peaks could be seen. This indicated DETA could gradually disorder molecular structures of OTCS SAM after contact. Then DETA was removed and the SAM surface was washed using water and studied again using SFG. The OTCS signal returned and showed slightly different peak ratios as compared to the original OTCS surface (Figure 3-18a, blue triangle). This indicated the partial recovery of the SAM ordering and the reorientation of SAM after DETA being washed away.

Since DETA can disorder OTCS SAM during contact, we can use this method to test if DETA can diffuse through the PET thin film. PET was dissolved into 2-chlorophenol for film preparation. It was impossible to spin coat PET 2-chlorophenol solution onto the OTCS SAM due to dewetting. However, the wettability of toluene was good on the OTCS SAM surface. Therefore, a 5 wt%  $d_8$ -PS solution in toluene was first spin coated for 30s on the OTCS SAM surface using 1500 rpm to form a thick  $d_8$ -PS film on the SAM. Then 2 wt% PET in 2-chlorophenol was fast spun on the  $d_8$ -PS film at 4000 rpm for 30s. The resulting surface showed no dewetting. In order

to prove the PET film existence on the resulting film, ATR-FTIR spectrum was collected and is shown in the Figure 3-19 (1722  $\text{cm}^{-1}$  peak could be detected). Then SFG spectrum of the film was collected and is shown in Figure 3-18c (black square). Similar to the bare OTCS case, strong SFG signal from OTCS could be detected, indicating good ordering of OTCS SAM at the silica/ $d_8$ -PS interface. After contacting the above sample with DETA, SFG signals at 2875 and 2940  $\text{cm}^{-1}$  significantly decreased quickly due to the change of the refractive indices. Then the signals gradually decreased to the baseline similar to the bare OTCS case (Figure 3-18d, Figure 3-18c red circle). This indicates that DETA can diffuse through the film and disorder the OTCS SAM. It was noticed that the signal decrease speed for the OTCS-polymer case (Figure 3-18d) was a little bit faster than the bare OTCS case (Figure 3-18b). This might be due to the interaction between polymer and OTCS, which might alter the properties of OTCS interacting with DETA. The signal decrease started right after the DETA contact, indicating the fast diffusion of DETA into PET. After contacting DETA, the OTCS-polymer sample was washed using water. SFG signal (Figure 3-18c blue triangle) showed that OTCS signal was recovered similar to the bare OTCS case (Figure 3-18a). The weaker intensity as compared to the original condition may be caused by the remaining of DETA molecules in the polymer matrix.

The above discussion shows that DETA can diffuse through the PET film after contact. Such a diffusion process plus the PET-DETA reaction modify not only the PET surface but also the interphase area, which play an important role in the interfacial crosslinking during the epoxy curing process.

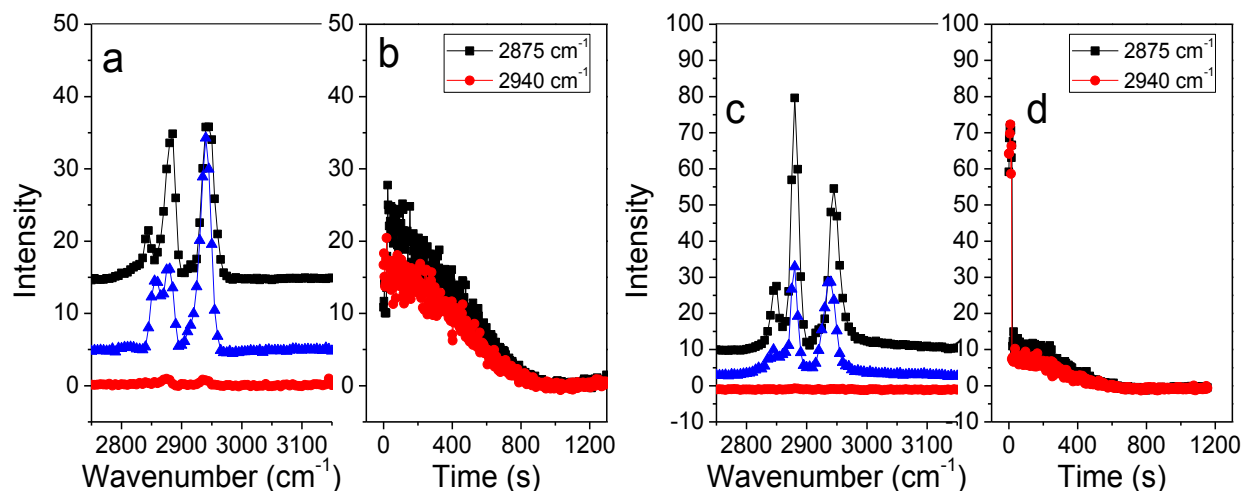


**Figure 3-18.** (a) SFG spectra of OTCS SAM (black square), OTCS SAM contacting with DETA after stabilization (red circle), OTCS SAM washed using water after contacting with DETA (blue triangle). (b) Time dependent SFG signal change of OTCS methyl group at 2875 and 2940 cm<sup>-1</sup> after contacting with DETA. (c) SFG spectra of PET coated on *d*<sub>8</sub>-PS deposited on an OTCS SAM (black square), the film was contacted with DETA after stabilization (red circle), the film was washed using water after contacting with DETA (blue triangle). (d) Time dependent SFG signal change of OTCS-*d*<sub>8</sub>-PS-PET film at 2875 and 2940 cm<sup>-1</sup> after contacting with DETA.

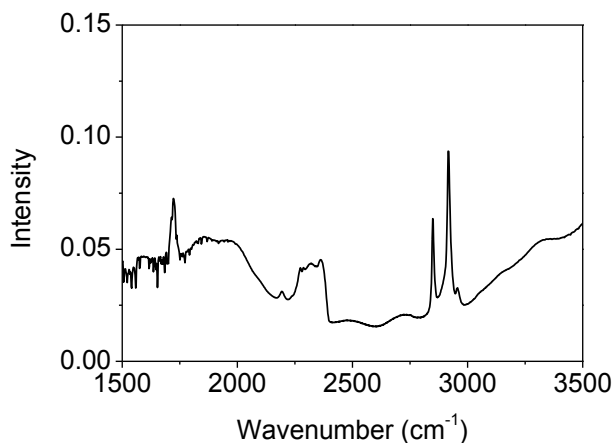


**Figure 3-19.** ATR-FTIR spectrum of a PET film spin coated on a *d*<sub>8</sub>-PS film on an OTCS SAM; PET C=O vibrational stretching signal at 1722 cm<sup>-1</sup> can be resolved.

### 3.4.5 Epoxy-amine/PET Interface

In the real adhesion applications, epoxy-amine mixtures are used instead of epoxy or amine alone. We contacted *d*<sub>4</sub>-PET with the BDDGE-DETA mixture and the CDDGE-DETA mixture



respectively and studied the resulting interfaces using ATR-FTIR and SFG.

We first studied the interactions between the BDDGE-DETA mixture and PET using ATR-FTIR before curing the sample. The ATR-FTIR spectrum detected more closely resembled that collected from the BDDGE/PET case (Figure 3-20a and Figure 3-13a) and is different from that in the DETA/PET case (Figure 3-16a). This is because the major component in the mixture was BDDGE instead of DETA. After curing, the C=O vibrational stretching intensity slightly decreased (Figure 3-20a). It is possible that more PET was dissolved and degraded in the curing process. When we separated the cured epoxy (with amine) from the substrate and tested the resulting substrate surface, the C=O vibrational signal intensity further decreased. This indicates that it is the interphase between PET and BDDGE-DETA mixture that was broken when we separated the cured epoxy from the substrate. Small PET C=O signal could still be detected on the remaining substrate surface, indicating a thin PET film still remained on the substrate surface.

For the CDDGE-DETA mixture case, similar results were found. However, as compared to the BDDGE-DETA mixture case, less PET was dissolved before and after curing the epoxy (Figure 3-20b). After breaking the interphase and removing the cured epoxy chunk, we also examined the resulting prism surface. It was found that the C=O signal intensity also decreased. Comparing to the BDDGE-DETA case, stronger C=O signal remained after breaking the interphase, indicating more PET was left on the substrate.

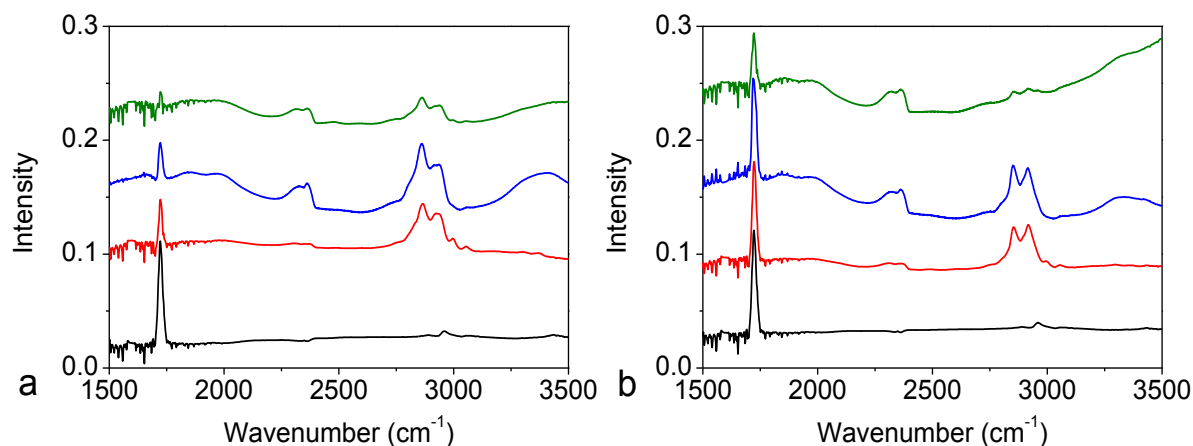


**Figure 3-20. ATR-FTIR spectra collected from (a) PET (black), PET contacting uncured BDDGE-DETA mixture (red), PET contacting cured BDDGE-DETA mixture (blue), the resulting PET surface after breaking the PET/BDDGE-DETA mixture interface (green); (b) PET (black), PET contacting uncured CDDGE-DETA (red), PET contacting cured CDDGE-DETA (blue), the resulting PET surface after breaking the PET/CDDGE-DETA mixture interface (green).**

It was demonstrated above that both epoxy and amine tend to diffuse into the  $d_4$ -PET film and adopt some order at the  $d_4$ -PET/silica prism interface; the  $d_4$ -PET and epoxy or amine has no clear boundary that could generate detectable SFG signal. Therefore, we believe that there is no distinct interface when  $d_4$ -PET is in contact with the epoxy-amine mixture due to their interactions and the diffusion of epoxy-amine mixture, generating no SFG signal. The SFG results showed that before curing the mixture, some SFG signal likely from the amine molecules dominated the SFG spectra (Figures 3-21a and 3-21e). The spectral features were quite similar to those shown in Figure 3-17 but different from those in Figure 3-15, which indicated that amine primarily determined the interfacial structure of the  $d_4$ -PET/silica substrate interface after the diffusion of epoxy-amine mixture through  $d_4$ -PET. After curing, the SFG spectra collected were similar to those collected before curing, but the signal intensities were comparably weaker (Figures 3-21b and 3-21f). Again we believe that these spectral features were likely generated from the  $d_4$ -PET/silica prism interface. No SFG signal is likely to be generated from the  $d_4$ -PET/epoxy-amine mixture interphase area,

indicating that the extensive chemical reaction, diffusion, and crosslinking occurred in such an area. This is an important feature for good adhesion.<sup>41</sup>

### **3.4.6 Silane Incorporation into Epoxy-amine System**

Our previous publication showed that strong SFG interfacial signal detected from the polymer epoxy-amine system indicated insufficient interfacial crosslinking or reaction which could lead to weak adhesion.<sup>43</sup> On the other hand, weak SFG signal indicated a disordered interfacial structure, very likely due to sufficient interfacial diffusion, crosslinking, or reaction which could lead to strong adhesion.<sup>41</sup> In order to generalize such a conclusion and develop further understanding of the adhesion mechanism, in this work, we incorporated reactive and non-reactive silanes to the epoxy-amine systems and performed SFG study and mechanical adhesion test on these samples.

Silanes are small molecules and are widely used as addition promoters to change adhesion properties and other mechanical properties of adhesives. In this work we used three types of silanes:  $\gamma$ -GPS, ATMS and OTMS(18C) (or OTMS), the molecular structures of which are shown in Figure 3-2. All silanes have the same functional methoxy head groups connected to a silicon atom. Methoxy groups can react with hydroxyl groups and link silane to the system releasing methanol molecules. In the epoxy-amine/PET system, methoxy headgroups can react with hydroxyl groups on PET grafted by the amine. Additionally,  $\gamma$ -GPS has an epoxide endgroup, which can react with amine. ATMS has an amino endgroup, which can react with epoxy. Therefore, both  $\gamma$ -GPS and ATMS can perform good crosslinking with the system. However, OTMS has a methyl endgroup, which cannot react with any functional groups in the system. Adding OTMS to the system can break the interfacial crosslinking network.

Silanes were incorporated into the BDDGE-DETA mixtures at 1.5 wt% before curing. Then

the interfacial structures of the mixtures in contact with  $d_4$ -PET were examined using SFG. As shown in Figures 3-21a and 3-21b, for the  $\gamma$ -GPS and ATMS cases, the interfacial structures were similar to the case where silanes were not incorporated both before and after curing. This means that such silanes do not affect interfacial structures of BDDGE-DETA mixtures at the  $d_4$ -PET interface. We also detected N-H signal centered at  $3300\text{ cm}^{-1}$  for all cases before curing and the signal disappeared after curing (Figure 3-22), indicating the reaction of amine N-H groups in the curing process. For the OTMS case, the interfacial signal in the C-H region was quite different. Shown in Figure 3-21c, time dependent SFG signal change could be detected at the interface when OTMS was incorporated into the mixture. As time increased, silane methoxy headgroups or methylene backbone groups ( $2840\text{-}2850\text{ cm}^{-1}$ ) as well as methyl endgroup ( $2880$  and  $2940\text{ cm}^{-1}$ ) gradually ordered at the interface. Strong methylene and methyl group ordering could be observed after curing the epoxy (shown in Figure 3-21d). Such time-dependent interfacial structural change and silane ordering at the interface were not observed for  $\gamma$ -GPS and ATMS cases. Since  $\gamma$ -GPS and ATMS are reactive silanes, they can react and crosslink with the epoxy system. However, OTMS has a nonreactive endgroup which cannot react with the epoxy system but forms an ordered layer at the interface, generating strong silane SFG signal.

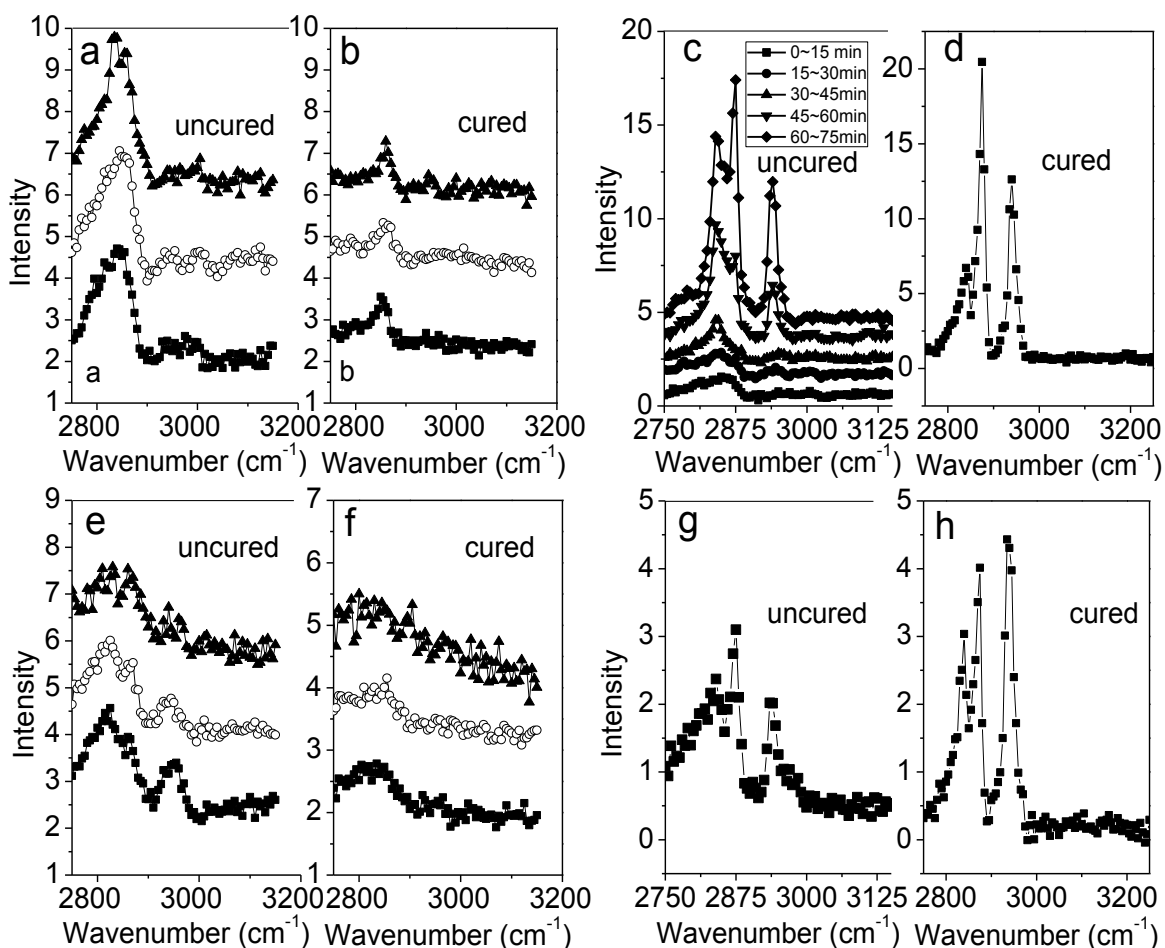


**Figure 3-21.** SFG spectra collected when  $d_4$ -PET was contacted by (a) uncured or (b) cured BDDGE-DETA mixtures with  $\gamma$ -GPS ( $\circ$ ) or ATMS ( $\blacktriangle$ ) or without silane ( $\blacksquare$ ) incorporated; (c) Time dependent SFG spectra of  $d_4$ -PET contacted with BDDGE-DETA mixture incorporated with OTMS silane before curing the sample. The time interval between spectra is 15 min; (d) SFG spectra of  $d_4$ -PET contacted with BDDGE-DETA mixture incorporated with OTMS silane after curing; SFG spectra collected when  $d_4$ -PET contacted by (e) uncured or (f) cured BDDGE-DETA mixtures with  $\gamma$ -GPS ( $\circ$ ) or ATMS ( $\blacktriangle$ ) or without silane ( $\blacksquare$ ) incorporated; SFG spectra of  $d_4$ -PET contacted with CDDGE-DETA mixture incorporated with OTMS silane (g) before and (h) after curing the sample.

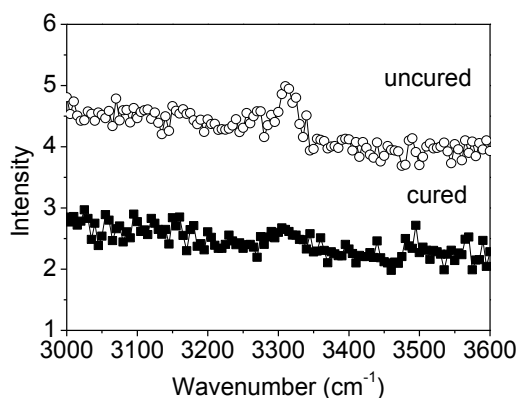


**Figure 3-22. SFG spectra in the N-H stretching frequency range at the interface between  $d_4$ -PET and uncured (○) or cured (■) BDDGE-DETA mixture coupled with ATMS silane. Other silane cases and the case without silane have similar results as shown.**

We also incorporated silanes into the CDDGE-DETA mixtures and contacted the mixtures with  $d_4$ -PET. Similarly, for the addition of  $\gamma$ -GPS and ATMS, the interfacial structures were quite similar to that without introducing the silanes (shown in Figures 3-21e and 3-21f). Very weak signal could be detected at such interfaces before and after curing. For the OTMS case, before curing the CDDGE-DETA mixture at the  $d_4$ -PET interface, some signals from the silane could be observed. Unlike the BDDGE epoxy case, here OTMS signal did not change with time before curing. The viscosity of CDDGE epoxy is higher than the BDDGE epoxy. Silanes may require higher energy to move and reorient in the CDDGE system. This may explain why after curing the CDDGE-DETA mixture with OTMS, SFG signals from silane were weaker than the BDDGE case but still increased as compared to the uncured condition (shown in Figures 3-21d, 3-21g and 3-21h). We believe that OTMS tends to form an ordered hydrophobic layer at the PET/epoxy-amine interface; such a layer is not adequately crosslinked with the epoxy system and is easier to break as compared to other crosslinked interfaces. Therefore, weak adhesion is expected when OTMS is incorporated into the epoxy-amine system while strong adhesion is expected for the other two silane cases. For convenience, all the vibrational peak assignments in this study are listed in Table

3-1.

Vibrational Frequency (cm <sup>-1</sup> )	Vibrational Modes (stretching)
<b>PET or <i>d</i><sub>4</sub>-PET</b>	
1722	C=O
2960-2970	C-H (O-CH <sub>2</sub> -C as)
3075	C-H (aromatic)
<b>Epoxy</b>	
2850	C-H (C-CH <sub>2</sub> -C s)
2920	C-H (C-CH <sub>2</sub> -C as)
2950-2970	C-H (O-CH <sub>2</sub> -C as)
3000	C-H (epoxide)
<b>Amine</b>	
2820-2850	C-H (N-CH <sub>2</sub> -C s)
2930-2960	C-H (N-CH <sub>2</sub> -C as)
3300	N-H
<b>Silane</b>	
2840-2850	C-H (O-CH <sub>3</sub> s, or C-CH <sub>2</sub> s)
2875	C-H (C-CH <sub>3</sub> s)
2940	C-H (C-CH <sub>3</sub> Fermi)

**Table 3-1. Summary of vibrational peak assignments for the SFG and ATR-FTIR spectra of molecules discussed in the paper. (s: symmetric; as: asymmetric; Fermi: Fermi resonance)**

Adhesion test was carried out to measure the adhesion strength between PET and epoxy-amine mixture. As shown in Figure 3-23 for both epoxies, when  $\gamma$ -GPS and ATMS were incorporated into the system, adhesion strength of the epoxy-amine silane mixture to PET was measured to be similar to the case without silane incorporated. Differently, when OTMS was incorporated to the epoxy-amine mixture, the adhesion strength was significantly reduced. This result further confirms that nonreactive silanes tend to segregate to the epoxy-amine/PET interface, forming an ordered silane layer and reducing the formation of interfacial crosslinking. It is also shown in Figure 3-23 that after the same curing condition, CDDGE-DETA tends to have much stronger adhesion to PET than BDDGE-DETA. This may be due to different reaction rates of epoxies with DETA. In the curing experiment, we found that CDDGE had higher reaction rate

with DETA as compared to BDDGE. Therefore, in the curing process on PET, CDDGE should also have higher reaction rate with grafted N-H groups on PET surface, resulting in better interfacial crosslinking and providing stronger adhesion. Additionally, comparing Figure 3-21b, 3-21d and 3-21f, 3-21h, we found that after curing, the CDDGE-DETA/ $d_4$ -PET interface generated weaker SFG signal as compared to the BDDGE-DETA/ $d_4$ -PET interface. Based on the previous hypothesis that weaker SFG signal indicates stronger adhesion,<sup>41</sup> it is reasonable that the CDDGE-DETA/ $d_4$ -PET interface has stronger adhesion.

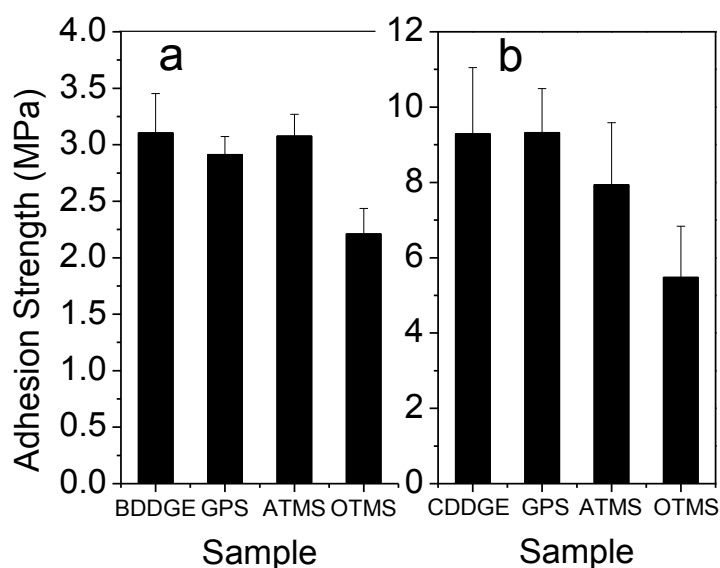


**Figure 3-23. Mechanical adhesion test results of PET blocks adhered by (a) BDDGE-DETA mixture and (b) CDDGE-DETA mixture with and without  $\gamma$ -GPS, ATMS and OTMS incorporated into the system.**

### 3.4.7 Adhesion Mechanism between PET and Epoxy-amine Mixture

Based on the above observations, we proposed a scheme for the adhesion between PET and epoxy-amine mixture, as shown in Figure 3-24. It is known that amine can modify the PET surface structure.<sup>38-40</sup> Amino and hydroxyl functional groups can be introduced to the PET surface during the amine-PET interaction.<sup>38-40</sup> We showed in this work that amine could



diffuse into PET and react with the polymer bulk at the interphase area. Therefore, in this area PET backbone tended to be broken with N-H and O-H groups tethered. At the initial contact of epoxy-amine mixture with PET, this reaction was triggered. In the curing process carried out at a higher temperature, this reaction was accelerated. Epoxy could also form an interphase with PET by dissolving part of the polymer. Therefore, in this interphase region, amine, epoxy and PET were all present. In the epoxy curing process, the grafted N-H and O-H functional groups on PET would react with epoxide groups in the epoxy to crosslink epoxy with PET. The reaction between the N-H group and the epoxide group dominated such crosslinking reactions, providing strong adhesion between epoxy-amine mixture and PET. The proposed reaction mechanism at the interphase is shown in Figure 3-24. Reactive silanes could sufficiently crosslink with the epoxy-amine-PET system through their endgroups, providing similar strong adhesion as the case when silane was not incorporated. In real applications in industry, fillers are used in the epoxy-amine mixture. In such cases the addition of such reactive silanes to the system could strengthen the material's mechanical property due to the stronger binding between the silanes and the fillers. On the other hand, nonreactive silane OTMS could not sufficiently crosslink with the system and tended to form an ordered layer at the interface, providing weak adhesion. The silane proportion in the epoxy-amine mixture was low (1.5 wt%). Therefore, the OTMS silane layer might not cover the entire epoxy polymer interface, leaving part of the interface well crosslinked. This explains why for the OTMS case, the adhesion strength was reduced as compared to other cases, but certain adhesion strength still remained (Figure 3-23).

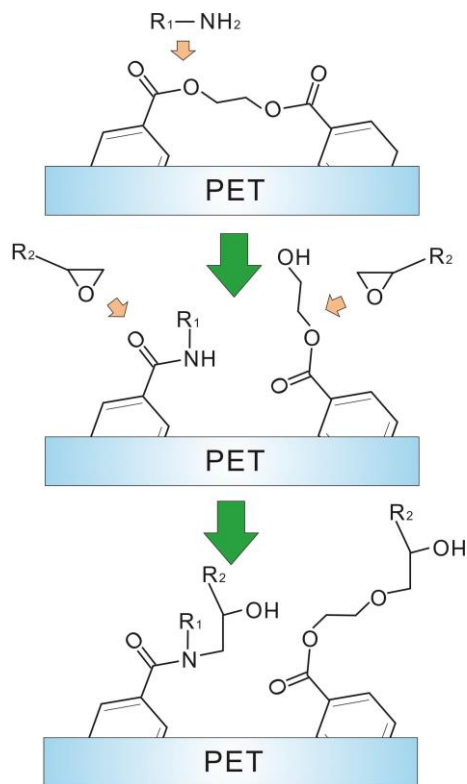


**Figure 3-24. The reaction of epoxy-amine mixture with PET.**

According to Figure 3-28, amine tends to modify PET by grafting amino and hydroxyl groups for further epoxy reaction. After curing, additional hydroxyl groups may still remain due to their weak reaction with epoxide groups. Therefore, the cured epoxy-amine/PET interface should be more hydrophilic as compared to the original PET surface. In packaging, it is well known that water molecule can diffuse into the epoxy-amine/substrate interface and delaminate the epoxy material from substrates under high humidity levels or at high temperatures.<sup>42-43</sup> It is highly possible that the interfacial reactions during epoxy-amine curing process make the interface more hydrophilic and thus allow water to easily diffuse through. This was proved by the water contact angle measurements of the fractured PET/epoxy-amine interfaces after curing.

After BDDGE-DETA or CDDGE-DETA was cured on the PET surface, the epoxy chunk was peeled off from the substrate. The water contact angle on the resulting surface (PET side) was measured (Table 3-2). For both cases, surface water contact angle decreased as compared to the

original PET surface. Furthermore, the BDDGE case had a smaller contact angle as compared to the CDDGE case. The results indicated that the hydrophobicity of PET/epoxy interface was lower than the original PET surface, suggesting the presence of hydrophilic groups such as O-H or N-H at the interphase. Such a decrease in hydrophobicity may result in water diffusion into the interface and causes epoxy delamination from the PET substrate. This result also explains why epoxy material has relatively poor water resistance compared to other adhesives such as silicone adhesives.<sup>44</sup>

PET surface	PET/BDDGE	PET/CDDGE
61.1±0.1°	25.8±0.2°	37.7±0.0°

**Table 3-2. Contact angle measurement results of the PET surface and the fractured PET/epoxy-amine interphase (after the removal of CDDGE-DETA or BDDGE-DETA epoxy chunk from the substrate after curing).**

### 3.4.8 Conclusion

In this work we studied the adhesion mechanism between epoxy-amine mixture and PET at the molecular level using SFG and ATR-FTIR spectroscopy. The results show that epoxies can dissolve part of the PET film during the contact and can diffuse into the PET film. Amine can diffuse into and react with PET by breaking chemical bonds in the polymer backbone and grafting amino and hydroxyl groups to PET. Both epoxy and amine tend to change PET surface structures at the initial contact. The reactions between grafted amino functional groups and epoxide groups in the epoxy occur during the curing process and provide good interfacial crosslinking at the PET/epoxy-amine mixture interface. Such crosslinking events lead to good interfacial adhesion. This hypothesis was further tested by coupling reactive and nonreactive silane molecules into the epoxy amine mixtures. Reactive silanes such as  $\gamma$ -GPS and ATMS tend to crosslink with the system

to provide strong adhesion. Nonreactive silane OTMS tends to order at the interface and prevents good crosslinking to happen, and thus leads to weak adhesion. Adhesion testing results further confirm the above analysis. This research provides an in-depth understanding of the adhesion mechanism between PET and epoxy materials at the molecular level. It can help to develop advanced adhesives and adhesion promoting materials with improved properties. It also shows the feasibility to combine ATR-FTIR and SFG spectroscopies to study buried adhesive interfaces *in situ* non-invasively.

### **3.5 Overall Summary**

In this Chapter, adhesion mechanisms between PET and epoxy-amine mixtures have been extensively investigated using both SFG and ATR-FTIR spectroscopies. Deduced interfacial molecular structures were correlated to the mechanical adhesion test results. We found that ordered interfacial structures can lead to weak adhesion, while randomized interfacial structures indicate strong adhesion. The adhesion mechanism between PET and epoxy-amine was proposed and was tested by SFG and ATR-FTIR spectroscopies as well as water contact angle measurements. This research provides an in-depth understanding of the adhesion mechanism between PET and epoxy materials at the molecular level. It can help to develop advanced adhesives and adhesion promoters. It also demonstrated the feasibility to combine ATR-FTIR and SFG spectroscopies as a non-invasive approach to study buried adhesive interfaces *in situ*.

### 3.6 References

1. Tong, H. M., *Mater. Chem. Phys.* **1995**, *40*, 147-161.
2. Wong, C., *Mater. Chem. Phys.* **1995**, *42*, 25-30.
3. Sham, M. L.; Kim, J. K., *Journal of Electronic Packaging* **2005**, *127*, 47-51.
4. Kornain, Z.; Jalar, A.; Rasid, R.; Abdullah, S., *Journal of Electronic Packaging* **2010**, *132*, 041012.
5. Luo, S. J.; Yamashita, T.; Wong, C. P., *Journal of Electronics Manufacturing* **2000**, *10*, 191-200.
6. Yung, K. C.; Liem, H., *J. Appl. Polym. Sci.* **2007**, *106*, 3587-3591.
7. Yacobi, B. G.; Martin, S.; Davis, K.; Hudson, A.; Hubert, M., *J. Appl. Phys.* **2002**, *91*, 6227-6262.
8. Hegde, S.; Pucha, R. V.; Sitaraman, S. K., *Journal of Materials Science-Materials in Electronics* **2004**, *15*, 287-296.
9. Zhang, Y. L.; Shi, D. X. Q.; Zhou, W., *Microelectronics Reliability* **2006**, *46*, 409-420.
10. Newby, B. M. Z.; Chaudhury, M. K.; Brown, H. R., *Science* **1995**, *269*, 1407-1409.
11. Sathyanarayana, M. N.; Yaseen, M., *Prog. Org. Coat.* **1995**, *26*, 275-313.
12. Pocius, A. V., *Adhesion and adhesives technology: an introduction*. Hanser Gardner Pubns: 2002.
13. Harding, P. H.; Berg, J. C., *J. Appl. Polym. Sci.* **1998**, *67*, 1025-1033.
14. Kinloch, A. J., *Adhesion and adhesives: science and technology*. Springer: 1987.
15. Shen, Y., *Nature* **1989**, *337*, 519-525.
16. Chen, Z.; Shen, Y.; Somorjai, G. A., *Annual review of physical chemistry* **2002**, *53*, 437-465.
17. Kataoka, S.; Cremer, P. S., *Journal of the American Chemical Society* **2006**, *128*, 5516-5522.
18. Baldelli, S., *Acc. Chem. Res.* **2008**, *41*, 421-431.
19. Ye, S.; Morita, S.; Li, G. F.; Noda, H.; Tanaka, M.; Uosaki, K.; Osawa, M., *Macromolecules* **2003**, *36*, 5694-5703.
20. Holinga, G. J.; York, R. L.; Onorato, R. M.; Thompson, C. M.; Webb, N. E.; Yoon, A. P.; Somorjai, G. A., *J. Am. Chem. Soc.* **2011**, *133*, 6243-6253.
21. Hayes, P. L.; Keeley, A. R.; Geiger, F. M., *J. Phys. Chem. B* **2010**, *114*, 4495-4502.
22. Perry, A.; Neipert, C.; Space, B.; Moore, P. B., *Chem. Rev.* **2006**, *106*, 1234-1258.
23. Buck, M.; Himmelhaus, M., *Journal of Vacuum Science & Technology a-Vacuum Surfaces and Films* **2001**, *19*, 2717-2736.
24. Williams, C. T.; Beattie, D. A., *Surf. Sci.* **2002**, *500*, 545-576.
25. Chen, P.; Kung, K. Y.; Shen, Y. R.; Somorjai, G. A., *Surf. Sci.* **2001**, *494*, 289-297.
26. Moad, A. J.; Simpson, G. J., *J. Phys. Chem. B* **2004**, *108*, 3548-3562.
27. Jayathilake, H. D.; Driscoll, J. A.; Bordenyuk, A. N.; Wu, L. B.; da Rocha, S. R. P.; Verani, C. N.; Benderskii, A. V., *Langmuir* **2009**, *25*, 6880-6886.
28. May, C. A., *Epoxy resins: chemistry and technology*. CRC Press: 1988.
29. Petrie, E. M., *Epoxy adhesives formulations*. Mc Grow-Hill: 2006.
30. Brown, H. R., *Macromolecules* **2001**, *34*, 3720-3724.
31. Kulasekere, R.; Kaiser, H.; Ankner, J. F.; Russell, T. P.; Brown, H. R.; Hawker, C. J.; Mayes, A. M., *Macromolecules* **1996**, *29*, 5493-5496.
32. Sikka, M.; Pellegrini, N. N.; Schmitt, E. A.; Winey, K. I., *Macromolecules* **1997**, *30*, 445-

455.

33. Bernard, B.; Brown, H. R.; Hawker, C. J.; Kellock, A. J.; Russell, T. P., *Macromolecules* **1999**, *32*, 6254-6260.
34. Loch, C. L.; Ahn, D.; Chen, C. Y.; Wang, J.; Chen, Z., *Langmuir* **2004**, *20*, 5467-5473.
35. Loch, C. L.; Ahn, D.; Chen, C.; Wang, J.; Chen, Z., *Langmuir* **2004**, *20*, 5467-5473.
36. Loch, C. L.; Ahn, D.; Chen, Z., *J. Phys. Chem. B* **2006**, *110*, 914-918.
37. Carrasco, F.; Lacorte, T.; Briceño, K., *J. Appl. Polym. Sci.* **2005**, *98*, 1524-1535.
38. Avny, Y.; Rebenfeld, L., *J. Appl. Polym. Sci.* **1986**, *32*, 4009-4025.
39. Nissen, K.; Stevens, M.; Stuart, B.; Baker, A., *J. Polym. Sci., Part B: Polym. Phys.* **2001**, *39*, 623-633.
40. Bech, L.; Meylheuc, T.; Lepoittevin, B.; Roger, P., *J. Polym. Sci., Part A: Polym. Chem.* **2007**, *45*, 2172-2183.
41. Zhang, C.; Hankett, J.; Chen, Z., *ACS Appl. Mater. Interfaces* **2012**, *4*, 3730-3737.
42. Zhou, J.; Lucas, J. P., *Polymer* **1999**, *40*, 5505-5512.
43. Lam, D.; Wang, J., *J. Electron. Mater.* **2007**, *36*, 226-231.
44. Myers, J. N.; Zhang, C.; Lee, K.-W.; Williamson, J. M.; Chen, Z., *Langmuir* **2013**, *30*, 165-171.

# CHAPTER 4

## SFG SPECTROSCOPIC STUDIES ON BIOLOGICAL INTERFACES SUPPLEMENTED BY ATR-FTIR SPECTROSCOPY: LIPID TRANSBILAYER MOVEMENT IN A MODEL CELL MEMBRANE

### 4.1 Background and Motivation

Gene therapy is a powerful and elegant method for a variety of disease treatments and genetic engineering. It requires effective and safe delivery of genetic material to the cell interior, which is inherently challenging. Viral vectors have excellent delivery efficiency but can cause severe immunotoxic or inflammatory issues.<sup>1</sup> Consequently, extensive research has been performed to develop non-viral gene transfer agents; the most successful ones are polycationic materials such as poly-L-lysine and polyethylenimine (PEI),<sup>2</sup> with PEI being the most characterized and most prominent polycation for gene delivery.<sup>3-7</sup> It is available in both linear and branched forms with a broad range of molecular weights (e.g., from several hundred Daltons to 1500 kDa). High molecular weight PEIs, especially those with the molecular weight larger than 25 kDa, have been widely used for nucleic acid delivery.<sup>7-12</sup> PEI can condense DNA or RNA to form polyplex nanostructures through electrostatic interactions for further endocytosis.<sup>13-15</sup> A myriad of research showed that the use of PEI can greatly improve gene delivery efficiency.<sup>10, 16</sup> The effects of branched and linear PEIs on gene delivery have also been compared in various studies.<sup>17-19</sup>

Although the use of PEI has several benefits over viral vectors, reports have attested that PEI in a biological system exhibits cytotoxicity.<sup>20-24</sup> PEI's cytotoxicity is quite complex, involving interactions with many different components in a biological system. Attempts to understand this mechanisms have resulted in many hypotheses, one of which is a two-stage PEI cytotoxic process, which includes an early necrotic-like cell membrane change followed by a later stage mitochondria apoptotic pathway.<sup>21, 25</sup> Both of the proposed steps are strongly related to the influence of PEI on lipid membrane including membrane damage, lipid translocation, or membrane potential change.<sup>22-24</sup> Therefore, an understanding of the interactions between PEI and lipid membranes is an important step to further reveal mechanisms behind the cytotoxicity of PEI. Previous publications demonstrated that one possible cause of such cytotoxicity was that in a PEI-based polyplex mixture, a large amount of highly charged PEIs remained in the free form, which might accelerate membrane destabilization events and induce cell dysfunction.<sup>26</sup> However, the presence of free PEI molecules might be essential for the permeation and incorporation of PEI/DNA complexes into cells.<sup>26</sup> Such an assumption has been tested by using purified PEI complexes with reduced free PEI amount, which exhibited reduced cytotoxicity, but at the cost of a decrease in transfection efficiency.<sup>26</sup> Therefore, understanding how PEI in the free form interacts with cell membranes at a molecular level can help to clarify the underlined mechanisms of PEI's cytotoxicity. Cell plasma membranes are a complicated mixture of many components including phospholipids, proteins, and cholesterol, where many of these different components may be involved in the PEI-membrane interactions. In order to simplify the study and understand PEI - cell membrane interactions systematically, this work focuses on examining the PEI - phospholipid bilayer interaction, since phospholipids are the most abundant component in the mammalian cell membranes and form the basic cell membrane bilayer structure. Typically, lipid transbilayer



movement occurs with the help of membrane proteins, however we aim to investigate whether PEI can induce lipid transbilayer movement in the absence of membrane proteins. Specifically, we studied the molecular interaction of a substrate supported lipid bilayer (serving as a model cell membrane) with free PEI molecules in solution in order to understand the PEI-bilayer interaction behavior. Although a variety of analytical techniques have been used to study PEI/DNA complexes,<sup>27-33</sup> understanding the molecular level PEI-cell membrane interaction *in situ* can help to further interpret PEI induced cytotoxicity.<sup>24</sup>

Traditional surface sensitive techniques, although many of them are powerful and use unique devices, are limited in their ability to study interactions between PEI and lipid bilayers. XPS<sup>34-35</sup> and SIMS<sup>36-37</sup> are widely used spectroscopic techniques for surface composition studies, however they require high vacuum to operate and thus have difficulty in finding applications in aqueous environments. SERS requires a rough metal surface to generate enhanced Raman spectrum,<sup>38-39</sup> making it incompatible with many bio-interfaces. ATR-FTIR is not intrinsic surface selective, since it relies on an evanescent wave that may penetrate several hundred nanometers deep into the sample.<sup>40-41</sup> ATR-FTIR can be used to monitor the presence of lipid bilayers and damage associated with lipid removal from the bilayer medium. However, it is impossible to use it to study lipid transbilayer movement between inner and outer leaflets in a lipid bilayer.

SFG vibrational spectroscopy has been shown to be a powerful tool to probe lipid bilayers at the molecular level.<sup>42-45</sup> SFG is a second order nonlinear optical spectroscopy with intrinsic sub-monolayer surface or interface sensitivity.<sup>46-52</sup> SFG can provide information about interfacial molecular presence, orientation, and dynamics *in situ* and in real time.<sup>45</sup> It has been developed to study various interfaces involving polymer materials<sup>53-59</sup> and biomolecules.<sup>43-44, 60-69</sup> As a vibrational spectroscopic technique, SFG detects signals from interfacial molecular vibrational

modes which provide interfacial molecular structural information. SFG has also been used to study lipid transbilayer movement, also known as lipid translocation or lipid ‘flip-flop’ in supported lipid bilayers.<sup>42, 70-74</sup> Conboy and his coworkers studied lipid translocations in model cell membranes at different temperatures with different lipid compositions.<sup>42, 70</sup> By preparing asymmetric bilayers using different lipid types for the inner and outer leaflets, SFG signal from each leaflet was detected simultaneously and monitored in real time.<sup>42</sup> Studies have also shown that lipid translocation in a bilayer can be affected by membrane-associated peptides<sup>71, 73</sup>, membrane lateral pressure,<sup>72</sup> cholesterol content,<sup>74</sup> etc. As such, it has been demonstrated that SFG is a powerful technique for bilayer lipid translocation studies *in situ* and in real time. However, SFG results cannot exclude possible lipid bilayer damage or removal from the substrate.

The goal of this research is to combine SFG and ATR-FTIR spectroscopies to study interactions of PEI with solid-supported lipid bilayers (serving as model cell membranes) at the molecular level, which can help to further understand the mechanism behind PEI’s cytotoxicity. SFG spectroscopy can be used to study the dynamics of PEI-induced lipid transbilayer movement in various model cell membranes, while ATR-FTIR spectroscopy can be used to monitor whether the supported lipid bilayer was damaged or removed by PEI molecules. This research helps to provide fundamental and systematic understanding on PEI’s molecular behavior while interacting with membrane bilayers and further elucidate its cytotoxic mechanism in biological systems.

## **4.2 Molecules Used in the Study**

Branched PEI (PEI-B, Mw = 25,000) was purchased from Sigma-Aldrich and dissolved in water at room temperature to form a 10,000 ppm concentration solution (used as stock solution). Linear PEI (PEI-L, Mw = 25,000) was purchased from Polysciences Inc. and was dissolved at > 60 °C in order to obtain the same stock concentration of 10,000 ppm. Both forms of PEI were

soluble in water at room temperature at  $\leq 100$  ppm concentration. Deionized water (18.2 M $\Omega$ ·cm, obtained from a Millipore Simplicity Water Purification System) was used throughout this study.

Phospholipids including hydrogenated dipalmitoylphosphatidylglycerol (DPPG) and deuterated  $d_{62}$ -DPPG (dDPPG), hydrogenated distearoylphosphatidylcholine (DSPC) and deuterated  $d_{70}$ -DSPC (dDSPC), hydrogenated dipalmitoylphosphatidylcholine (DPPC) and deuterated  $d_{62}$ -DPPC (dDPPC) were purchased from Avanti Polar Lipid. Lipids were dissolved in chloroform (Fluka) at 5 mg/mL for preparing bilayers. DPPG is a negatively charged lipid while both DPPC and DSPC are zwitterionic lipids with no net charge. DSPC has two more methylene groups on each fatty acid chain as compared to DPPC. The detailed lipid molecular formulas are listed in Figure 4-1. Here, DSPC lipid is used as a model for phosphatidylcholine (PC), which is abundant in mammalian cell membranes. DSPC also serves as a model for zwitterionic lipids in a membrane. Phosphatidylglycerol (PG) is found in many membranes to provide specific functions. In this work, DPPG is chosen to represent negatively charged lipids in a membrane.

CaF<sub>2</sub> right angle prisms were purchased from Altos Photonics Inc. and were soaked in toluene (Sigma Aldrich) overnight. They were then washed multiple times with ethanol and Contrex AP detergent water solution (Decon Laboratories) before being rinsed with deionized water and dried with nitrogen gas. Prisms were further cleaned using oxygen plasma (PE-50, Plasma Etch. Inc.) for two minutes before lipid monolayer deposition.

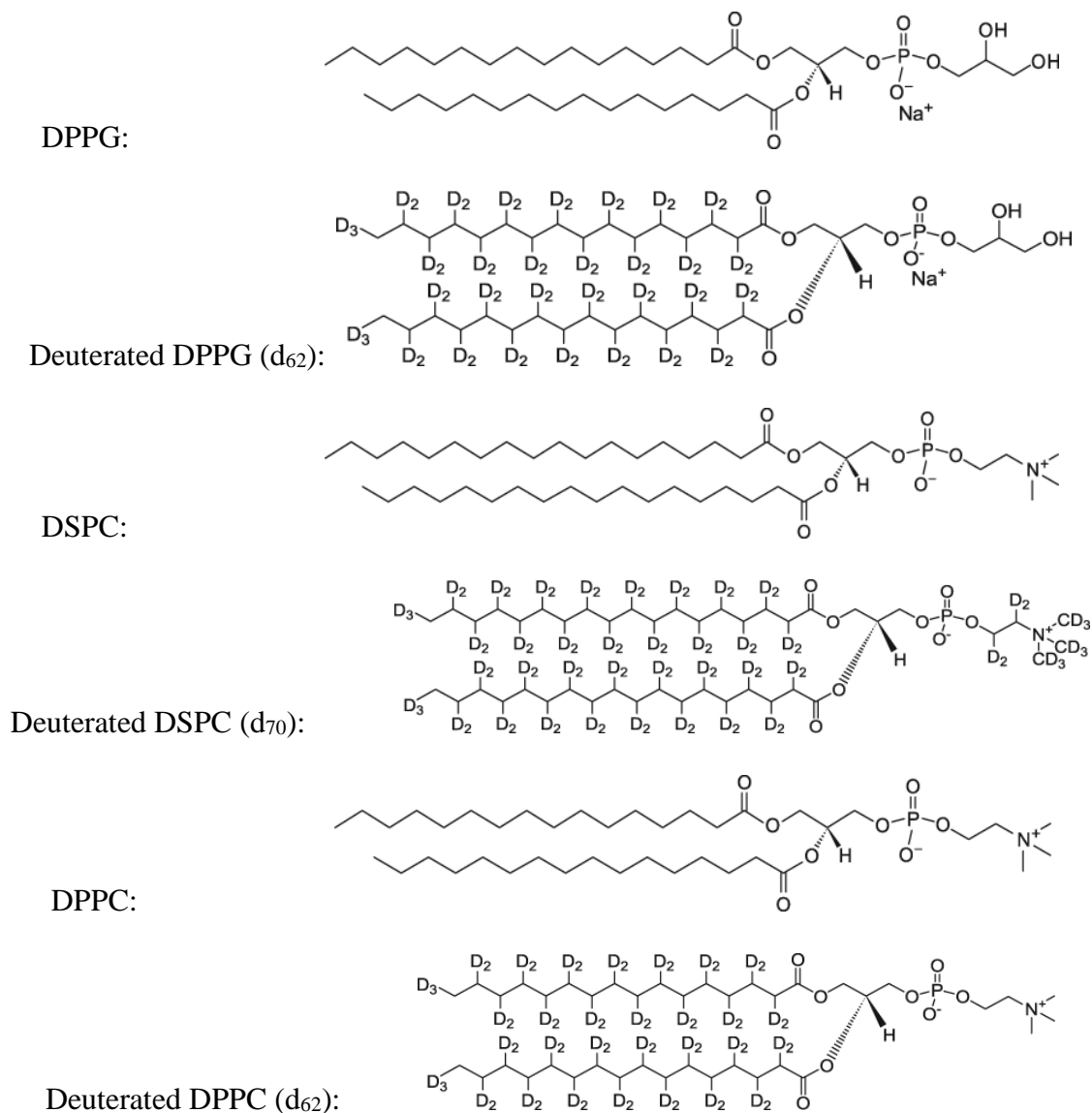


**Figure 4-1. Molecular formulas of lipid molecules used in the research.**

## 4.3 SFG Spectroscopic Study of Lipid Transbilayer Movement

### 4.3.1 SFG Experimental Geometry

As introduced in Chapter 1, SFG is a second order nonlinear optical spectroscopic technique capable of probing buried interfaces *in situ* with sub-monolayer sensitivity. Additionally, SFG has the ability to monitor real-time interfacial structural evolution, which

provides a direct insight into interfacial molecular dynamics and is crucial for studies on lipid translocations in bilayers.<sup>45</sup> For the lipid bilayers in this study, the inner leaflet was composed of deuterated lipids and the outer leaflet contained hydrogenated lipids. Such isotopically asymmetric bilayer arrangement allows for the generation of strong SFG signals from both leaflets. Lipid translocation inside such a bilayer tends to increase the degree of bilayer symmetry, and as a result, decreases SFG signal. Monitoring such time-dependent SFG signal decrease can provide a direct observation of lipid translocation dynamics in a lipid bilayer.

The details of our SFG spectrometer have been introduced in Chapter 1. The visible beam pulse energy used here was  $\sim 25 \mu\text{J}$ . The IR beam had a pulse energy of  $\sim 80 \mu\text{J}$  at  $2070 \text{ cm}^{-1}$  and  $\sim 150 \mu\text{J}$  at  $2875 \text{ cm}^{-1}$ . The focal spot diameter of the visible beam was  $\sim 400 \mu\text{m}$ . In this work, all the SFG spectra and time dependent SFG signals were collected using the ‘ssp’ polarization combination.

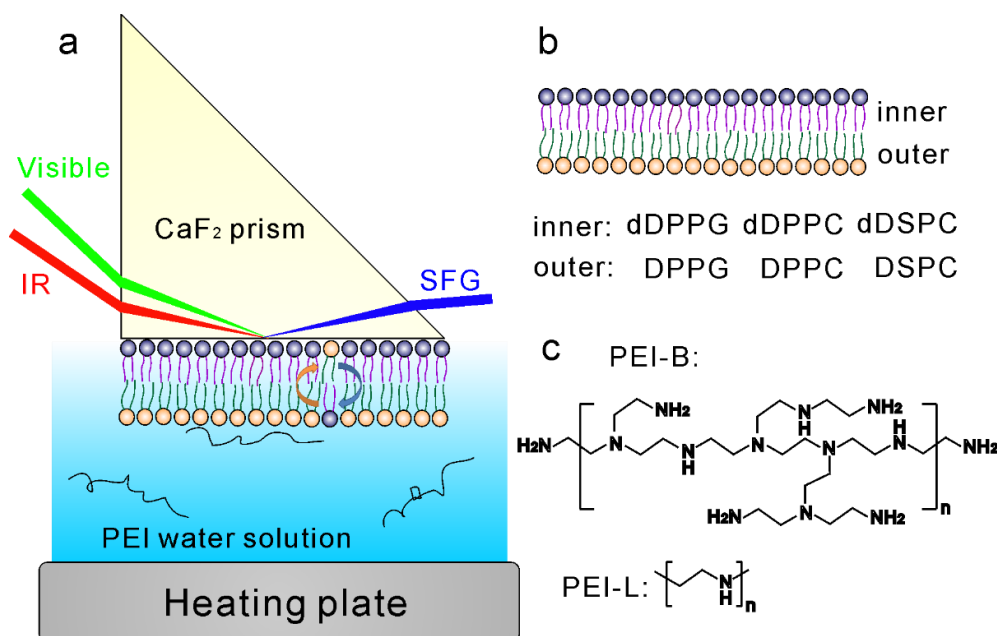


**Figure 4-2.** (a) Schematic of the SFG experimental geometry for lipid translocation study (different components are not drawn to scale), (b) lipid compositions of the initial supported bilayers (top leaflet is attached to the prism, bottom leaflet is facing subphase), and (c) molecular structures of polyethylenimines (PEIs). PEI-B: branched PEI, PEI-L: linear PEI.

A schematic of the experimental geometry used for SFG study is shown in Figure 4-2a. The lipid bilayer geometry and PEI molecular formulas are shown in Figures 4-2b and 4-2c, respectively.

#### **4.3.2 Using SFG to Measure Lipid Translocation in a Lipid Bilayer**

Lipid bilayers on CaF<sub>2</sub> prisms were constructed using Langmuir-Blodgett (LB) and Langmuir-Schaeffer (LS) method.<sup>75-76</sup> In this study, a deuterated lipid layer was used as the proximal leaflet (or inner leaflet, attached to the prism), whereas a hydrogenated lipid layer was used as the distal leaflet (or outer leaflet, in contact with PEI solution). A KSV2000 LB system (KSV NIMA) was used for the lipid monolayer deposition on CaF<sub>2</sub> prisms. One right-angle face of a CaF<sub>2</sub> prism was perpendicularly immersed into water in the LB trough. Lipid dissolved in chloroform was spread on the water surface and chloroform was allowed to evaporate. After stabilization, the surface was compressed by two barriers in the LB system at a speed of 5 mm/min until the surface pressure reached 34 mN/m. The prism was then lifted out from the water with a speed of 1 mm/min while a constant surface tension (34 mN/m) was maintained. This process deposited the first lipid layer (deuterated lipid layer) onto the CaF<sub>2</sub> prism. This deuterated lipid monolayer then came into contact with a hydrogenated lipid monolayer spread on the water surface (34 mN/m) to form a bilayer. After the lipid bilayer was formed, PEI stock solution (10,000 ppm) was injected into the subphase in contact with the lipid bilayer for SFG study. Different amounts of PEI solutions were used to achieve different final PEI concentrations in the subphase. A magnetic stir bar was used in the subphase to increase the diffusion rate of PEI. For experiments performed at near physiological temperature (39 °C), the subphase was heated using a hotplate (Isotemp) and the temperature of the interface area was measured using a thermometer (CSC32 SERIES Mini Benchtop Controller, Omega Engineering). Heating started after the

formation of each lipid bilayer. PEI was injected into the subphase 30 min after heating started. Temperature of 39 °C was chosen as a “near” physiological temperature relevant to PEI interactions in biological systems. Since the thermometer was placed near the bottom of the prism, in contact with the aqueous subphase, and there may be a small temperature difference between the supphase and the lipid bilayer, the subphase was heated to 39 °C (slightly above 37 °C). This way we believe that the lipid bilayer temperature should be ~37 °C.

Macroscopically, SFG signal intensity is proportional to the square of the effective second order nonlinear optical susceptibility  $\chi_{\text{eff}}^{(2)}$ . The resonance contribution of  $\chi_{\text{eff}}^{(2)}$  can be modeled as sums of Lorentzian functions:<sup>45, 55</sup>

$$I \propto \left| \chi_{\text{eff}}^{(2)} \right|^2 = \left| \chi_{\text{NR}}^{(2)} + \sum_q \frac{A_q}{\omega_q - \omega_{\text{IR}} - i\Gamma_q} \right|^2 \quad (4.1)$$

Here  $\chi_{\text{NR}}^{(2)}$  is the nonresonance background of the spectrum.  $A_q$ ,  $\omega_q$ ,  $\omega_{\text{IR}}$  and  $\Gamma_q$  are the signal amplitude, peak center of the vibrational transition, input IR beam frequency, and damping coefficient (or peak width), respectively.

$\chi_{\text{eff}}^{(2)}$  can be further correlated to the local second order nonlinear optical susceptibility  $\chi_{\text{IJK}}^{(2)}$  through Fresnel coefficients, which are functions of the laser input angles and the refractive indices of the materials forming the interface.<sup>50</sup> For a specific interface with fixed laser input angles:

$$\chi_{\text{eff}}^{(2)} \propto \chi_{\text{IJK}}^{(2)} \quad (4.2)$$

Macroscopic local nonlinear optical susceptibility  $\chi_{\text{IJK}}^{(2)}$  is determined by the surface number density N, the molecular hyperpolarizability  $\beta_{\text{ijk}}^{(2)}$ , and the transformation matrix R from the molecular frame (a,b,c) to the lab fixed frame (x,y,z).<sup>45</sup>

$$\chi_{IJK}^{(2)} = N \sum_{IJK=x,y,z} \langle R_{Ii} R_{Jj} R_{Kk} \rangle \beta_{ijk}^{(2)} \quad ijk = a,b,c \quad (4.3)$$

For the lipid translocation experiments performed in this study, SFG signal intensity contribution from the CD<sub>3</sub> (or CH<sub>3</sub>) stretching vibration was proportional to the square of net population difference of the deuterated (or hydrogenated) lipid molecules between the two (inner and outer) leaflets. This can be expressed as:<sup>70</sup>

$$I_{CD_3 \text{ or } CH_3} \propto |N_{\text{inner}} - N_{\text{outer}}|^2 \quad (4.4)$$

Here,  $N_{\text{inner}}$  and  $N_{\text{outer}}$  are the fractions of deuterated (or hydrogenated) lipid molecules in the inner and outer leaflets of the bilayer. At the initial contact of the two leaflets,  $I_{CD_3 \text{ or } CH_3}$  has its largest value. Lipid translocation tends to decrease the deuterated or hydrogenated lipid fraction difference between the two leaflets. Therefore,  $I_{CD_3 \text{ or } CH_3}$  will decrease until the lipids are homogeneously mixed in two leaflets; in the limit where  $N_{\text{inner}} = N_{\text{outer}}$ ,  $I_{CD_3 \text{ or } CH_3} = 0$ . This signal decrease can be monitored through SFG signal change as a function of time, which provides a way to quantitatively study lipid translocation dynamics.

It has been shown that the time dependent CD<sub>3</sub> or CH<sub>3</sub> symmetric stretching SFG signal intensity can be expressed as,<sup>70</sup>

$$I_{CD_3 \text{ or } CH_3} = I_{\text{max}} \cdot e^{-4kt} + I_{\text{min}} \quad (4.5)$$

Here  $I_{\text{max}}$  and  $I_{\text{min}}$  are the maximum and minimum SFG signal intensities observed from a certain stretching mode of either CD<sub>3</sub> or CH<sub>3</sub>. The lipid translocation rate constant is expressed as  $k$ . In this work, equation (4.5) was subsequently used to fit the time-dependent SFG data in order to quantitatively compare the lipid translocation rates in different conditions.



### 4.3.3 Lipid Translocation in dDPPG-DPPG Bilayer Induced by PEI at Different Temperatures

PG is a negatively charged lipid which is found in low concentration in most mammalian cell membranes (1-2 %). Certain membranes such as lung surfactants or bacterial cell membranes contain higher PG lipid content (more than 10 %). PG is typically used as a model for negatively charged lipid in membrane dynamics study. Here we studied the PEI interaction with dDPPG-DPPG bilayers at different temperatures. In the initial bilayer, hydrophobic interactions between the lipid alkyl chains and the presence of water around the lipid head group region strongly ordered the lipid molecules, generating strong SFG C-D and C-H stretching signals. In the C-D stretching frequency range, the strongest peak at  $2070\text{ cm}^{-1}$  was attributed to the C-D symmetric vibrational stretching of the deuterated methyl end group in the lipid alkyl chain from the inner leaflet (Figure 4-3a, black square). In the C-H stretching frequency range, peaks centered around 2875 and  $2940\text{ cm}^{-1}$  had contributions from the symmetric stretching and the Fermi resonance mode of the hydrogenated methyl end group in the lipid alkyl chain from the outer leaflet (Figure 4-3b, black square). In the following time-dependent SFG study, we monitored signal intensity changes of the  $2070$  and  $2875\text{ cm}^{-1}$  peaks simultaneously to study lipid dynamics of the inner and outer leaflets.

The lipid translocation of the dDPPG-DPPG bilayer at  $21\text{ }^{\circ}\text{C}$  without the addition of PEI into the subphase was very slow, and the change in SFG signal from this process can be ignored in this work. Upon the addition of PEI to the subphase forming a 100 ppm solution at  $21\text{ }^{\circ}\text{C}$ , SFG signal intensities of both the C-D and C-H stretching showed a sudden, yet small decrease before reaching equilibrium, as shown in Figure 4-4. SFG spectra of the bilayer were collected after adding PEI to the subphase (in Figure 4-3, 100 ppm PEI-L in subphase; the results of PEI-B addition were similar and thus were not shown). The broad SFG water signal disappeared. This was due to the disordering of interfacial water molecules after the adsorption of PEI-L to the

bilayer, likely causing the observed small signal decrease of lipid C-H peaks (water O-H signal is broad and can affect signal intensity in C-H stretching frequency range). Since only a slight decrease of the lipid SFG signal was observed with no further intensity change (Figure 4-4), it is believed that at 21 °C, PEI does not significantly induce lipid translocation inside a DPPG bilayer.

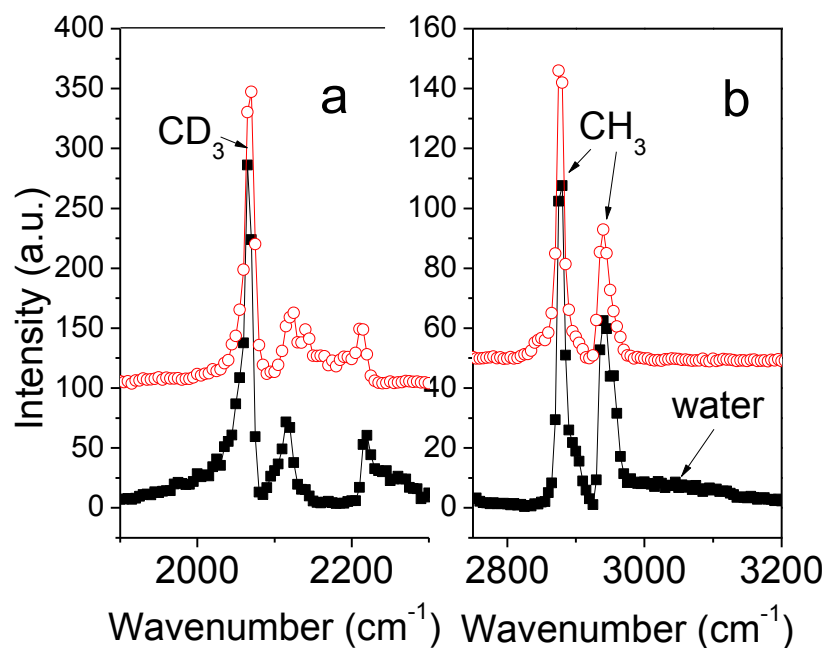


**Figure 4-3. SFG spectra in the (a) C-D and (b) C-H stretching frequency ranges of the dDPPG-DPPG bilayer before (black square) and after (red circle) the addition of PEI-L stock solution to the subphase to reach a 100 ppm PEI-L concentration at 21 °C.**

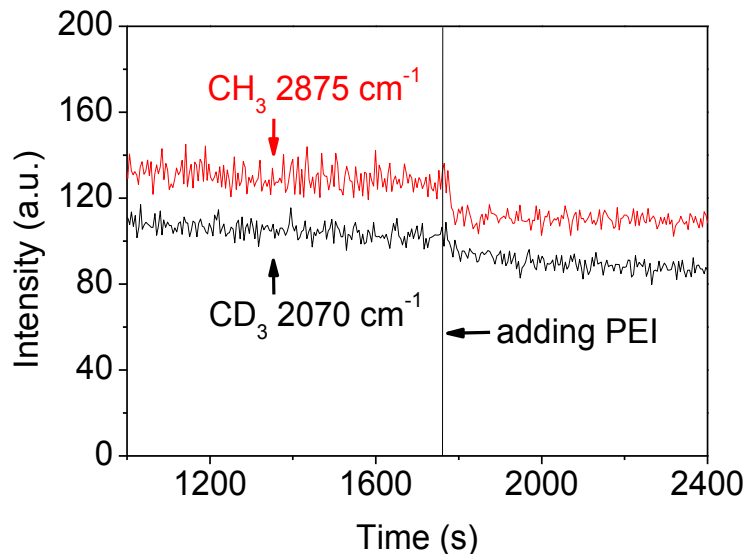


**Figure 4-4. Time-dependent SFG signals detected from the dDPPG-DPPG bilayer at 21 °C before and after the introduction of 100 ppm PEI-L to the subphase. SFG signals were monitored at 2070 (black) and 2875 (red)  $\text{cm}^{-1}$ . PEI stock solution was added to the subphase at ~1760 s.**

At 39 °C, the PEI-DPPG bilayer interaction behavior was quite different as compared to that occurred at 21 °C. Different volumes of the PEI stock solution were added to the subphase to form PEI solutions with different concentrations (10, 20, 50, and 100 ppm) in contact with the bilayer. Such concentrations were chosen based on previous PEI cytotoxicity studies.<sup>21-22, 25</sup> Time-dependent SFG signals monitored at 2070  $\text{cm}^{-1}$  showed that at all the above concentrations, bilayer SFG signal was significantly affected by the introduction of PEI to the subphase. As shown in Figure 4-5, a higher PEI concentration in the subphase led to a faster SFG signal decrease. At the same PEI concentration, PEI-B tended to induce a faster rate of SFG signal decrease as compared to PEI-L. Assuming no bilayer damage/removal was caused by the PEI solution, such SFG signal decrease was thus an observation of lipid translocation. Lipid translocation rate can be obtained by fitting the time dependent SFG signal curve using equation (4.5). The ‘k’ values derived from fitting results (including both C-D and C-H time dependent SFG signals) are shown in Figure 4-6.

They show that the DPPG lipid translocation rate constants ( $k$ ) of the inner (C-D) and outer leaflets (C-H) were similar for the same PEI-B or PEI-L concentration. This evidence suggests that the observed SFG signal decrease was more likely caused by lipid translocation, which decreased SFG signals from both leaflets simultaneously with similar dynamics (similar exponential decay constant), rather than by lipid bilayer damage or removal, which usually causes different dynamics of the two leaflets and exhibits different SFG signal decrease behavior.<sup>76</sup> Figure 4-6 further shows that PEI-B, as compared to PEI-L, induced a higher lipid translocation rate of the dDPPG-DPPG bilayer at the same subphase concentration. The charge associated with both the negatively charged lipid bilayer as well as the positively charged PEI molecules allowed the interaction of both be dictated by electrostatic force, and as a result, PEI-B had a stronger interaction with the negatively charged lipid bilayer as compared to PEI-L at the same subphase concentration due to a higher positive charge density. Furthermore, we found that lipid translocation rate induced by PEI had linear dependence on the PEI concentration in the range of 10-100ppm. This was evidenced by performing linear fitting to the data in Figure 4-6.

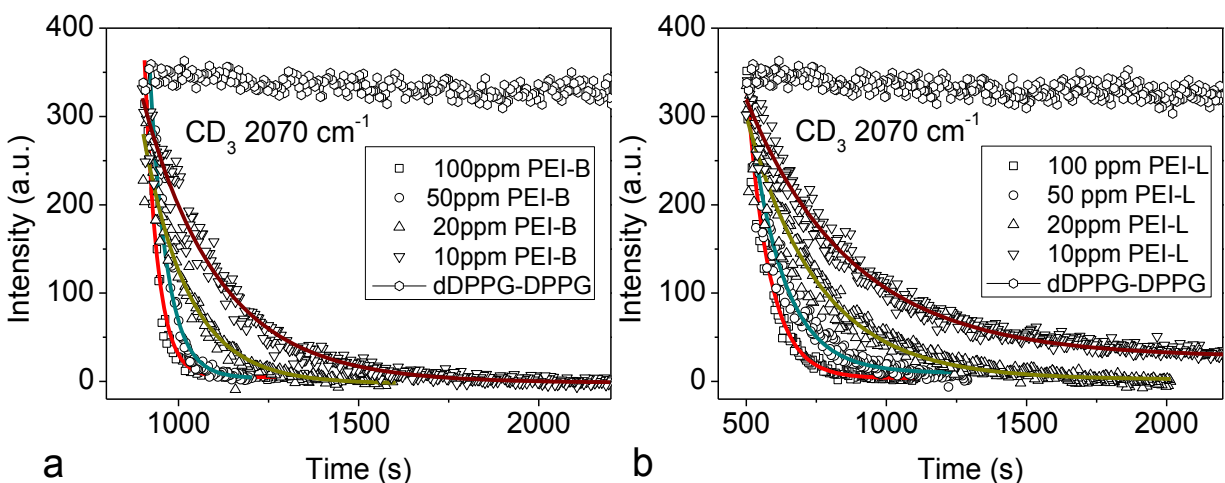


**Figure 4-5. Time-dependent SFG signals of C-D stretching vibrational peak ( $2070\text{ cm}^{-1}$ ) from the dDPPG-DPPG bilayer at  $39\text{ }^\circ\text{C}$  in contact with the subphase without and with 10 ppm, 20 ppm, 50 ppm, and 100 ppm concentrations of (a) PEI-B and (b) PEI-L. Dots are data points measured in the experiment; lines are fitting results using equation (4.5).**

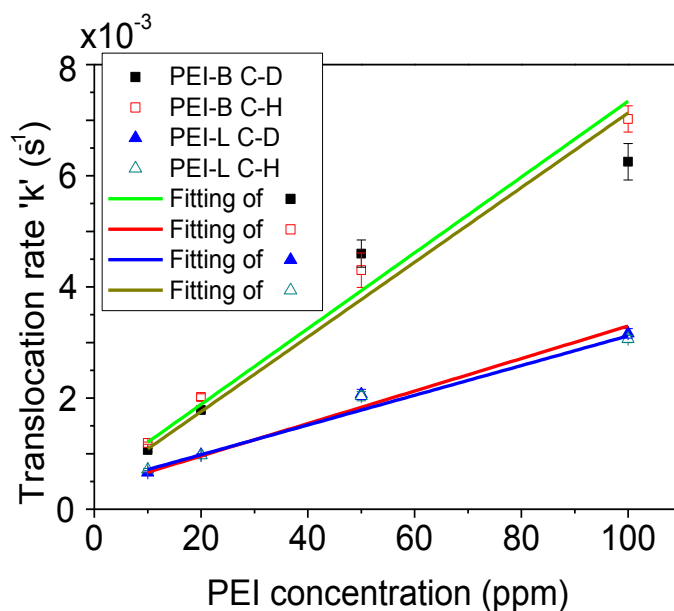


**Figure 4-6. dDPPG-DPPG bilayer lipid translocation rates as functions of PEI concentrations in the subphase at 39 °C. Squares: PEI-B, triangles: PEI-L, Open: C-H signal, Filled: C-D signal. Lines are linear fitting results of the data points.**

#### 4.3.4 Lipid Translocation in dDSPC-DSPC Bilayer Induced by PEI at Different Temperatures

Similar SFG studies were performed on the interaction between PEI and a zwitterionic dDSPC-DSPC lipid bilayer. PC is the major lipid component in mammalian cell membranes, and it is also used to mimic zwitterionic lipid in a model membrane. For the dDSPC-DSPC bilayer, in the C-D stretching frequency range, the peak at 2070  $\text{cm}^{-1}$  was also well resolved in the SFG spectrum (Figure 4-7a, black square). Two strong C-H stretching peaks at around 2875 and 2940  $\text{cm}^{-1}$  also dominated the spectrum in the C-H stretching frequency range (Figure 4-7b, black square). A peak at around 2850  $\text{cm}^{-1}$  shown as a shoulder of the 2875  $\text{cm}^{-1}$  peak is a result of the C-H symmetric stretching of the methylene group in the DSPC alkyl chain. This indicates that the lipid alkyl chains were not perfectly symmetric in the lipid bilayer. Upon a comparison of the dDPPG-DPPG to dDSPC-DSPC bilayer systems, the latter showed less ordered lipid alkyl chains. In this research, we studied the lipid-PEI interaction at 21 °C and 39 °C. According to the previous

publication, at both temperatures, in our  $< 3$  h observation time scale, the intrinsic lipid translocation rate of the dDSPC-DSPC bilayer can be ignored.<sup>42</sup> We added the PEI-B or PEI-L stock solution to the water subphase in contact with the dDSPC-DSPC bilayer to form a 100 ppm concentration PEI solution at 21 °C. Figure 4-8 shows the time-dependent SFG signals detected from the lipid bilayers before and after the PEI-B stock solution was added to the subphase (the results of PEI-L were similar and thus are not shown). The C-D stretching signal increased slightly while the C-H stretching signal decreased slightly. No further signal change was observed after such, indicating that 100 ppm PEI-B is not able to induce significant bilayer translocation. SFG spectra were collected from the lipid bilayer before and after the addition of PEI-B to the subphase (Figure 4-7). In the C-D range the SFG spectra were quite similar while in the C-H/O-H range, water O-H stretching signal disappeared after the PEI addition. This indicates the adsorption of PEIB to the lipid leaflet and the decrease in water molecule ordering associated with the lipid (due to the electrostatic interaction between adsorbed PEI and zwitterionic lipid head groups). The C-H stretching signal decrease at  $2850\text{ cm}^{-1}$  indicates the slight increase in lipid ordering of the outer leaflet after the PEI-B addition.

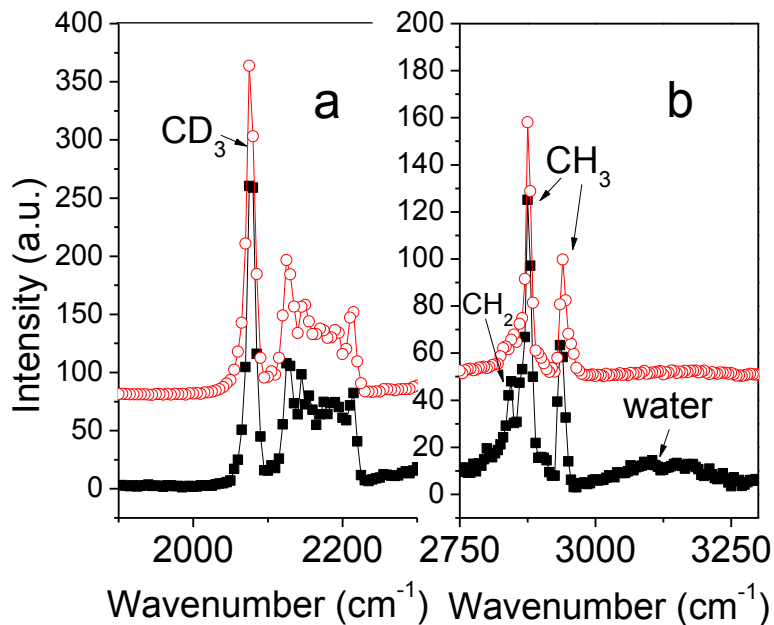


**Figure 4-7.** SFG spectra in the (a) C-D and (b) C-H stretching frequency ranges of the dDSPC-DSPC bilayer before (black square) and after (red circle) the addition of PEI-B to the subphase to reach 100 ppm at 21 °C.

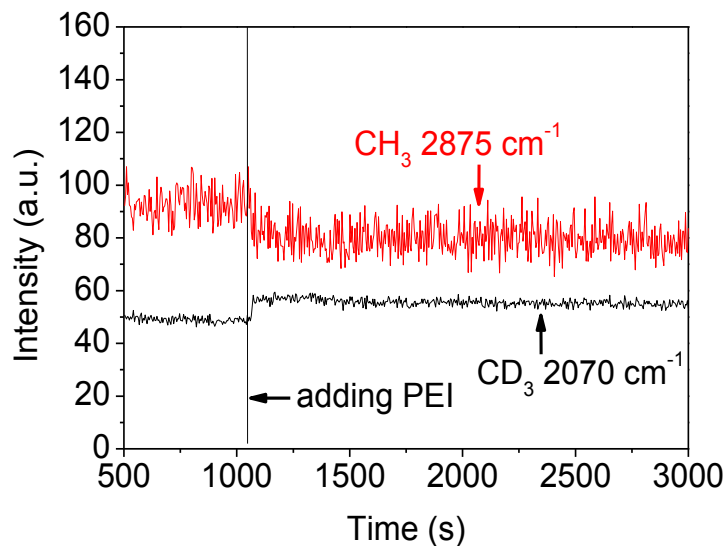


**Figure 4-8.** Time-dependent SFG signals detected from the dDSPC-DSPC bilayer at 21 °C before and after the introduction of 100 ppm PEI-B to the subphase. SFG signals were monitored at 2070 (black) and 2875 (red)  $\text{cm}^{-1}$ . PEI-B stock solution was added to the subphase at  $\sim 1050$  s.

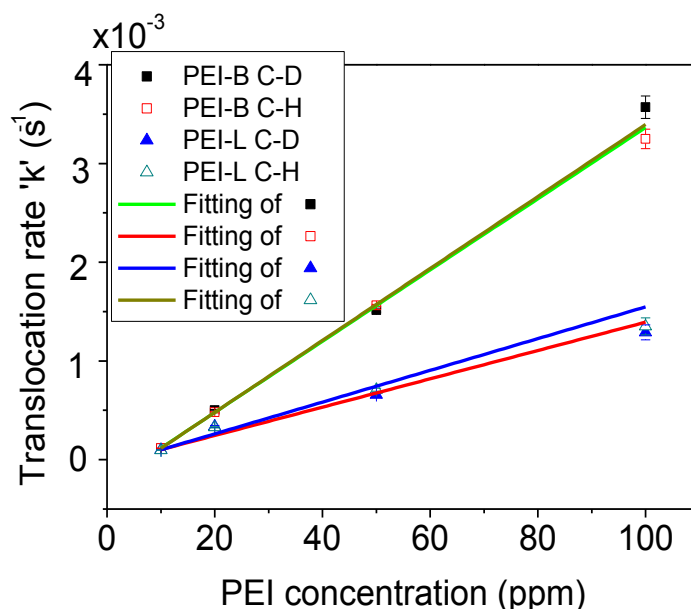


**Figure 4-9. dDSPC-DSPC bilayer lipid translocation rates as functions of PEI concentrations in the subphase at 39 °C. Squares: PEI-B, triangles: PEI-L, Open: C-H signal, Filled: C-D signal. Lines are linear fitting results of the data points.**

Similarly to the experiments with dPPPG-DPPG bilayer, the addition of PEI to the subphase solution at 39 °C also decreased the dDSPC-DSPC bilayer SFG signal as a function of time. Such signal decrease was more likely due to the lipid translocation because of the similar dynamics of inner and outer leaflets. The lipid translocation rate constants obtained from fitting the time dependent SFG signals at different PEI concentrations are plotted in Figure 4-9. Lipid translocation rates were similar for both inner and outer leaflets at a particular subphase PEI concentration and were linearly dependent on the PEI concentration for both PEI-B and PEI-L in the 10-100 ppm range. PEI-B and PEI-L had weaker effect on the translocation rate of the DSPC bilayer as compared to that of the DPPG bilayer due to the different electrostatic interactions between PEI and different kinds of lipids. PEI is a highly positively charged polyelectrolyte that tends to interact strongly with negatively charged DPPG bilayers through electrostatic interactions. For the zwitterionic DSPC bilayer, PEI interacts with the bilayer to a lesser degree but can still



interact with the negatively charged phosphate group, changing the membrane potential and lipid translocation rate in the bilayer. For all the cases, PEI-B demonstrated a stronger effect on lipid translocation as compared to PEI-L due to the higher charge density.

#### **4.3.5 Lipid Translocation in dDPPC-DPPC Bilayer Induced by PEI at Room Temperature**

Results from previous sections have shown that PEI tended to increase lipid translocation rate in the bilayers at physiological temperature. However, at room temperature, the addition of PEI to the subphase did not show detectable increase of the lipid translocation rate of either a DPPG or a DSPC bilayer due to the slow changing dynamics. From the results it is unclear that if the addition of PEI is able to ‘slow down’ the lipid transbilayer movement or decrease the translocation rate. Collecting data on a much longer time scales is not feasible with our current equipment. Here, an alternative method was used to clarify this by monitoring the lipid translocation of a dDPPC-DPPC bilayer as a function of time induced by PEI solution. DPPC has the similar molecular structure but a shorter fatty acid chain and a lower phase transition temperature as compared to DSPC. Intrinsic lipid translocation in a dDPPC-DPPC bilayer is much faster than in a dDSPC-DSPC bilayer. Therefore, it is possible to follow its translocation dynamics within a reasonable experimental time scale at room temperature using SFG.

Time-dependent SFG signals detected from the dDPPC-DPPC bilayer at 2070 and 2875  $\text{cm}^{-1}$  showed significant signal decreases at 21 °C. Such signal changes from the two leaflets were similar and thus only C-D signals at 2070  $\text{cm}^{-1}$  are shown in Figure 4-10. When PEI-B or PEI-L was added to the sub-phase to reach 100 ppm concentration, SFG signals showed similarities in trend, both showing decrease as a function of time. The translocation rate constants ( $k$ ) were obtained through fitting the time-dependent SFG signals ( $8.3 \times 10^{-4} \text{ s}^{-1}$ ,  $8.5 \times 10^{-4} \text{ s}^{-1}$ , and  $8.3 \times 10^{-4} \text{ s}^{-1}$ ) for the dDPPC-DPPC bilayer, the bilayer in contact with 100 ppm PEI-B, and the bilayer in

contact with 100 ppm PEI-L, indicating that PEI molecules do not significantly change the lipid translocation rate in dDPPC-DPPC bilayers at room temperature. Based on the similar molecular structures of DPPC and DSPC molecules, we conclude that at room temperature, PEI does not decrease lipid translocation rates of zwitterionic DPPC and DSPC lipid bilayers.

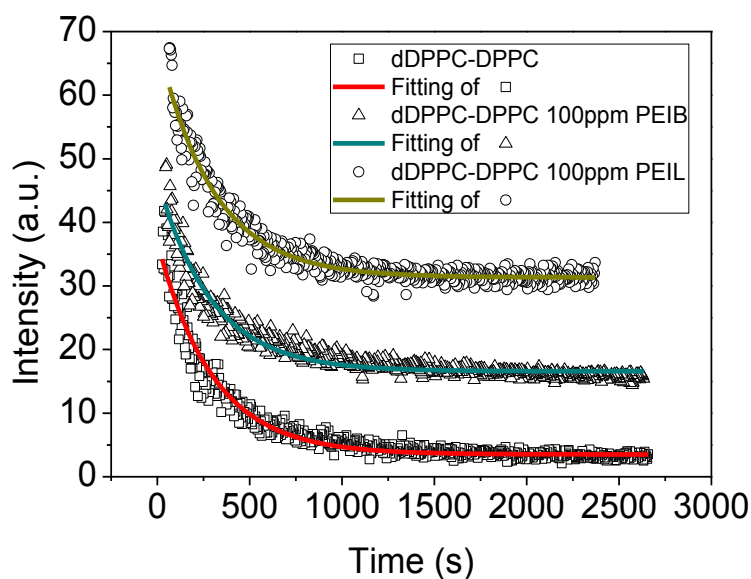


**Figure 4-10.** Time-dependent SFG signals at  $2070\text{ cm}^{-1}$  detected from the dDPPC-DPPC bilayer (square); dDPPC-DPPC bilayer in contact with the subphase of 100 ppm PEI-B (triangle); dDPPC-DPPC bilayer in contact with the subphase of 100 ppm PEI-L (sphere) at  $21\text{ }^{\circ}\text{C}$ . SFG signal curves are offset in the figure. Dots are data points measured in the experiment; lines are fitting results using equation (4.5).

#### 4.4 ATR-FTIR Spectroscopic Study of PEI lipid bilayer Interaction

Observations of a decrease in SFG signal described in sections 4.3.3 and 4.3.4 have two possible causes: (1) lipid translocation, supported by the similar rates deduced for both leaflets, or (2) bilayer damage/lipid removal induced by PEI molecules. To eliminate the possibility of the lipid bilayer removal from the substrate, ATR-FTIR experiment was performed. The method used to construct a lipid bilayer on an ATR crystal and the detailed methods used in the ATR-FTIR experiment are presented below.

#### 4.4.1 The Formation of a Lipid Bilayer on an ATR Crystal

In the ATR-FTIR experiment, lipid bilayers were constructed on an ATR crystal. The method to construct a lipid bilayer on the ATR crystal is demonstrated in Figure 4-11 and is presented in detail below:

(1) A lipid monolayer was first constructed on the ATR crystal using the LB method as discussed above.

(2) Lipids on sides B, C and D of the ATR crystal were removed using ethanol.

(3) The ATR crystal was placed on a commercial ATR crystal mount (not fastened). The ATR crystal mount was put on a  $z$ -direction translation stage. A clean glass plate was clamped to the ATR crystal mount to create a chamber for water storage. A separate ATR crystal holder mounted onto an  $x$ - $y$ - $z$  three dimensional stage was used to hold the crystal separately.

(4) The ATR crystal was then lifted up by the ATR crystal holder. The ATR crystal mount plus the glass plate and clamps were then immersed into the water.

(5) A lipid monolayer with a proper surface tension (34 mN/m) was constructed on the water surface.

(6) The ATR crystal was lowered to contact the water surface to form a lipid bilayer on its bottom side (side A) (This was using the LS method).

(7) The ATR crystal mount was lifted in order to catch the ATR crystal and the lipid bilayer in the water.

(8) The ATR crystal was released from the holder and was fastened on the ATR crystal mount.

(9) The ATR crystal and mount were flipped 180 degrees and the clamps were removed. The outside of the ATR crystal and mount were dried before being placed on the ATR-FTIR

instrument to collect FTIR spectrum. The amount of water inside the chamber was controlled to be 1.6 mL.

(10) A heating plate and a thermometer were added to the system to perform temperature control experiments. Temperature was controlled using the above mentioned hotplate (Isotemp) and was calibrated using a CSC32 SERIES Mini Benchtop Controller (Omega Engineering). The ATR chamber was purged with nitrogen gas to reduce IR absorption from water vapor and carbon dioxide. Before heating, the lipid bilayer on the ATR crystal was washed using ultrapure water multiple times. For the ATR-FTIR experiment at 39 °C, spectra were collected 30 minutes after the start of heating. In order to inject PEI stock solution into the subphase, the glass plate and the heating plate were removed temporarily and were placed back after injection.

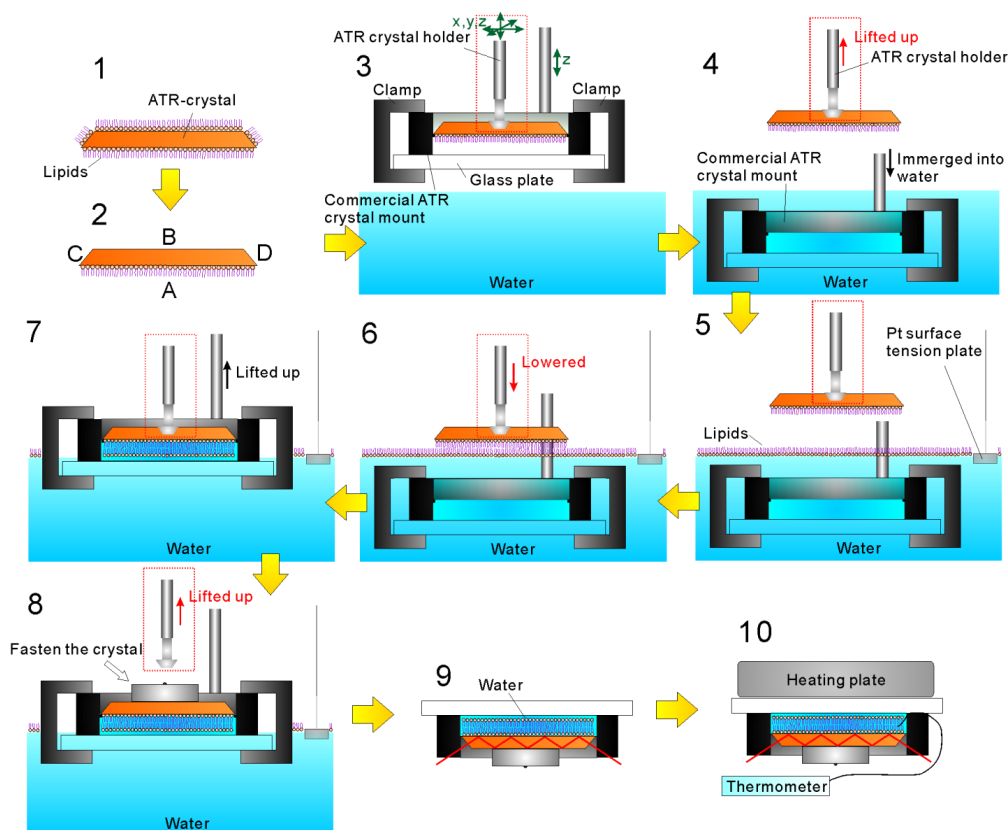


**Figure 4-11.** The construction of a lipid bilayer on an ATR crystal for the ATR-FTIR spectroscopic study.

The 100 ppm PEIB solution in contact with DPPG and DSPC bilayers was studied using ATR-FTIR because results from SFG indicate that this subphase PEI concentration showed the fastest signal decrease rate, indicating the strongest PEI-bilayer interaction. In order to improve signal to noise ratio, symmetric DPPG-DPPG or DSPC-DSPC bilayer was used for ATR-FTIR.

#### **4.4.2 ATR-FTIR Experimental Results**

Figure 4-12a shows ATR-FTIR spectra of a DPPG-DPPG bilayer in the C-H stretching frequency range with and without the addition of PEI-B to the subphase. The bare bilayer at 21 °C showed two strong peaks in the ATR-FTIR spectrum at  $\sim 2850$  and  $2925\text{ cm}^{-1}$  from the methylene symmetric and asymmetric C-H stretching in the lipid alkyl chains. ATR-FTIR spectrum was collected again from the bilayer when the subphase temperature was increased to 39 °C (Figure 4-12a). The  $\sim 2850$  and  $2925\text{ cm}^{-1}$  peaks were still observable with no noticeable change in intensity. Here, the water signal background was corrected for all the ATR-FTIR spectra. As shown in the above SFG experiments, SFG signal from the dDPPG-DPPG bilayer disappeared within 100 s after interacting with 100 ppm PEI-B solution. If the lipid bilayer was destroyed or removed, the lipid ATR-FTIR signal would also decrease because less lipid would be available on the ATR crystal surface. However, after adding 100 ppm PEI-B, significant decreases in C-H IR signal was not observed for experiments running 20 minutes (Figure 4-12a). Therefore, such results prove that the decrease in SFG signal was due to lipid translocation which decreased symmetric order of the lipids, instead of PEI-induced bilayer damage or removal. PEI-B concentration was further increased to 200 ppm and 1000 ppm with no significant lipid signal decrease observed in the ATR-FTIR spectra (Figure 4-12a), indicating the gel-phase bilayer integrity was maintained in the presence of PEI-B with these concentrations under study.

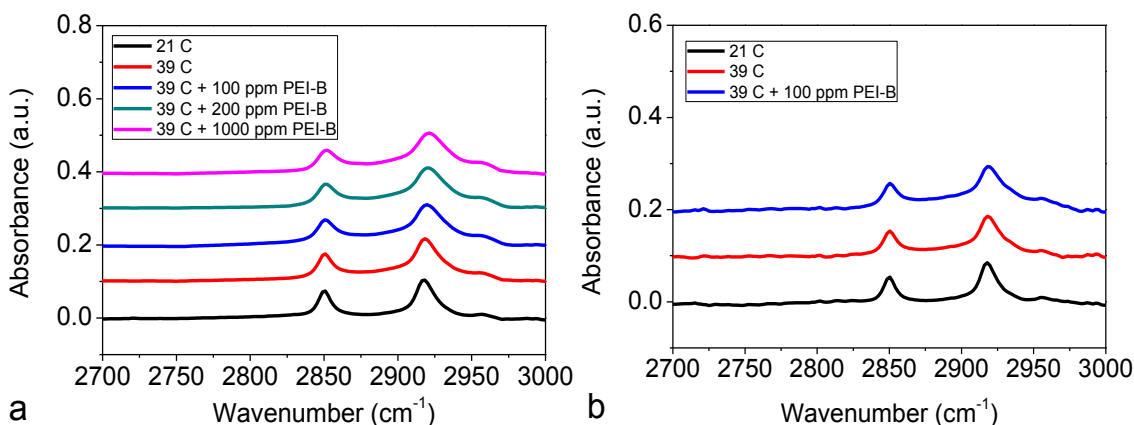


**Figure 4-12. ATR-FTIR spectra of the (a) DPPG and (b) DSPC bilayers at different temperatures (21 and 39 °C) with and without PEI-B injected into the subphase.**

Figure 4-12b shows the ATR-FTIR spectra of a DSPC-DSPC bilayer in the C-H stretching frequency range with and without PEI-B in the subphase. Similar results were obtained with DPPG-DPPG bilayers. As expected, 100 ppm PEI-B did not alter the DSPC lipid bilayer ATR-FTIR signal, indicating that the bilayer was not destroyed or removed by PEI-B in the solution.

In order to show that PEI molecules do not contribute ATR-FTIR signals in the measurement, we performed the following control experiment: PEI-B solution was added to the water subphase attached to a clean ATR crystal with no lipid bilayer deposited. After reaching a concentration of 100 ppm PEI-B in the subphase solution, an ATR-FTIR spectrum was collected (Figure 4-13). No C-H signal could be observed. Here the background used for spectral subtraction was collected at the water/ATR crystal interfacial area before adding PEI to the subphase. The water background was corrected to avoid confusion.

Since it has been demonstrated that PEI-L has a weaker interaction with the lipid bilayers as compared to PEI-B, gel phase lipid bilayer integrity should also remain intact in the presence of PEI-L at the concentration range used in this SFG study (10-100 ppm).

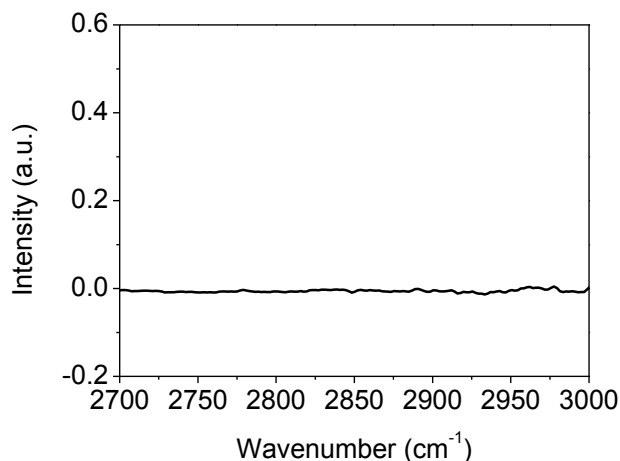


**Figure 4-13. ATR-FTIR spectrum collected from the ATR crystal/100 ppm PEI-B solution interface. The water background was corrected to avoid confusion.**

#### 4.5 Significance of the Research

Transbilayer movement or translocation of the lipids in a membrane is crucial for membrane function and homeostasis. The local heterogeneous distribution of lipids is important for maintaining membrane lateral pressure, membrane protein function, or other membrane behaviors. Previous publication has shown that PEI can strongly interact with model supported bilayers.<sup>30</sup> It has also been demonstrated that the cytotoxicity of PEI has a strong correlation to the membrane dynamics of both cell and mitochondria membranes.<sup>22</sup> The change of membrane potential, lipid translocation induced by proteins, or membrane damage were highly likely related to PEI's toxic behavior.<sup>22</sup> In this research, it has been shown that free PEI in low concentrations can also induce transbilayer movement of PG and PC lipids at physiological temperatures without the help of membrane proteins. This suggests that the influence of PEI on cell membranes may not be only restricted to the regions with membrane proteins, but in fact may have effect on the lipid molecules themselves. Such PEI-induced membrane change may affect or reverse some of the lipid transportation induced by membrane proteins such as aminophospholipid translocase VA,

resulting in cell apoptosis. From this study, it was also found that PEI molecules interacted more strongly with negatively charged lipids as compared to zwitterionic lipids. This indicates that PEI may influence more on PG, phosphatidic acid (PA) or phosphatidylserine (PS) than on PC or phosphatidylethanolamine (PE). It is also shown that PEI-B had stronger interactions with lipids than PEI-L, which indicated a higher toxicity of PEI-B.<sup>19, 77-78</sup> The observation of PEI induced lipid translocation in supported lipid bilayers can help to further understand PEI's cytotoxicity. To depict a more complete picture of PEI - membrane interaction, future studies using more complicated membrane systems will be performed based on the method developed in this work. This research provides novel understanding on PEI's cytotoxicity, which will help develop gene transfectants with an anticipated lower toxicity.

#### **4.6 Conclusion**

Previous research has shown that cytotoxicity of PEI is correlated to lipid membrane dynamics such as membrane damage, membrane potential change, or lipid redistribution. In this study we combined SFG and ATR-FTIR spectroscopies to study molecular interactions between PEIs and supported lipid bilayers (serving as model cell membranes) in order to understand PEI-induced lipid translocation and possible bilayer damage. At room temperature (21 °C), the lipid translocation rates of both PG and PC bilayers were not significantly altered by PEI. At a near physiological temperature (39 °C), both branched and linear PEIs induced lipid translocation in the gel-phase PG and PC bilayers with the absence of membrane proteins. This indicates that PEI can affect lipid translocation from not only membrane protein associated lipid transport, but also the lipid molecules themselves. Results of this study show that PEI had stronger interaction with the negatively charged bilayer as compared to the zwitterionic bilayer due to electrostatic interaction. Concentration dependent studies of PEI indicated that the lipid translocation rate



affected by PEI was linearly dependent on the PEI concentration in the subphase. Branched PEI had a stronger interaction with lipid bilayers as compared to the linear PEI due to a higher charge density, indicating the possible higher toxicity of branched PEI. Complimentary ATR-FTIR results showed that for DPPG and DSPC bilayers, there was no significant lipid bilayer destruction/removal by PEI solution in the concentration range studied. Results of both linear and nonlinear vibrational spectroscopies provide an insight in PEI - lipid bilayer interactions at the molecular level *in situ* and can help to further clarify PEI's cytotoxicity mechanism. It opens possibilities for future studies using more complicated model cell membranes and PEI-biomolecule complexes to establish extensive understanding on PEI and PEI-complex induced cytotoxicity in gene delivery systems, which will help develop low toxic transfectants. This work also demonstrates a unique way by combining SFG and ATR-FTIR spectroscopies to examine interactions between lipid bilayers and polyelectrolytes.

## 4.7 References

1. Thomas, C. E.; Ehrhardt, A.; Kay, M. A., *Nat. Rev. Genet.* **2003**, *4*, 346-358.
2. Luten, J.; van Nostrum, C. F.; De Smedt, S. C.; Hennink, W. E., *J. Control. Release* **2008**, *126*, 97-110.
3. Godbey, W. T.; Barry, M. A.; Saggau, P.; Wu, K. K.; Mikos, A. G., *J. Biomed. Mater. Res.* **2000**, *51*, 321-328.
4. Merdan, T.; Kopecek, J.; Kissel, T., *Adv. Drug Delivery. Rev.* **2002**, *54*, 715-758.
5. Sonawane, N. D.; Szoka, F. C.; Verkman, A. S., *J. Biol. Chem.* **2003**, *278*, 44826-44831.
6. Suh, J.; Wirtz, D.; Hanes, J., *Proc. Natl. Acad. Sci. U. S. A.* **2003**, *100*, 3878-3882.
7. Akinc, A.; Thomas, M.; Klibanov, A. M.; Langer, R., *J. Gene Med.* **2004**, *7*, 657-663.
8. Boussif, O.; Lezoualc'h, F.; Zanta, M. A.; Mergny, M. D.; Scherman, D.; Demeneix, B.; Behr, J.-P., *Proc. Natl. Acad. Sci. U. S. A.* **1995**, *92*, 7297-7301.
9. Kircheis, R.; Wightman, L.; Schreiber, A.; Robitza, B.; Rössler, V.; Kursa, M.; Wagner, E., *Gene Ther.* **2001**, *8*, 28-40.
10. Thomas, M.; Lu, J. J.; Ge, Q.; Zhang, C.; Chen, J.; Klibanov, A. M., *Proc. Natl. Acad. Sci. U. S. A.* **2005**, *102*, 5679-5684.
11. Lungwitz, U.; Breunig, M.; Blunk, T.; Göpferich, A., *Eur. J. Pharm. Biopharm.* **2005**, *60*, 247-266.
12. Werth, S.; Urban-Klein, B.; Dai, L.; Höbel, S.; Grzelinski, M.; Bakowsky, U.; Czubayko, F.; Aigner, A., *J. Control. Release* **2006**, *112*, 257-270.
13. Godbey, W.; Wu, K. K.; Mikos, A. G., *J. Control. Release* **1999**, *60*, 149-160.
14. Kircheis, R.; Wightman, L.; Wagner, E., *Adv. Drug Delivery. Rev.* **2001**, *53*, 341-358.
15. Kichler, A., *J. Gene Med.* **2004**, *6*, S3-S10.
16. Neu, M.; Fischer, D.; Kissel, T., *J. Gene Med.* **2005**, *7*, 992-1009.
17. Wightman, L.; Kircheis, R.; Rössler, V.; Carotta, S.; Ruzicka, R.; Kursa, M.; Wagner, E., *J. Gene Med.* **2001**, *3*, 362-372.
18. Pun, S. H.; Bellocq, N. C.; Liu, A.; Jensen, G.; Machemer, T.; Quijano, E.; Schlupe, T.; Wen, S.; Engler, H.; Heidel, J., *Bioconjug. Chem.* **2004**, *15*, 831-840.
19. Kafil, V.; Omid, Y., *BioImpacts: BI* **2011**, *1*, 23.
20. Fischer, D.; Bieber, T.; Li, Y.; Elsässer, H.-P.; Kissel, T., *Pharm. Res.* **1999**, *16*, 1273-1279.
21. Moghimi, S. M.; Symonds, P.; Murray, J. C.; Hunter, A. C.; Debska, G.; Szewczyk, A., *Mol. Ther.* **2005**, *11*, 990-995.
22. Hunter, A. C., *Adv. Drug Delivery. Rev.* **2006**, *58*, 1523-1531.
23. Kumar, C. S., *Nanomaterials for medical diagnosis and therapy*. Wiley. com: 2007; Vol. 10.
24. Parhamifar, L.; Larsen, A. K.; Hunter, A. C.; Andresen, T. L.; Moghimi, S. M., *Soft Matter* **2010**, *6*, 4001-4009.
25. Hunter, A. C.; Moghimi, S. M., *Biochimica et Biophysica Acta (BBA)-Bioenergetics* **2010**, *1797*, 1203-1209.
26. Boeckle, S.; von Gersdorff, K.; van der Piepen, S.; Culmsee, C.; Wagner, E.; Ogris, M., *J. Gene Med.* **2004**, *6*, 1102-1111.
27. Godbey, W.; Wu, K. K.; Mikos, A. G., *Proc. Natl. Acad. Sci. U. S. A.* **1999**, *96*, 5177-5181.
28. Petersen, H.; Fechner, P. M.; Martin, A. L.; Kunath, K.; Stolnik, S.; Roberts, C. J.; Fischer, D.; Davies, M. C.; Kissel, T., *Bioconjug. Chem.* **2002**, *13*, 845-854.

29. Clamme, J. P.; Azoulay, J.; Mély, Y., *Biophys. J.* **2003**, *84*, 1960-1968.
30. Hong, S. P.; Leroueil, P. R.; Janus, E. K.; Peters, J. L.; Kober, M. M.; Islam, M. T.; Orr, B. G.; Baker, J. R.; Holl, M. M. B., *Bioconjug. Chem.* **2006**, *17*, 728-734.
31. Lee, Y.; Mo, H.; Koo, H.; Park, J.-Y.; Cho, M. Y.; Jin, G.-w.; Park, J.-S., *Bioconjug. Chem.* **2007**, *18*, 13-18.
32. Lu, B.; Xu, X.-D.; Zhang, X.-Z.; Cheng, S.-X.; Zhuo, R.-X., *Biomacromolecules* **2008**, *9*, 2594-2600.
33. Shim, M. S.; Kwon, Y. J., *Bioconjug. Chem.* **2009**, *20*, 488-499.
34. McArthur, S. L., *Surf. Interface Anal.* **2006**, *38*, 1380-1385.
35. Roach, P.; Parker, T.; Gadegaard, N.; Alexander, M., *Surf. Sci. Rep.* **2010**, *65*, 145-173.
36. Benninghoven, A., *Surf. Sci.* **1975**, *53*, 596-625.
37. Henry, M.; Dupont-Gillain, C.; Bertrand, P., *Langmuir* **2003**, *19*, 6271-6276.
38. Moskovits, M.; Suh, J., *J. Phy. Chem.* **1984**, *88*, 5526-5530.
39. Moskovits, M., *J. Raman Spectrosc.* **2005**, *36*, 485-496.
40. Harrik, N., *Internal reflection spectroscopy*. Interscience: New York, 1967.
41. Axelsen, P. H.; Citra, M. J., *Prog. Biophys. Mol. Biol.* **1996**, *66*, 227-253.
42. Liu, J.; Conboy, J. C., *J. Am. Chem. Soc.* **2004**, *126*, 8376-8377.
43. Chen, X.; Wang, J.; Boughton, A. P.; Kristalyn, C. B.; Chen, Z., *J. Am. Chem. Soc.* **2007**, *129*, 1420-1427.
44. Chen, X.; Boughton, A. P.; Tesmer, J. J. G.; Chen, Z., *J. Am. Chem. Soc.* **2007**, *129*, 12658-12659.
45. Zhang, C.; Myers, J. N.; Chen, Z., *Soft Matter* **2013**, *9*, 4738-4761.
46. Shen, Y. R., *Nature* **1989**, *337*, 519-525.
47. Bain, C. D., *J. Chem. Soc., Faraday Trans.* **1995**, *91*, 1281-1296.
48. Eisenthal, K. B., *Chem. Rev.* **1996**, *96*, 1343-1360.
49. Miranda, P. B.; Shen, Y. R., *J. Phys. Chem. B* **1999**, *103*, 3292-3307.
50. Zhuang, X.; Miranda, P.; Kim, D.; Shen, Y., *Phys. Rev. B* **1999**, *59*, 12632-12640.
51. Richmond, G. L., *Chem. Rev.* **2002**, *102*, 2693-2724.
52. Lahann, J.; Mitragotri, S.; Tran, T. N.; Kaido, H.; Sundaram, J.; Choi, I. S.; Hoffer, S.; Somorjai, G. A.; Langer, R., *Science* **2003**, *299*, 371-374.
53. Zhang, D.; Dougal, S.; Yeganeh, M., *Langmuir* **2000**, *16*, 4528-4532.
54. Gautam, K. S.; Schwab, A. D.; Dhinojwala, A.; Zhang, D.; Dougal, S. M.; Yeganeh, M. S., *Phys. Rev. Lett.* **2000**, *85*, 3854-3857.
55. Chen, Z.; Shen, Y. R.; Somorjai, G. A., *Annu. Rev. Phys. Chem.* **2002**, *53*, 437-465.
56. Lu, X.; Han, J.; Shephard, N.; Rhodes, S.; Martin, A. D.; Li, D.; Xue, G.; Chen, Z., *J. Phys. Chem. B* **2009**, *113*, 12944-12951.
57. Chen, Z., *Prog. Polym. Sci.* **2010**, *35*, 1376-1402.
58. Zhang, C.; Shephard, N. E.; Rhodes, S. M.; Chen, Z., *Langmuir* **2012**, *28*, 6052-6059.
59. Zhang, C.; Hankett, J.; Chen, Z., *ACS Appl. Mater. Interfaces* **2012**, *4*, 3730-3737.
60. Vogel, V., *Curr. Opin. Colloid Interface Sci.* **1996**, *1*, 257-263.
61. Kim, J.; Somorjai, G. A., *J. Am. Chem. Soc.* **2003**, *125*, 3150-3158.
62. Wang, J.; Clarke, M. L.; Zhang, Y.; Chen, X.; Chen, Z., *Langmuir* **2003**, *19*, 7862-7866.
63. Holman, J.; Davies, P. B.; Nishida, T.; Ye, S.; Neivandt, D. J., *J. Phys. Chem. B* **2005**, *109*, 18723-18732.
64. York, R. L.; Holinga, G. J.; Somorjai, G. A., *Langmuir* **2009**, *25*, 9369-9374.
65. Nguyen, K. T.; Le Clair, S. V.; Ye, S.; Chen, Z., *J. Phys. Chem. B* **2009**, *113*, 12169-12180.

66. Nguyen, K. T.; King, J. T.; Chen, Z., *J. Phys. Chem. B* **2010**, *114*, 8291-8300.
67. Holinga, G. J.; York, R. L.; Onorato, R. M.; Thompson, C. M.; Webb, N. E.; Yoon, A. P.; Somorjai, G. A., *J. Am. Chem. Soc.* **2011**, *133*, 6243-6253.
68. Boughton, A. P.; Yang, P.; Tesmer, V. M.; Ding, B.; Tesmer, J. J. G.; Chen, Z., *Proc. Natl. Acad. Sci. U. S. A.* **2011**, *108*, E667-E673.
69. Li, H.; Ye, S.; Wei, F.; Ma, S.; Luo, Y., *Langmuir* **2012**, *28*, 16979-16988.
70. Liu, J.; Conboy, J. C., *Biophys. J.* **2005**, *89*, 2522-2532.
71. Anglin, T. C.; Liu, J.; Conboy, J. C., *Biophys. J.* **2007**, *92*, L01-L03.
72. Anglin, T. C.; Conboy, J. C., *Biophys. J.* **2008**, *95*, 186-193.
73. Anglin, T. C.; Brown, K. L.; Conboy, J. C., *J. Struct. Biol.* **2009**, *168*, 37-52.
74. Liu, J.; Brown, K. L.; Conboy, J. C., *Faraday Discuss.* **2013**, *161*, 45-61.
75. Tamm, L. K.; McConnell, H. M., *Biophys. J.* **1985**, *47*, 105-113.
76. Chen, X.; Wang, J.; Kristalyn, C. B.; Chen, Z., *Biophys. J.* **2007**, *93*, 866-875.
77. Gad, S. C., *Handbook of pharmaceutical biotechnology*. Wiley. com: 2007; Vol. 2.
78. Ramalingam, M.; Tiwari, A.; Ramakrishna, S.; Kobayashi, H., *Integrated Biomaterials for Biomedical Technology*. Wiley. com: 2012; Vol. 6.

## **CHAPTER 5**

### **THE DEVELOPMENT OF MULTIMODAL SYSTEMS INVOLVING SFG SPECTROSCOPY**

#### **5.1 Motivation**

As shown in the previous chapters, SFG has been applied to study various surfaces and interfaces involving polymer materials and biomolecules, providing important molecular level insight into surface or interface structures. However, sometimes SFG spectroscopy alone is not enough to characterize complicated samples. In order to depict a clearer physical picture of interfacial structures and other sample properties, SFG has been combined with other techniques including QCM,<sup>1</sup> XPS,<sup>2</sup> ultraviolet-visible spectroscopy,<sup>3</sup> infrared spectroscopy,<sup>4</sup> Raman spectroscopy,<sup>5</sup> etc. Combining SFG spectroscopy with other interfacial characterization techniques for multimodal interfacial studies is an important topic for modern SFG research and also has significance in interface science.

The purpose of this chapter is to design new SFG spectroscopy platforms by combining other analytical techniques with SFG for multimodal analytical studies. SFG spectroscopy was successfully combined with CARS spectroscopy, optical microscopy, and TIRF microscopy for studying various sample systems. The integration of diverse analytical techniques for studying samples in the same environment simultaneously can avoid potential errors caused by sample variations, time-dependent changes, and environmental differences. More importantly, multimodal

systems can provide unique sample measurement and information that individual techniques cannot provide.

## **5.2 Combine SFG with CARS Spectroscopy for Material Studies**

### **5.2.1 Motivation**

SFG can probe vibrational modes of functional groups at interfaces, providing molecular insight into interfacial structures of complicated molecules. However, SFG cannot provide structural information in a bulk phase with inversion symmetry. Surface structures may or may not be related to the structures of the bulk. To understand properties of the material, it is important to study both surface and bulk structures. Vibrational spectroscopic techniques such as ATR-FTIR spectroscopy, conventional Raman spectroscopy, and CARS spectroscopy, which do not have the intrinsic surface selectivity, have been used to examine the structures of bulk or thin films.

In many occasions it is important to study the material's surface and bulk structures in the exact same environment; a slightly varied environment may lead to sample changes. Accordingly, it is important to develop vibrational spectroscopic techniques which can probe both surface and bulk structures without moving the sample or varying the sample environment. ATR-FTIR is a linear absorption spectroscopy which can be used to probe the chemical structures throughout a thin film sample, e.g., with a thickness of tens to hundreds of nanometers. The combination of ATR-FTIR with SFG allows for measurements of both the bulk and surface structure of a thin film. But two measurement techniques require different experimental geometries. Therefore it is difficult to investigate the same sample in the same environment using SFG and ATR-FTIR. Problems may be caused by alignment and sample mounting in different instruments or sample exposure to changing environments. Conventional Raman spectroscopy is also a linear optical spectroscopy. Its signal collection efficiency is low, and its experimental geometry is quite

different from that of SFG. Therefore using a combination of SFG and these linear optical spectroscopies to study both surface and bulk structures in an identical environment is challenging.

The purpose of this work is to design a platform for simultaneously performing SFG and CARS measurements.

### **5.2.2 System Design for the Combined Spectroscopic Technique**

The experimental setup for SFG spectroscopy was introduced in Chapter 1. In this work we will integrate CARS spectroscopy capability with our commercial SFG spectrometer through some optical modifications.

To collect CARS spectrum using our SFG spectrometer, we used the signal output from the OPG/OPA system as the Stokes beam, and the 532 nm visible beam as the pump/probe beam. The pulse energies for the pump/probe and Stokes beams are  $\sim 300 \mu\text{J}$  and  $\sim 100 \mu\text{J}$  respectively. An additional delay line is used to provide temporal overlap of the input beams on sample when shifting from SFG to CARS spectral collection. The CARS Stokes beam reaches the sample at the same angle as the SFG input IR beam. The CARS signal, which can be calculated according to the input Stokes and pump/probe beam directions, is generated at a different angle compared to the SFG signal. A He-Ne laser is used to track the calculated CARS signal, which is collected by the same monochromator and PMT as in SFG. Flip mirrors are used to change between SFG and CARS spectral collections. In this study, SFG spectra were collected using ssp and sps polarization combinations. CARS spectra were collected using ssss (s-polarized CARS, s-polarized probe, s-polarized Stokes, s-polarized pump) and spsp polarization combinations. Additionally, using a black paper to block the reflection beam from the bottom side of the silica window is necessary to avoid the overwhelming background generated from the supporting substrate. The system setup is demonstrated in Figure 5-1.

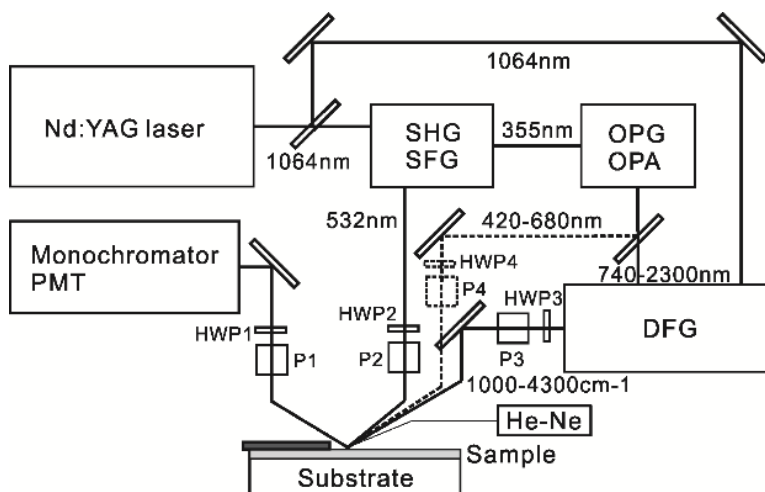


**Figure 5-1. Experimental setup.** SHG, Second harmonic generation; SFG, sum frequency generation; OPG/OPA, optical parametric generation/amplification; HWP1-4, half wave plates; P1-P4, polarizers; PMT, photomultiplier tube. Dotted line indicates CARS beam path.

### 5.2.3 Polymer Thin Film Study Using the Combined Spectroscopic Technique

We first performed polymer thin film studies using our CARS spectrometer to show some proof of principle results.

Poly(methyl methacrylate (PMMA,  $M_w=75000$ ) and polystyrene (PS,  $M_w=19300$ ) films (~40nm) were prepared by spin coating 1 wt% polymer solutions onto clean silica windows at 3000 rpm. We collected SFG and CARS spectra (Figure 5-2) from polymer thin films before and after a 5 second air plasma treatment. For PMMA, the dominant peak at 2955 cm<sup>-1</sup> in the ssp SFG spectrum (Figure 5-2a) is attributed to the C-H symmetric stretch of the methyl ester group, showing that the surface is dominated by the methyl ester groups.<sup>6</sup> After the plasma treatment, the SFG signal intensity decreases, indicating surface ester methyl groups undergo changes. Figure 5-2b shows ssss CARS spectra of PMMA films. The strong 2955 cm<sup>-1</sup> and weak 3005 cm<sup>-1</sup> peaks are due to the methyl ester group symmetric and asymmetric C-H stretching.<sup>6</sup> Two peaks at 2845 and 2885 cm<sup>-1</sup> are from the backbone methylene groups. The shoulder at 2935 cm<sup>-1</sup> is from the



alpha methyl groups. The CARS signals are contributed from the entire PMMA film, so compared with SFG which only probes the surface (dominated by the ester methyl groups), different peaks can be detected. However, PMMA CARS spectra before and after plasma treatment are the same. This indicates that even though the surface structure changes substantially after the plasma treatment, the polymer bulk does not change noticeably. In the PS SFG spectra, various phenyl vibrational modes between 3023~3081  $\text{cm}^{-1}$  can be recognized by spectral fitting (Figure 5-2c).<sup>7</sup> After the 5 second plasma treatment, no SFG signal can be resolved. In CARS measurement, both signals from aromatic side groups (3023~3081  $\text{cm}^{-1}$ ) and backbone methylene groups (2850 and 2905  $\text{cm}^{-1}$ ) were observed (Figure 5-2d). Similar to PMMA, plasma treatment creates significant changes for the PS surface<sup>8</sup> (disorders originally ordered surface aromatic side groups), but not the PS bulk.

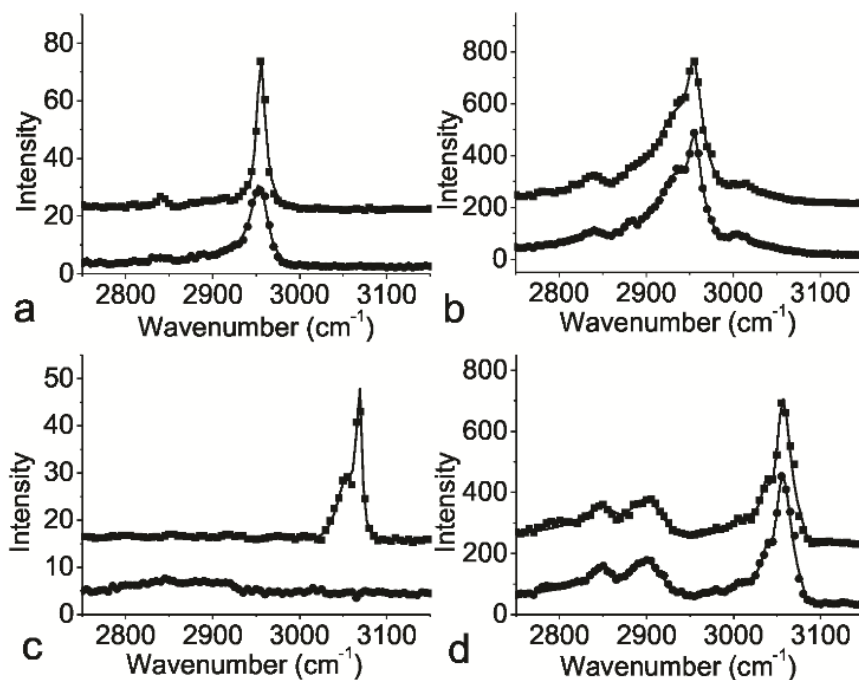


**Figure 5-2.** (a)/(b) SFG/CARS spectra of PMMA film before (top) and after (bottom) plasma treatment; (c)/(d) SFG/CARS spectra of PS film before (top) and after (bottom) plasma treatment. Dots are spectra collected in the experiments, lines are fitting results.

### 5.2.4 The Sensitivity Measurement of the CARS Spectroscopy System

We tested CARS sensitivity by varying the polymer film thicknesses and using a lipid monolayer. Polymer film thicknesses were varied by using different polymer solution concentrations in toluene (0.2 wt%, 0.5 wt%, 1 wt%, 2 wt% and 3 wt%) and measured using a depth profilometer.

CARS signal intensity can be expressed as:

$$I_{CARS} \propto |\chi^{(3)}|^2 I_p I_s I_{pr} \quad (5.1)$$

$I_p$ ,  $I_s$ ,  $I_{pr}$  are intensities of the pump, Stokes and probe beams respectively, and  $\chi^{(3)}$  has the nonresonant  $\chi_{NR}^{(3)}$  and resonant  $\chi_R^{(3)}$  contributions:

$$|\chi^{(3)}|^2 = |\chi_{NR}^{(3)} + \chi_R^{(3)}|^2 = \left| \chi_{NR}^{(3)} + \sum_i \frac{A_i}{\Omega_i - (\omega_p - \omega_s) + i\Gamma_i} \right|^2 \quad (5.2)$$

The resonant contribution is modeled as the sum of Lorentzians with signal strength or amplitude  $A_i$ , frequency  $\Omega_i$ , and linewidth  $\Gamma_i$ . Resonant susceptibility  $\chi_R^{(3)} \propto N$ , while  $N$  is the number of molecules probed. For thin films, the film thickness is proportional to  $N$ . Equation (5.2) was used to fit the CARS spectra, and the fitted amplitude/width ratio has a linear dependence on the film thickness (when the film thickness is thinner than the coherence length, which is ~94 nm in our experiment, Figure 5-3). Since the noise level in the CARS spectra is below 1 count, Figure 5-3 indicates the feasibility to detect CARS signal from films as thin as several nanometers. We further demonstrated this by probing a monolayer of lipid molecules.

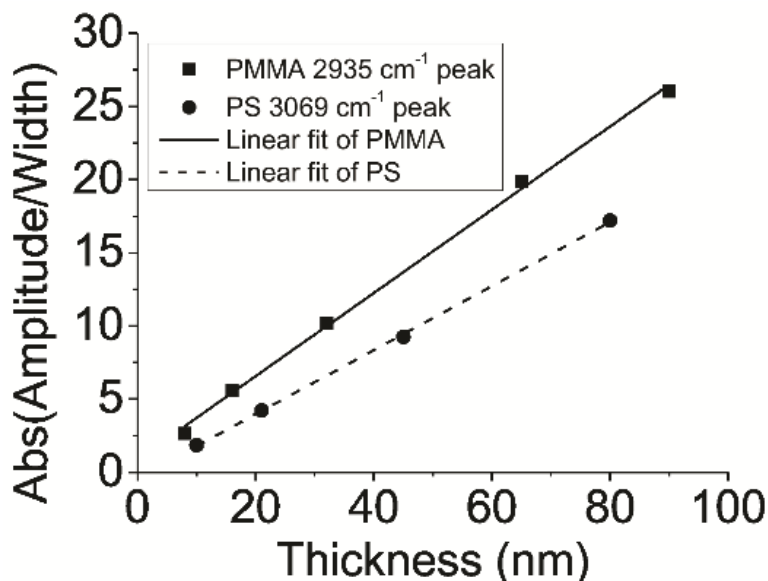


**Figure 5-3. Absolute value of the peak amplitude/width ratio of the PMMA or PS mode centered at 2935 or 3069  $\text{cm}^{-1}$  as a function of the polymer film thickness.**

We used the Langmuir-Blodgett method to deposit a monolayer of DPPG on glass slides.<sup>9</sup> Figure 5-4a shows ssp and sps SFG spectra from a DPPG monolayer. The 2880 and 2945  $\text{cm}^{-1}$  peaks are attributed to the symmetric stretch and Fermi resonance of the terminal methyl group. A peak at 2960  $\text{cm}^{-1}$  is due to the methyl asymmetric stretch and can be extracted by spectral fitting. Only the asymmetric methyl stretch at 2960  $\text{cm}^{-1}$  is resolvable in the sps spectrum. Figure 5-4b shows ssss and spsp CARS spectra. Two peaks at 2845 and 2885  $\text{cm}^{-1}$  correspond to the methylene symmetric and asymmetric stretchings, respectively.<sup>10</sup> In the spsp CARS spectrum, only the methylene asymmetric stretch at 2885  $\text{cm}^{-1}$  was observed. This demonstrates that like SFG, CARS can be used to study monolayers. Since SFG and CARS measure different functional groups and structural parameters,<sup>11</sup> the combined SFG and CARS studies on monolayer materials may lead to a more completed picture of its structure.

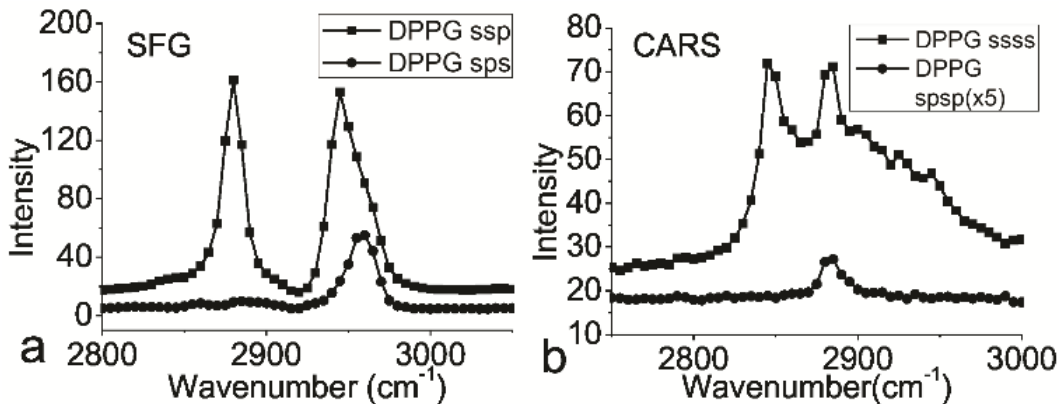


**Figure 5-4. (a) DPPG monolayer SFG spectra collected with ssp and sps polarization combinations; (b) DPPG monolayer CARS spectra collected with ssss and spsp polarization combinations.**

### 5.2.5 Applying SFG and CARS Spectroscopies to Study Plasticizers

The constructed SFG and CARS multimodal spectroscopy system found applications in polymer thin film studies. It has also been applied to study plasticizer migrations in polyvinyl chloride (PVC) matrix. Plasticizers including bis-2-ethylhexyl phthalate (DEHP)<sup>12</sup>, diethyl phthalate (DEP) and dibutyl phthalate (DBP)<sup>13</sup> have been extensively studied in the PVC system before and after plasma treatment. Characterization of different properties of a sample using the same platform in the same environment can avoid possible experimental errors caused by separate measurements. Such work demonstrated the uniqueness of the system for thin film characterizations.

### 5.2.6 Conclusion

In conclusion, we demonstrate that both second and third order nonlinear optical spectroscopic measurements can be performed using the same spectrometer to probe surface and bulk. The same experimental geometry can be adopted and spectral collection can be switched conveniently with flipping mirrors. In the combined spectroscopic studies, surface changes of polymer thin films were observed before and after the plasma treatment, but the changes in the

bulk were negligible. CARS spectra can be collected from monolayers under different polarization combinations. This system was also successfully applied to investigate plasticizer behaviors in PVC systems, showing its potential applications in polymer thin film characterizations. In Chapter 6, we will utilize this system to perform CARS spectroscopy measurements on a PDMS thin film as experimental supports for the theoretical calculation.

### **5.3 Combine SFG Spectroscopy with Optical Microscopy for Buried Biointerface Studies**

#### **5.3.1 Motivation**

As mentioned in Chapter 1, SFG has been widely used in studying polymers and biomolecules.<sup>14-16</sup> SFG can provide *in situ* molecular level structural information of a buried interface that is accessible by laser beams. Polarized SFG spectra can be used to derive orientation information of various functional groups such as methyl, methylene, and phenyl groups, as well as protein secondary structures at various interfaces.<sup>7, 17-19</sup> SFG can also be used to study time dependent interfacial behaviors of various molecules.<sup>20</sup> Such advantages make SFG spectroscopy unique in material science and biological studies.<sup>18</sup>

However, the majority of SFG experiments have performed on homogeneous samples. The focused input laser beam size on a sample is usually  $\sim 500 \mu\text{m} \times 500 \mu\text{m}$  with no beam tracking capability. SFG signals from the entire focal spot are collected and summed to generate a spectrum. It is difficult to apply conventional SFG to study heterogeneous biological samples with different features smaller than such laser beam size at different locations. A few conventional SFG studies have been performed on real biological samples including cells. In such studies, a separate optical microscopic technique was used with SFG spectroscopy to characterize the sample morphology.<sup>21-</sup>

<sup>23</sup> This method cannot be used to track the desired sample locations and also cannot rule out

possible errors caused by different experimental conditions or sample locations studied using separate techniques.

SFG imaging, which can obtain important surface structural information with good spatial resolution, has been developed using picosecond or femtosecond lasers with high<sup>24-26</sup> or low repetition rates.<sup>27-31</sup> However, traditional SFG imaging has limitations for buried interfacial studies. For example, most SFG imaging systems use transmission geometry. Therefore, the input laser beams may need to pass multiple layers to reach the sample/substrate interface under study. All the interfaces between different layers in the beam pass may generate SFG signals, thereby complicating spectral analysis and making it difficult or impossible to distinguish signals generated from buried interface to probe. The transmission geometry used in most SFG imaging systems also limits the detection of weak signals generated at buried interfaces by biological samples. Furthermore, if the input laser beams are perpendicular to the sample interface, the capability of using different polarizations to derive molecular orientations from polarized SFG spectra is lost.

SFG performed in a total-internal reflection (TIR) configuration (TIR-SFG) utilizes the evanescent wave from the TIR beam to examine interfacial molecular structures.<sup>27, 32-33</sup> This geometry ensures that SFG spectra are collected primarily from the sample/substrate interface. Another advantage of this geometry is the capability of detecting weak SFG interfacial signals generated from biological samples<sup>34-35</sup> with low input laser powers due to the large input angle and total signal reflection. However, in most of the previous TIR-SFG studies, model biological systems and homogeneous surfaces were investigated. Most real biological samples are heterogeneous and may only generate very weak SFG signals at buried interfaces. Such problems limit the extension of SFG spectroscopy to buried interfacial studies of real biological samples.

Here we want to design a platform for extending SFG spectroscopy to study buried heterogeneous biological interfaces. We will combine an optical microscope with our commercial SFG spectrometer performed in TIR geometry to examine such biointerfaces. We show the feasibility of using our system for single cell and underwater marine tissue/substrate interfacial studies, providing interfacial structural information of such heterogeneous biological samples.

### **5.3.2 System Design of TIR-SFG Spectroscopy Combined with Optical Microscopy**

Figure 5-5 shows a schematic of our system configuration. Here we use an ‘inverted’ TIR-SFG geometry (lasers enter from the bottom) to ensure that the biological samples (such as cells) are attached to the substrate. The visible and IR input beams were focused using two CaF<sub>2</sub> lenses both with 100 mm focal lengths. A right angle prism substrate was used to support the samples as well as guide the input beams to the specimens. The large incident angle of the visible beam guaranteed visible and signal TIR at air/substrate and water/substrate interfaces. The visible beam at the sample plane could be focused down to about 20 μm × 70 μm. The beam size can be varied by changing the focusing lens positions in the x direction. Theoretically, the beam width was stretched 3.5 times in the x direction, and also has an elliptical shape due to an incident angle of 73.6° at the silica/sample interface, as used in the experiment. An optical microscope sitting above the prism allowed for visual monitoring of the sample and laser spot in real time. A telescope system above the microscope objective was used to expand the light view to fill a complementary metal–oxide–semiconductor (CMOS) camera used for collecting real time bright-field (BF) images. The three dimensional translation stage on microscope was used to find the microscope focusing position and visible laser spot. Then the stage on the prism holder can be used for finding the desired sample feature for study and overlap it with the visible laser spot. The procedures to find and overlap laser beams and the desired sample locations are shown in Figure 5-6. A

collimated white light source illuminated the microscope field of view from the side. For SFG system signal optimization, a calibration film (Such as a poly(methyl methacrylate) film) which usually generates very strong SFG signal was usually used first<sup>36</sup>. Once the system was optimized, samples with unknown SFG spectral features could be directly measured without further adjustment. When the sample was moved in x direction (Figure 5-5), the beam overlap might need to be re-optimized.

The entire system resided on a movable breadboard and could be transitioned conveniently (the installation took only several minutes). All of the SFG spectra in this study were collected using an polarization combination of ssp, although other polarization combinations can also be used<sup>18</sup>. The system still has the capability of deriving molecular orientations based on polarized SFG experiments. Microscope calibration was performed using a USAF 1951 resolution test pattern.

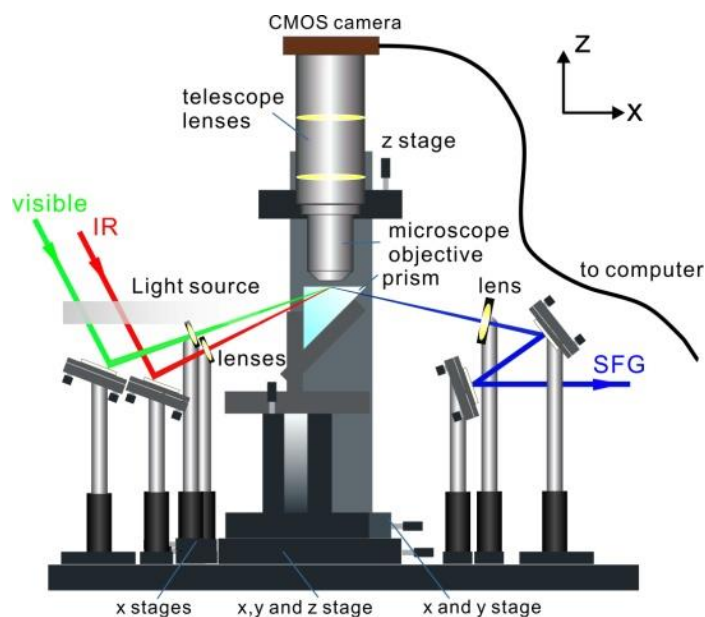


**Figure 5-5. Schematic of the beam tracking TIR-SFG system; The SFG spectrometer is not shown in the figure.**



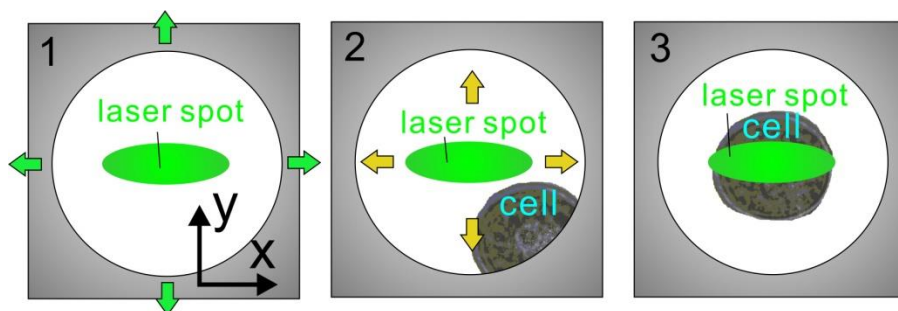


**Figure 5-6. Procedures of using the system to find desired location for sample studies. 1. Using the three dimensional translation stage on the microscope to find the focused laser beam spot on the sample surface; 2. Using the translation stage on the sample holder to find the desired sample location for SFG study; 3. Overlapping the desired sample location with the laser beam spot for SFG data collection.**

### 5.3.3 Proof of Concept Experiments

Before applying this system to biological samples, we first demonstrate the monitoring of laser-induced polymer film photo-damage to illustrate the advantage of real time laser beam tracking in an SFG experiment for valid spectral measurements. A PMMA ( $M_w \approx 75,000$ ) thin film was deposited onto a fused silica substrate by spin coating a 1 wt% PMMA in toluene solution. Surface images of the PMMA film were taken using a microscope objective working in air (Olympus PLN 40X). SFG spectra were collected from the PMMA surface with different visible beam pulse energies while the laser irradiation spot was monitored using optical microscopy in real time. With 10 or 20  $\mu\text{J}$  visible beam pulse energy, no damage to the sample surface was observed (not shown). However, with 30  $\mu\text{J}$  visible pulse energy, the PMMA surface showed noticeable damage during SFG signal collection. The strong scattering of the laser beam on the surface shown in Fig. 5-7B is due to this surface photo-damage. The altered area can be identified using the optical microscope but not by the naked eye, as shown in Fig. 5-7C. The SFG spectrum collected with 10 or 20  $\mu\text{J}$  visible beam energy (Figure 5-7A) had a peak at  $2955 \text{ cm}^{-1}$ , which can be assigned to the symmetric stretching of the PMMA methyl ester group. The peak intensity

increased linearly as a function of the input laser energy with similar peak widths. However, the SFG spectrum collected with 30  $\mu\text{J}$  input visible pulse energy showed a much wider peak with slightly decreased vibrational strength as compared to the 20  $\mu\text{J}$  case. Surface damage tends to randomize the methyl ester group orientation on the surface. The damage resulted in less ordered surface methyl ester groups with a broader orientation distribution, consequently a wider peak with a weaker intensity was observed. This application demonstrates the importance of tracking laser beams in real time during an SFG experiment, which can effectively avoid possible experimental error caused by sample damage or defects.

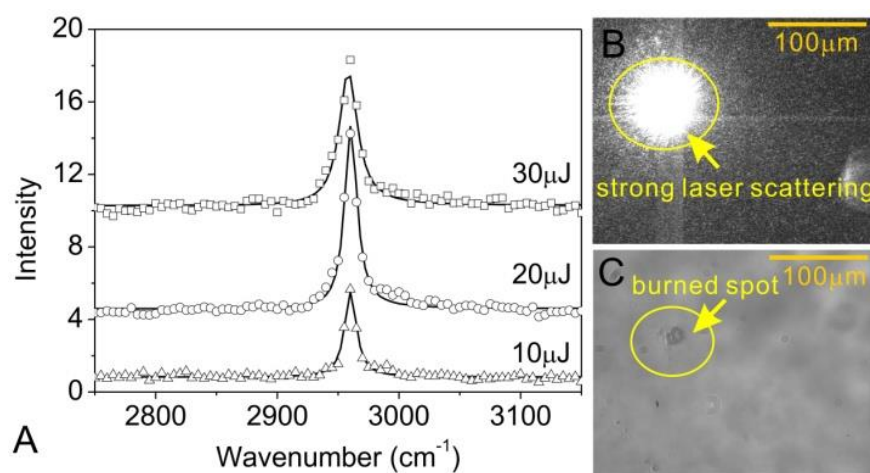


**Figure 5-7. (A) SFG spectra of a PMMA surface in air using 10, 20 and 30  $\mu\text{J}$  (bottom to top) incident visible pulse energies. The spectra were fit (lines) using the method showed in Chapter 1. (B) BF image of the PMMA surface when the SFG spectrum was being collected with 30  $\mu\text{J}$  incident visible pulse energy. Strong scattering indicates the surface photo-damage. (C) BF image of the same sample location collected using a white light source without the input lasers after the SFG experiment.**

### 5.3.4 TIR-SFG Study of Cells and Solid Substrate Interface

The buried interface between a cell and a solid surface is an important biotic/abiotic boundary, the knowledge of which may impact areas including cell biology, biomedical devices, and biofouling, etc. Molecular level studies of cell/solid substrate interfaces may bring about

understanding of interacting mechanisms between cells and substrates, which play crucial roles in cell adhesion, cell culturing, and biocompatibility. Currently, extensive research has not been performed on such buried interface at the molecular level due to the lack of appropriate techniques. Here we demonstrate the feasibility and uniqueness of our system in such studies through examining the buried interface between a single live cell and a solid surface.

In this work, meiotically incompetent germinal vesicle intact (GVI) oocytes were collected from female CF-1 mice (Harlan) at days 11-13 by manual rupturing of pre-antral follicles. Procedures used for oocyte culture were similar to those of previous reports.<sup>37</sup> No anchor coating agent was used and the cell was attached to the silica prism by gravity and self-adhesion. In order to avoid strong perturbation of the cell, the visible input beam used for this SFG study was  $<2 \mu\text{J}$ . Figure 5-8A shows a BF image detected when the SFG input lasers did not irradiate the mouse oocyte. The image was taken using a water immersion microscope objective (Olympus UMPLFLN 20XW). The SFG spectrum collected from this area (the circle area shown in Figure 5-8A) is shown in Figure 5-8C (top spectrum), which exhibits a broad water O-H band from 2800 to 3300  $\text{cm}^{-1}$  (from strongly bonded, or 'tetrahedrally coordinated' interfacial water molecules<sup>38</sup>) as well as some C-H signals between 2900 and 3000  $\text{cm}^{-1}$ . When the sample was moved so that the oocyte was overlapped with the laser spot (Figure 5-8B), the SFG signal (Figure 5-8C bottom spectrum) showed that the water signal was slightly increased and there was no significant C-H contribution that interfered with the O-H signal. These results indicate that at the cell/substrate and the buffer/substrate interfacial areas, the molecular structures are different. At the 'blank' buffer/substrate interface, C-H signals were detected, contributed by the ordered proteins (mostly bovine serum albumin used in the oocyte preparation) adsorbed at the interface. The oocyte zona pellucida (ZP, a glycoprotein layer outside of oocyte lipid membrane) can randomize this adsorbed

protein layer, resulting in no C-H SFG signals from the cell/substrate interfacial area. The SFG water O-H signal from the same interfacial area slightly increased (from spectra fitting), showing that water molecules were more ordered in this area. This increase in water ordering is likely to be induced by the glycoprotein in the ZP zone, which has abundant hydroxyl groups. We believe this is the first time a single live cell induced pure buried interfacial structural change was observed by SFG spectroscopy. This application also shows the feasibility of examining buried heterogeneous biointerfaces with our SFG system.

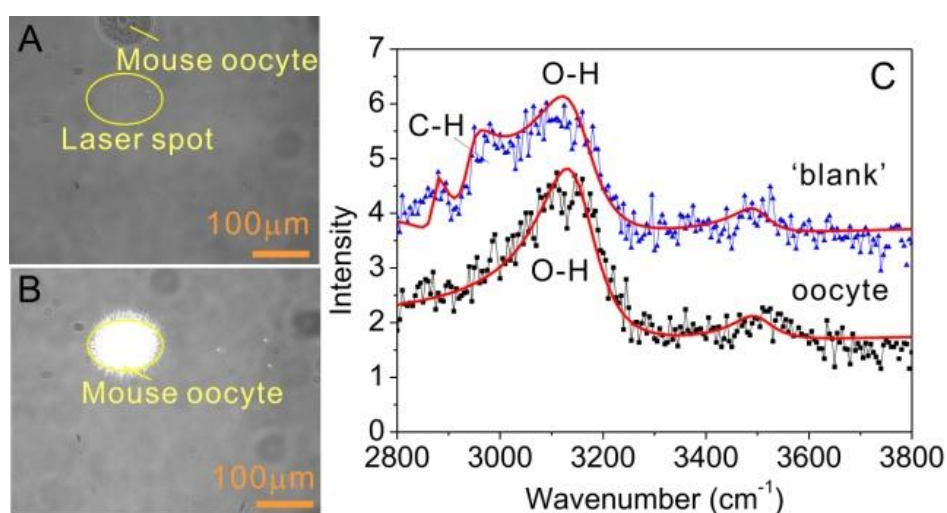


**Figure 5-8. (A) BF image of the visible beam focused on the buffer/substrate interface. (B) BF image of the visible beam focused on a mouse oocyte/substrate interface. (C) SFG spectra taken in (A) (top) and (B) (bottom). Dots are experimental collected data and lines are the fitting results.**

### 5.3.5 TIR-SFG Study of Mussel Adhesive and Substrate Interface

We further applied this system to study the interfacial structure of marine mussel adhesive attached to a solid surface in water. Mussels can strongly adhere to underwater surfaces using plaques which contain adhesive proteins. Studying the structure of the interface between a mussel plaque and a solid substrate can help us to understand the origins of marine biofouling and also help to develop better synthetic glues for both dry and underwater applications<sup>39</sup>. Here we studied

and compared the interfacial regions between mussel adhesive/substrate and water/substrate interfaces, shown in Figure 5-9A. The mussel adhesive plaques were deposited onto a CaF<sub>2</sub> prism by live mussels. The prism had adhesive plaques only in certain regions and thus the sample area was heterogeneous. Figure 5-9B shows a BF image with the SFG input laser irradiating in the mussel plaque area. The SFG spectra are collected in the C=O and C-H/O-H stretching frequency range, respectively. The strong signal centered at 1660 cm<sup>-1</sup> (Figure 5-9D) can be assigned to a protein amide I bond stretching and the crosslinked dihydroxyphenylalanine (DOPA) quinone at the interfacial area. In Figure 5-9E, weak C-H and strong N-H signals can be detected at ~2880 cm<sup>-1</sup> and ~3300 cm<sup>-1</sup> which were also attributed to interfacial proteins. These results indicate that proteins at the mussel adhesive/CaF<sub>2</sub> substrate interfacial area were strongly ordered. When the input laser irradiation area moved to a ‘blank’ region to examine the water/substrate interface, shown in Figure 5-9C, strong O-H signal from water and weak C-H contribution were detected (Figure 5-9F). However, this water SFG signal was not clearly resolved in the mussel plaque region (Figure 5-9E). SFG spectrum collected from a similar sample interface in D<sub>2</sub>O exhibited similar features as that displayed in Figure 5-9E. Consequently, the ordered water molecules were significantly removed between the mussel plaque and the CaF<sub>2</sub> substrate. Mussel proteins tend to attach to the substrate without an ordered water layer in between, which is different from the interface between the substrate and the live cell discussed above. This application shows the feasibility of extending SFG spectroscopy to examine buried biointerfaces formed by thick underwater tissue and the substrate.

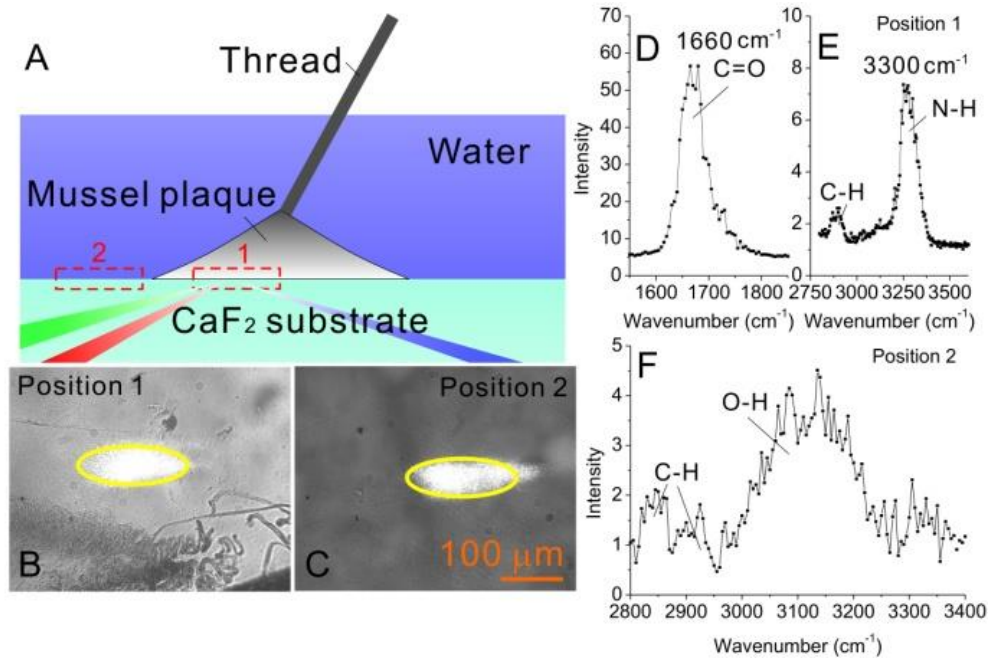


**Figure 5-9.** (A) Schematic of the SFG experiment at a mussel plaque/CaF<sub>2</sub> interface and a water/CaF<sub>2</sub> interface. (B) BF image of a position within the mussel plaque demonstrated in A. (C) BF image of a position in a ‘blank’ water/CaF<sub>2</sub> area, demonstrated in A. (D) SFG spectrum in the C=O range collected in position 1. (E) SFG spectrum of the C-H/O-H range collected in position 1. (F) SFG spectrum of the C-H/O-H range collected in position 2.

### 5.3.5 Conclusion

In conclusion, we have shown that SFG vibrational spectroscopy performed in a TIR geometry combined with a compact optical microscopic system allowed for the study of buried heterogeneous biological interfaces. The optical microscope can locate a specific sample region in real time for SFG analysis. The TIR geometry ensures that the SFG signal is generated predominantly from the buried sample/substrate interfacial area and is sensitive to biointerfaces that generate weak SFG signals. We detected the interfacial molecular structural changes induced by a single mouse oocyte on silica substrate. The system was also applied to investigate the buried mussel adhesive plaque/solid substrate interface, showing that mussel adhesive plaques removed the ordered interfacial water molecules. This work helps to extend SFG spectroscopy to real

biological interfacial systems. This research also illustrates the feasibility of combining SFG spectroscopy with other microscopic techniques including TIR-fluorescence microscopy or nonlinear optical imaging to construct multimodal analytical systems. The integration of diverse analytical techniques for studying samples in the same environment simultaneously can avoid potential errors caused by sample variations, time-dependent changes, and environmental differences.

## **5.4 Combine SFG Spectroscopy with TIRF Microscopy to Study Buried Biointerfaces**

### **5.4.1 Motivation**

Fluorescence microscopy is the most widely used optical microscopic technique in biology and biomedical related research. TIRF microscopy is a fluorescence technique that utilizes evanescent waves of the excitation beam to excite molecules at the interfacial area.<sup>40-41</sup> Benefit from the shallow penetration depth of the evanescent wave, TIRF can only excite fluorophores within several hundred nanometers of the interfaces, without the excitation of background fluorescence molecules outside the range. TIRF has been extensively used for observing kinetics and equilibria for various chemical or biological processes at liquid/solid interfaces, providing important understanding of biointerfaces.<sup>42-45</sup> TIRF monitors the fluorescent emissions from interfacial molecules. This is very different from SFG, which probes intrinsic vibrational transition modes of molecules at the interface. The combination of the two techniques on a single platform, and the simultaneous measurement from both TIRF and SFG is expected to provide important insights into interfacial structures and dynamics. SFG can help to provide important interfacial molecular structural information which cannot be obtained by TIRF alone; TIRF, as a well-established microscopy for bio-interfacial studies, can help to extend SFG spectroscopy research to real biological systems.

The motivation of this work is to design a platform combining TIRF microscopy and TIR-SFG spectroscopy for biological interfacial studies. We designed the system based on some modifications on our previous TIR-SFG and optical microscopy multimodal system. Proof of principle experiments showed that SFG and TIRF can supplement each other in understanding interfacial molecular presence and structures in more detail. We believe the technique we developed in this work could find extensive applications in biological interfacial studies.

#### **5.4.2 System Design of TIR-SFG Spectroscopy Combined with TIRF Microscopy**

The platform we designed to combine SFG with TIRF microscope is shown in Figure 5-10. As compared to the previous setup as shown in Figure 5-5, the detector was changed to a charge-coupled device (CCD) used for image collection. The electron-multiplying CCD (EMCCD, IXON Andor) used here allowed for single molecule fluorescence detection. A band-pass filter was used to block the TIRF excitation beam and allow the TIRF signal to pass through. In this experiment, the microscope objectives used for TIRF studies were from Olympus (air: PLN 40X; water immersion: LUMPLFLN 40X). For TIRF microscopy experiment, the optical microscope was used to collect TIRF signal. The OPG/ OPA system in SFG can generate a frequency tunable visible beam which covers 420-680 nm wavelength range. This visible beam can be used to excite various fluorescence labels using different wavelengths. In this work, the visible beam with 532 nm fixed frequency was used as the excitation beam for TIRF. In TIRF experiment, the CaF<sub>2</sub> lenses used for beam focusing for SFG experiments need to be removed. These lenses were mounted on magnetic bases and could be removed or reinstalled easily. In this work collimated visible beam was focused down to ~2 mm × 2 mm for TIRF excitation (on the sample, the beam shape was stretched to elliptical). The visible beam pulse energy was 80 μJ (20 Hz repetition rate). The beam



could also be focused using a different lens to a relatively smaller size on the sample (such as  $\sim 1 \text{ mm} \times \sim 1 \text{ mm}$ ), which could increase the signal to noise ratio of TIRF imaging.

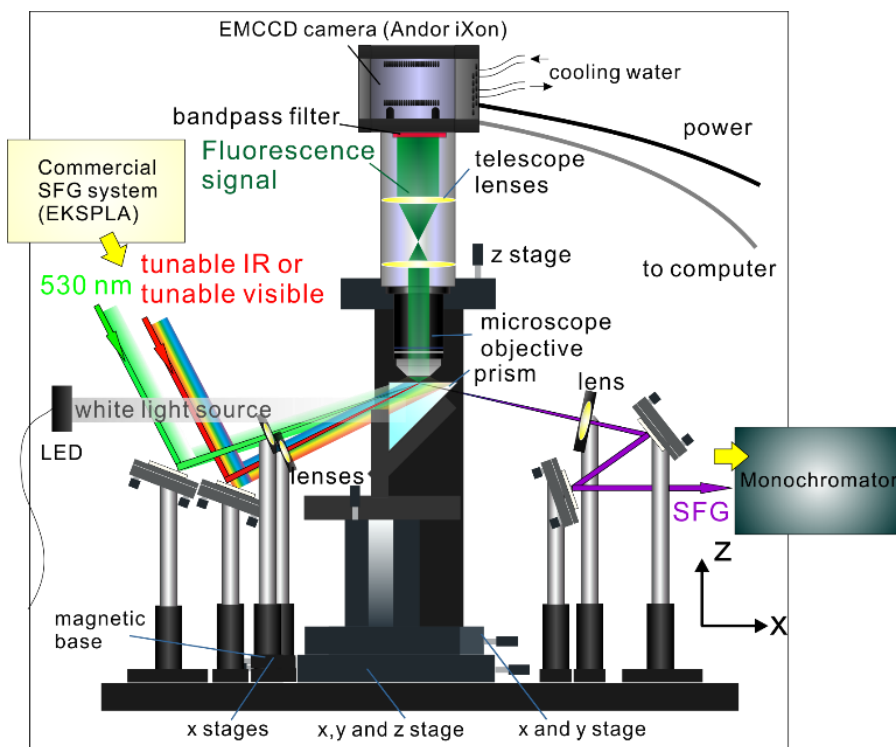


**Figure 5-10. Schematic of our SFG-TIRF multimodal system used for interfacial studies.**

### 5.4.3 SFG and TIRF Study of Polystyrene Fluorescent Beads

The fluorescent PS beads used here were purchased from Phosphorex Inc. ( $3 \mu\text{m}$ , Ex/Em: 530 nm/580 nm) and were deposited on a right angle silica prism by drop casting. Collected using an air objective lens, TIRF images showed that the beads distribution was heterogeneous. Images in Figures 5-11a and c show the PS beads on surfaces with high and low surface coverage. SFG spectra were collected from different surface locations as circled on the images. The spectra of different PS bead surface coverage areas showed similar features in the C-H stretching frequency range (Figures 5-11b and d). Strong peaks centered at  $2850$ ,  $2875$  and  $2940 \text{ cm}^{-1}$  correspond to  $\text{CH}_2$  symmetric stretching,  $\text{CH}_3$  symmetric stretching, and  $\text{CH}_3$  Fermi resonance vibrational

modes, respectively. A small peak at  $2920\text{ cm}^{-1}$  which appears as a shoulder of the  $\text{CH}_3$  Fermi resonance peak is attributed to the  $\text{CH}_2$  asymmetric C-H stretching. The SFG spectra shown in Figure 5-11 do not share the same spectral characteristics as those detected from pure PS film in air or at interfaces,<sup>7, 36</sup> which show strong peaks between  $3030\sim 3080\text{ cm}^{-1}$  from aromatic C-H stretching in phenyl rings with undetectable  $\text{CH}_2$  signal. This indicates that the surface structures of substrate and PS beads were strongly modified by other molecules. The purchased PS beads were suspended in aqueous solution with a small amount of surfactants and sodium azide to minimize beads aggregation. We believe that the spectral features detected in Figures 5-11b and 5-11d are attributed to the surfactant molecules, which usually show strong  $\text{CH}_2$  and  $\text{CH}_3$  signals in SFG spectra.<sup>46</sup> The above results indicate that the surfactant molecules in the PS bead solution tend to be adsorbed to the silica surfaces and cover the PS beads as well as the rest of the silica surface. Their molecular structural features dominate the surfaces and interfaces as seen in SFG spectra collected. This proof of principle experiment shows that our SFG and TIRF multimodal system can be used to study heterogeneous sample surface morphology and the corresponding interfacial molecular structures.

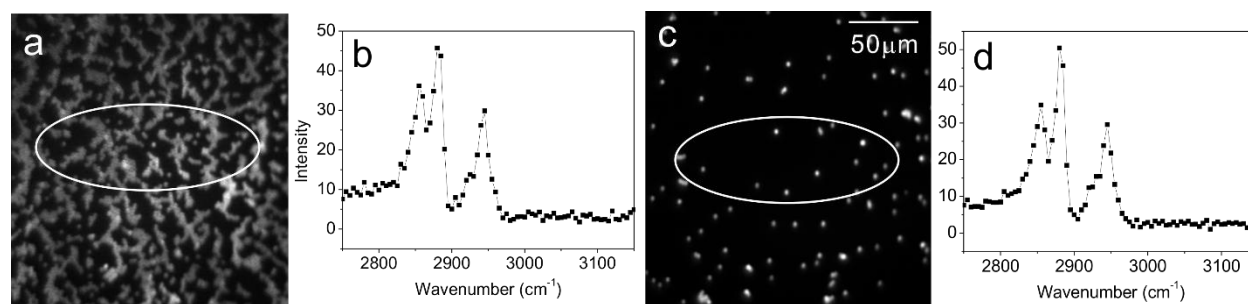


**Figure 5-11. TIRF images of  $3\ \mu\text{m}$  fluorescent PS beads with high (a) and low (c) surface coverage on a silica prism. The corresponding SFG spectra in the circled locations are shown in (b) and (d), respectively.**

#### 5.4.4 SFG and TIRF Study of Fluorescent Labeled Lipid Monolayer

We further applied our SFG and TIRF multimodal system to study a lipid monolayer deposited on a silica prism labeled using fluorescence molecules. The lipid used in the experiment was DPPG purchased from Avanti Polar Lipid. Dil was purchased from Invitrogen and was used for fluorescence labeling. Dil is weakly fluorescent until associated with lipid membranes. Lipid and Dil were mixed with 1000:1 ratio and were dissolved in chloroform to form a solution with 5 mg/ml DPPG concentration. The solution was sonicated for 20 min before being used for monolayer deposition. The lipid monolayer was deposited on a silica prism surface using Langmuir Blodgett method<sup>47</sup> and was covered half of the prism surface. TIRF microscopy can be used to find the boundary of the DPPG monolayer and the ‘blank’ area, as shown in Figure 5-12a (air objective). The heterogeneity of the fluorescence signal indicates the presence of the lipid monolayer and also the aggregation of Dil molecules in the monolayer. We can collect SFG spectra in different locations of the sample as circled in Figure 5-12a. The corresponding spectra are shown in Figure 5-12b. It was found that the lipid monolayer had strong signals centered at 2875, 2940 and 2960  $\text{cm}^{-1}$  corresponding to symmetric stretching, Fermi resonance, and asymmetric stretching of the  $\text{CH}_3$  endgroup in lipid alkyl chain. The 2960  $\text{cm}^{-1}$  peak appeared as a shoulder of the stronger 2940  $\text{cm}^{-1}$  peak. The strong SFG signal indicated the good surface packing and ordering of DPPG molecules in the monolayer. This spectrum was quite similar to that of generated by the lipid monolayer without Dil labeling.<sup>36</sup> This indicates that the Dil labeling in the experiment does not significantly alter the lipid monolayer structure. The ‘blank’ area, which had no lipid molecules, showed no vibrational peaks in the SFG spectrum.

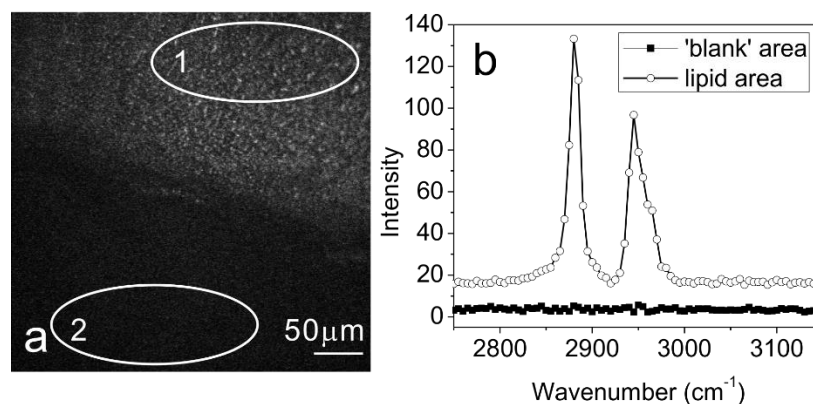


**Figure 5-12. (a) TIRF image of the boundary between a DPPG monolayer labeled using Dil and the ‘blank’ area with no lipids. (b) The corresponding SFG spectra of the lipid area (area 1) and the ‘blank’ area (area 2) in (a).**

DPPG lipid monolayer was also studied in different environments using SFG and TIRF. In air, similar to what we found previously, the lipid monolayer generated strong SFG signal from  $\text{CH}_3$  endgroups and showed Dil fluorescence signal at interfaces in TIRF image (Figures 5-13a and 5-13b). When the monolayer was placed in contact with water, lipid signal in the SFG spectrum disappeared while strong SFG signal from water O-H stretching was observed (Figure 5-13d, the broad spectrum from 2800 to 3500  $\text{cm}^{-1}$  is attributed to water O-H stretching). This indicates that only water molecules were strongly ordered at the interface. However, there are several possibilities for the absence of the lipid methyl C-H stretching signal: (1) Most likely some or most lipid molecules form bilayer structures or liposomes at the interface, creating an inversion symmetry and decreasing the methyl group SFG signal; (2) Due to the unfavorable interactions between water molecules and lipid methyl endgroups, such methyl group might be disordered; (3) lipid molecules might be removed from the interface and dissolved by water. Because SFG signal intensity is both surface coverage dependent and molecular order/symmetry dependent, the signal change observed can be interpreted by all of the above three possibilities. TIRF, which is not dependent on molecular order, can help to monitor the existence of the lipid molecules at the

interface. From the TIRF image (Figure 5-13c), we found that Dil signal was still present at the substrate/water interface (using a water immersion objective), indicating that the lipid molecules were still present at the interface. Therefore, the disappearance of the SFG lipid signal in water was caused by either the lipid alkyl chain randomization or the formation of bilayers or liposomes (with inversion symmetry), or both. We removed the sample from water and exposed it to air again. The resulting surface was studied using SFG and TIRF. Figure 5-13e shows TIRF signal from Dil can still be detected, whereas in the corresponding SFG spectrum (Figure 5-13f), lipid signal partially recovered with weaker intensities. This further confirmed the presence of the lipid monolayer at the water/substrate interface after water contact. The restructured lipid film SFG spectrum showed strong  $\text{CH}_3$  signal at 2875 and 2940  $\text{cm}^{-1}$  (from methyl symmetric stretching and Fermi resonance) plus a relatively bigger shoulder at 2850  $\text{cm}^{-1}$  (from  $\text{CH}_2$  symmetric stretching). The signal intensity difference for the lipid film before and after the water exposure may be caused by less ordered methyl groups due to water interaction, or part of the lipid bilayer ‘flipping’ to create a film with half monolayer and half trilayer in air. The latter structure might be formed because the lipid alkyl chain is hydrophobic and tend to face to air. From our currently analysis it is impossible to confirm which case dominates the interfacial lipid behavior. It is highly possible that both cases occur after the water removal. However, the existence of lipid molecules on the substrate surface was undisputedly proved by TIRF. Comparing TIRF images in Figure 5-13a, b and c, Dil showed less aggregation after water exposure. This was caused by the lateral movement of Dil molecules at the presence of water.

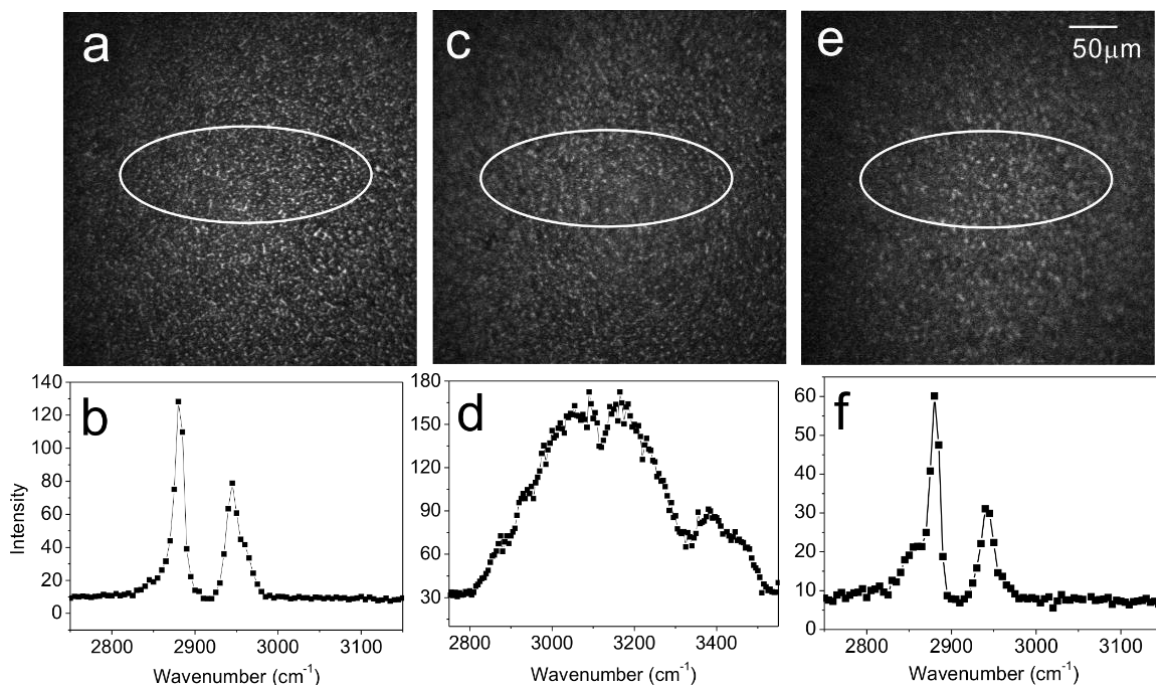


**Figure 5-13. (a) TIRF image of a DPPG monolayer labeled using Dil in air and (b) the corresponding SFG spectrum in circled area. (c) TIRF image of the DPPG monolayer labeled using Dil in water and (d) the corresponding SFG spectrum in circled area. (e) TIRF image of the DPPG monolayer in air after contacting water and (f) the corresponding SFG spectrum from the restructured surface in circled area.**

From TIRF measurement, we found that before and after the water contact, the images showed similar intensities. TIRF imaging and Dil labeling can help to prove the existence of the lipid molecules on the substrate surface. Additionally, experiments with ATR-FTIR spectroscopy were further performed to prove lipid existence on the substrate, since unlike SFG, ATR-FTIR signal is not dependent on molecular order/symmetry. ATR-FTIR experiment was carried out using a commercial instrument (Nicolet 6700 FTIR, Thermo scientific Inc.). The lipid monolayer was deposited on the ATR crystal using the LB method as mentioned previously. The ATR-FTIR spectra from a lipid monolayer collected in air and after the water contact were shown in Figure 5-14. Lipid signals at 2850, 2920 and 2960  $\text{cm}^{-1}$  (corresponding to methylene symmetric, asymmetric, and methyl asymmetric stretching) show only small signal decreases after the water

contact. The subtracted signal difference before and after the water exposure was shown in Figure 5-14 (blue). The ATR-FTIR results indicate that lipid molecules were only slightly removed from the substrate; the majority of the lipid molecules were still on the substrate surface, as we observed in TIRF.

We want to point out that in this experiment, both TIRF and ATR-FTIR can be used to confirm the lipid bilayer existence on the substrate surface. However, when studying heterogeneous samples or real biological systems, it might be difficult or impossible to locate the same interfacial area in separate SFG and ATR-FTIR measurements. Additionally, the environment variations and sample movement for using different techniques to study the same sample can cause irreversible sample perturbation or variation, leading to inaccurate results. In such conditions, the TIR-SFG and TIRF multimodal system developed in this work will further show its uniqueness in examining structures and presence or localization associated properties of interfacial molecules.

This experiment shows that combining SFG and TIRF techniques provides more interfacial molecular information and can help depict a clearer picture of biological interfaces. It also shows the potential of simultaneously monitoring interfacial dynamics and probing interfacial molecular structures using this multimodal system. TIRF is a widely used microscopy technique in biological research. The integration of SFG and TIRF techniques can help extend SFG to study more complex biological systems, as well as provide molecular structural information of biointerfaces which cannot be provided by TIRF.

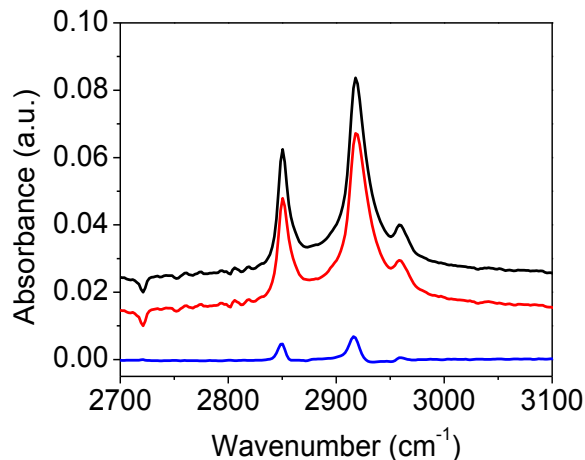


**Figure 5-14. ATR-FTIR spectra of a DPPG monolayer in air (black), the same sample in air after contacting water (red), and their signal difference ((blue curve) = (black curve) – (red curve)).**

#### 5.4.5 Conclusion

In conclusion, we designed and built an SFG and TIRF multimodal system to probe interfacial molecular structures and morphology on the same sample. SFG spectroscopy performed in a TIR configuration guarantees that SFG signal must be mostly generated from the buried interface between the sample and the substrate. Utilizing the same TIR geometry, TIRF images can be acquired to monitor interfacial fluorescent molecules. The system was applied to study interfacial structures of fluorescence PS beads with different surface coverage, showing that surfactant in the beads solution dominates the interfacial structures. DPPG lipid monolayer labeled using Dil has also been studied in different environments. We showed that TIRF could provide supplementary information which could help to interpret SFG spectra. SFG could also help TIRF microscopy to provide molecular structural information at interfaces. The combined surface sensitive spectroscopic and microscopic techniques could help to depict a clearer picture of molecular behaviors of various interfaces. The technique developed in this work is expected to have further impact in the study of biofilms, biosensors and other biological related interfaces.



## 5.5 References

1. Onorato, R. M.; Yoon, A. P.; Lin, J. T.; Somorjai, G. A., *J. Phys. Chem. C* **2012**, *116*, 9947-9954.
2. Morkel, M.; Kaichev, V. V.; Rupprechter, G.; Freund, H. J.; Prosvirin, I. P.; Bukhtiyarov, V. I., *J. Phys. Chem. B* **2004**, *108*, 12955-12961.
3. Humbert, C.; Busson, B.; Abid, J. P.; Six, C.; Girault, H.; Tadjeddine, A., *Electrochim. Acta* **2005**, *50*, 3101-3110.
4. Zhang, D.; Shen, Y.; Somorjai, G. A., *Chem. Phys. Lett.* **1997**, *281*, 394-400.
5. Ma, G.; Allen, H. C., *J. Phys. Chem. B* **2003**, *107*, 6343-6349.
6. Wang, J.; Chen, C.; Buck, S. M.; Chen, Z., *J. Phys. Chem. B* **2001**, *105*, 12118-12125.
7. Gautam, K. S.; Schwab, A. D.; Dhinojwala, A.; Zhang, D.; Dougal, S. M.; Yeganeh, M. S., *Phys. Rev. Lett.* **2000**, *85*, 3854-3857.
8. Zhang, D.; Dougal, S.; Yeganeh, M., *Langmuir* **2000**, *16*, 4528-4532.
9. Nguyen, K. T.; Le Clair, S. V.; Ye, S.; Chen, Z., *J. Phys. Chem. B* **2009**, *113*, 12358-12363.
10. Snyder, R.; Hsu, S.; Krimm, S., *Spectrochimica Acta Part A: Molecular Spectroscopy* **1978**, *34*, 395-406.
11. Wang, J.; Paszti, Z.; Clarke, M. L.; Chen, X.; Chen, Z., *J. Phys. Chem. B* **2007**, *111*, 6088-6095.
12. Hankett, J. M.; Zhang, C.; Chen, Z., *Langmuir* **2012**, *28*, 4654-4662.
13. Zhang, X.; Zhang, C.; Hankett, J. M.; Chen, Z., *Langmuir* **2013**, *29*, 4008-4018.
14. Shen, Y. R., *Nature* **1989**, *337*, 519-525.
15. Chen, Z.; Shen, Y. R.; Somorjai, G. A., *Annu. Rev. Phys. Chem.* **2002**, *53*, 437-465.
16. Lambert, A. G.; Davies, P. B.; Neivandt, D. J., *Appl. Spectrosc. Rev.* **2005**, *40*, 103-145.
17. Jena, K. C.; Hung, K.-K.; Schwantje, T. R.; Hore, D. K., *J. Chem. Phys.* **2011**, *135*, 044704.
18. Zhang, C.; Myers, J. N.; Chen, Z., *Soft Matter* **2013**, *9*, 4738-4761.
19. Roeters, S.; van Dijk, C.; Torres-Knoop, A.; Backus, E.; Campen, R.; Bonn, M.; Woutersen, S., *J. Phys. Chem. A* **2013**, *117*, 6311-6322.
20. Liu, J.; Conboy, J. C., *J. Am. Chem. Soc.* **2004**, *126*, 8376-8377.
21. Howell, C.; Diesner, M. O.; Grunze, M.; Koelsch, P., *Langmuir* **2008**, *24*, 13819-13821.
22. Diesner, M. O.; Howell, C.; Kurz, V.; Verreault, D.; Koelsch, P., *J. Phys. Chem. Lett.* **2010**, *1*, 2339-2342.
23. Bulard, E.; Guo, Z.; Zheng, W.; Dubost, H.; Fontaine-Aupart, M. P.; Bellon-Fontaine, M. N.; Herry, J. M.; Briandet, R.; Bourguignon, B., *Langmuir* **2011**, *27*, 4928-4935.
24. Inoue, K.; Fujii, M.; Sakai, M., *Appl. Spectrosc.* **2010**, *64*, 275-281.
25. Kogure, S.; Inoue, K.; Ohmori, T.; Ishihara, M.; Kikuchi, M.; Fujii, M.; Sakai, M., *Opt. Express* **2010**, *18*, 13402-13406.
26. Raghunathan, V.; Han, Y.; Korth, O.; Ge, N. H.; Potma, E. O., *Opt. Lett.* **2011**, *36*, 3891-3893.
27. Flörsheimer, M.; Brillert, C.; Fuchs, H., *Langmuir* **1999**, *15*, 5437-5439.
28. Hoffmann, D.; Kuhnke, K.; Kern, K., *Rev. Sci. Instrum.* **2002**, *73*, 3221-3226.
29. Cimatu, K.; Baldelli, S., *J. Phys. Chem. B* **2006**, *110*, 1807-1813.
30. Hieu, H. C.; Tuan, N. A.; Li, H.; Miyauchi, Y.; Mizutani, G., *Appl. Spectrosc.* **2011**, *65*, 1254-1259.
31. Smith, K. A.; Conboy, J. C., *Anal. Chem.* **2012**, *84*, 8122-8126.
32. Yeganeh, M. S.; Dougal, S. M.; Silbernagel, B. G., *Langmuir* **2006**, *22*, 637-641.
33. Liu, Y.; Messmer, M. C., *J. Phys. Chem. B* **2003**, *107*, 9774-9779.

34. Wang, J.; Chen, X. Y.; Clarke, M. L.; Chen, Z., *Proc. Natl. Acad. Sci. U. S. A.* **2005**, *102*, 4978-4983.
35. Nguyen, K. T.; Le Clair, S. V.; Ye, S.; Chen, Z., *J. Phys. Chem. B* **2009**, *113*, 12169-12180.
36. Zhang, C.; Wang, J.; Khmaladze, A.; Liu, Y.; Ding, B.; Jasensky, J.; Chen, Z., *Opt. Lett.* **2011**, *36*, 2272-2274.
37. Acevedo, N.; Ding, J.; Smith, G. D., *Biol. Reprod.* **2007**, *77*, 872-879.
38. Ye, S.; Nihonyanagi, S.; Uosaki, K., *Phys. Chem. Chem. Phys.* **2001**, *3*, 3463-3469.
39. Silverman, H. G.; Roberto, F. F., *Mar. Biotechnol.* **2007**, *9*, 661-681.
40. Axelrod, D., *The Journal of cell biology* **1981**, *89*, 141-145.
41. Schneckenburger, H., *Curr. Opin. Biotechnol.* **2005**, *16*, 13-18.
42. Watkins, R. W.; Robertson, C. R., *J. Biomed. Mater. Res.* **1977**, *11*, 915-938.
43. Lok, B. K.; Cheng, Y.-L.; Robertson, C. R., *J. Colloid Interface Sci.* **1983**, *91*, 87-103.
44. Axelrod, D., *Traffic* **2001**, *2*, 764-774.
45. Serulle, Y.; Sugimori, M.; Llinás, R. R., *Proc. Natl. Acad. Sci. U. S. A.* **2007**, *104*, 1697-1702.
46. Gragson, D.; McCarty, B.; Richmond, G., *J. Phy. Chem.* **1996**, *100*, 14272-14275.
47. Nguyen, K. T.; Soong, R.; Im, S. C.; Waskell, L.; Ramamoorthy, A.; Chen, Z., *J. Am. Chem. Soc.* **2010**, *132*, 15112-15115.

## CHAPTER 6

# INTERPRETATION OF PDMS COHERENT ANTI-STOKES RAMAN SCATTERING SPECTRA

### 6.1 Motivation

Since the first report of the coherent anti-Stokes Raman scattering (CARS) phenomenon,<sup>1</sup> CARS technique has been gradually developed into a powerful analytical tool for chemical, material, and biological analysis. CARS is a coherent four-wave mixing process resulting in a coherent anti-Stokes Raman signal which is usually many orders of magnitude stronger than the spontaneous Raman signal in the detection direction. The anti-Stokes Raman signal is generated at a wavelength shorter than the input laser beams and thus can effectively discriminate the possible fluorescence background in signal collection. The stronger and directed signal also leads to significantly reduced signal collection time as compared to spontaneous Raman measurement. The above advantages granted CARS unique applications in many areas. The theory of CARS has been developed and reviewed systemically.<sup>2</sup> CARS spectroscopy found extensive applications in studies of gases,<sup>3-10</sup> liquids or solutions,<sup>11-14</sup> and solid phase materials.<sup>15-19</sup> It has also been developed as a tool for the standoff detection of explosive materials.<sup>20-25</sup>

Recently, CARS microscopy has been developed for biological and material studies.<sup>25-29</sup> With the help of the laser scanning technique, fast image collection rate for CARS microscopy was achieved.<sup>30</sup> Thanks to recent fast advancement of laser technologies and the excellent research efforts from various research groups, CARS microscopic systems have been significantly improved with better sensitivity, lower nonresonant background, broader spectral imaging

windows, stronger capability and wider applications.<sup>31-38</sup> CARS microscopy has been extensively applied to lipid detection and diagnosis.<sup>39-42</sup> Various technical improvements have been made on CARS microscopy such as epi-detection CARS,<sup>43</sup> polarization sensitive CARS,<sup>34</sup> heterodyne CARS,<sup>37</sup> single pulse CARS,<sup>44</sup> holographic CARS,<sup>45</sup> hyperspectral CARS,<sup>46</sup> etc. Such works advanced CARS to be a powerful microscopy and imaging tool for biomedical applications.

Although significant advancement of technical development and applications in CARS have been made in the last two decades, theoretical work, especially quantitative physical interpretation of CARS spectrum based on molecular symmetries, has achieved to a lesser extent. Such quantitative understanding of the basic third order nonlinear susceptibility under different symmetry conditions is important for the advanced CARS spectral analysis and imaging applications. One of the key aspects of such quantitative interpretation lies on the explanation and prediction of ratios between different susceptibility tensor elements of functional group vibrational modes in a molecule. To obtain such information requires the theoretical connection between the macroscopic susceptibility tensor and the hyperpolarizabilities of the molecular vibrations considering their properties under different symmetry conditions. Such understanding can help to predict vibrational intensity relationships of different vibrational modes of a certain functional group; it can also help to improve the vibrational peak assignment. For third order nonlinear optical processes, the vibrational transition selection rules have been studied systemically previously considering different molecular symmetry arrangements.<sup>47</sup> However, the detailed quantitative understanding on signal intensity relationship between different vibrational modes of a functional group has not been achieved. For second order nonlinear vibrational spectroscopies such as sum frequency generation (SFG) spectroscopy, such theoretical understanding has been systemically developed.<sup>48-53</sup> One of the most widely used methods in such study, bond additivity method, has

been applied to quantitatively interpret SFG spectra.<sup>49, 54-57</sup> Using bond additivity model, the ratios of second order hyperpolarizability tensor elements of a functional group with various symmetry arrangements could be obtained for their different vibrational modes and showed good agreements with the experimental results.

The goal of this work is to develop a theory with the help of the bond additivity method to quantitatively interpret relative intensities of CARS signals from different vibrational modes of a molecule considering the molecular symmetries. We want to build a theoretical connection between CARS measurement and Raman measurement. We also want to compare our theoretically deduced results to the experimental measurement results. Such quantitative understanding of CARS spectra should have important applications in spectral analysis in CARS spectroscopy and microscopy.

## 6.2 Theoretical Development of Bond Additivity Method in CARS

### 6.2.1 Third Order Nonlinear Susceptibility and Molecular Hyperpolarizability

As introduced in Chapter 1, CARS is a third order nonlinear optical process. Its signal intensity is related to the input laser beam intensities through the following equation:

$$I_{CARS} \propto |\chi_{eff}^{(3)}|^2 I_p^2 I_s \quad (6.1)$$

Here  $I_{CARS}$  is the output CARS signal intensity,  $I_p$  is the intensity of the pump or probe beam and  $I_s$  is the intensity of the input Stokes beam. In most CARS experiments, pump and probe share the same beam.  $\chi_{eff}^{(3)}$  is the effective third order nonlinear optical susceptibility of the sample generating CARS signal.

$$\chi_{eff}^{(3)} = \chi_{NR}^{(3)} + \frac{\mathbf{A}_T}{\omega_T - 2\omega_p - i\Gamma_T} + \frac{\mathbf{A}_R}{\omega - (\omega_p - \omega_s) - i\Gamma_R} \quad (6.2)$$

The first term  $\chi_{NR}^{(3)}$  is the nonresonant contribution from virtual states; the second term is the enhanced nonresonant contribution from the two-photon electronic resonance; the third term is the vibrational resonance contribution from the coherent Raman transition.<sup>26</sup>  $\omega_T$  is the electronic transition frequency (can possibly be reached by two-photon absorption);  $\omega_p$  is the pump/probe beam frequency;  $\omega_s$  is the Stokes beam frequency;  $\omega$  is the output or signal frequency.  $\mathbf{A}_T$  and  $\mathbf{A}_R$  are amplitudes of the two-photon absorption transition and the Raman transition, respectively;  $\Gamma_T$  and  $\Gamma_R$  are damping factors of the two-photon transition and the Raman transition, respectively. The combination of the first two terms, especially the second one, is usually responsible for the strong nonresonant line-shape distortion in CARS spectroscopy. In this research we focus on the study of the third term because it is related to the vibrational transition that carries the fingerprint chemical information of the sample and also dominates our spectrum. Theoretically, CARS spectra can be fitted using equation (6.2). For samples with negligible two-photon absorption, the second term can be combined with the first term, and the contribution of the first two terms can be treated as a constant.

The CARS experimental geometry used in this study is shown in Figure 6-1a. The energy diagram of CARS spectroscopy is shown in Figure 6-1b. We collected CARS signal of the sample deposited on an optical window (fused silica window) in a ‘reflective’ geometry. Here polarized CARS measurement was performed. For a specific vibrational mode, the effective third order nonlinear susceptibility elements  $\chi_{eff,ABCD}^{(3)}$  can be correlated to the local nonlinear susceptibility elements  $\chi_{IJKL}^{(3)}$  (defined in the lab frame coordinate system (x, y, z)) of the sample through the following equation:

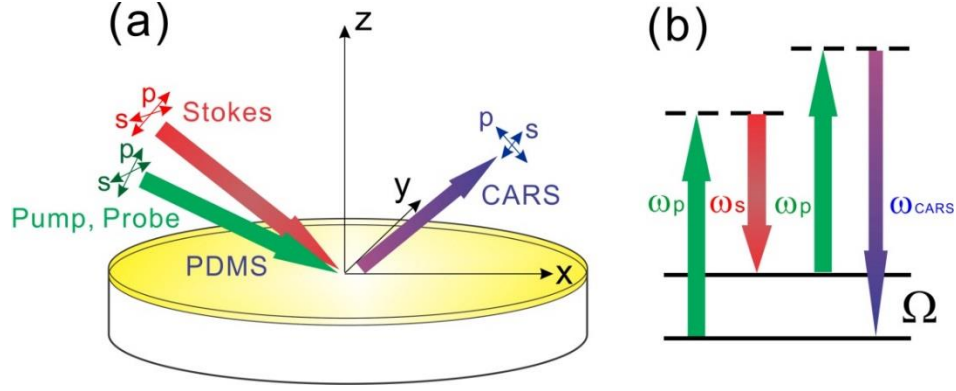


**Figure 6-1. (a) CARS experimental geometry used in this study. The pump/probe and Stokes beams lie in the x-z plane. The s and p polarizations are defined as perpendicular and parallel with respect to the x-z plane, respectively. (b) Energy diagram of CARS spectroscopy.**

$$\chi_{eff,ABCD}^{(3)} = \sum_{IJKL=x,y,z} M \cdot L_{AI}(\omega_{CARS})L_{BJ}(\omega_p)L_{CK}(\omega_p)L_{DL}(\omega_s) \cdot \chi_{IJKL}^{(3)}, \quad A, B, C, D = s, p \quad (6.3)$$

Here  $L_{AI}, L_{BJ}, L_{CK}, L_{DL}$  are local field correction coefficients of the input and output laser beams, known as the Fresnel coefficients.<sup>52</sup> The equations to calculate such Fresnel coefficients and their deduced values in this work are listed in the section 6.4.  $M$  is a factor that combines (multiplies) all the trigonometric factors of the input electric field amplitude projected on the lab frame coordinate axis as demonstrated in Figure 6-1.<sup>58</sup> A, B, C, D indices represent polarization combinations (s or p) of the CARS experiment; I, J, K, L indices represent coordinates in the lab frame system (x, y, z) as shown in Figure 6-1a. The polarization combination ‘ABCD’ indicates: A-polarized CARS signal beam, B-polarized pump beam, C-polarized probe beam, D-polarized Stokes beam. Giving two specific examples of equation (6.3):

$$\chi_{eff,ssss}^{(3)} = 1 \cdot L_{sy}(\omega_{CARS})L_{sy}(\omega_p)L_{sy}(\omega_p)L_{sy}(\omega_s) \cdot \chi_{yyyy}^{(3)} \quad (6.4)$$

$$\begin{aligned}
\chi_{\text{eff},spps}^{(3)} = & \cos^2 \theta_p \cdot L_{sy}(\omega_{\text{CARS}})L_{px}(\omega_p)L_{px}(\omega_p)L_{sy}(\omega_s) \cdot \chi_{yxxy}^{(3)} \\
& + \cos \theta_p \sin \theta_p \cdot L_{sy}(\omega_{\text{CARS}})L_{px}(\omega_p)L_{pz}(\omega_p)L_{sy}(\omega_s) \cdot \chi_{yxzy}^{(3)} \\
& + \sin \theta_p \cos \theta_p \cdot L_{sy}(\omega_{\text{CARS}})L_{pz}(\omega_p)L_{px}(\omega_p)L_{sy}(\omega_s) \cdot \chi_{yzxy}^{(3)} \\
& + \sin^2 \theta_p \cdot L_{sy}(\omega_{\text{CARS}})L_{pz}(\omega_p)L_{pz}(\omega_p)L_{sy}(\omega_s) \cdot \chi_{yzzy}^{(3)}
\end{aligned} \tag{6.5}$$

$\chi_{\text{eff},ssss}^{(3)}$  only has one nonzero corresponding local susceptibility term  $\chi_{yyyy}^{(3)}$  because the s-polarized electric field is along the y axis.  $\chi_{\text{eff},spps}^{(3)}$  has four terms because the p-polarized electric field can be projected on both the x and z axes. The projection onto x generates  $\cos \theta_p$  and the projection onto z leads to  $\sin \theta_p$ . These examples show that the measured effective third order nonlinear susceptibility components under certain polarization combinations can be related to the local third order nonlinear susceptibility components of the sample.

The next step is to correlate the local third order nonlinear susceptibility to the molecular hyperpolarizability  $\gamma_{ijkl}^{(3)}$ . Such relation can be expressed as:

$$\chi_{IJKL}^{(3)} = N \sum_{IJKL=x,y,z} \langle R_{Ii} R_{Jj} R_{Kk} R_{Ll} \rangle \gamma_{ijkl}^{(3)} \quad ijkl = a, b, c \tag{6.6}$$

In this equation, N is the number density of the molecules contributing the CARS signal. R represents the elements of the transformation matrix from the molecular frame (a,b,c) to the lab frame (x,y,z) coordinate system. Such a transformation matrix **R** is usually a function of three rotational angles: azimuthal angle  $\phi$ , tilt angle  $\theta$  and twist angle  $\psi$ , as defined in Figure 6-2 based on the Euler angle definition. The angle brackets here indicate ensemble average. This equation means that the macroscopic third order nonlinear susceptibility is the ensemble average of the hyperpolarizability of each molecule projected to the lab frame multiplied by the number density of molecules. The transformation matrices of counter-clockwise rotations with respect to x, y, z or a, b, c axes (pointing towards the observer) for  $\alpha$  degree are:



$$\begin{aligned}
R_{x(\text{or } a)} &= \begin{bmatrix} 1 & 0 & 0 \\ 0 & \cos \alpha & \sin \alpha \\ 0 & -\sin \alpha & \cos \alpha \end{bmatrix}, \\
R_{y(\text{or } b)} &= \begin{bmatrix} \cos \alpha & 0 & -\sin \alpha \\ 0 & 1 & 0 \\ \sin \alpha & 0 & \cos \alpha \end{bmatrix}, \\
R_{z(\text{or } c)} &= \begin{bmatrix} \cos \alpha & \sin \alpha & 0 \\ -\sin \alpha & \cos \alpha & 0 \\ 0 & 0 & 1 \end{bmatrix}
\end{aligned} \tag{6.7}$$

For the three dimensional rotations in an Euler angle system, there are multiple basic rotation combinations to overlap the two coordinate systems. Each combination consists of three rotation operations. Here we choose the ‘z-y-z’ rotation combination: the first rotation is with respect to z axis (azimuthal angle  $\phi$ ), the second rotation is with respect to y axis (tilt angle  $\theta$ ), the third rotation is with respect to z axis again (twist angle  $\psi$ ). The resulting transformation matrix is:

$$\begin{aligned}
\mathbf{R}_{z-y-z} &= \begin{bmatrix} \cos \psi & \sin \psi & 0 \\ -\sin \psi & \cos \psi & 0 \\ 0 & 0 & 1 \end{bmatrix} \begin{bmatrix} \cos \theta & 0 & -\sin \theta \\ 0 & 1 & 0 \\ \sin \theta & 0 & \cos \theta \end{bmatrix} \begin{bmatrix} \cos \phi & \sin \phi & 0 \\ -\sin \phi & \cos \phi & 0 \\ 0 & 0 & 1 \end{bmatrix} \\
&= \begin{bmatrix} \cos \phi \cos \theta \cos \psi - \sin \phi \sin \psi & \cos \theta \cos \psi \sin \phi + \cos \phi \sin \psi & -\cos \psi \sin \theta \\ -\cos \psi \sin \phi - \cos \phi \cos \theta \sin \psi & \cos \phi \cos \psi - \cos \theta \sin \phi \sin \psi & \sin \theta \sin \psi \\ \cos \phi \sin \theta & \sin \phi \sin \theta & \cos \theta \end{bmatrix} \tag{6.8}
\end{aligned}$$

Calculating the nonlinear susceptibility using equation (6.6) for a bulk material in which molecules adopt random orientations, all the azimuthal angle  $\phi$ , tilt angle  $\theta$  and twist angle  $\psi$  need to be averaged by taking the angle integration (0 to  $2\pi$  for  $\phi$  and  $\psi$ ; 0 to  $\pi$  for  $\theta$ ).

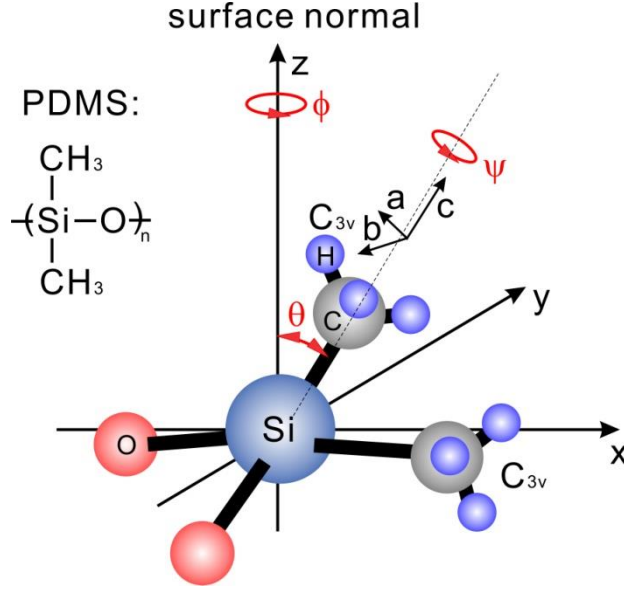


**Figure 6-2. Left: the molecular formula of PDMS. Right: Schematic of a PDMS molecule residue in a lab frame coordinate system (x, y, z) defined in Figure 6-1. Each methyl group presents a  $C_{3v}$  symmetry. The molecular coordinate is shown by (a, b, c). Azimuthal angle  $\phi$ , tilt angle  $\theta$  and twist angle  $\psi$  are also defined.**

The third order nonlinear susceptibility tensor  $\chi^{(3)}$  has 81 elements. However, many elements may equal to zero due to the symmetry properties of the functional group under consideration. Furthermore, as shown in equations (6.4) and (6.5), CARS signals detected under certain polarization combinations only probe certain elements. For example, the ssss polarization combination only probes  $\chi_{yyyy}^{(3)}$ . The macroscopic symmetry of the sample can also reduce the number of nonzero terms in  $\chi^{(3)}$ . For example, for an azimuthally symmetric achiral thin film in the x-y plane, all the  $\chi^{(3)}$  elements with even numbers of x or y are zero. In such a case, there are only 21 nonzero tensor elements:

$$\begin{aligned} \chi_{xxxx}^{(3)} &= \chi_{yyyy}^{(3)}, & \chi_{yyzz}^{(3)} &= \chi_{xxzz}^{(3)}, & \chi_{zzyy}^{(3)} &= \chi_{zzxx}^{(3)}, & \chi_{zyyz}^{(3)} &= \chi_{zaxz}^{(3)}, \\ \chi_{yzzy}^{(3)} &= \chi_{xzax}^{(3)}, & \chi_{yzzy}^{(3)} &= \chi_{xzax}^{(3)}, & \chi_{zyzy}^{(3)} &= \chi_{zaxx}^{(3)}, & \chi_{xxyy}^{(3)} &= \chi_{yyxx}^{(3)}, \\ \chi_{xyxy}^{(3)} &= \chi_{yxyx}^{(3)}, & \chi_{xyxy}^{(3)} &= \chi_{yxxy}^{(3)}, & \chi_{zzzz}^{(3)} & & & \end{aligned} \quad (6.9)$$

A methyl group is usually treated as having a  $C_{3v}$  symmetry. Although the validity of such treatment has been discussed, it is generally accepted that the coupling between the C-H vibration in a methyl group and the vibrational modes of other parts of the molecule can be ignored (i.e. the  $C_{3v}$  symmetry treatment of a methyl is reasonable).<sup>54</sup> In this work, we will treat a Si-CH<sub>3</sub> group as adopting  $C_{3v}$  symmetry for CARS signals analysis. Our results show that such treatment and analysis are acceptable.

The third order hyperpolarizability  $\gamma_{ijkl}^{(3)}$  is defined as:

$$\gamma_{ijkl}^{(3)} \propto \frac{\partial \alpha_{ij}}{\partial Q_q} \frac{\partial \alpha_{kl}}{\partial Q_q} = \alpha'_{ij} \alpha'_{kl} \quad (6.10)$$

Here  $\alpha'_{ij}$  and  $\alpha'_{kl}$  are Raman polarizability derivatives with respect to the normal mode coordinate of the qth vibrational mode. Therefore, the third order nonlinear hyperpolarizability that determines CARS functional group vibrational modes can be derived from the Raman tensor derivatives of the same functional group. Next, we will use the bond additivity method to derive the forms of such derivatives for a PDMS methyl group.

### 6.2.2 Bond Additivity for Methyl Group C-H Vibrational Stretching

The basic idea of ‘bond additivity’ is to obtain a parameter (e.g. dipole moment, Raman polarizability) of a molecule by combining the corresponding parameter of each related chemical bond forming the molecule, considering the molecular geometry. For example, using bond additivity method to obtain the polarizability of a certain C-H mode of a methyl group, we can combine the polarizability of each C-H group considering the vibrational modes and methyl group geometry. An individual C-H bond can be considered possessing  $C_{\infty v}$  symmetry. Its Raman tensor derivatives satisfy  $\alpha'_{aa} / \alpha'_{cc} = \alpha'_{bb} / \alpha'_{cc} = r$ , with all other components of the tensor equaling to zero. Here the single C-H bond coordinate system is defined by (a', b', c') and the c' axis of the

molecular coordinate is set along the C-H bond, as depicted in Figure 6-3a. We can combine the three C-H bonds in a methyl group in the molecular coordinate system (a, b, c) shown in Figure 6-3b to deduce the Raman tensor derivative of the entire CH<sub>3</sub> group for different vibration modes.

The combining of the three C-H bonds requires the rotation of the single bond coordinate system (Figure 6-3a) to project each C-H bond to the methyl group coordinate system (Figure 6-3b). The transformation of the Raman tensor derivative after rotation is:

$$\mathbf{\alpha}'_{C-H,b} = \mathbf{T}\mathbf{\alpha}'_{C-H,a}\mathbf{T}^T \quad (6.11)$$

$\mathbf{T}$  is the transformation matrix tensor for each bond and  $\mathbf{T}^T$  is the transpose of  $\mathbf{T}$ .  $\mathbf{\alpha}'_{C-H,a}$  is the Raman tensor derivative in coordinate 1 (before rotation) while  $\mathbf{\alpha}'_{C-H,b}$  is the Raman derivative in coordinate 2 (after rotation).

The Raman tensor derivative of a single C-H bond (C<sub>∞v</sub> symmetry) has the form:

$$\mathbf{\alpha}'_{C-H} = \alpha'_{cc} \begin{bmatrix} r & 0 & 0 \\ 0 & r & 0 \\ 0 & 0 & 1 \end{bmatrix} \quad (6.12)$$

Each single C-H bond can rotate freely along its principle axis. Therefore, we can choose a coordinate system for the C-H bond 1 (a', b', c') as demonstrated in Figure 6-3b. Here the b' axis for the C-H bond is along the b axis defined for the entire methyl group. Figures 6-3c and 6-3d depict such coordinate system from projections on a-b and a-c planes respectively for clearer demonstration. The only rotation required to overlap the (a', b', c') coordinate system with the (a, b, c) system is the rotation of  $-\sigma$  angle with respect to b' axis. According to the methyl group geometry,  $\sigma$  is calculated to be 70.5°. We can define this rotation as  $R_{b',-71}$ . Thus we have:

$$\mathbf{\alpha}'_{C-H1} = R_{b',-71}\mathbf{\alpha}'_{C-H}R_{b',-71}^T \quad (6.13)$$

For the second C-H bond, we choose the coordinate ( $a''$ ,  $b''$ ,  $c''$ ) as defined in Figure 6-3b. Here,  $b''$  axis is perpendicular to the plane formed by C-H bond 2 and the  $c$  axis of the methyl group;  $c''$  is along the same C-H bond 2. Two rotations are needed to overlap the ( $a''$ ,  $b''$ ,  $c''$ ) system with the ( $a$ ,  $b$ ,  $c$ ) system: a rotation of  $-71^\circ$  with respect to  $b''$ ; after the first rotation, another rotation of  $-120^\circ$  with respect to  $c''$ . Thus we have

$$\mathbf{a}'_{C-H2} = R_{c'':-120}(R_{b'':-71}\mathbf{a}'_{C-H}R_{b'':-71}^T)R_{c'':-120}^T \quad (6.14)$$

Similarly for the third C-H bond we have:

$$\mathbf{a}'_{C-H3} = R_{c''':120}(R_{b''':-71}\mathbf{a}'_{C-H}R_{b''':-71}^T)R_{c''':120}^T \quad (6.15)$$

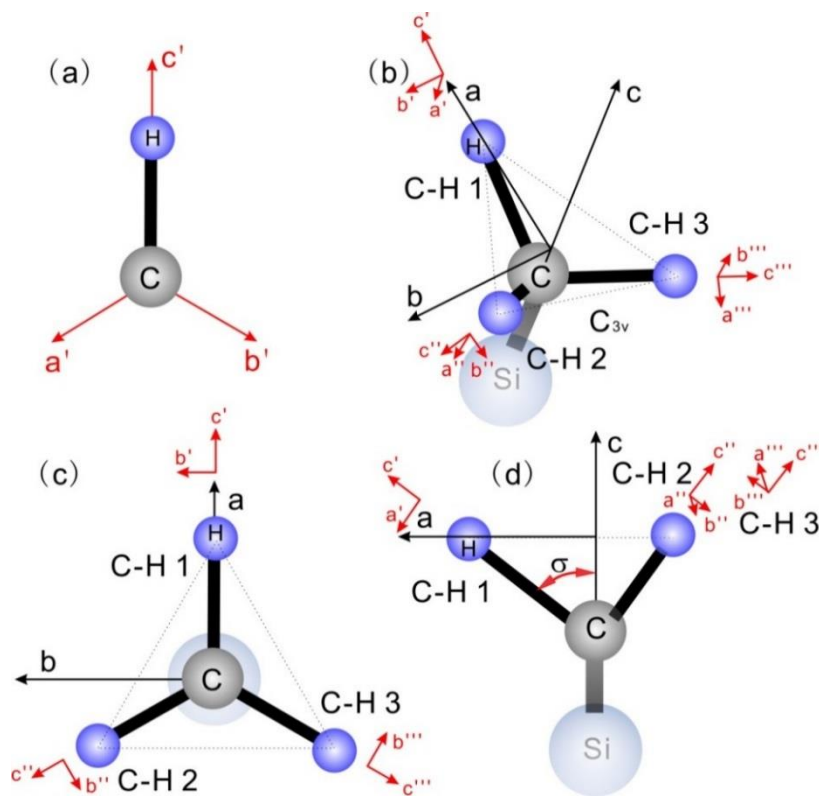


**Figure 6-3.** (a) A single C-H bond and the molecular coordinate system ( $a'$ ,  $b'$ ,  $c'$ ) chosen for the bond. (b) A methyl group and its molecular coordinate system ( $a$ ,  $b$ ,  $c$ ). Three C-H bonds and their independent molecular systems are also defined ( $a''$ ,  $b''$ ,  $c''$ ;  $a'''$ ,  $b'''$ ,  $c'''$ ). C-H bond 1 is in the  $a$ - $c$  plane. The  $c$  axis is set along the methyl group principal axis. (c) The 'top view' ( $a$ - $b$  plane projection) of the picture depicted in (b), the  $c$  axis is perpendicular to the paper. (d) The 'side view' ( $a$ - $c$  plane projection) of the picture depicted in (b), the  $b$  axis is perpendicular to the paper.

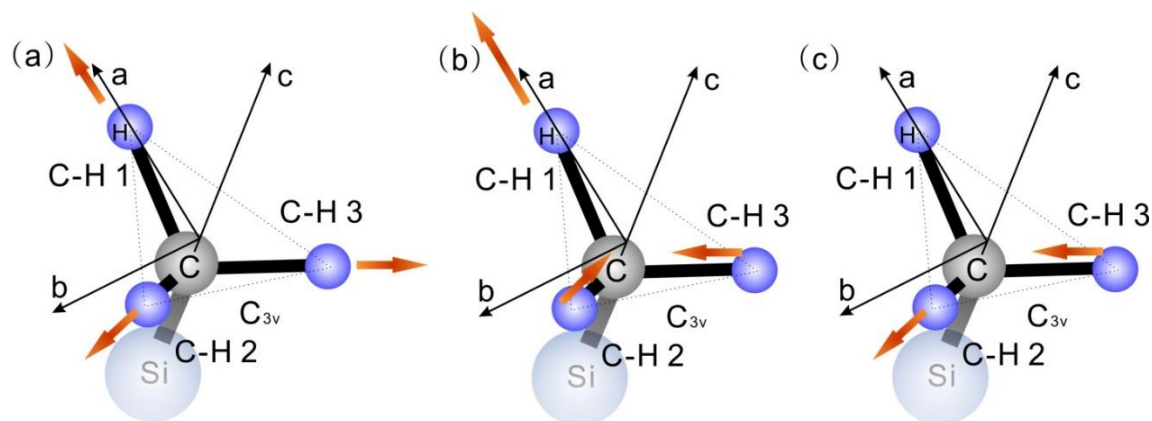


**Figure 6-4. C-H vibrational stretching modes of a methyl group: (a) symmetric  $A_1$  mode; (b) asymmetric  $E_a$  mode; (c) asymmetric  $E_b$  mode.**

In the process of bond additivity, different vibrational modes need to be taken into consideration. For example, a methyl group with  $C_{3v}$  symmetry has three C-H stretching modes. Of these three modes, one is a symmetric stretching ( $A_1$ ) mode while the other two are degenerate asymmetric stretching ( $E_a$  and  $E_b$ ) modes, as demonstrated in Figure 6-4.

Such vibrational modes can be expressed in the normal mode coordinates:<sup>49, 54</sup>

$$\begin{aligned}
 Q_{A_1} &= (\Delta r_1 + \Delta r_2 + \Delta r_3) / (3G_{A_1})^{1/2} \\
 Q_{E_a} &= (2\Delta r_1 - \Delta r_2 - \Delta r_3) / (6G_{E_a})^{1/2} \\
 Q_{E_b} &= (\Delta r_2 - \Delta r_3) / (2G_{E_b})^{1/2}
 \end{aligned}
 \tag{6.16}$$

Here  $\Delta r_n$  is the bond displacement vector along the direction of the  $n$ th C-H bond.  $G_{A_1}$  and

$G_E$  are inverted reduced mass of  $A_1$  and E modes:<sup>54</sup>

$$\begin{aligned}
 G_{A_1} &= \frac{1 + 2\cos\tau}{M_C} + \frac{1}{M_H} \\
 G_E &= \frac{1 - \cos\tau}{M_C} + \frac{1}{M_H}
 \end{aligned}
 \tag{6.17}$$

$\tau$  is the H-C-H bond angle which is  $109.5^\circ$ .  $M_C$  and  $M_H$  are atomic masses of the carbon and hydrogen atoms. We can then obtain  $G_{A_1} = 1.03$  and  $G_E = 1.11$ .

We have calculated the Raman tensor derivative for each of the three C-H bonds above. For the  $A_1$  mode as shown in Figure 6-4a, we can combine the three C-H bonds by simply sum them together and then divided by  $(3G_{A_1})^{1/2}$ , according to equation (6.16):

$$\begin{aligned} \mathbf{\alpha}'_{C-H,A_1} = & (R_{b':-71} \mathbf{\alpha}'_{C-H} R_{b':-71}^T \\ & + R_{c':-120} (R_{b':-71} \mathbf{\alpha}'_{C-H} R_{b':-71}^T) R_{c':-120}^T \\ & + R_{c'':120} (R_{b'':-71} \mathbf{\alpha}'_{C-H} R_{b'':-71}^T) R_{c'':120}^T) / (3G_{A_1})^{1/2} \end{aligned} \quad (6.18)$$

Using equation (6.7) and (6.12), we have:

$$\mathbf{\alpha}'_{C-H,A_1} = \alpha'_{cc} \begin{bmatrix} 0.763+0.944r & 0 & 0 \\ 0 & 0.763+0.944r & 0 \\ 0 & 0 & 0.181+1.526r \end{bmatrix} \quad (6.19)$$

The asymmetric E modes are degenerate for the methyl group, as demonstrated in Figures 6-4b and 6-4c. Using equation (6.16), we can derive the Raman tensor derivatives of the E modes:

$$\begin{aligned} \mathbf{\alpha}'_{C-H,E_a} = & (2R_{b':-71} \mathbf{\alpha}'_{C-H} R_{b':-71}^T \\ & - R_{c':-120} (R_{b':-71} \mathbf{\alpha}'_{C-H} R_{b':-71}^T) R_{c':-120}^T \\ & - R_{c'':120} (R_{b'':-71} \mathbf{\alpha}'_{C-H} R_{b'':-71}^T) R_{c'':120}^T) / (6G_E)^{1/2} \end{aligned} \quad (6.20)$$

$$\begin{aligned} \mathbf{\alpha}'_{C-H,E_b} = & (R_{c':-120} (R_{b':-71} \mathbf{\alpha}'_{C-H} R_{b':-71}^T) R_{c':-120}^T \\ & - R_{c'':120} (R_{b'':-71} \mathbf{\alpha}'_{C-H} R_{b'':-71}^T) R_{c'':120}^T) / (2G_E)^{1/2} \end{aligned} \quad (6.21)$$

$$\begin{aligned} \mathbf{\alpha}'_{C-H,E} = & \mathbf{\alpha}'_{C-H,E_a} + \mathbf{\alpha}'_{C-H,E_b} \\ = & \alpha'_{cc} \begin{bmatrix} 0.519-0.519r & -0.519+0.519r & 0.358-0.358r \\ -0.519+0.519r & -0.519+0.519r & 0.358-0.358r \\ 0.358-0.358r & 0.358-0.358r & 0 \end{bmatrix} \end{aligned} \quad (6.22)$$

Equations (6.19) and (6.22) can be used to derive the CARS molecular hyperpolarizability tensor components with equation (6.10). Furthermore, they can be used to deduce the third order

nonlinear susceptibility of the material for different C-H vibrational modes using equation (6.6). However, the value ‘r’ needs to be known for the quantitative interpretation of the symmetric and asymmetric vibrational spectra. In this work, we performed an empirical approach to determine r value using the relationship between r and the Raman depolarization ratio  $\rho$ .

### 6.2.3 Connecting CARS Measurement with Raman Depolarization Measurement

Raman depolarization can be expressed as:<sup>54, 59</sup>

$$\rho = \frac{3\gamma^2}{45\alpha^2 + 4\gamma^2} \quad (6.23)$$

Here,  $\gamma$  and  $\alpha$  are defined by the derivatives of the Raman polarizability tensor elements:<sup>54, 59</sup>

$$\begin{aligned} \alpha &= \frac{1}{3}[\alpha'_{aa} + \alpha'_{bb} + \alpha'_{cc}] \\ \gamma^2 &= \frac{1}{2}[(\alpha'_{aa} - \alpha'_{bb})^2 + (\alpha'_{bb} - \alpha'_{cc})^2 + (\alpha'_{cc} - \alpha'_{aa})^2 \\ &\quad + 6(\alpha'_{ab} + \alpha'_{bc} + \alpha'_{ca})^2] \end{aligned} \quad (6.24)$$

For functional groups with  $C_{3v}$  symmetry, the Raman tensor derivative elements of the symmetric stretching mode satisfies  $\alpha'_{aa} / \alpha'_{cc} = \alpha'_{bb} / \alpha'_{cc} = R$ , which can also be seen in equation (6.19). Other tensor elements equal to zero. This ‘R’ is the tensor element ratio of the entire group with  $C_{3v}$  symmetry, such as a methyl group, which is different from the ‘r’ discussed previously, which is the tensor element ratio of a single C-H bond. Here for a methyl group:

$$R = \frac{0.763 + 0.944r}{0.181 + 1.526r} \quad (6.25)$$

Using  $\alpha'_{aa} / \alpha'_{cc} = \alpha'_{bb} / \alpha'_{cc} = R$  and equations (6.23)-(6.24), we can calculate the depolarization ratio for the methyl symmetric stretching:



$$\rho_s = \frac{3}{4 + 5[(1 + 2R)/(R - 1)]^2} \quad (6.26)$$

The Raman depolarization ratio  $\rho_s$  of methyl C-H symmetric stretching can be measured using Raman experiment. Once  $\rho_s$  is known, the values of R and r can be derived. Plugging the r value in equations (6.19) and (6.22), the third order nonlinear hyperpolarizability  $\gamma_{ijkl}^{(3)}$  can be calculated. Further using equations (6.10), (6.6) and (6.3), quantitative CARS peak intensity ratio between symmetric and asymmetric C-H stretching modes of a methyl group can be derived.

### 6.3 Experimental Results

In this work we collected CARS spectra from a PDMS film and analyzed such spectra to compare with our theoretical predictions. PDMS is a widely used material in industry which can generate very strong CARS signals from symmetric and asymmetric methyl C-H stretching. The optical transparency of the PDMS can be as low as ~250 nm. Therefore, using the 532 nm pump/probe laser for the CARS experiment, we did not observe significant enhanced two-photon absorption transition background. PDMS has been extensively studied by Raman spectroscopy. In this work, a commercial PDMS sample Sylgard 184 base was deposited on a fused silica window to form a film of about 50  $\mu\text{m}$  thickness. The CARS signal was collected using the reflection geometry as depicted in Figure 6-1a. The input angles of the pump/probe and Stokes beams used in this experiment were ~62° and 58°, respectively.

Details of the CARS system we used in this work were published previously and also mentioned in Chapter 5.<sup>19</sup> Briefly, the system was built based on a commercial SFG vibrational spectrometer. A 532 nm beam was used as the pump/probe beam for CARS experiment. The visible beam tunable from 420~680 nm was used as the Stokes beam source. The Stokes beam was tuned continuously while the CARS signal was detected and plotted as a function of Raman

transition frequency. In the experiment, blocking the reflection beam from the other side of the silica window is necessary to avoid the overwhelming background generated from the substrate. The CARS spectra were collected in the ssss and spps polarization combinations.

The CARS spectrum of PDMS in C-H range using ssss polarization is shown in Figure 6-5a. The spectrum has two peaks. The dominant peak centered at  $2912\text{ cm}^{-1}$  is due to the symmetric C-H stretching of the Si-CH<sub>3</sub> group. The other weaker peak centered at  $2971\text{ cm}^{-1}$  is from the asymmetric C-H stretching of the same group. CARS spectral fitting was performed to obtain quantitative analysis of these two peaks. The spectral fitting was carried out using equation (6.2) by combining the two-photon resonant contribution with the virtual state nonresonant term into one nonresonant constant  $\chi_{NR}^{(3)}$ . The fitting results are listed in Table 6-1. The symmetric and asymmetric C-H stretching peak strength ratio can be calculated as

$$\chi_{ssss,s}^{(3)} / \chi_{ssss,as}^{(3)} = (\mathbf{A}_{A_1} / \mathbf{\Gamma}_{A_1}) / (\mathbf{A}_E / \mathbf{\Gamma}_E) \approx 4.93$$

In the spectrum collected using the spps polarization, only one peak centered at around  $2968\text{ cm}^{-1}$  was detected, due to the C-H asymmetric stretching of the methyl group. No signal from the symmetric stretching mode at  $\sim 2910\text{ cm}^{-1}$  was detected. The spectral fitting of this asymmetric stretching peak was also performed and the results are also listed in Table 6-1.

CARS spectra collected using different polarization combinations are very different. Additionally the symmetric and asymmetric C-H stretching peaks in the ssss spectrum have very different intensities. In the next section we will deduce the symmetric and asymmetric C-H stretching peak strength ratio using the bond additivity method developed above and compare the theoretical results with these experimental data.

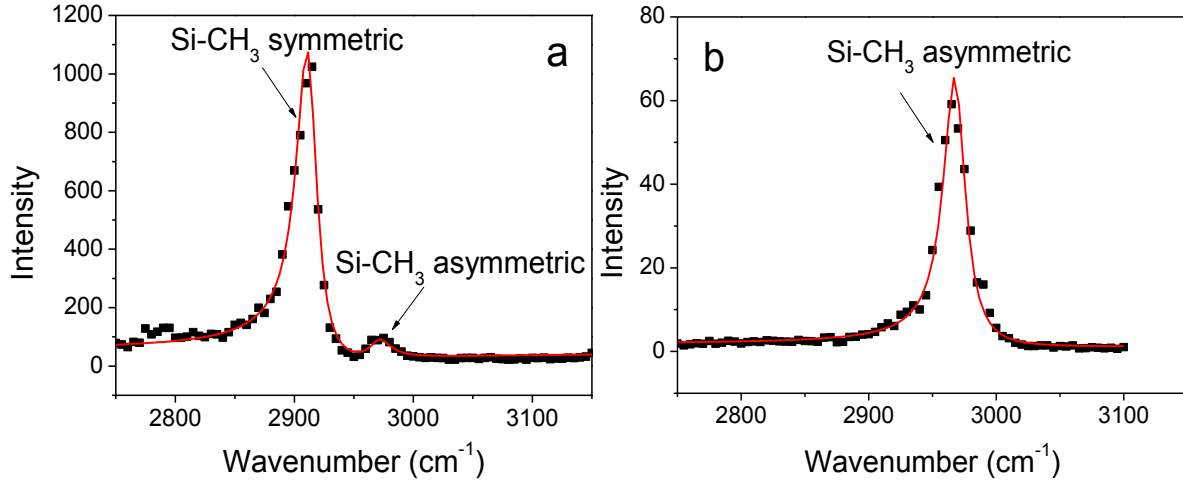


**Figure 6-5. (a) CARS spectrum of PDMS film collected using ssss polarization combination; (b) CARS spectrum of PDMS film collected using spps polarization combination. Dots are experimental data, lines are spectral fitting results using equation (6.2).**

		Value	
(a)	Offset (ssss)		35.0 a.u.
	$\chi_{NR}^{(3)}$ (ssss)		-3.9 a.u.
	Symmetric mode (ssss)	$\mathbf{A}_{A_1}$	328.7 a.u.
		$\Omega_{A_1}$	2912 $\text{cm}^{-1}$
		$\Gamma_{A_1}$	10.5 $\text{cm}^{-1}$
	Asymmetric mode (ssss)	$\mathbf{A}_E$	66.7 a.u.
		$\Omega_E$	2971 $\text{cm}^{-1}$
$\Gamma_E$		10.5 $\text{cm}^{-1}$	
(b)	Offset (spps)		1.3 a.u.
	$\chi_{NR}^{(3)}$ (spps)		-0.6 a.u.
	Asymmetric mode (spps)	$\mathbf{A}_{A_1}$	83.4 a.u.
		$\Omega_{A_1}$	2968 $\text{cm}^{-1}$
$\Gamma_{A_1}$		10.5 $\text{cm}^{-1}$	

**Table 6-1. Spectral fitting parameters used for the fitting in Figure 6-5.**

## 6.4 Discussion

In section 6.2, we stated that in order to theoretically calculate the third order nonlinear susceptibility tensor element ratio corresponding to the symmetric and asymmetric stretching modes of a methyl group, Raman depolarization ratio of the symmetric stretching mode needs to be known (in order to obtain the value of  $r$ ). In this work PDMS was chosen as an example for the quantitative methyl group spectral analysis. The Raman depolarization ratio of PDMS has been well characterized. From previous publications, we know that with zero extension ratio (used in this work),  $\rho_{s,PDMS}$  ranges from 0.018 to 0.022 for the methyl symmetric stretching.<sup>60-61</sup> The molecular weight of the PDMS does not significantly alter the depolarization ratio value. Here we will adopt this value range for our calculation.

Using equation (6.26) we can determine that  $R$  is in the range of 1.8 to 2.0. There are two possible  $R$  solutions corresponding to each  $\rho_{s,PDMS}$  value. Here we only choose the one that gives  $R > 1$ , because for  $C_{3v}$  symmetry, generally  $1 < R < 4$ .<sup>54</sup> We can then obtain the value of  $r$  using equation (6.25) and its value is in the range of 0.24 to 0.20.

We can plug our derived  $r$  value into equations (6.19) and (6.22) to obtain Raman tensor derivatives for methyl symmetric and asymmetric stretching modes. Further we can insert equation (6.19) and (6.22) into equation (6.10) and (6.6) and average all the azimuthal, tilt and twist angles to derive the values of the susceptibility elements which can provide resonance strength ratio of symmetric and asymmetric modes.

Equation (6.6) can be written in another form for bulk materials with random molecular orientations:

$$\chi^{(3)} = \frac{N}{4\pi^3} \int_0^\pi \int_0^{2\pi} \int_0^{2\pi} \mathbf{R} \otimes \mathbf{R} \otimes \mathbf{R} \otimes \mathbf{R} \cdot \gamma^{(3)} \sin\theta d\phi d\psi d\theta \quad (6.27)$$

In this expression,  $\chi^{(3)}$  is a nonlinear susceptibility matrix which is an 81 by 1 matrix.  $\gamma^{(3)}$  is the third order molecular hyperpolarizability matrix which is also an 81 by 1 matrix.  $\mathbf{R}$  is a rotation transformation matrix which is defined in equation (6.8). The angular average was performed by integrating from 0 to  $2\pi$  for  $\phi$  and  $\psi$ , and from 0 to  $\pi$  for  $\theta$ , then multiplying by  $1/4\pi^3$ . The sign  $\otimes$  means kronecker product.

Another way to express  $\gamma^{(3)}$  is to use a 9 by 9 matrix formed by  $\mathbf{a}' \otimes \mathbf{a}'$ , where each  $\mathbf{a}'$  is a 3 by 3 matrix. The detailed  $\gamma^{(3)}$  matrix form (detailed element arrangements) is shown in the Appendix 6.6. If we use such expression (9 by 9 matrix),  $\chi^{(3)}$  satisfies:

$$\chi^{(3)} = \frac{Nc}{4\pi^3} \int_0^\pi \int_0^{2\pi} \int_0^{2\pi} \mathbf{R} \otimes \mathbf{R}(\mathbf{a}' \otimes \mathbf{a}')(\mathbf{R} \otimes \mathbf{R})^T \sin\theta d\phi d\psi d\theta \quad (6.28)$$

Here  $\chi^{(3)}$  is a 9 by 9 matrix representing the same susceptibility elements as in equation (6.27).  $c$  is a constant ratio between  $\gamma^{(3)}$  and  $\alpha'_{ij}\alpha'_{kl}$  as shown in equation (6.10). Mathematically equation (6.27) and (6.28) are identical expressions. The only difference is the rearrangement of the matrix elements.

When we take the susceptibility ratio between the symmetric and asymmetric stretching modes in a certain polarization combination:

$$\frac{\chi_s^{(3)}}{\chi_{as}^{(3)}} = \frac{\int_0^\pi \int_0^{2\pi} \int_0^{2\pi} \mathbf{R} \otimes \mathbf{R}(\mathbf{a}'_{C-H,A_1} \otimes \mathbf{a}'_{C-H,A_1})(\mathbf{R} \otimes \mathbf{R})^T \sin\theta d\phi d\psi d\theta}{\int_0^\pi \int_0^{2\pi} \int_0^{2\pi} \mathbf{R} \otimes \mathbf{R}(\mathbf{a}'_E \otimes \mathbf{a}'_E)(\mathbf{R} \otimes \mathbf{R})^T \sin\theta d\phi d\psi d\theta} \quad (6.29)$$

Inserting equations (6.8), (6.19) and (6.22) into equation (6.29) with the derived value of  $r$  (here we used minimum and maximum values 0.20 and 0.24), we can obtain all the third order nonlinear susceptibility elements relations for symmetric and asymmetric modes. The detailed results are shown in the Appendix 6.6. In this work we are interested in the ratio  $\chi_{yyyy,s}^{(3)} / \chi_{yyyy,as}^{(3)}$ ,

which is measured using CARS experiment in the ssss polarization (the CARS signal measured using the ssss polarization combination is only related to  $\chi_{yyy}^{(3)}$ , as shown in equation (6.4)). We used Mathematica 7.0 to calculate such results and obtained:  $\chi_{yyy,s}^{(3)} / \chi_{yyy,as}^{(3)} = 4.7$  when  $r = 0.20$ ;  $\chi_{yyy,s}^{(3)} / \chi_{yyy,as}^{(3)} = 5.9$  when  $r = 0.24$ .

In the previous CARS experiment, signals generated by the symmetric and asymmetric modes of a methyl group were detected in the same ssss polarization combination. Therefore, the Fresnel coefficients in equation (6.4) are the same for both modes. For the measured peak intensity ratio, we have  $\chi_{yyy,s}^{(3)} / \chi_{yyy,as}^{(3)} = \chi_{sss,s}^{(3)} / \chi_{sss,as}^{(3)} = 4.93$  (from Table 6-1). This measured value falls into the range from 4.7 to 5.9 as we calculated above. This indicates that our theoretical work can be used to quantitatively interpret and predict the CARS vibrational stretching intensities of different methyl vibrational modes.

Using the bond additivity method, we can also calculate some characteristics of the vibrational signals detected using other polarization combinations. For example, from equation (6.5) we know that  $\chi_{eff,spps}^{(3)}$  is related to  $\chi_{yxy}^{(3)}$ ,  $\chi_{yxz}^{(3)}$ ,  $\chi_{yzx}^{(3)}$ , and  $\chi_{yzy}^{(3)}$ . Assuming that the PDMS film is isotropic in the x-y plane and a methyl group is adopting  $C_{3v}$  symmetry, susceptibilities tensor elements  $\chi_{yxz}^{(3)}$  and  $\chi_{yzx}^{(3)}$  equal to zero, as we showed in equation (6.9). Therefore,  $\chi_{eff,spps}^{(3)}$  is only related to  $\chi_{yxy}^{(3)}$  and  $\chi_{yzy}^{(3)}$ . Based on our calculation results (shown in the Appendix 6.6), for the  $r = 0.20$  case,

$$\chi_{yyy,s}^{(3)} / \chi_{yxy,s}^{(3)} = \chi_{yyy,s}^{(3)} / \chi_{yzy,s}^{(3)} = 0.42 / 0.0088 \approx 48$$

$$\chi_{yyy,as}^{(3)} / \chi_{yxy,as}^{(3)} = \chi_{yyy,as}^{(3)} / \chi_{yzy,as}^{(3)} = 0.088 / 0.066 \approx 1.3$$

If we want to compare the CARS signal strengths collected using different polarization combinations, Fresnel coefficients need to be considered, as shown in equation (6.5). It is difficult to deduce the exact Fresnel factors for the experiments. However, the approximate (the order of magnitude) values can be obtained.

The equations used for calculating the Fresnel coefficients are:<sup>52</sup>

$$\begin{aligned}
 L_{sy} &= \frac{2n_1(\omega) \cos \theta}{n_1(\omega) \cos \theta + n_2(\omega) \cos \gamma}, \\
 L_{px} &= \frac{2n_1(\omega) \cos \gamma}{n_1(\omega) \cos \gamma + n_2(\omega) \cos \theta}, \\
 L_{pz} &= \frac{2n_2(\omega) \cos \theta}{n_1(\omega) \cos \gamma + n_2(\omega) \cos \theta} \left( \frac{n_1(\omega)}{n'(\omega)} \right),
 \end{aligned} \tag{6.30}$$

In this work, three layers are considered: the air layer (refractive index  $n_1(\omega)$ ); the silica window layer (refractive index  $n_2(\omega)$ ); the PDMS layer (refractive index  $n'(\omega)$ ). Here  $\theta$  is the input angle of the laser beam,  $\gamma$  is the refractive angle in the silica window.  $\omega$  is the input laser frequency. The input angles of the pump/probe and Stokes beams used in this experiment are  $\sim 62^\circ$  and  $58^\circ$ , respectively. The refractive indices are:  $n_1(\omega) = 1.00$ ,  $n_2(\omega) = 1.46$ ,  $n'(\omega) = 1.41$ . The pump/probe beam frequency is 532 nm; the Stokes beam for PDMS 2910  $\text{cm}^{-1}$  frequency is 628 nm; the CARS signal is generated at 461 nm.

Inserting the numbers into the following equations for methyl group calculation:

$$\begin{aligned}
 \chi_{\text{eff},ssss}^{(3)} &= 1 \cdot L_{sy}(\omega_{\text{CARS}}) L_{sy}(\omega_p) L_{sy}(\omega_p) L_{sy}(\omega_s) \cdot \chi_{yyyy}^{(3)} \\
 \chi_{\text{eff},spps}^{(3)} &= \cos^2 \theta_p \cdot L_{sy}(\omega_{\text{CARS}}) L_{px}(\omega_p) L_{px}(\omega_p) L_{sy}(\omega_s) \cdot \chi_{yxxy}^{(3)} \\
 &\quad + \sin^2 \theta_p \cdot L_{sy}(\omega_{\text{CARS}}) L_{pz}(\omega_p) L_{pz}(\omega_p) L_{sy}(\omega_s) \cdot \chi_{yzyz}^{(3)}
 \end{aligned}$$

We can obtain:

$$\frac{\chi_{ssss,s}^{(3)}}{\chi_{spps,s}^{(3)}} \approx \frac{0.11\chi_{yyyy,s}^{(3)}}{0.084\chi_{yxy,s}^{(3)} + 0.056\chi_{yzzy,s}^{(3)}} \approx \frac{0.11\chi_{yyyy,s}^{(3)}}{0.14\chi_{yxy,s}^{(3)}} = 0.79 \frac{\chi_{yyyy,s}^{(3)}}{\chi_{yxy,s}^{(3)}} \quad (6.31)$$

Inserting the susceptibility tensor element ratios we obtained for the methyl symmetric and asymmetric stretching modes into equation (6.31), we have:

$$\frac{\chi_{ssss,s}^{(3)}}{\chi_{spps,s}^{(3)}} \approx 0.79 \frac{\chi_{yyyy,s}^{(3)}}{\chi_{yxy,s}^{(3)}} \approx 38$$

$$\frac{\chi_{ssss,s}^{(3)}}{\chi_{spps,s}^{(3)}} \approx 0.79 \frac{\chi_{yyyy,s}^{(3)}}{\chi_{yxy,s}^{(3)}} \approx 1$$

These results indicate that for the symmetric stretching mode, the value of third order susceptibility element detected using the spps polarization combination is much smaller than that detected using the ssss polarization. For the asymmetric stretching mode however, the values are similar. Since the CARS signal intensity is proportional to the square of the nonlinear susceptibility as shown in equation (6.1), in the spps polarization, the symmetric stretching signal intensity should be approximately 1400 times weaker than that in the ssss polarization; however, CARS signal intensities for the asymmetric stretching in two polarizations are similar. The ssss signal intensities for the methyl C-H symmetric and asymmetric stretching modes (as shown in Figure 6-5a) are ~1000 a.u. and ~50 a.u., respectively. Therefore, we can predict that in the spps polarization spectrum, the dominating peak should be the methyl asymmetric stretching mode, with no resolvable signal from the symmetric stretching mode ( $1000/1400 \approx 0.7$  a.u., below the noise level). The CARS spectrum of the PDMS film collected using spps polarization is shown in Figure 6-5b. We found that as predicted, only strong asymmetric stretching peak center at  $\sim 2968 \text{ cm}^{-1}$  could be detected. No symmetric stretching signal at  $\sim 2910 \text{ cm}^{-1}$  was resolvable. The fitting results show that  $\mathbf{A}_{spps,E} / \mathbf{\Gamma}_{spps,E} \approx 7.98$ , which is slightly different from  $\mathbf{A}_{ssss,E} / \mathbf{\Gamma}_{ssss,E} \approx 6.38$  measured



in the ssss polarization. This gives  $\chi_{ssss,as}^{(3)} / \chi_{spps,as}^{(3)} \approx 1.25$ , which is slightly bigger than 1 (obtained from our calculation). Such small difference perhaps caused by the inaccuracy in the Fresnel coefficient calculation for different polarization combinations (input angle error, refractive index error, laser fluctuations in different polarizations, etc.). The susceptibility matrices calculated for the methyl symmetric and asymmetric modes using  $r=0.20$  and  $r=0.24$  are shown in the Appendix 6.6. The above spectral analysis in spps polarization is based on  $r=0.20$ ; using  $r=0.24$  similar conclusions could be obtained.

In this work, the CARS experiment was performed using a reflection BOXCARS geometry.<sup>62</sup> However, the results obtained here are also valid for the collinear CARS configuration used for CARS imaging. In a laser scanning CARS microscopy system, two input laser beams are usually collimated collinearly, directed perpendicularly to the sample and focused using objective lenses. In such a geometry, the ssss polarization equals to the two input laser beams (pump/probe and Stokes) enter the sample with the same linear polarization; the spps polarization equals to the two linearly polarized input laser beams enter the sample with perpendicular polarizations. For the first case, if CARS is used to image PDMS methyl groups, the symmetric vibrational stretching signal should dominate the spectrum; for the latter case, the asymmetric stretching signal should dominate the spectrum, with an overall spectral intensity significant lower as compared to the intensity of the symmetric mode measured in the ssss case.

## 6.5 Conclusion

Theoretical work used for quantitatively interpretation of methyl group CARS spectra was developed in this research. Methyl symmetric and asymmetric C-H vibrational stretching intensity ratios measured in different polarization combinations were calculated using the bond additivity model and the Raman depolarization ratio. Additionally, a home-built BOXCARS system was

used to measure CARS signal from a PDMS film in the C-H range. The theoretical calculated results agreed well with the experimental data. We introduced a way to quantitatively interpret and predict the CARS vibrational spectral intensity ratios of different vibrational modes in different polarization combinations based on bond additivity method and Raman depolarization ratio. This work help develop in-depth understanding in vibrational stretching properties measured by CARS spectroscopy. Quantitative understanding and interpretation of CARS spectrum can add knowledge in basic third order nonlinear spectroscopy theory and will have important applications in CARS spectroscopy and microscopy for advanced signal analysis.

## **6.6 Appendix**

### **6.6.1 The General Form of Third Order Nonlinear Hyperpolarizability Tensor**

Using a 9 by 9 matrix to represent the tensor  $\gamma^{(3)}$ , we have the following form:

$$\begin{aligned}
\boldsymbol{\gamma}^{(3)} &= c\boldsymbol{\alpha}' \otimes \boldsymbol{\alpha}' = c \begin{bmatrix} \alpha'_{aa} & \alpha'_{ab} & \alpha'_{ac} \\ \alpha'_{ba} & \alpha'_{bb} & \alpha'_{bc} \\ \alpha'_{ca} & \alpha'_{cb} & \alpha'_{cc} \end{bmatrix} \otimes \begin{bmatrix} \alpha'_{aa} & \alpha'_{ab} & \alpha'_{ac} \\ \alpha'_{ba} & \alpha'_{bb} & \alpha'_{bc} \\ \alpha'_{ca} & \alpha'_{cb} & \alpha'_{cc} \end{bmatrix} \\
&= c \begin{bmatrix} \alpha'_{aa}\alpha'_{aa} & \alpha'_{aa}\alpha'_{ab} & \alpha'_{aa}\alpha'_{ac} & \alpha'_{ab}\alpha'_{aa} & \alpha'_{ab}\alpha'_{ab} & \alpha'_{ab}\alpha'_{ac} & \alpha'_{ac}\alpha'_{aa} & \alpha'_{ac}\alpha'_{ab} & \alpha'_{ac}\alpha'_{ac} \\ \alpha'_{aa}\alpha'_{ba} & \alpha'_{aa}\alpha'_{bb} & \alpha'_{aa}\alpha'_{bc} & \alpha'_{ab}\alpha'_{ba} & \alpha'_{ab}\alpha'_{bb} & \alpha'_{ab}\alpha'_{bc} & \alpha'_{ac}\alpha'_{ba} & \alpha'_{ac}\alpha'_{bb} & \alpha'_{ac}\alpha'_{bc} \\ \alpha'_{aa}\alpha'_{ca} & \alpha'_{aa}\alpha'_{cb} & \alpha'_{aa}\alpha'_{cc} & \alpha'_{ab}\alpha'_{ca} & \alpha'_{ab}\alpha'_{cb} & \alpha'_{ab}\alpha'_{cc} & \alpha'_{ac}\alpha'_{ca} & \alpha'_{ac}\alpha'_{cb} & \alpha'_{ac}\alpha'_{cc} \\ \alpha'_{ba}\alpha'_{aa} & \alpha'_{ba}\alpha'_{ab} & \alpha'_{ba}\alpha'_{ac} & \alpha'_{bb}\alpha'_{aa} & \alpha'_{bb}\alpha'_{ab} & \alpha'_{bb}\alpha'_{ac} & \alpha'_{bc}\alpha'_{aa} & \alpha'_{bc}\alpha'_{ab} & \alpha'_{bc}\alpha'_{ac} \\ \alpha'_{ba}\alpha'_{ba} & \alpha'_{ba}\alpha'_{bb} & \alpha'_{ba}\alpha'_{bc} & \alpha'_{bb}\alpha'_{ba} & \alpha'_{bb}\alpha'_{bb} & \alpha'_{bb}\alpha'_{bc} & \alpha'_{bc}\alpha'_{ba} & \alpha'_{bc}\alpha'_{bb} & \alpha'_{bc}\alpha'_{bc} \\ \alpha'_{ba}\alpha'_{ca} & \alpha'_{ba}\alpha'_{cb} & \alpha'_{ba}\alpha'_{cc} & \alpha'_{bb}\alpha'_{ca} & \alpha'_{bb}\alpha'_{cb} & \alpha'_{bb}\alpha'_{cc} & \alpha'_{bc}\alpha'_{ca} & \alpha'_{bc}\alpha'_{cb} & \alpha'_{bc}\alpha'_{cc} \\ \alpha'_{ca}\alpha'_{aa} & \alpha'_{ca}\alpha'_{ab} & \alpha'_{ca}\alpha'_{ac} & \alpha'_{cb}\alpha'_{aa} & \alpha'_{cb}\alpha'_{ab} & \alpha'_{cb}\alpha'_{ac} & \alpha'_{cc}\alpha'_{aa} & \alpha'_{cc}\alpha'_{ab} & \alpha'_{cc}\alpha'_{ac} \\ \alpha'_{ca}\alpha'_{ba} & \alpha'_{ca}\alpha'_{bb} & \alpha'_{ca}\alpha'_{bc} & \alpha'_{cb}\alpha'_{ba} & \alpha'_{cb}\alpha'_{bb} & \alpha'_{cb}\alpha'_{bc} & \alpha'_{cc}\alpha'_{ba} & \alpha'_{cc}\alpha'_{bb} & \alpha'_{cc}\alpha'_{bc} \\ \alpha'_{ca}\alpha'_{ca} & \alpha'_{ca}\alpha'_{cb} & \alpha'_{ca}\alpha'_{cc} & \alpha'_{cb}\alpha'_{ca} & \alpha'_{cb}\alpha'_{cb} & \alpha'_{cb}\alpha'_{cc} & \alpha'_{cc}\alpha'_{ca} & \alpha'_{cc}\alpha'_{cb} & \alpha'_{cc}\alpha'_{cc} \end{bmatrix} \\
&= \begin{bmatrix} \gamma_{aaaa}^{(3)} & \gamma_{aaab}^{(3)} & \gamma_{aaac}^{(3)} & \gamma_{abaa}^{(3)} & \gamma_{abab}^{(3)} & \gamma_{abac}^{(3)} & \gamma_{acaa}^{(3)} & \gamma_{acab}^{(3)} & \gamma_{acac}^{(3)} \\ \gamma_{aaba}^{(3)} & \gamma_{aabb}^{(3)} & \gamma_{aabc}^{(3)} & \gamma_{abba}^{(3)} & \gamma_{abbb}^{(3)} & \gamma_{abbc}^{(3)} & \gamma_{acba}^{(3)} & \gamma_{acbb}^{(3)} & \gamma_{acbc}^{(3)} \\ \gamma_{aaca}^{(3)} & \gamma_{aacb}^{(3)} & \gamma_{aac}^{(3)} & \gamma_{abca}^{(3)} & \gamma_{abcb}^{(3)} & \gamma_{abcc}^{(3)} & \gamma_{acca}^{(3)} & \gamma_{accb}^{(3)} & \gamma_{accc}^{(3)} \\ \gamma_{baaa}^{(3)} & \gamma_{baab}^{(3)} & \gamma_{baac}^{(3)} & \gamma_{bbaa}^{(3)} & \gamma_{bbab}^{(3)} & \gamma_{bbac}^{(3)} & \gamma_{bcaa}^{(3)} & \gamma_{bcab}^{(3)} & \gamma_{bcac}^{(3)} \\ \gamma_{baba}^{(3)} & \gamma_{bab}^{(3)} & \gamma_{bab}^{(3)} & \gamma_{bbba}^{(3)} & \gamma_{bbbb}^{(3)} & \gamma_{bbbc}^{(3)} & \gamma_{bcba}^{(3)} & \gamma_{bcbb}^{(3)} & \gamma_{bcbe}^{(3)} \\ \gamma_{baca}^{(3)} & \gamma_{bacb}^{(3)} & \gamma_{bacc}^{(3)} & \gamma_{bbca}^{(3)} & \gamma_{bbcb}^{(3)} & \gamma_{bbcc}^{(3)} & \gamma_{bcc}^{(3)} & \gamma_{bccb}^{(3)} & \gamma_{bcc}^{(3)} \\ \gamma_{caaa}^{(3)} & \gamma_{caab}^{(3)} & \gamma_{caac}^{(3)} & \gamma_{cbaa}^{(3)} & \gamma_{cbab}^{(3)} & \gamma_{cbac}^{(3)} & \gamma_{ccaa}^{(3)} & \gamma_{ccab}^{(3)} & \gamma_{ccac}^{(3)} \\ \gamma_{caba}^{(3)} & \gamma_{cabb}^{(3)} & \gamma_{cab}^{(3)} & \gamma_{cbba}^{(3)} & \gamma_{cbbb}^{(3)} & \gamma_{cbbc}^{(3)} & \gamma_{ccba}^{(3)} & \gamma_{ccbb}^{(3)} & \gamma_{ccbc}^{(3)} \\ \gamma_{caca}^{(3)} & \gamma_{cacb}^{(3)} & \gamma_{cacc}^{(3)} & \gamma_{cbca}^{(3)} & \gamma_{cbcb}^{(3)} & \gamma_{cbcc}^{(3)} & \gamma_{ccca}^{(3)} & \gamma_{cccb}^{(3)} & \gamma_{cccc}^{(3)} \end{bmatrix}
\end{aligned}$$

The form of  $\boldsymbol{\chi}^{(3)}$  is similar as  $\boldsymbol{\gamma}^{(3)}$  but change  $\gamma^{(3)}$  to  $\chi^{(3)}$ . The indices: a~x, b~y, c~z.

For example,  $\chi_{ssss}^{(3)}$  measures  $\chi_{yyyy}^{(3)}$ , corresponds to  $\gamma_{bbbb}^{(3)}$ , equals to  $c\alpha'_{bb}\alpha'_{bb}$ .

## 6.6.2 The Calculated Susceptibility Matrices

Symmetric stretching r=0.20

$$\chi^{(3)} = Nc \begin{bmatrix} 0.42 & 0 & 0 & 0 & 0.0088 & 0 & 0 & 0 & 0.0088 \\ 0 & 0.40 & 0 & 0.0088 & 0 & 0 & 0 & 0 & 0 \\ 0 & 0 & 0.40 & 0 & 0 & 0 & 0.0088 & 0 & 0 \\ 0 & 0.0088 & 0 & 0.40 & 0 & 0 & 0 & 0 & 0 \\ 0.0088 & 0 & 0 & 0 & 0.42 & 0 & 0 & 0 & 0.0088 \\ 0 & 0 & 0 & 0 & 0 & 0.40 & 0 & 0.0088 & 0 \\ 0 & 0 & 0.0088 & 0 & 0 & 0 & 0.40 & 0 & 0 \\ 0 & 0 & 0 & 0 & 0 & 0.0088 & 0 & 0.40 & 0 \\ 0.0088 & 0 & 0 & 0 & 0.0088 & 0 & 0 & 0 & 0.42 \end{bmatrix}$$

Asymmetric stretching  $r=0.20$

$$\chi^{(3)} = Nc \begin{bmatrix} 0.088 & 0 & 0 & 0 & 0.066 & 0 & 0 & 0 & 0.066 \\ 0 & -0.044 & 0 & 0.066 & 0 & 0 & 0 & 0 & 0 \\ 0 & 0 & -0.044 & 0 & 0 & 0 & 0.066 & 0 & 0 \\ 0 & 0.066 & 0 & -0.044 & 0 & 0 & 0 & 0 & 0 \\ 0.066 & 0 & 0 & 0 & 0.088 & 0 & 0 & 0 & 0.066 \\ 0 & 0 & 0 & 0 & 0 & -0.044 & 0 & 0.066 & 0 \\ 0 & 0 & 0.066 & 0 & 0 & 0 & -0.044 & 0 & 0 \\ 0 & 0 & 0 & 0 & 0 & 0.066 & 0 & -0.044 & 0 \\ 0.066 & 0 & 0 & 0 & 0.066 & 0 & 0 & 0 & 0.088 \end{bmatrix}$$

Symmetric stretching  $r=0.24$

$$\chi^{(3)} = Nc \begin{bmatrix} 0.46 & 0 & 0 & 0 & 0.0076 & 0 & 0 & 0 & 0.0076 \\ 0 & 0.45 & 0 & 0.0076 & 0 & 0 & 0 & 0 & 0 \\ 0 & 0 & 0.45 & 0 & 0 & 0 & 0.0076 & 0 & 0 \\ 0 & 0.0076 & 0 & 0.45 & 0 & 0 & 0 & 0 & 0 \\ 0.0076 & 0 & 0 & 0 & 0.46 & 0 & 0 & 0 & 0.0076 \\ 0 & 0 & 0 & 0 & 0 & 0.45 & 0 & 0.0076 & 0 \\ 0 & 0 & 0.0076 & 0 & 0 & 0 & 0.45 & 0 & 0 \\ 0 & 0 & 0 & 0 & 0 & 0.0076 & 0 & 0.45 & 0 \\ 0.0076 & 0 & 0 & 0 & 0.0076 & 0 & 0 & 0 & 0.46 \end{bmatrix}$$

Asymmetric stretching  $r=0.24$

$$\chi^{(3)} = Nc \begin{bmatrix} 0.079 & 0 & 0 & 0 & 0.059 & 0 & 0 & 0 & 0.059 \\ 0 & -0.040 & 0 & 0.059 & 0 & 0 & 0 & 0 & 0 \\ 0 & 0 & -0.040 & 0 & 0 & 0 & 0.059 & 0 & 0 \\ 0 & 0.059 & 0 & -0.040 & 0 & 0 & 0 & 0 & 0 \\ 0.059 & 0 & 0 & 0 & 0.079 & 0 & 0 & 0 & 0.059 \\ 0 & 0 & 0 & 0 & 0 & -0.040 & 0 & 0.059 & 0 \\ 0 & 0 & 0.059 & 0 & 0 & 0 & -0.040 & 0 & 0 \\ 0 & 0 & 0 & 0 & 0 & 0.059 & 0 & -0.040 & 0 \\ 0.059 & 0 & 0 & 0 & 0.059 & 0 & 0 & 0 & 0.079 \end{bmatrix}$$

## 6.5 References

1. Maker, P.; Terhune, R., *Phys. Rev.* **1965**, *137*, A801.
2. Tolles, W. M.; Nibler, J.; McDonald, J.; Harvey, A., *Appl. Spectrosc.* **1977**, *31*, 253-271.
3. PR REGNIER, F. M.; Taran, J., *AIAA Journal* **1974**, *12*, 826-831.
4. Schrötter, H.; Berger, H.; Boquillon, J.; Lavorel, B.; Millot, G., *J. Raman Spectrosc.* **1990**, *21*, 781-789.
5. Moya, F.; Druet, S.; Taran, J., *Opt. Commun.* **1975**, *13*, 169-174.
6. Hall, R., *Combust. Flame* **1979**, *35*, 47-60.
7. Klick, D.; Marko, K. A.; Rimai, L., *Appl. Opt.* **1981**, *20*, 1178-1181.
8. Eckbreth, A. C., *Laser diagnostics for combustion temperature and species*. CRC Press: 1996; Vol. 3.
9. Hassel, E. P.; Linow, S., *Meas. Sci. Technol.* **2000**, *11*, R37.
10. Miles, R.; Laufer, G.; Bjorklund, G., *Appl. Phys. Lett.* **1977**, *30*, 417-419.
11. Itzkan, I.; Leonard, D. A., *Appl. Phys. Lett.* **1975**, *26*, 106-108.
12. Joo, T.; Albrecht, A., *J. Chem. Phys.* **1993**, *99*, 3244-3251.
13. Nestor, J.; Spiro, T. G.; Klauminzer, G., *Proc. Natl. Acad. Sci. U. S. A.* **1976**, *73*, 3329-3332.
14. Schmidt, S. C.; Moore, D. S., *Acc. Chem. Res.* **1992**, *25*, 427-432.
15. Moore, D.; Schmidt, S.; Shaw, M.; Johnson, J., *J. Chem. Phys.* **1989**, *90*, 1368-1376.
16. Hellwig, H.; Daniels, W. B.; Hemley, R. J.; Mao, H.-k.; Gregoryanz, E.; Yu, Z., *J. Chem. Phys.* **2001**, *115*, 10876-10882.
17. Wen, X.; Chen, S.; Dlott, D. D., *J. Opt. Soc. Am. B* **1991**, *8*, 813-819.
18. Grisch, F.; Pealat, M.; Bouchardy, P.; Taran, J.; Bar, I.; Heflinger, D.; Rosenwaks, S., *Appl. Phys. Lett.* **1991**, *59*, 3516-3518.
19. Zhang, C.; Wang, J.; Khmaladze, A.; Liu, Y.; Ding, B.; Jasensky, J.; Chen, Z., *Opt. Lett.* **2011**, *36*, 2272-2274.
20. Portnov, A.; Rosenwaks, S.; Bar, I., *Appl. Phys. Lett.* **2008**, *93*, 041115.
21. Katz, O.; Natan, A.; Silberberg, Y.; Rosenwaks, S., *Appl. Phys. Lett.* **2008**, *92*, 171116.
22. Li, H.; Harris, D. A.; Xu, B.; Wrzesinski, P. J.; Lozovoy, V. V.; Dantus, M., *Opt. Express* **2008**, *16*, 5499-5504.
23. Natan, A.; Levitt, J. M.; Graham, L.; Katz, O.; Silberberg, Y., *Appl. Phys. Lett.* **2012**, *100*, 051111.
24. Portnov, A.; Bar, I.; Rosenwaks, S., *Appl. Phys. B* **2010**, *98*, 529-535.
25. Bremer, M. T.; Wrzesinski, P. J.; Butcher, N.; Lozovoy, V. V.; Dantus, M., *Appl. Phys. Lett.* **2011**, *99*, 101109.
26. Cheng, J.-X.; Xie, X. S., *J. Phys. Chem. B* **2004**, *108*, 827-840.
27. Rodriguez, L. G.; Lockett, S. J.; Holtom, G. R., *Cytometry A* **2006**, *69*, 779-791.
28. El-Diasty, F., *Vib. Spectrosc.* **2011**, *55*, 1-37.
29. Duncan, M. D.; Reintjes, J.; Manuccia, T., *Opt. Lett.* **1982**, *7*, 350-352.
30. Evans, C. L.; Xie, X. S., *Annu. Rev. Anal. Chem.* **2008**, *1*, 883-909.
31. Zumbusch, A.; Holtom, G. R.; Xie, X. S., *Phys. Rev. Lett.* **1999**, *82*, 4142-4145.
32. Evans, C. L.; Potma, E. O.; Puoris' haag, M.; Côté, D.; Lin, C. P.; Xie, X. S., *Proc. Natl. Acad. Sci. U. S. A.* **2005**, *102*, 16807-16812.
33. Cheng, J.-X.; Jia, Y. K.; Zheng, G.; Xie, X. S., *Biophys. J.* **2002**, *83*, 502-509.
34. Cheng, J.-X.; Book, L. D.; Xie, X. S., *Opt. Lett.* **2001**, *26*, 1341-1343.

35. Cheng, J.-X.; Volkmer, A.; Xie, X. S., *J. Opt. Soc. Am. B* **2002**, *19*, 1363-1375.
36. Volkmer, A.; Cheng, J.-X.; Xie, X. S., *Phys. Rev. Lett.* **2001**, *87*, 023901.
37. Potma, E. O.; Evans, C. L.; Xie, X. S., *Opt. Lett.* **2006**, *31*, 241-243.
38. Yue, S.; Slipchenko, M. N.; Cheng, J. X., *Laser Photon. Rev.* **2011**, *5*, 496-512.
39. Potma, E. O.; Xie, X. S., *J. Raman Spectrosc.* **2003**, *34*, 642-650.
40. Cheng, J.-x.; Volkmer, A.; Book, L. D.; Xie, X. S., *J. Phys. Chem. B* **2002**, *106*, 8493-8498.
41. Nan, X.; Cheng, J.-X.; Xie, X. S., *J. Lipid Res.* **2003**, *44*, 2202-2208.
42. Zumbusch, A.; Langbein, W.; Borri, P., *Prog. Lipid Res.* **2013**, *52*, 615-632.
43. Cheng, J.-x.; Volkmer, A.; Book, L. D.; Xie, X. S., *J. Phys. Chem. B* **2001**, *105*, 1277-1280.
44. Dudovich, N.; Oron, D.; Silberberg, Y., *Nature* **2002**, *418*, 512-514.
45. Shi, K.; Li, H.; Xu, Q.; Psaltis, D.; Liu, Z., *Phys. Rev. Lett.* **2010**, *104*, 093902.
46. Kee, T. W.; Cicerone, M. T., *Opt. Lett.* **2004**, *29*, 2701-2703.
47. Davis, R. P.; Moad, A. J.; Goeken, G. S.; Wampler, R. D.; Simpson, G. J., *J. Phys. Chem. B* **2008**, *112*, 5834-5848.
48. Hirose, C.; Akamatsu, N.; Domen, K., *Appl. Spectrosc.* **1992**, *46*, 1051-1072.
49. Hirose, C.; Akamatsu, N.; Domen, K., *J. Chem. Phys.* **1992**, *96*, 997-1004.
50. Wang, H. F.; Gan, W.; Lu, R.; Rao, Y.; Wu, B. H., *Int. Rev. Phys. Chem.* **2005**, *24*, 191-256.
51. Wei, X.; Zhuang, X.; Hong, S. C.; Goto, T.; Shen, Y., *Phys. Rev. Lett.* **1999**, *82*, 4256-4259.
52. Zhuang, X.; Miranda, P.; Kim, D.; Shen, Y., *Phys. Rev. B* **1999**, *59*, 12632-12640.
53. Zhang, C.; Chen, Z., *J. Phys. Chem. C* **2013**, *117*, 3903-3914.
54. Wu, H.; Zhang, W.-k.; Gan, W.; Cui, Z.-f.; Wang, H.-f., *J. Chem. Phys.* **2006**, *125*, 133203.
55. Wei, X.; Hong, S.-C.; Zhuang, X.; Goto, T.; Shen, Y., *Phys. Rev. E: Stat., Nonlinear, Soft Matter Phys.* **2000**, *62*, 5160-5172.
56. Nguyen, K. T.; Le Clair, S. V.; Ye, S.; Chen, Z., *J. Phys. Chem. B* **2009**, *113*, 12169-12180.
57. Nguyen, K. T.; King, J. T.; Chen, Z., *J. Phys. Chem. B* **2010**, *114*, 8291-8300.
58. Zhang, C.; Myers, J. N.; Chen, Z., *Soft Matter* **2013**, *9*, 4738-4761.
59. Allemand, C. D., *Appl. Spectrosc.* **1970**, *24*, 348-353.
60. Maxfield, J.; Shepherd, I., *Chem. Phys.* **1973**, *2*, 433-444.
61. Maxfield, J.; Shepherd, I., *Chem. Phys. Lett.* **1973**, *19*, 541-545.
62. Bloembergen, N.; Chen, K. H.; Lü, C. Z.; Mazur, E., *J. Raman Spectrosc.* **1990**, *21*, 819-825.

## **CHAPTER 7**

### **SUMMARY AND CONCLUSIONS**

The research focus of this thesis can be summarized in four parts: (1) the applications of SFG spectroscopy in understanding interfacial molecular structures of various adhesive materials, more specifically silicone and epoxy adhesives, to elucidate their adhesion mechanisms to different substrates; (2) the applications of SFG spectroscopy supplemented by ATR-FTIR spectroscopy for studying lipids dynamics in supported lipid bilayers used to mimic biological membranes; (3) the development of new analytical platforms to integrate SFG spectroscopy with other optical techniques for multimodal sample studies; (4) the quantitative interpretation of the spectral measurements in CARS spectroscopy with the help of bond additivity method and Raman depolarization ratio. In this last chapter, we will summarize the major conclusions and accomplishments discussed in this thesis.

First of all, SFG spectroscopy was utilized to study the interfaces between PDMS and various substrates to understand adhesion mechanisms at such interfaces. We developed an advanced method to determine PDMS methyl group orientations at interfaces. We also showed that the traditional way to deduce the orientation of a single methyl group is no longer valid for PDMS methyl group orientation analysis, which is due to the geometry of two adjacent methyl groups bonded with a fixed angle in a PDMS molecule. The calculation methodology developed in our work considered the two bonded methyl groups as a whole and derived both the tilt and twist angles of the entire group. We found that at the PET/PDMS interface, the methyl groups tend



to have large tilt angles and small twist angles, indicating that they tend to ‘lie down’ at the interface. However, at the silica/PDMS interface, methyl groups tend to have broader tilt angle distributions with large twist angles. Additionally, we developed a method to obtain the absolute orientations of such methyl groups at interfaces, from the interfacial SFG signal interference with the nonresonant signal generated from a TiO<sub>2</sub> film deposited beneath the sample. With the help of substrate surface hydrophobicity measurements, the absolute dipole orientation of methyl groups at interfaces could be determined. We found that the interfacial PDMS methyl group orientations could be well correlated to the substrate surface hydrophobicity properties.

In order to understand the adhesion promotion mechanisms of silane molecules, SFG was applied to investigate the silane behaviors at PDMS/PET interfaces. We also developed a mechanical adhesion strength test method to correlate the adhesion strength to interfacial molecular structures measured using SFG. The molecular structures were studied quantitatively through SFG spectral fitting. The results showed that silane methoxy or ethoxy headgroups play important roles in the interfacial chemical reaction or crosslinking, which decreases SFG signal from such groups at the interfaces. The correlation with adhesion test showed that such headgroup signal decrease observed in SFG spectra indicates interfacial adhesion promotion which usually leads to strong adhesion.

Additionally, the adhesion study was extended to polymer/epoxy interfaces. Epoxy materials are widely used in industry, especially as underfills for microelectronic devices. Understanding their adhesion to various substrates can provide further knowledge in preventing epoxy failures and developing better epoxy materials for industrial applications. In our work we systematically studied the interfacial molecular structures and their relations to adhesion. We found that randomized interfacial structures, which usually generate weak SFG signals, lead to

good adhesion; ordered interfacial structures with methyl groups, which usually have strong SFG signals, indicate poor adhesion. The conclusion was drawn using a model epoxy system and later was tested using two commercial epoxies. We further extensively investigated the adhesion mechanism between epoxy-amine mixtures and PET substrates using both SFG and ATR-FTIR spectroscopies. Based on our observations and analysis, an adhesion mechanism was proposed. This work developed deeper insight in adhesion mechanisms of epoxy adhesives.

We believe that SFG is a powerful technique to help elucidate molecular structures of buried interfaces and the underlined mechanisms for polymer adhesion. SFG is ready to be used to investigate more complicated adhesive interfaces important in industrial applications. One example is to apply SFG to examine buried interfaces of commercial underfill materials to understand their adhesion mechanisms and possible failure mechanism at high temperatures and high humidity levels. This research is currently being carried out in our lab.

Furthermore, we combined SFG and ATR-FTIR to study the lipid transbilayer movements in a supported membrane bilayers induced by PEI molecules. PEI is a positively charged polyelectrolyte widely used in gene delivery as transfection agent. It has been reported that PEI has cytotoxicity which can lead to cell apoptosis. Our research aim to further understand PEI's cytotoxicity in a biological system through studying its interaction with membrane bilayers. Using SFG, we found that PEI molecules tend to interact with lipid molecules through electrostatic interactions. PEI can significantly induce lipid transbilayer movement at near physiological temperature, but not at room temperature. It tends to have stronger interaction with negatively charged lipids as compared to zwitterionic lipids. Comparing different PEI structures we also found that the branched PEI tends to have stronger interactions with bilayers than the linear PEI, indicating that the branched PEI has higher toxicity. ATR-FTIR data was used to supplement SFG

data to further confirm that the observation in SFG is due to the lipid transbilayer movement, rather than lipid bilayer damage or removal from the substrate. This work provided additional knowledge in further understanding of PEI's cytotoxicity. It also showed that the combined SFG and ATR-FTIR investigation is powerful for studying bilayer interactions with polyelectrolytes as well as with other materials/molecules such as nanomaterials and drug molecules. Nanomaterials have been extensively used for drug delivery and they need to interact with cell membranes to enter into cells. Similarly, drug molecules also extensively interact with cell membranes in biological systems. The method developed in this chapter is currently being used to study molecular interactions between lipid bilayers and gold nanoparticles, polymer nanomaterials, dendrimers, chlorpromazine and amantadine.

Besides applications of SFG to study adhesion mechanisms and molecular interactions at model cell membranes, we were also interested in developing new research platforms by combining SFG with other techniques to perform multimodal sample characterization. We first combined SFG with CARS spectroscopy to perform surface and bulk spectral measurements of a sample in the same environment with the same experimental geometry. This can effectively avoid possible experimental errors caused by varied sample geometry and sample environment studied using different techniques. The system we developed here was further applied to study polymer thin films before and after plasma treatments, as well as to study the plasticizer migrations in PVC matrix. This system can be used to study surface and bulk structures of many materials in different chemical environments. For example, one current project in our lab is to use this system to study surface, interfacial, and bulk structures of low dielectric constant materials after different treatments for microelectronic industry.

SFG was further combined with optical microscopy to study buried heterogeneous biointerfaces. We successfully developed a platform utilizing the advantages of both TIR-SFG configuration and optical microscopy. The laser beam spot can be tracked to study the desired sample locations while SFG signal was mainly contributed from the sample/substrate interface without the interference of other layer above such buried interface. We used the system to track laser induced photo-damage. We also studied interfacial molecular structure changes induced by a single mouse oocyte. Furthermore, we showed that the system can be used to study buried interface between marine tissue and underwater surface. Different biological organisms adhere underwater surfaces differently with very different interfacial molecular structures. One important application of this new system is to investigate interactions between a surface and single cell – the optical microscope can be used to locate the single cell and SFG spectra can be collected between this single cell and various surfaces.

Additionally, we upgraded our combined SFG and optical microscopy system to achieve SFG spectroscopy and TIRF microscopy measurement. Benefit from our OPG/OPA system in SFG spectrometer, multi-wavelength TIRF imaging could be achieved. Proof of principle experimental results showed that our system can almost simultaneously perform SFG measurement with TIRF imaging, providing interfacial molecular structural information with fluorescent label dynamics information. TIRF is a widely used microscopy technique in biological science. The combined SFG and TIRF platform can help to extend SFG to more biological interfacial studies. Additionally, fluorescence microscopy can be used to study enzymatic activity while SFG spectroscopy can be used to study interfacial enzyme molecular structure to achieve the structure-function relationship of enzyme or other biomolecules at interfaces.

In order to achieve quantitative interpretation of CARS spectra in different polarization combinations, we developed a theory by connecting Raman depolarization ratio measurement with CARS measurement with the help of bond additivity method. Using this methodology, we deduced the symmetric and asymmetric peak ratio of PDMS methyl groups which showed good agreement with experimental data. The method developed here can be used for spectral analysis of other vibrational modes of other functional groups. This work has significance in quantitative understanding of CARS measurement and can help to improve signal analysis for advanced CARS spectroscopy and microscopy.

In summary, this thesis involves theoretical, application, and technical development research in nonlinear vibrational spectroscopy. We mainly focused on SFG and CARS spectroscopies, with supplemental ATR-FTIR spectroscopy and other techniques. The contributions of this thesis research are reported in several journal publications<sup>1-9</sup> as well as some manuscripts under-review or ready for submission<sup>10-11</sup>. Chapter 1 was partially adapted from reference 4. Chapter 2 was adapted from references 2, 3 and 6. Chapter 3 was partially adapted from reference 5. Chapter 4 was partially adapted from reference 9. Chapter 5 was partially adapted from references 1, 7 and 8. This thesis also has adaptation from other unpublished manuscripts (references 10-11).

As a label free technique, vibrational spectroscopy has great advantages in research in many different disciplines such as chemistry, physics, materials science, and biomedical engineering. Nonlinear vibrational spectroscopy would keep finding novel applications in basic science and industry-driven research. In order to achieve better understanding of the measurement results, the theoretical advancement in nonlinear spectroscopy is still an important direction in the future, without which the physical picture behind the spectra could not be fully depicted.

Additionally, the technical development in spectroscopy systems would also play an important role in extending the applications of nonlinear vibrational spectroscopy to new research areas.

## References

1. Zhang, C.; Wang, J.; Khmaladze, A.; Liu, Y.; Ding, B.; Jasensky, J.; Chen, Z., *Opt. Lett.* **2011**, *36*, 2272-2274.
2. Zhang, C.; Shephard, N. E.; Rhodes, S. M.; Chen, Z., *Langmuir* **2012**, *28*, 6052-6059.
3. Zhang, C.; Chen, Z., *Langmuir* **2013**, *29*, 610-619.
4. Zhang, C.; Myers, J. N.; Chen, Z., *Soft Matter* **2013**, *9*, 4738-4761.
5. Zhang, C.; Hankett, J.; Chen, Z., *ACS Appl. Mater. Interfaces* **2012**, *4*, 3730-3737.
6. Zhang, C.; Chen, Z., *J. Phys. Chem. C* **2013**, *117*, 3903-3914.
7. Zhang, C.; Jasensky, J.; Leng, C.; Del Grosso, C.; Smith, G. D.; Wilker, J. J.; Chen, Z., *Opt. Lett.* **2014**, *39*, 2715-2718.
8. Zhang, C.; Jasensky, J.; Wu, J.; Chen, Z. SPIE BiOS, 2014; pp 894712-894712-894718.
9. Zhang, C.; Wu, F.-g.; Hu, P.; Chen, Z., *J. Phys. Chem. C in press*.
10. Zhang, C.; Wang, J.; Ding, B.; Jasensky, J., *Under review*.
11. Zhang, C.; Myers, J. N.; Chen, Z., *Ready for submission*.